Philipps Universität
Marburg

Surface Modification and Functionalization of Colloidal Nanoparticles

Dissertation
zur Erlangung des Doktorgrades
der Naturwissenschaften
(Dr. rer. nat.)

dem
Fachbereich Physik
der Philipps-Universität Marburg
vorgelegt von
Zulqurnain Ali
aus
Pakistan
Marburg/Lahn, 2011

Vom Fachbereich Physik der Philipps-Universität

Als Dissertation angenommen am

Erstgutachter: Prof. Dr. Wolfgang J. Parak

Zweitgutachter: Prof. Dr. Wolfram Heimbrodt

Tag der mündlichen Prüfung:

Zusammenfassung

Den Schwerpunkt dieser Dissertation stellt die Synthese multifunktionaler Nanopartikel, sowie deren Oberflächen-Modifikation und –Funktionalisierung für biologische Anwendungen dar. Kolloidale Nanopartikel haben gemeinsame, größenabhängige physikalische und chemische Eigenschaften inne, die in einer Weise kontrollierbar sind, wie es für makroskopische Festkörper nicht möglich ist.

Multimodale, molekulare Bildgebung ist die synergetische Kombination aus zwei oder mehr Detektionstechniken, ermöglicht durch multimodale Objekte und Bildgebungsverfahren und gewährleistet eine verbesserte Visualisierung biologischer Materialien. Einige Prototypen, die auf multimodalen Nanopartikeln basieren, sind entwickelt worden. Kolloidale Nanopartikel, aufgebaut aus einem anorganischen Kern und einer Polymerhülle wurden synthetisiert. Sowohl der Kern als auch die Polymerhülle können je nach Zweckmäßigkeit für die Bildgebung/Detektion fluoreszent, magnetisch oder radioaktiv sein. Das Polymer enthält Carboxygruppen, die die Partikel durch elektrostatische Repulsion stabilisieren und darüber hinaus als Bindungsstellen für weitere chemische Funktionalisierungen zur Verfügung stehen. Hydrophobe Nanopartikel (CdSe/ZnS, Fe_2O_3 oder Gold-198) wurden anhand unterschiedlich modifizierter Polymere (mit Gadolinium, organischen Fluorophoren oder Indium-111) in eine wässrige Phase überführt.

Zur Untersuchung nanopartikel-basierter Sensoren wurde eine FRET-Struktur eingeführt, in der ein organischer Farbstoff (ATTO-590) als Akzeptor direkt in die Polymerhülle eingebettet wurde, die die kolloidale Stabilität der als Donor fungierenden CdSe/ZnS Quantenpunkte generierte. Zur Detektion von Protonen wurden sowohl negativ als auch positiv geladene Goldnanopartikel mit einem ionensensitiven Farbstoff (SNARF) modifiziert. Es wurde außerdem demonstriert, dass das Sensor-Signal nicht durch die reale Konzentration, sondern die lokale Konzentration, in der „nano“-Umgebung der Partikeloberfläche generiert wird.

Darüber hinaus wurde in einer kollaborativen Arbeit demonstriert, dass Nanopartikel-Kerne kombiniert mit Polymerhüllen für die Induktion von Zellschädigungen verantwortlich sind, nicht jedoch die Hüllen allein. Es wurde festgestellt, dass das Aufnahmeverhalten und die zellulär unfreundlichen Effekte von der Dauer der Aussetzung, vom Zelltyp und der Zellkultur abhängen. Außerdem wurden Goldnanopartikel mit und ohne PEG-Modifizierung in der „rainbow trout gill“ Zelllinie RTGill-W untersucht, wobei Goldnanopartikel mit PEG-Modifizierung eine geringere Toxizität auf die Alge als nicht PEG-modifizierte Partikel zeigten.

Abstract

The principle focus of this dissertation is the synthesis of multifunctional nanoparticles, their surface modification and functionalization for biological applications. Colloidal nanoparticles possess unique size dependent physical and chemical properties that can be controlled in a manner that is not possible in bulk size materials.

Multi modal molecular imaging is the synergistic combination of two or more detection techniques, enabled by multi modal probes and imaging agents and ensures enhanced visualization of biological materials. Some prototypical probes based on multimodal nanoparticles have been developed. Colloidal nanoparticles composed of an inorganic corematerial and a polymer shell have been synthesized. Both, the core and the polymer shell can be fluorescent, magnetic, or radioactive for appropriate imaging / detection. The polymer contains carboxylic groups that stabilize the particles by electrostatic repulsion and moreover provide anchor groups for further chemical functionalization. Hydrophobic nanoparticles (CdSe/ZnS, Fe_2O_3 or Gold-198) have been transferred to an aqueous phase by means of modified polymers (with Gadolinium, Organic fluorophores or Indium-111).

For the study of sensors based on nanoparticles, a FRET geometry has been introduced, in which the organic dye (ATTO-590) as an acceptor is directly incorporated into the polymer shell used to provide colloidal stability for the CdSe/ZnS quantum dot donor. For the detection of protons, gold nanoparticles coated with negatively or positively charged polymers have been modified with an ion sensitive dye (SNARF). It has been demonstrated that sensor read-out should be thus not determined by the bulk ion concentration, but by the local ion concentration in the “nano”-environment of the nanoparticles surface.

In a collaborative work it was moreover demonstrated that nanoparticle~~s~~ cores combined with the polymer shells are responsible for the induction of proinflammatory effects and not the shells alone. It is concluded that the uptake behavior and the proinflammatory response upon particle exposure are dependent on the time, cell type, and cell culture. In addition gold nanoparticles with and without PEG modification have been investigated in “rainbow trout gill” cell line RTGill-W and it was observed that the PEG modified goldnanoparticles were found to be less toxic to the alga compared to the non PEG modified particles.

Acknowledgement

Thanks God, the merciful and the passionate, for answering my prayers and providing me the opportunity to step in the excellent world of science. To be able to step strong and smooth in this way, I have also been supported by many people to whom I would like to express my deepest gratitude.

First and foremost, I would like to thank my adviser, Prof. Wolfgang J. Parak, for his understanding, encouraging and personal guidance has provided a good basis for the present thesis. His wide knowledge and logical way of thinking have been of great value for me.

I am gratefully acknowledging Dr. Feng Zhang, for his advice, supervision, and crucial contribution. His extensive discussions around my work and interesting explorations in experiments have been very helpful for this study. I have also benefited by advice and guidance from Ralph Sperling, many thanks for the interesting and fruitful scientific discussions, his critical but open minded attitude taught me a lot.

I wish to thank Prof. Wolfram Heimbrodt and Tobias Niebling for time resolved optical spectroscopy and Prof. Andreas Seubret, Jürgen Knöll and David Nette for ICP-MS from university Marburg. I would extend my thanks to Prof. Anne Feltz, Dr. Martin Oheim and Aleksey V. Yakovlev from University Paris, France for single particle FRET detection. I also wish to thank Dr. Barbara Rothen-Rutishauser, Andrea D. Lehmann and Christina Bradenberger from university of Bern, Switzerland for fruitful collaboration in field of biological application of nanoparticles.

I would especially thanks to Prof. Wolfgang Kreyling and Alexander Wenk from our collaboration group at the Helmholtz Zentrum München, Geramny for radioactivity experiments. Dr. Maria F. Casula from University of Cagliari, Italy is highly acknowledged for magnetic resonance imaging of multifunctional nanoparticles. Also many thanks to Karen Van Hoecke from Ghent University Belgium for examining gold nanoparticle's toxicity.

Furthermore, I would like to thank Frau Sigrid Thomas and Frau Stefanie Kramer for administrative work. Especially many thanks go to Andreas Rentzos who helped for computer problems and other technical stuff.

I would like to thank Dr. Adnan Sarfraz for proof reading of this manuscript and finalize it for submission. Vielen danke for Dominik Huehn for translating abstract in German language.

I would like to thank Higher Education Commission of Pakistan (HEC) and German Academic Exchange Service (DAAD) for financial support of PhD and stay in Germany.

I am indebted to all my current and old lab fellows for providing a stimulating and fun environment, to learn and grow. Thanks biophotonics for kicker matches and having much more fun with my cooking.

I would **not** like to thank to Azhar, Waqas and Faheem during my stay in Marburg. As I always cooked delicious dishes for them and they enjoyed a lot my company; love u guys. Especially, Waqas for destroying my surprise planned visit to Berlin and my lab partner, Faheem who always stole gels from my boxes; thanks for useless scientific discussions. I would really appreciate all my friends in Berlin, who really mange fun in Berlin.

Most importantly, my parents Madad Shah and Niaz Fatima who receive my deepest gratitude and love for their dedication, whose foresight and values paved the way for a privileged education. To my brother Subtain who gently offer counsel and unconditional support at each turn of the road. My heartful thank to my sisters for financing my school, college life and always praying for my success. Thanks to my bhabi Iram for moral support and prayers. I cannot find words to thank my cousins Zagham and Asim for taking my family responsibilities in my absence in Pakistan.

Last but not least, I owe my loving thanks to my wife Samia for her unwavering understanding, selfless love and everyday fight dose. God gifted us a beautiful angel Rayan during write up and brightened my whole life.

Dedicated

To Rayan, Samia and my brother Subtain

Table of Contents

List of Figures

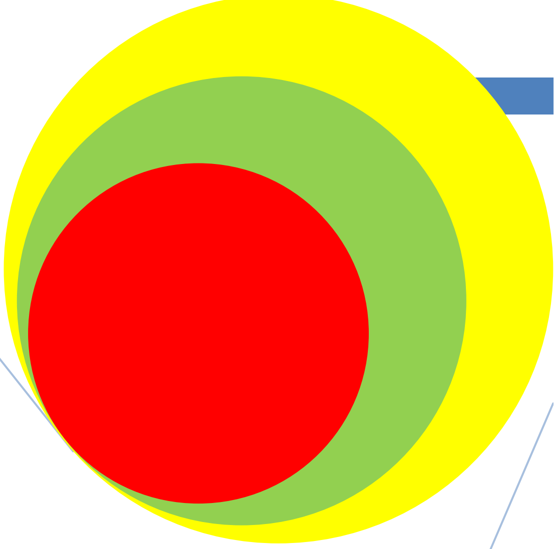

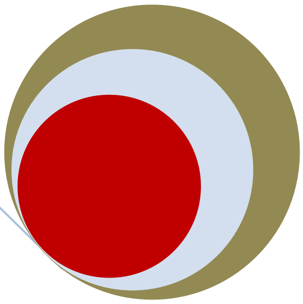

Chapter 1

Surface Modification and Functionalization of Colloidal Nanoparticles

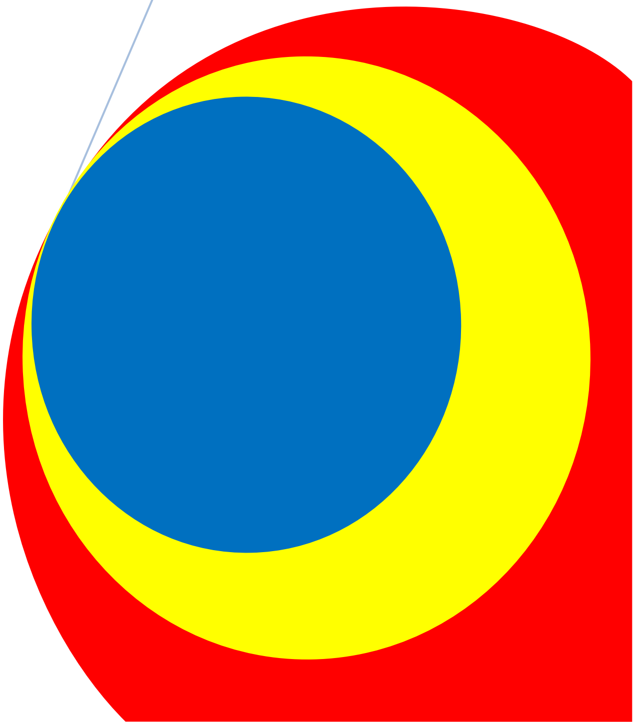

1. Aims and Objectives

The main focus of dissertation is modification and functionalization of nanoparticles in particular gold and semiconductor nanoparticles. The cumulative dissertation consists of one chapter of general introduction of research work. Finally the results pertaining to field are summarized by enlisting publications. In appendixes [A–H], the corresponding papers are attached.

The main work surrounded by synthesis of multifunctional nanoparticles (NPs) based probes for appropriate dual imaging application. Dual modality imaging is the combination of two detection techniques, made possible by dual modal probes and imaging agents and ensures enhanced visualization of biological materials and better reliability of collected data. No single modality is perfect and sufficient to obtain all the necessary information. The NPs have an inorganic core that provides the first label. The NPs are then integrated in a polymer shell that comprises the second label. In this way 9 different label combinations are demonstrated [Appendix A]. Inorganic CdSe/ZnS core-shell quantum dots have been coated with amphiphilic polymers in order to enable their transfer to aqueous solutions. Additionally, ATTO-590 dye molecules have been embedded in the polymer shell. In this geometry ATTO-590 acts as acceptor of the quantum dot donor's excitation. The energy transfer dynamics has been investigated in detail within the system by steady state optical spectroscopy [Appendix B, C].

Ion sensing has applications from analytical chemistry to cellular biology. Fluorescence detection of ions by molecular recognition can be achieved with NPs. Negatively and positively charged gold NPs have been synthesized and attached SNARF to their surface using different poly ethylene glycol (PEG) spacers. Besides the possible quenching of fluorescence of surface proximal fluorophores, the NP surface charge also shifts the ion binding constant, due to the attraction of counter ions to the charged particle surfaces [Appendix D]. Gold and iron-platinum NPs have also functionalised with PEG spacers and fluorescent fluorophores. These systems have been used to investigate their intracellular localization in lung cells and their potential to induce a pro-inflammatory response dependent on concentration and incubation time [Appendix E-G].

2. Introduction

Nanotechnology, the creation of functional materials, devices, and systems through the control of nanoscale materials, has recently become one of the most active research field. Particles with diameters in the range of 2 to 100 nm, called NPs, have become a major interdisciplinary area of research during recent decades [1-4]. In fact, since the seventeenth century, noble metallic nanomaterials, though not understood, have been obtained and used to give rise to a brilliant rose colour throughout Europe in stained glass windows of cathedrals and by the Chinese in colouring vases and other ornaments [5]. The scientific preparation of NPs dates back to the nineteenth century, with Faraday reporting the preparation of colloids of relatively monodispersed gold NPs. Colloidal NPs are solution grown, nanometer sized, inorganic particles that are stabilized by a layer of surfactants attached to their surface. The term colloid is used primarily to describe a broad range of solid-liquid or liquid-liquid mixtures, all of which contain distinct solid particles which are dispersed to various degrees in a liquid medium. Impressive progress has been made in synthesis of colloidal NPs with well-defined structures.

The past couple of decades have witnessed an exponential growth of activities in this field worldwide, driven both by the excitement of understanding new science and by the potential hope for applications and economic impacts[6]. Many efforts have been devoted for the investigation of the synthesis, characterization, and application of NPs [7-10]. The inorganic cores possess useful properties that are controlled by their composition, size and shape. The surfactant coating not only control the growth but also ensures the colloidal stability of NPs. Size dependent property changes include quantum confinement in semiconductor particles (CdSe/ZnS [10, 11] or CdTe [12, 13]), surface plasmon resonance in some metal particles (Au [14] or Ag [15, 16]) and superparamagnetism in magnetic particles (Fe_2O_3 [17] or Co [18]. This combination of features makes colloidal NPs attractive and promising building blocks for advanced materials and devices.

3. *Colloidal Nanoparticle Synthesis*

Interest of gold has got the attention of humans since a thousand years ago; application of gold NPs has grabbed the interest of researchers in the information age. Gold NPs possess unique optical and electronic properties due to the large surface to volume ratio with high density and show excellent biocompatibility with varied ligands [19]. Gold NPs are stable materials that can be readily fabricated either through chemical reduction of gold salts or physical treatment of bulk gold. Gold NPs synthesis method pioneered by *J. Turkevich et al* [20] in 1951, developed a simple synthetic method of gold colloids by the treatment of hydrogen tetrachloroaurate ($HAuCl_4$) with citric acid in boiling water. In the solution of $HAuCl_4$, addition of reducing agents nucleates the gold particles [20]. Phosphine has been used as the capping agent to prepare small gold clusters [21]. Monodisperse gold NPs in diameters of 1–2 nm are obtained by reduction of $AuCl(PPh_3)$ with diborane or sodium borohydride. Gold ions adsorb electrons from the reducing agents and become atoms, where the core of gold atoms nucleates when reducing agents provide electrons. Several atoms aggregate to nucleate the particle center in particular nanostructure. Aqueous synthesis is commonly carried out by the citrate reduction route that yields gold NPs with a narrow size distribution. The average particle diameter can be controlled between about 2–200 nm by the stoichiometry of the reagents, i.e. precursor salt and reduction agent [14, 19]. The particles are stabilized by citrate ions bound to the surface of the NPs, resulting in negatively charged particles that repel each other by electrostatic repulsion.

Table 1: *Synthesis methods and capping agents for gold NPs of diverse core sizes*

Core size diameter	Synthesis Method	Capping agents
1-2nm	Reduction of $AuCl(PPh_3)$ with diborane or sodiumborohydride	Phosphine [21]
1.5-6nm	Biphasic reduction of $HAuCl_4$ by sodiumborohydride in the presence of thiol capping agents	Alkane thiol [22, 23]
5-8nm	Reduction of $HAuCl_4$ by sodiumborohydride in the presence of TOAB	(TOAB) [24]
8-20nm	Reduction of $HAuCl_4$ in Oleylamine	Oleylamine[25]
10-40nm	Reduction of $HAuCl_4$ by sodium citrate	Citrate [14, 26, 27]

In the 1990s, a breakthrough in gold NPs synthesis was achieved, involving the transfer of $HAuCl_4$ from aqueous phase to toluene phase by the surfactant tetraoctylammonium bromide (TOAB) and the subsequent reduction by sodium borohydride in the presence of alkane thiols to generate NPs that are soluble in organic solvents [22]. The particles usually obtained are monodisperse with a size typically between 1.5–6 nm, controlled by stoichiometry or reaction conditions [23]. Thiol protected gold NPs possess superior stability to most of the other gold NPs due to the synergistic effect of strong thiol gold interactions and van der Waals interaction of the ligands. Hiramatsu *et al* [28] gives another approach to make bigger gold NPs by reducing tetrachloroauric acid by alphatic amines. The reducing equivalents in the reaction are provided by the amine group, which can undergo metal ion induced oxidation to nitriles. The initially formed gold atoms self nucleate to form a fixed number of seeds during the first stage of the reaction and particles then continue to grow by diffusion driven deposition of gold atoms onto these existing seeds. The weakly absorbed alphatic amine on the NPs can be readily displaced with aliphatic thiols. The size controlled by stoichiometry or reaction conditions is typically between 6–21 nm.

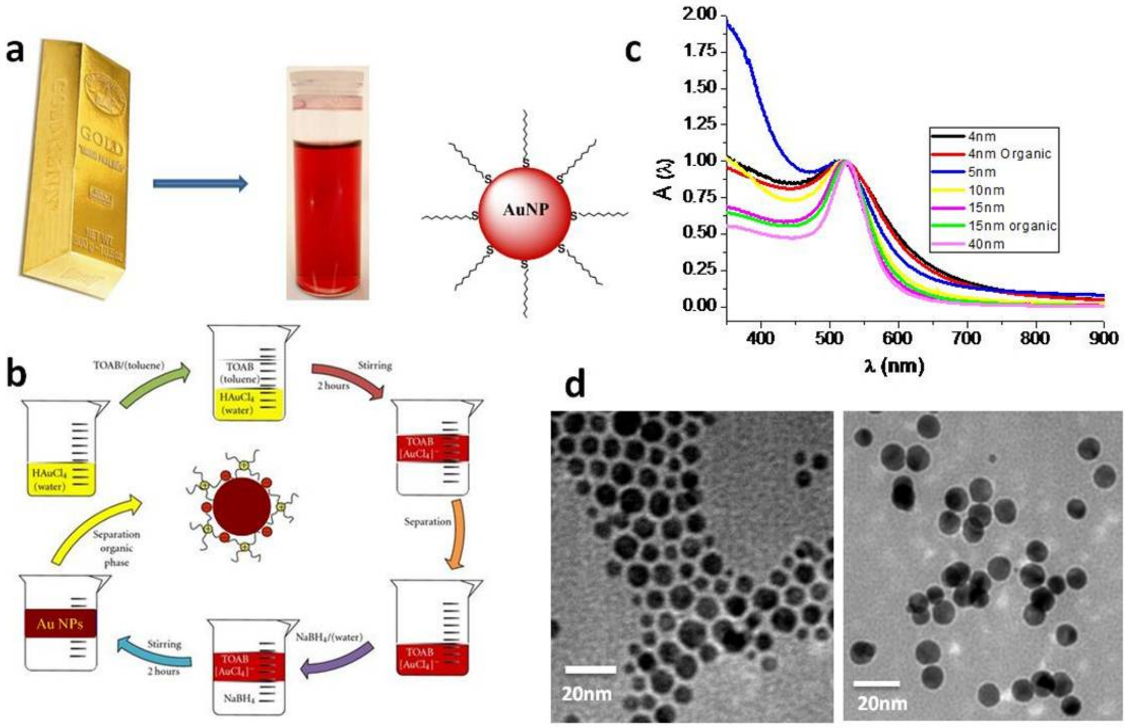

***Figure 1**: a) Schematics of bulk to thiol capped gold NPs, b) schematic of thiol capped gold NP synthesis, c) absorbance spectra of different sizes of gold NPs, and d)TEM pictures of 4nm and 15nm gold NPs in organic solvents.*

Material chemists have surprised biologists with their ability to customize organometallic reactions for the nucleation and growth of assorted multicolor to size selected monochromatic quantum dots (QDs) from various combinations among transition metals and chalcogens. The term “quantum dot” was first contrived by Mark A. Reed in 1988 and denotes nanocrystalline semiconducting fluorophores, whose excitons are confined in all three spatial dimensions; quantum confinement: strict confinement of electrons and holes, when the NPs radius is below the exciton Bohr radius and have typical diameters of 2–20 nm. QDs exhibit unique optical properties derived from quantum confinement effects [29]. Generally they are binary systems composed of a core of semiconducting material enclosed within a shell of another semiconductor. QDs fluorescence is caused by the bandgap between the valence and the conduction electron bands and absorption of a photon. Higher in energy than the spectral bandgap of the core semiconductor, results in electron excitation to the conduction band, generating an electron-hole pair (exciton). Since the physical size of the bandgap determines the photon's emission wavelength, it is possible to control the fluorescence wavelength by varying the size of the QD. Simply put, the larger the QD, the redder its emission. They luminate with very sharp spectral resolution upon UV-vis irradiation. Such properties make this class of optical materials very attractive in a variety of applications, such as fluorescent biological labelling, lasers, and electrochromic displays [30].

Synthesis is usually carried out by thermal decomposition of organometallic precursors in a coordinating solvent which provides a micelle like ligand shell that controls the growth of the particles. There are many synthesis routes to QDs, the most common is high temperature thermolysis involved a material system CdSe in trioctylphosphine/oxide (TOP/TOPO) serving as the solvent and surfactant. Also hexadecylamine or other amines are commonly used ligands for CdSe QDs [31]. Other Cd based [12, 32, 33] or different material systems such as ZnS [34], PbS [35] were also reported.

Besides noble metal NPs, the ones with novel magnetic properties are attracting more and more attention with regard to bioapplications [36-39]. As far as magnetism is concerned, magnetic particles with diameters smaller than some certain critical value usually show properties different from their bulk counter parts. A superparamagnetic property indicates that magnetic moments in the particles are free to align with the field during the measuring time at room temperature. This phenomenon is caused by the fact that in such small particles, because of the thermal fluctuation the magnetic moments can rotate freely despite the magnetic energy barrier. This characteristic allows a promising future in application of the magnetic NPs in biomedicine, particularly in magnetic resonance imaging (MRI), tissue engineering, and drug delivery [36, 40, 41].

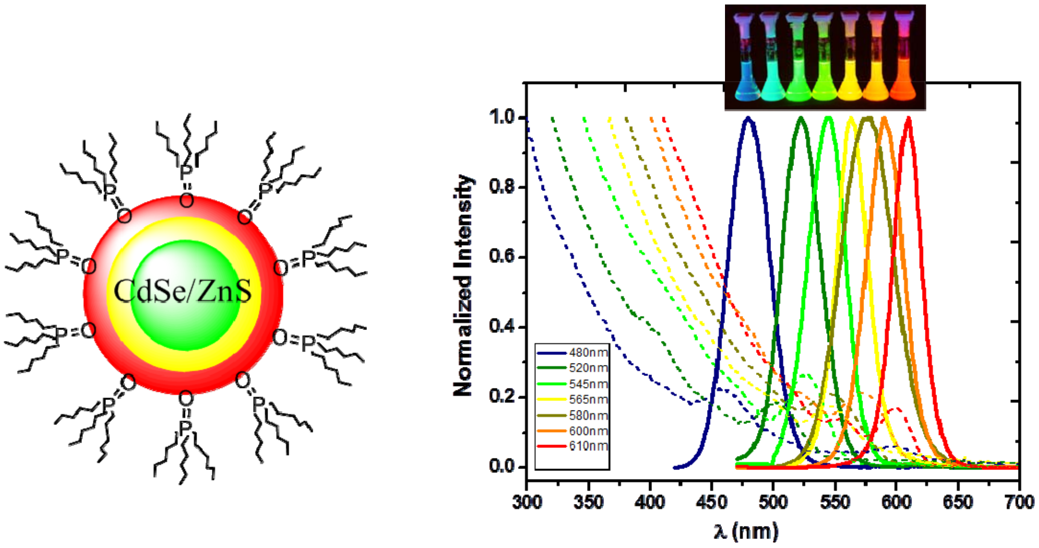

***Figure 2**: Right: CdSe/ZnS QDs capped with TOPO ligands and on left absorbance (dotted line) and fluorescence spectra with change in diameter from 2-6 nm QDs.*

A number of suitable methods have been developed for the synthesis of magnetic NPs of different compositions including iron oxides, such as Fe_3O_4 and γ-Fe_2O_3 [42, 43], pure metals; such as Fe and Co [44, 45] ferromagnetic, such as $MgFe_2O_4$, $MnFe_2O_4$, and $CoFe_2O_4$ [46] as well as alloys, such as $CoPt_3$ and FePt [47].

Beyond from above mentioned particles variety of particles can be synthesized e.g. Ni, Ag/Pd, various alloys, silicon, silica or phosphorescent NPs based on rare earth doped materials such as $NaYF_4$ and also other shapes like rods, tetrapods and hollow shells can be synthesized.

4. Biocompatibility of NPs

Significant progress has been made in synthesis of colloidal NPs with well defined structures. Among the known chemical routes, high-temperature thermolysis of organometallic species in nonpolar solvents has been widely shown to be an approach capable of producing colloidal nanostructures with narrow size distribution, low crystalline defects, and tunable shapes. Despite success in synthesizing a wide variety of NPs, these approaches typically produces NPs with hydrophobic surfaces. The resulting insolubility of the NPs in water greatly limits their applications in important fields such as drug delivery, biolabeling, and catalysis in aqueous solution. To this end, several strategies have been developed to transfer NPs with hydrophobic surfaces into water. A variety of strategies have been used; however, amphiphilic or bifunctional molecules are common to all approaches. Ligand exchange, silica coatings and polymer coatings are the most widely adopted chemistries.

4.1 Ligand Exchange

One popular method for phase transfer from organic to aqueous is based on ligand exchange, where the hydrophobic surfactants on the particle surfaces are replaced by small molecules containing polar groups on both ends. Thiol groups that bind strongly to inorganic surfaces of NPs are commonly used for ligand exchange.

One of the most widespread approach to create water soluble QDs is ligand exchange with thioalkyl acids such as mercaptoacetic acid (MAA), mercaptopropionic acid (MPA), or mercaptoundecanoic acid (MUA). In their thiolate forms, these molecules coordinate strongly with the metal ions on the exterior of QDs (e.g., Cd^{+2}, Zn^{+2}, Pb^{+2}), thus exposing the polar and potentially charged carboxylic acid group to the surrounding solution and imparting aqueous solubility. Most procedures for ligand exchange using a thiol-based ligand involve incubating the QDs (usually coated with TOPO ligands) [48] in a solution containing an excess of the thiol ligand of interest. In general, it seems that these preparations are stable over periods ranging from weeks to months. At sufficiently basic pH, the carboxylic acid groups are negatively charged and electrostatic repulsion helps maintain the dispersion of the QDs in aqueous media. However, at acidic pH values or in solutions of high ionic strength, there is a greater tendency for aggregation due to the neutrality of the carboxylic acid groups. It has shown that more acidic thioalkyl acid ligands yield QDs that are more resistant to aggregation at low pH [49]. For example, mercaptosuccinic acid (MSA) capped QDs aggregate and precipitate more slowly than MAA capped QDs [50]. Instability can also be generated by desorption of the thioalkyl acid ligands from the surface of the QD with time. It has been reported that preparations which use bidentate thioalkyl acids such as dihydrolipoic acid (DHLA) increase the shelf life of the preparations to periods ranging from several months to a year [51]. However, an unavoidable side effect of thioalkyl acid ligand exchange is that it tends to reduce quantum yields of QDs relative to capped with TOP/TOPO in the organic phase [52, 53]. Both the particle surface and possibly the thiol group of the ligands are prone to oxidation.

Following the Brust [22] method of gold NP synthesis in non polar solvents, there are several reports for their biocompatibility with aqueous media. Capping gold NPs with the amino acid lysine enables storage of the lysine stabilized gold NPs as a stable powder that may be readily redispersed in water [54]. A general robust ligand exchange method that uses short chain hydrophilic polyelectrolyte molecules to replace the original hydrophobic ligands at an elevated temperature in a glycol solvent was reported [55]. In a typical process, a toluene solution containing hydrophobic NPs is rapidly injected into a heated mixture of diethylene glycol and exchanging ligands. The NPs can then be precipitated by adding excess amount of diluted aqueous solution of hydrochloric acid and finally redispersed in water by transforming remaining uncoordinated groups into the ionized form.

4.2 Silica Encapsulation

Silica encapsulation involves the growth of a silica layer on the surface of NPs. Functional organosilane molecules are incorporated in the shell to provide surface functionalities for bioconjugation. Various methods for the coating of different colloids with silica can be found in the literature [56]. The method comprises of a ligand exchange procedure in which a first layer of silanes is bound to the NPs surface. Then, using this first layer a polymeric crosslinked inorganic silica shell is deposited on the particles which can be further derivatized. The silica encapsulated particles have primary amines on the outer surface for further functionalization [56]. Different NPs like silver [57], magnetite [58], QDs (CdSe/ZnS [56, 59], PbSe [60]) have been coated with silica shells. These silica coated NPs are extremely stable because the silica layer is highly cross linked. However, the method is very laborious and the silica layer may be hydrolyzed [61].

4.3 Polymer Coating

For a number of applications, particularly in biological targeting and imaging studies, it has been desirable to coat NPs with polymers in order to confer useful properties while maintaining a relatively small hydrodynamic volume. Amphiphilic polymers are ideal for this purpose, as their hydrophobic component can be used to bind them to the surface of similarly hydrophobic (e.g., TOPO coated) while their hydrophilic component can render the resulting composite materials water soluble. When coating NPs with amphiphilic polymers, care must be taken as in addition to discrete NP-polymer composites, micelles can be formed. Strong hydrophobic interactions between hydrophobic ligand of NPs and layer of amphiphilic polymer results in phase transfer. Individual NPs can be encapsulated in phospholipid block copolymer micelles (polyethylene glycol phosphatidylethanolamine and phosphatidylcholine) [62] by hydrophobic interactions. The advantage of these micelles is that they are very regular in size, shape, and structure. In addition, their outer surface comprises a dense layer of PEG polymers that is poorly immunogenic and antigenic and acts as excellent repellent for biomolecules. Furthermore, both the PEG content and length can be adjusted precisely. Another approach by use of triblock polymer [63] consists of a polybutylacrylate segment (hydrophobic), a polyethylacrylate segment (hydrophobic), a polymethacrylic acid segment (hydrophilic) and a hydrophobic hydrocarbon side chain. Poly acrylic acid is a highly charged linear polyelectrolyte. Its carboxylic groups can be modified with aliphatic amines via an amide bond. For the phase transfer of NPs, poly acrylic acid with a molecular weight of 2000 g/mol modified with 40% octylamine (in respect to the number of carboxylic groups) has been used [64]. The surface was further cross linked by N-(3-Dimethylaminopropyl)-N′-ethylcarbodiimide hydro-chloride (EDC) mediated coupling to lysine prior to conjugation to various biomolecules via the carboxyl groups on the polymer backbone.

A comb like structure of amphiphilic polymer, poly (maleic anhydride alt-1-tetradecene) [65] makes NPs become water soluble upon hydrolyzation of the anhydride groups. Same class of another polymer, Poly (maleic anhydride-alt-1-octadecene) has been reported recently leads to intercalation of the polymeric (aliphatic) side chains among the surfactant molecules on the

NP's surface, with the anhydride groups exposed to the solvent coupled with triamine [66], polyethylene glycol [67] or dimethylaminopropyl amine [68]. Amphiphilic polymer coating, for transferring hydrophobic NPs into aqueous solution should be extendable to any NP system in which hydrophobic tails are exposed to the external environment. Recently, another design for amphiphilic polymer has been presented combining the advantage of maleic anhydride moieties for pre modification and custom modification with side-chains. Hydrophobic side chains consisting of dodecylamine are grafted to a poly (maleic anhydride) based backbone, leaving a part of the anhydride rings intact. If desired, additional functional molecules like fluorescent dyes, sugars, biotin or PEG can be covalently grafted to the polymer if they exhibit an amine function [69]. The comb like polymer is soluble in organic solvent and can be added to hydrophobic NPs, e.g. QDs with TOP/TOPO ligands. After evaporation of the solvent, the solid can be dissolved in an aqueous buffer, yielding stable, single NPs. In order to increase the stability, the polymer shell has been further cross linked with lysine by EDC chemistry. The same kind polymer has been used to disperse QDs in ethanol [70]. A longer poly acrylic acid backbone has been modified with a mixture of octylamine and isopropylamine [71]. The synthesis of CdTe/CdSe QDs has been carried out in presence of poly acrylic acid with 40 % modification with dodecylamine, yielding amphiphilic NPs which were soluble in a number of organic solvents as well as in water, where the polymer is assumed to form a double layer around the particle [72].

QDs coated with branched poly (ethyleneimine) PEI, could be dispersed in both aqueous and organic solution [73]. Dextrane coating of NPs also allows them water solubility, in particular superparamagnetic iron oxide [74] with dextran coating, were used for various application in bio imaging.

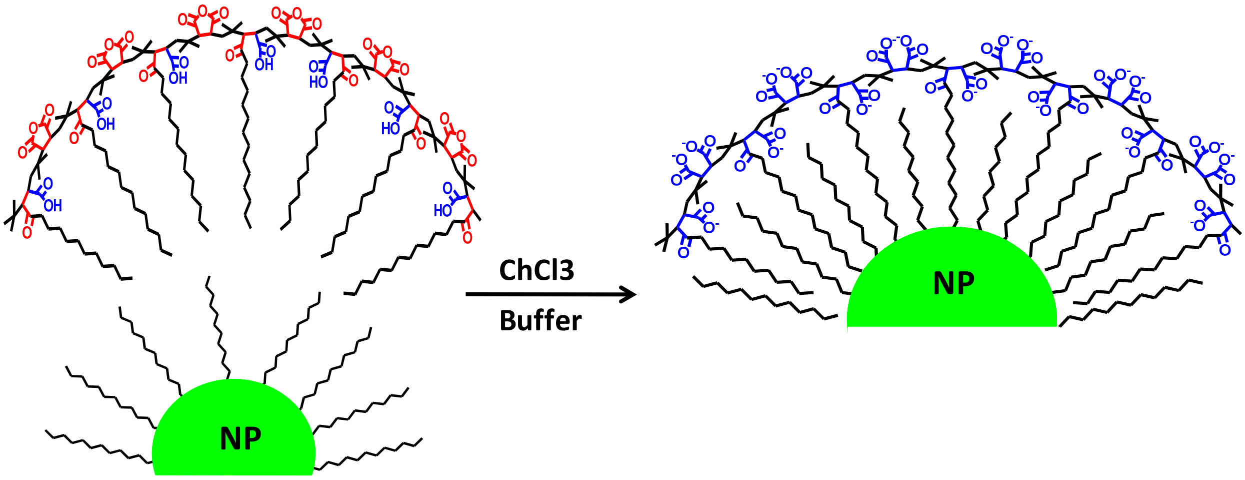

Figure 3: Scheme of polymer coating of NPs with Amphiphilic polymer[69]

5. Surface Modification and Functionalization of NPs

Chemical attachment of one molecule to another molecule or NP has caused the birth of billion dollar industries serving research, diagnostics and therapeutic markets. The advantage of a larger surface area to volume ratio as well as homogeneity in aqueous solution, results in promising applications of biocompatible NPs. Modification of NPs depends upon two interrelated chemical reactions: the reactive functional group present on cross linking or derivatizing reagents and the functional group present on the target NP's surface. NPs with different core material and functional groups on their surface can be functionalized with proteins, peptides, sugars, amino acids, antibody, DNA, Biotin, organic fluorophores, radioactive labels and many others. Present study will not cover all the modifications but some of them are discussed below.

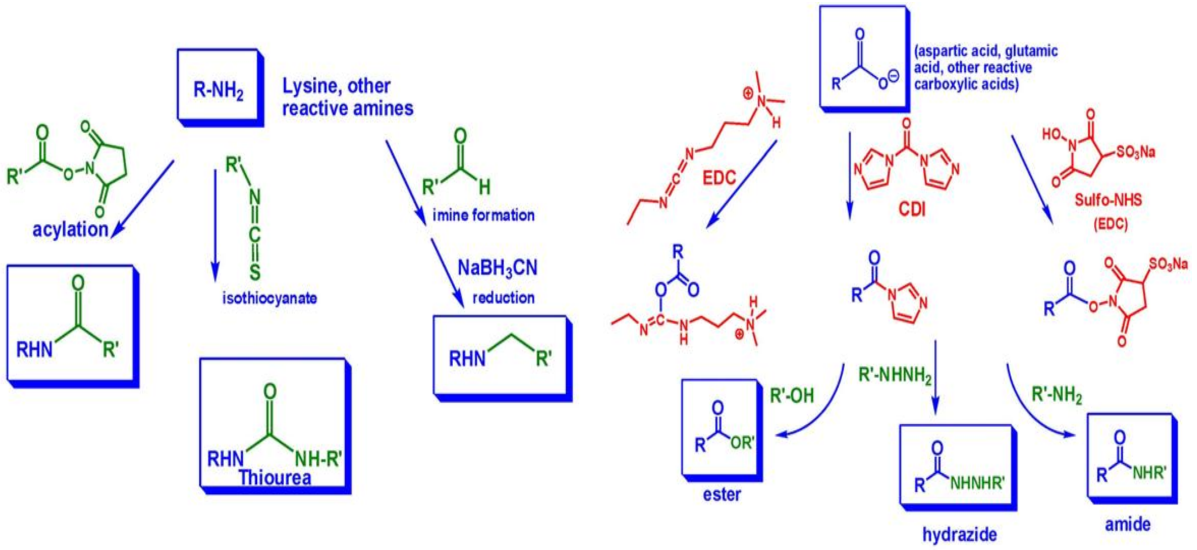

Figure 4: Conjugation techniques used for surface modification of different chemical groups present on surface of NPs.

5.1 Fluorescent Labelling

Organic fluorophores [75], fluorescent proteins [76, 77] and rare earth metal chelate [78] are mostly used fluorescent labels. NPs, depending upon their surface functional group can be modified with all fluorescent labels.

Binding of dye molecules to metal NPs enhance their photoactivity and suitable for light harvesting and optoelectronic applications. Gold NPs themselves show limited photoactivity under UV-Vis irradiation. Gold NPs produced by thiocyanate reduction method were modified with Rhodamine 6G [79]. Close packing of the cationic dye molecules on the gold surface induces intermolecular and inter cluster interactions. Furthermore, the adsorption of the cationic dye on the gold surface results in surface charge neutralization causing the gold/dye assembly to aggregate. Citrate stabilized gold NPs modified with lissamine-rhodamine B [80] by grafting in two steps: first, a primary grafting of thiols consisting both of stabilisers and of linker molecules and secondly the grafting of dye on these previously attached linkers. Dye molecules are attached to gold NPs via a thioether group in presence of triethylamine [81] and studied radiative and nonradiative decay rates of dye molecules. For dye attached to the smallest 2 nm gold NP corresponds to a quenching efficiency of 99.8%, mainly induced by a reduction of the radiative rate. Another approach is to link dye molecule with DNA and then modify gold NPs via disulphide coupling [82]. Core-shell slica NPs has been functionalized with near infrared dyes (650-900nm) via covalent incorporation of dye with maleimide conjugation chemistry [83].

Superparamagnetic iron oxide NPs can be modified with fluorescent dyes to obtain additional fluorescence properties. The coupling of the fluorescent dye was performed on particles that were dispersed in an acidic medium. The process is based on the strong interaction between dimercaptosuccinic acid (DMSA) and the positively charged surface of Fe_2O_3 [84]. Negative surface charges due to the acid-base behaviour of grafted DMSA cause repulsive particle interactions and prevent aggregation. Amino dextran coated NPs were modified with FITC via NHS coupling [85]. A controlled weight percentage of rhodamine B and gumarabic was prepared and mixed with Fe_3O_4 NPs. Gumarabic could be attached to Fe_3O_4 via the interaction between the carboxylic groups of gumarabic and the surface hydroxyl groups of Fe_3O_4 [86]. Near infrared fluorescent (NIRF) docyanine (Cy5.5) through a polypeptide link was facile using the coupling of a terminal amine group and a maleimide group attached to Cy5.5, and conjugation of cross-linked iron oxide occurred through a disulfide link or a thioester linker [87]. Enhanced levels of NIRF indicated the presence of a protease which cleaves the molecule, separating the NIRF dye and the iron oxide NPs and activating the fluorescence.

Amino modified dyes can be embedded in polymer shell by covalent bonding with carboxyl groups of polymer and then coating of NPs gold [88] and iron platinum [89] for biological applications. Gold NPs could be act like pH sensor when linked with pH sensitive dye SNARF-1 [90]. Amphiphilic polymer [69] was modified with amino modified SNARF-1 with different PEG spacers, was used for polymer coating of dodecanethiol stabilized gold NPs [22, 91]. The SNARF binding equilibrium is shifted to higher bulk pH values when the dye is bound close to the surface. In this way surface charge significantly impacts the ion binding and affects the read-out. Sensor read-out should be thus not determined by the bulk ion concentration, but by the local ion concentration in the nano environment of the NP's surface.

Another class of fluorescent semiconductor QDs can also be labelled with fluorescent labels for multi emission or energy transfer applications. QDs are very famous for energy donors to organic dyes. Mercaptoacetic acid capped water soluble CdSe/ZnS QDs were first conjugated to biotinylated bovine serum albumin (bBSA, with 11 bBSA per QD) via a thiol linkage, although free bBSA was still present in solution. In a separate reaction, streptavidin was covalently labelled with tetramethyl Rhodamine and used as acceptor [92]. In the same way QDs protein dye assembly can be prepared by capping CdSe/ZnS QDs with dihydrolipoic acid ligands which were functionalised with facile electrostatic conjugation of dye labelled maltose binding protein [93-95]. CdSe/ZnS QDs coated with a thick passivating and functionalized polymer layer and conjugated to streptavidin as FRET donors with proximal biotin modified dyes; specific interactions between biotin and streptavidin brought the acceptor in close proximity to the QD centre [94, 96, 97]. The carboxyl functionalized CdSe/ZnS QDs, coated with lipid-PEG for water solubility and fluidity of this micellular lipid-PEG coating is reason why polyhistidine interact directly with QD surface. The polyhistidine sequence was inserted at the N-terminus of three fluorescent proteins from the mFruit family: mCherry and mOrange, both monomeric, while tdTomato is a tandem dimer [98]. Another approach by using nagetively charged dye modified DNA sequence with CdTe QDs modified with cationic polymer (polydiallyl dimethyl ammonium chloride).These positively charged CdTe QDs were react with dye through electrostatic and hydrophobic interactions [99]. A similar facile approach has been demonstrated for the detection of DNA hybridization, which is based on fluorescent energy transfer (FRET) from a complex of conjugated blue emitting polymer and CdTe QDs to the dye labelled DNA [100]. The conjugated polymer provides a dual advantage of (i) a light-harvesting antenna enhancing the emission of QDs and thus potentially offering improved assay sensitivity and (ii) inverting the sign of originally negatively charged QDs and thus providing a positively charged counterpart for negatively charged DNA molecules to electrostatically absorb on polymer-QD complexes. CdSe/ZnS QDs of different sizes in organic solvents were polymer coated with dye functionalized amphiphilic polymer [101, 102]. Polymer was used for bringing QDs to aqueous phase and also dye in the polymer shell act as acceptor for QD-dye FRET assembly. Amino functionalised ATTO-590 dye was conjugated with carboxyl groups of amphiphilic polymer shell, by varying the molar ratios of dye to polymer [102] and size of QDs [101] results in different FRET efficiencies.

Luminescent lanthanides are the most prominent class of long lifetime dyes used for energy transfer applications in biophysical research. Four lanthanides emit in the visible region: terbium, europium, samarium and dysprosium. Commonly used are terbium and europium cations because of their high intensity of emission [78]. Lanthanide labels have been brought in very close vicinity to CdTe QDs. The investigation regarding competitive binding assays, where QDs have been coated with protein binders recognizing small analyte molecules and their competing lanthanide labelled analogues have been developed. Carboxylated CdTe particles were activated with 1-ethyl-3-(3-dimethylaminopropyl) carbodiimide and sulfosuccinimide and add streptavidin (three-fold molar excess) orestradiol specific antibody Fab fragment (1.5 fold molar excess). Terbium and europium isothiocyanato chelates were coupled with biotin and bovine serum albumin for QDs with streptavidin and antibody assay [103]. Another assay with same but different chemistry was achieved by modification of CdSe/ZnS QDs with biotin and use streptavidin functionalized lanthanide complex [104].

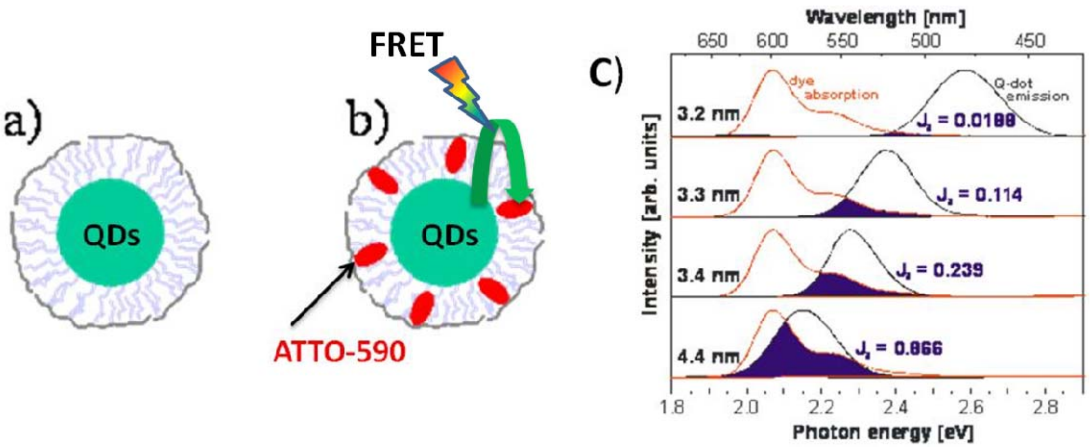

***Figure** 5:a) Polymer coated QDs, b)FRET assembly; Polymer coated QDs modified with ATTO-590 dye, c)Overlap integral was calculated from spectra of QDs emission and dye absorption[102]*

5.2 Magnetic and Radioactive Labelling

Multi modal imaging using a small molecule based probe is challenging due to the limited number of attachment points, however NPs have large surface areas where multiple functional moieties can be incorporated for multi modality molecular imaging. Combination of modified NPs of different core material with radionuclide [105] and commonly used contrast agents [106] provides application of dual modality molecular imaging probes. Bi-functional ligands for metal chelation are widely used for labelling magnetic contrast agents and radio isotopes. Most commonly use ligands are DTPA (diethylenetriaminepenta-acetic acid) and DOTA (1,4,7,10-tetraazacyclododecane-N,N´,N´´,N´´´´tetraaceticacid), that can be functionalized with different chemical reactive groups for coupling[107]. Bifunctional ligands can be modified on NP surface with and without metal chelation.

The most commonly used contrast agents nowadays are low molecular weight gadolinium (Gd^{+3}) compounds [106, 108] which are thermodynamically and kinetically stable,. Glutathione coated CdSeTe/CdS QDs has been functionalised with DOTA-NHS ester and purified from free DOTA by dialysis. Addition of $GdCl_3$, efficiently chelated by DOTA and excess gadolinium was removed by filtration [109]. From the UV spectral data, an average number of Gd-DOTA complexes per QD were calculated to be 77±18. The silica-shelled QD micelle conjugated with Gd-DTPA isothiocyanate can be attached to the surface of the silica sphere or it can have Al^{TM}Gd (an amphiphilic Gd compound) incorporated inside the silica sphere [110, 111]. Another approach by using silanized CdSe/ZnS QDs and gold NPs is by direct coupling of maleimide activated Gd-DOTA [112]. Glyco NPs are multivalent sugar coated gold NPs. Sugar coating confers water solubility and biological activity to the NPs. The paramagnetic gold glycol NPs were prepared using different ratios of thiol ending sugar conjugates and tetraazacyclododecane-triacetic acid (DO3A) ligands [113]. DO3A ligands were selected to chelate the Gd^{+3} cation. Gold NPs (2-2.5 nm) have been synthesized in the presence of dithiolated DTPA. The modification of DTPA by two thiol moieties; is ensuring the quasi-irreversible grafting of the ligand onto the gold NPs, consequently providing for enhanced colloidal stability [114]. The presence of DTPA on gold NPs allows Gd^{+3} to be immobilized on the particles by chelation. Same approach has been adopted with mono layer of thiol DTPA to gold NPs surface and chelates Gd^{+3} for paramagnetic gold NPs applications [115]. Citrate coated gold NPs of size 12 nm modified with DTPA bis(amide) of 4-aminothiophenol [116] and DTPA bis(amide) conjugate of penicillamine [117] via thiol gold reaction. Gd^{+3} was chelated after modification and purification of excess DTPA.

Radio isotopes for imaging are gamma and positron emitters with alpha and beta particle emitters of interest for targeted radiotherapy applications. Clinically used metal isotopes include ^{99m}Tc, ^{111}In, ^{68}Ga, ^{64}Cu, and ^{90}Y, with many more under investigation [107]. The selection of potential targeted radionuclide for tumour imaging and for internal radiotherapy involves the physical half-life, decay mode and the emission properties of the radionuclide. Gamma emitters with energy range between 130 and 370 keV can be used for gamma imaging or single photon emission tomography (SPECT). The high-energy positron emitters with annihilation energy at 511 keV energy can be applied for positron emission tomography (PET). There are different approaches for labelling radionuclide on NP surface. Modification of bifunctional metal chelators on NP surface by different conjugation chemistry results in chelation of radionuclide on NPs. Chelators can be modified on NP's surface with and without loading radionuclide [118]. DTPA ligand was modified with cystein and lysine and further modified with fluorescein, offered a single primary amine and a single thiol. Since thiols react strongly with gold surface, it was reacted with the surface of gold NPs,. Amine functionalized CdTe/ZnS QDs with VEGF protein and macrocyclic chelating agent DOTA, for VEGFR recognition and ^{64}Cu labeling for PET imaging [119]. DOTA was activated by EDC and sulpho-NHS, along with a heterobifunctional linker, NHS–MAL to react with amine functionalized QDs. DOTA-QD was radiolabelled by the addition of $^{64}CuCl_2$ and purified by size exclusion chromatography. Same approach has been adopted to evaluates the quantitative biodistribution of commercially available amino functionalized CdSe QDs (Emission 525-800nm) in mice [120]. In addition DOTA has been modified with PEG spacers and liked with QDs via amide linkage.

Superparamagnetic iron oxide NPs modified with radio nuclide provide exciting probes for multifunctional imaging applications. About 100 nm amino silane coated Fe_2O_3 NPs (10nm core) exhibit multiple NH_2 groups, bound to a silicon atom, serving as the reactive group and enabling the covalent linkage. NP's surface has been activated by sulpho-NHS and EDC and modified with HIV-1 tat linked to the fluorescent dye fluorescein isothiocyanate [121]. Simply the positron emitting radionuclide ^{68}Ga and the γ-emitter ^{111}In without adding a chelating agent was linked with modified particles. An additional PEG coating was used to block adjacent amino functions and prevent particle aggregation. Another approach has been adopted for Fe_3O_4 NPs coated with polyaspartic acid (PASP). PASP has two kinds of functional groups: carboxylates and amines. Therefore, NPs have been coated with PASP through the carboxyl group and the remaining amine group could be used for DOTA linkage

[122]. DOTA was first activated by EDC and sulpho-NHS, which results in DOTA ester which can link with amino groups present on surface of particles. After purification, the radionuclide ^{64}CuCl$_2$ was chelated in buffer according to standard protocols [123]. Dextran sulphate coated superparamagnetic iron oxide NPs conjugated with *S*-2-(4-isothiocyanatobenzyl)-1,4,7,10-tetraazacyclodo-decane-1,4,7,10-tetraacetic acid (*p*-SCNBz-DOTA) via amide linkage and labelled with ^{64}Cu [124] and ^{111}In [74].

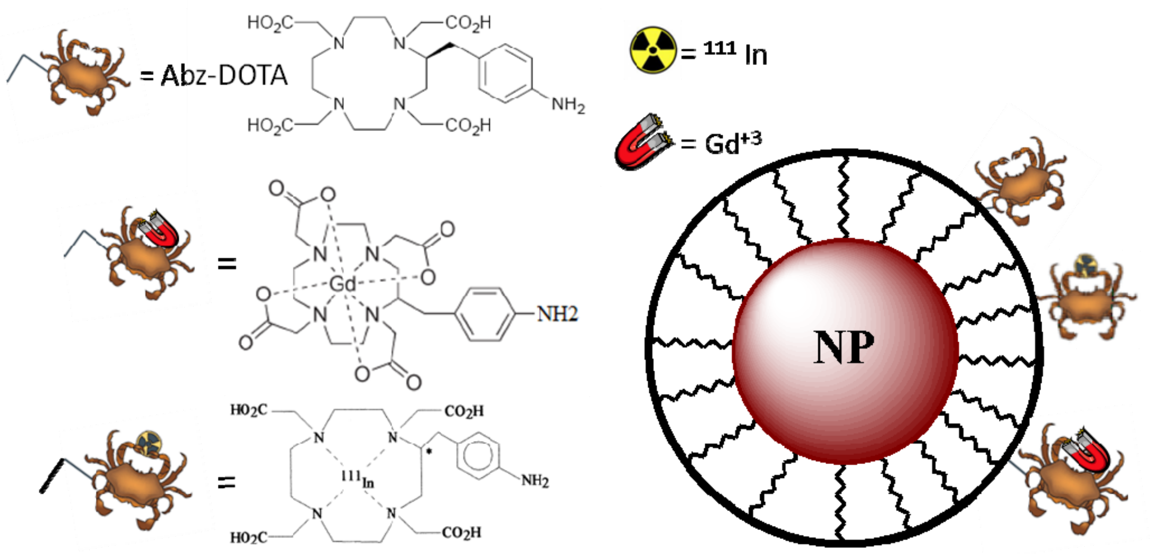

***Figure 6**: Schematic diagram for labeling of NPs with metal chelators and then further modification with magnetic (Gd^{+3}) and radioactive (^{111}In) [125, 126]*

5.3 Modification with Polyethylene Glycol

Polyethylene glycol (PEG) is a linear polymer consisting of repeated units of CH_2-CH_2-O, depending on the molecular weight. It has also been known as polyethylene oxide (PEO) or polyoxyethylene (POE), depending on its molecular weight. PEGs are well soluble in a number of organic polar and apolar solvents, as well as in water where it is heavily hydrated, forming random coils with diameters much larger than proteins of comparable molecular weight. PEGylation is the process of covalent attachment of PEG polymer chains to another molecule, normally a drug or therapeutic protein or NP. An increasing variety of mono, homo and heterobifunctional PEG reagents are commercially available, with different functional groups and molecular weights [127].

The terminal hydroxyl group of the PEG molecule provide a ready site for covalent attachment to other molecule or surface. Coatings with PEG are quite often used in nanomedical applications since this material is biocompatible, stabilizes the particles, and reduces their reactivity [128, 129]. Bifunctional PEG molecule widely used for phase transfer of organic NPs to aqueous phase [130-133] and also to introduce new functional group on surface of NPs. Particle synthesis can already be carried out in presence of these ligands [134, 135]. New PEG containing ligands can be introduced by place-exchange reactions or added as additional molecules like lipids [62] or polymers [136] that have been modified with PEG before used for the coating process.

PEGylated NPs can also be modified with ion sensitive dyes to change their nano environment to bulk for sensing [91, 137]. Carboxyl rich, polymer coated gold NPs functionalized with SNARF to their surface using different PEG-spacers. Diamino PEG molecules of different molecular weights (0.1KDa, 2KDa, 6KDa and 10KDa) were bound to the NPs by linking one of the amino terminals of the PEG with the carboxyl groups on the NP surface using EDC chemistry. NHS modified SNARF was then reacted to the amino terminals of PEGylated gold NPs. PEG-SNARF conjugates significantly and changes their spectral response once they were linked to the surface of negatively charged polymer coated gold NPs. The conjugation to PEG does not change the pH-sensitivity of SNARF [91]. Defined number of functional group per NP could be prepared by functionalization of polymer coated [65] NPs with bifunctional PEG spacers; molecular weight ≥5000g/mol. Discrete bands could be separated by gel electrophoresis [138]. Same approach has been adopted to get monovalent streptavidin molecule per QD which further allow the conjugation with single antibody [139].

Hydrophobic magnetic Fe_3O_4 NPs stabilized by oleylamine were further functionalized with PEG by ligand exchange reactions. Dopamine terminal of PEG was used to couple with Fe_3O_4 NPs and carboxy terminal was used for phase transfer to water. By varying the spacer length uptake of NPs has been studied [140]. In another example FePt [141] NPs has been PEGylated by thiol modified PEG spacer. However use of carboxyl and ammonium terminated PEG did provide water soluble FePt NPs [133].

As for any additional shell, the overall particle diameter is increased by PEG modification. Increasing grafting density and molecular weight of the employed PEG molecules yields thicker shells, which can be found in the order of a few to tens of nanometres. The thickness of about the order of the hydrodynamic diameter of a free PEG molecule that forms a random coil [142].

5.4 Biomolecules

To be useful and biocompatible for biomedical application, the NPs must be coated or linked with suitable molecules. Progress in utilizing inorganic NPs for biomedical applications has advanced rapidly owing to extensive research on modification of NPs with biomolecules such as lipids, peptides, proteins, antibody, and nucleic acids. These surface-modified NPs have been examined for their uses as new tools not only for the investigation of biological processes but also for sensing, drug delivery, and treating diseases [86, 105, 143-145]. Biofunctionalized NPs bring together the unique properties and functionality of both materials, for example fluorescence or magnetic moment of the inorganic particles and e.g. the ability of biomolecules for highly specific binding by molecular recognition [146].

The biofunctionalization of NPs is not trivial because it involves several stages where it is essential that they remain stable. Since there is a wide variety of nanoparticles (magnetic, gold, quantum dots, etc.) and nanostructured materials (carbon nanotubes, etc.) very different in terms of size, surface area, density of reactive groups, colloidal stability, etc., there are no standard functionalization protocols necessary to optimize for each particular case. Regarding the realization of the bioapplication of the NPs, the technique that allows us to modify the surface of the NPs must play the determinative role. These chemistries are not compatible with every desired application, and the result is that the development of additional routes in general toward nanoparticle functionalization is still necessary for their use in emerging nanotechnologies.

Natural strong binding of avidin for a small molecule biotin is one of the most popular methods of non covalent conjugation. Avidin is a glycoprotein found in egg whites, giving an intact molecular weight of 66,000 Da, having four identical binding sites for biotin (or vitamin H)[147]. Streptavidin is another biotin binding protein that can overcome some of the non specificities of avidin. Similar to avidin, streptavidin contains four subunits, each with single biotin binding site. The strength of non-covalent avidin-biotin interaction makes it extraordinarily useful in bioconjugation. A large variety of avidin or streptavidin and biotin are available with functional groups; such as amine, sulfohydryl, and carboxyl reactive and labelled with PEG or other biomolecules [148].

Aggregation of electrostatically stabilized gold NPs can be assembled in a solution, using the streptavidin-biotin analogue via two different routes. The first route involves the modification of gold NPs by chemisorption of a disulfide biotin analogue, followed by the subsequent addition streptavidin, while the second route involves the binding of disulfide biotin analogue to the streptavidin prior to addition to gold NPs. In both cases, the color change has been attributed to the distance dependent optical properties of NPs [149, 150]. Biotin-streptavidin interaction has been monitored by electrochemical method, based on the use of colloidal gold as an electrochemical label.

Biotinylated albumin is adsorbed on the pretreated surface of a carbon paste electrode. This modified electrode is immersed in colloidal gold-streptavidin labelled solutions. Adsorptive voltammetry is used to monitor colloidal gold bound to streptavidin [151]. A multiplexed assay system of proteases and their inhibition by measuring the energy transfer between QDs and gold NPs on a glass slide has been developed [152]. Monomaleimide functionalized gold NPs were functionalized with biotinylated cysteine terminated peptide. On the other hand commercially available streptavidin modified QDs [153-155] has been used for different assays. Biotinlyted gold NPs are associated with streptavidin bound QDs that had been deposited on a glass slide to form the gold NPs-QDs conjugates by typical biotin streptavidin association.

By exploiting the functional groups on the protein surface, streptavidin has been covalently linked to QDs with carboxylic groups [64, 156] or primary amines [157], commonly by EDC/NHS chemistry. Alternatively streptavidin has been bound by direct adsorption to the inorganic QDs surface via a polyhistidine tag, also in the case of monovalent streptavidin [139]. Two photon excitation fluorescence cross correlation spectroscopy assay has been developed by using two colors of QDs. One color conjugated with biotin whiles other with streptavidin. It has been observed that conjugation to the QDs does affect the binding constant and off rate for the streptavidin-biotin interaction [158]. Tetraethylene glycol based bidentate functionalized with dihydrolipoic acid and biotin has been used to promote biocompatibility of luminescent QDs. The new biotin appended ligand effectively cap exchanged with the native TOP/TOPO and provided QDs which are water soluble over extended periods of time and biologically active [159, 160].

Humans are made up of billions and billions of cells and all these cells working together in order to maintain life. Cells do not have a brain, so they are controlled by a very important hereditary material; deoxyribonucleic acid (DNA). DNA is very complex and very tightly regulated chemical sequence that contains all the information that our cells require to grow, perform functions, and replicate. Synthetic DNA oligomers of arbitrary sequences and with a large variety of functional end groups, which are commercially available, can be conveniently attached in aqueous solution to gold NPs by a thiol-gold bond, in the same way as a place exchange reaction [161-163]. Also conjugation chemistry can be employed to covalently bind the DNA to functional groups available on the NPs surface. This has been carried out with EDC chemistry to bind amino-functionalized DNA to NPs with carboxylic groups, thiol-modified DNA to maleimide groups [164], and by biotin avidin functionalization of NPs and DNA [165].

Further examples can be found in a number of publications about bioconjugation of NPs with proteins, peptides nucleic acid, and enzymes [2, 146, 166-168].

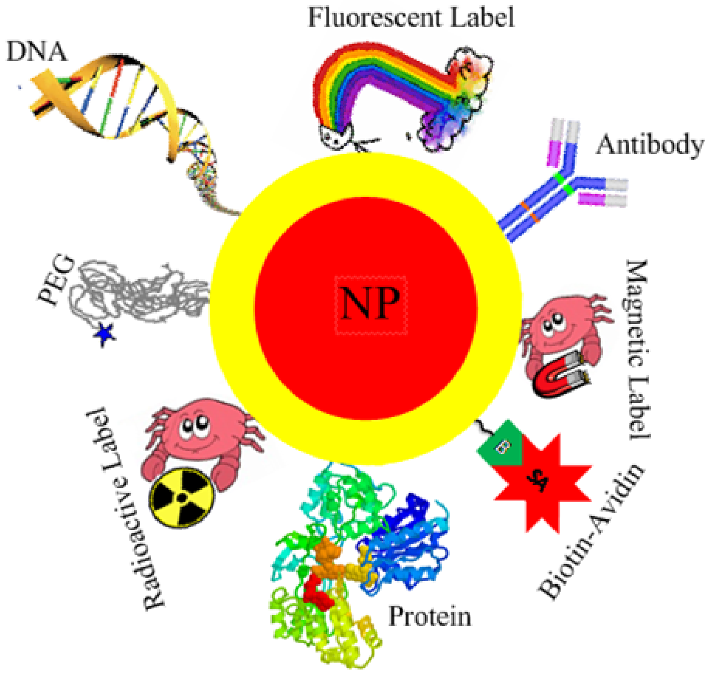

***Figure 7**: Schematic diagram for modification of NPs with bio molecules, PEG, fluorescent, magnetic and radioactive labeling (not drawn to scale).*

6. Applications and Outlook

The current and potential applications for nanoparticles are growing and cover an extremely broad range of markets industries including biomedical & cancer treatment, renewable energy, environmental protection, pharmaceuticals, personal care, surface coatings, plastics, textiles, food, building materials, electronics, automotives, etc. In this dissertation the focus will be on application of multifunctional NPs for:

I. Sensing
II. Imaging and labelling

6.1 Nano bio sensors

Nanobiotechnology is predicted to be a major research area for this next century. However several stumbling blocks need to be overcome to ensure a close marriage of biology and nanotechnology. A variety of medical processes occur at nanometer length scales. Among the approaches for exploiting developments in nanotechnology in medicine, nanoparticles offer some unique advantages as sensing. Many types of nanoparticles, including metal nanoparticles, oxide nanoparticles, semiconductor nanoparticles, and even composite nanoparticles, have been widely used in electrochemical sensors and biosensors. Although nanoparticles play a different role in different electrochemical sensing system; based on their unique properties. The basic functions of nanoparticles can be mainly classified as immobilization of biomolecules, catalysis of electrochemical reactions, enhancement of electron transfer, labeling biomolecules and acting as reactant.

In the area of biosensors, QDs are particularly attractive due to their long term photostability, allowing real time and continuous monitoring. QD based FRET nanosensors will be particularly appealing for intracellular sensing, where their high photo bleaching thresholds and substantial reduction in direct excitation of dye and fluorescent protein acceptors could permit the monitoring of intracellular processes over longer periods of time. [169]. QDs have been shown to be very efficient FRET donors with organic fluorophores, due to the large overlap between the quantum dot emission wavelength and the absorption spectra of the dyes [94, 95]. As the emission characteristics of the QDs can be continuously tuned so it is possible to create a FRET donor for any number of organic dyes that emit between approximately 510 and 640 nm [94, 102, 170]. Multi analyte sensing QDs [171]; simultaneously detected two different types of ions, K^+ and Cl^-. By using polyacrylic particles containing QDs and two kinds of ion sensitive dyes, while the QDs were used to excite the organic dyes and thus generating two different FRET pairs. The presence of anions, such as F^-, Cl^- or CH_3COO^- was result in 90% quenching of QDs acted as donor and dye as the acceptor [172, 173]. Other anions like Br^- or HSO_4^- did not show significant quenching effects. To demonstrate real intracellular sensing, a Nile blue dye conjugated with BSA modified QDs [174] delivered the complex into Hela cells by electroporation to sense the intracellular nicotinamide adenine dinucleotide (NAD^+) dependent metabolism. In the presence of NADH, Nile blue does not absorb in the visible region and hence, QD donor emission will not match the Nile blue acceptor absorption; thus no FRET occurs.

A prototype sensor for the specific detection of the nutrient sugar maltose in solution using a QD-Maltose binding proteins (MBP) conjugate. This sensing assembly used QDs as both energy donors and structural scaffolds to array multiple protein receptors. Time-resolved fluorescence data collected for this system showed a decrease in the QD lifetime when the dye labelled analog was bound to MBP and recovery of the QD lifetime when maltose was added to the system. The nanosensor also shows high specificity by responding only to sugars having the MBP-recognized a-1,4-glucosidic linkage, which proves that QD-bound proteins maintain their intrinsic binding properties [96, 175]. Peptides expressing a cysteine at one terminus and labelled with a rohdamine dye at the other end as substrates were prepared. The peptide dyes were used to functionalize CdSe/ZnS QDs via cap exchange. The center section of the peptide sequence was designed to be recognized and cleaved by either of the peptidases, trypsin, or collagenase. Incubating the pre-assembled QD-peptide-dye conjugates (which are partially quenched) with either enzyme produced recovery of the QD emission. Furthermore, the presence of an inhibitor was shown to substantially decrease the rate of fluorescence recovery and indicated a reduction in protease activity. The authors also showed that the conjugate sensor could detect the presence of extracellular secreted proteases in cancerous cell cultures. This study demonstrated that proteolytic activity could be qualitatively followed over time with QD-peptide substrates both in vitro and in clinically relevant cell culture samples [176].

Among the NPs used for the immobilization of proteins, gold NPs are probably the most frequently used. Electrochemical immunosensors based on the immobilization of antigen or antibody with NPs is also extensively studied. A reagentless amperometric immunosensor based on the immobilization of a fetoprotein antibody onto gold NPs, exhibited good long term stability. They also prepared a label free immunosensor for Japanese B encephalitis vaccine [19] through the immobilization of related antibody with gold nanoparticles. As antibodies and antigens are both proteins, their immobilization mechanism with NPs is the same as the immobilization of enzymes.

Interestingly, the presence of gold NPs changed the dynamics of DNA strand hybridization [177-179]. The detection was based on the change of position of the plasmon band of a colloidal solution (and thus on a change of color) triggered by aggregation of the particles. Aggregation was controlled by DNA hybridization [161]. Two batches of gold NPs with oligonucleotides [180] (single-stranded DNA) terminated with a thiol function were prepared. One with DNA strands that will name A and the other with B, and then mixed together. In the presence of a free duplex containing on one end a strand complementary to A, on the other a strand complementary to B, the DNA strands hybridized and the distance between two consecutive nanoparticles was reduced dramatically. The natural consequence was a change in color from bright red for non aggregated NPs to purple for aggregated NPs [181]. The powerful detection method based on aggregation and deaggregation of gold NPs was extended for sensing all sorts of biorelevant molecules [163, 182, 183].

6.2 Imaging and Labeling

Molecular and cellular imaging is a branch of the biomedical sciences born from the merging of two areas: detection technology (i.e. scanners and imaging devices) and the probes (radioactive, luminescent, paramagnetic, etc.) that makes imaging possible. Molecular imaging is one of the most exciting and rapidly growing areas of science [184]. It involves the non-invasive study of biological processes in vivo at the cellular and molecular level and a key role for chemists is the design of imaging agents that make molecular processes visible, quantifiable and traceable over time, aiming to probe molecular abnormalities. A multi modal contrast agent with optical, radioactive, and magnetic properties could help in preoperative diagnostics and intraoperative surgical resection of brain tumor or other surgical lesions [185]. Various imaging modalities (e.g. positron emission tomography (PET), single photon emission computed tomography (SPECT), magnetic resonance imaging (MRI), and optical ultrasound) can be used to assess specific molecular targets. Certain modalities are well suited for some applications, whilst very poorly suited for other applications. As no one imaging modality can provide information on all aspects of structure and function, interrogation of a subject using multiple imaging modalities is clearly attractive [186, 187]. Multi modal imaging using a small molecule based probe is challenging due to the limited number of attachment points and the potential interference with its receptor binding affinity. However, NPs have large surface areas where multiple functional moieties can be incorporated for multi modality molecular imaging. NPs based probes have found tremendous success in recent years as labels in biological systems and have shown great potential for bioimaging and diagnostics [188].

MRI/optical probes present the possibility of tracking cells in the body on a cellular scale through optical imaging but with additional cross-sectional anatomical information from MRI. Paramagnetic contrast agents change the rate at which protons decay from their excited state to the ground state, allowing more rapid decay through energy transfer to a neighboring nucleus. As a result, regions containing the paramagnetic contrast agent appear darker in an MRI than regions without the agent [189]. When multifunctional QDs are delivered to the liver, the uptake rate of QDs by healthy liver cells is much higher than that by diseased cells. Consequently, the healthy regions are darker than the diseased regions [110, 190, 191]. Water soluble QDs yielded very high relaxivities (~2000 $mM^{-1}s^{-1}$) suitable for MRI and good selectivity for endothelial cells observed from an in vitro study using fluorescence microscopy [190]. The relaxivities R_1 and R_2 were found to be 20.5 and 151 $mM^{-1}s^{-1}$, respectively. Compared to commercially available contrast agents, Gd-functionalized QDs exhibited higher R_1 and R_2 values under the same magnetic field strength of 4.7 T [192]. Superparamagnetic iron oxide NPs has been extensively studied as MR imaging agents due to their ability to enhance the T_2-weighted MRI signal, and as biologically being alternatives to Gd based systems. One of the earliest examples of a dual MRI and optical probe was that of a cross-linked iron oxide (CLIO) NPs consisting of a surface of cross-linked dextran functionalised with amine groups. Attachment of the indocyanine dye Cy5.5 through a polypeptide link was facile using the coupling of a terminal amine group and a maleimide group attached to Cy5.5 [193]. Early detection has been shown to be possible in vivo using a Cy5.5-CLIO imaging probe functionalized with a protein which has a specific affinity for the antigen. The same probe has also been shown to be able to track tumor response to chemotherapy in real time in vivo with the potential of saving a great deal of time and cost in the development of cancer therapeutics [194]. The fusion of radionuclear and optical methods is still a less frequently used multi-modal imaging strategy, perhaps due to misconceptions and technical difficulties including the absence of a standard optical imaging system and the lack of approved target specific optical molecular probes. CdSe/ZnS QDs labelled with radionuclide ^{64}Cu [120] studied both with conventional well counting and by serial micro PET with ROI analysis. A report has utilized small animal PET and bioluminescence imaging as an important tool in cancer research. This technology was combined with small animal CT to obtain fusion images with both anatomical and molecular information. The multi modal imaging was used to detect xenografts of different cell lines and metastases of a melanoma cell line, and validation studies showed a good co-registration of images from both PET and CT. The ^{18}F labelled NPs [195], PET/CT allowed detection and localization of lesions that were not seen with CT because of poor contrast resolution. The study shows that the combination of PET, small animal CT and bioluminescence allows a sensitive and improved quantification of tumors in mice [196]. It is hoped that the method will find application in sentinel node imaging of human tumors [197].

PET and MRI are largely complementary techniques and combination would certainly be a ‘marriage of convenience’. Combination of PET exceptionally sensitive, metabolically functional but with poor spatial resolution synergistically linked to MRI giving supremely high resolution anatomic information in the sub-millimeter range [122]. ^{64}Cu radiolabeling of dextran sulfate coated superparamagnetic iron oxide NPs; these are targeted toward inflammatory events, such as atherosclerotic plaques. The labeling was done by coordination of the ^{64}Cu to the chelating bifunctional ligand DOTA and then conjugation to the NPs [124]. In another approach dextran and PEG coated superparamagnetic iron oxide NPs, nanoferrites and radioimmunoconjugate NPs linked to a fluorescent dye and radiolabelled with ^{111}In [74], ^{18}F [195] and ^{68}Ga [121] have been used to (1) deliver heat selectively at the microenvironment of tumors with external magnetic field [198] and (2) image and trace the NP kinetics in vivo [74]. Radiotracer was utilized on NPs to establish targeting in the tumor, to predict thermal dose in the tumor and to quantify NPs tissue biodistributions.

Fluorescence labeling of biological systems [200-202], as a tool for developing immunoassays, cellular labeling, and tissue imaging, is one of the most commonly used approaches in modern biotechnology. Cells can be labelled using QDs in a nonspecific or targeted manner. Hydrophobic and electrostatic interactions between capping molecules in QDs and biomolecules in cells induce passive nonspecific labelling. Water soluble QDs have been introduced into large multicellular animals (mice) to preferentially stain vascular and lymphatic systems tumors, showing that higher contrast and imaging depth can be obtained at a lower excitation power than with organic dyes. Imaging of targeted QD delivery in live mice was achieved by intravenously injecting them with QDs functionalized with antibodies [63] to prostate specific membrane antigen. Many studies have shown the great potential of using quantum dots as new probes in vivo [196, 203, 204]. The long fluorescence lifetime of QDs (15 to 20 ns) enables the use of time gated detection [205] to separate their signals from those of shorter lived species, such as background auto fluorescence encountered in cells. When the fluorescence lifetime instrumentation currently available is used, greater signal-to-noise ratios are possible. Recent developments in QD synthesis and bioconjugation, their applications in molecular and cellular imaging, as well as promising directions for future research are reviewed by many authors [145, 206-210].

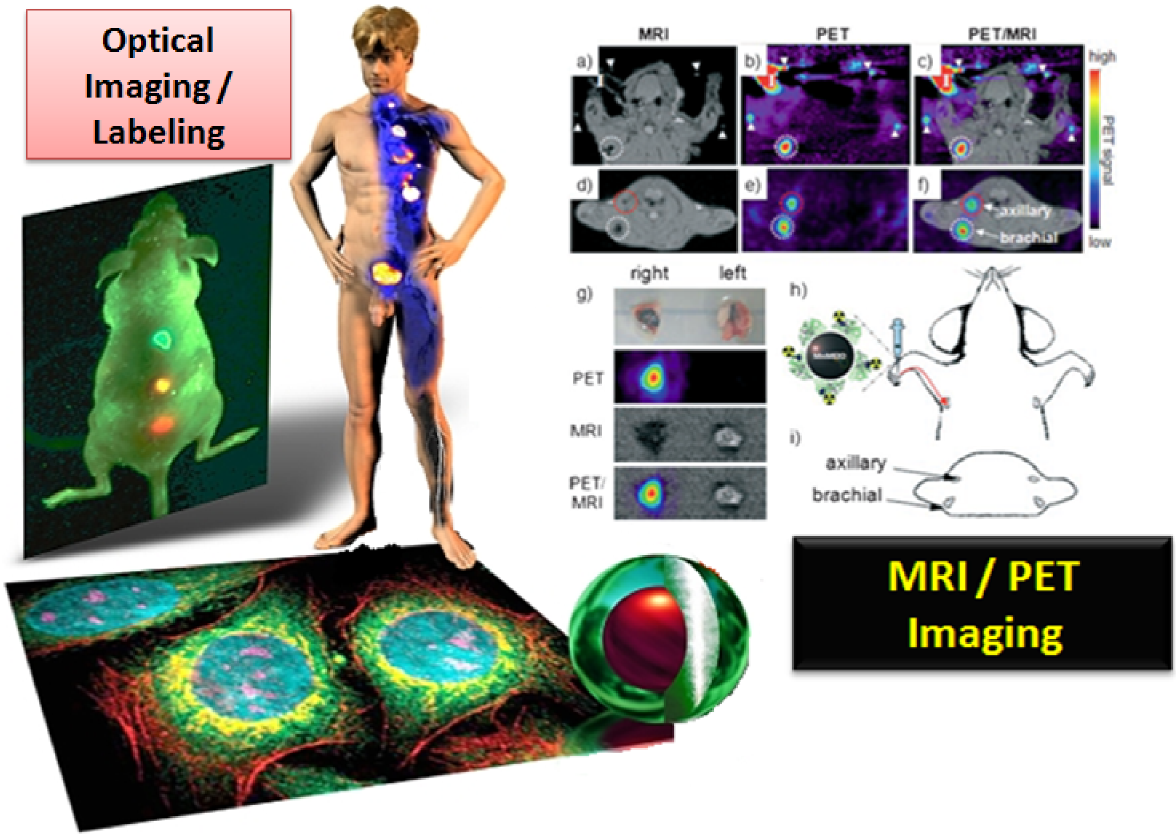

Figure 8: *Application of multi functional NPs for imaging and labeling. Picture on left side are typical images of QDs as fluorescent labels. Right side image belong to bimodal MnMEIO NPs label with* ^{124}*I inject to fore paw of rat and imaged by PET (b and e), MRI (a and d) and fusion of both (c and f) (with courtesy from ref [199])*

Besides their superior properties as fluorescent labels, the increasingly popular application of QD based labels for biological studies of living organisms has required that QD toxicity be examined since it is well known that QDs contain toxic elements. Studies have shown that quantum dot toxicity is due to cadmium ions [211, 212] being released into cells. This is exacerbated by oxygen, UV exposure, and the large exposed surfaces of the spherical QDs. To avoid these problems, surfaces are added to the QDs, traditionally consisting of zinc-sulfide compounds. [211, 213-215].

7. Conclusion

Based on the novel properties of NPs, lots of approaches emerge that aim at their employment in bioapplications. However, if safety is taken into account, there still are some obstacles to overcome. Multifunctional NPs for imaging approaches will have a significant impact on biomedical research and drug discovery and development; indeed many industrial companies have set up medical imaging divisions and are integrating molecular imaging into their drug development efforts. Imaging targets in body/cell/tissue and investigating interaction of targets with substrates and receptor occupancy are vital in pre-clinical and clinical research. The design of the appropriate multi modal imaging probe is the key and any real advances in molecular imaging will be due to the interdisciplinary efforts of synthetic chemists, molecular biologists, biomedical, and imaging scientists.

Finally, principle experiments have successfully achieved multifunctional NPs based probes, which need to be further used by biologist for application in-vivo and in-vitro. As research on NPs with novel properties continues, it should be possible to overcome drawbacks and to develop multifunctional, multimodal NPs based systems for better biological imaging. The challenge is moving discoveries from the laboratory to the clinic and out to the market. There is commercial and clinical demand for new multifunctional NPs based probes, but few ways to complete the preclinical safety and regulatory work needed to bridge the research from laboratory to the clinic.

8. Publication list and Author's contribution

A. "Multifunctional Nanoparticles for dual imaging" Z. Ali, A. Z. Abbasi, F. Zhang, P. Arosio, A. Lascialfari, M.F. Casula, A. Wenk, W. Kreyling, R. Plapper, M. Seidel[6], R. Niessner, J. Knöll, A. Seubert, W. J. Parak. Submitted to Analytical Chemistry

All sample preparation and optical characterization by UV-Vis and fluorescence spectrometer and data evaluation.

B. "Excitation dynamics in polymer-coated semiconductor quantum dots with integrated dye molecules: The role of reabsorption" Tobias Niebling, Feng Zhang, Zulqurnain Ali, Wolfgang J. Parak, and Wolfram Heimbrodt. Journal of Applied Physics 106, 104701 (2009)

Synthesis of Quantum dot as donar and dye as acceptor assembly, purification of samples and steady state fluorescence measurements.

C. "Wrapping Nanocrystals with an Amphiphilic Polymer Preloaded with Fixed Amounts of Fluorophore Generates FRET-Based Nanoprobes with a Controlled Donor/Acceptor Ratio" Aleksey V. Yakovlev, Feng Zhang, Ali Zulqurnain, Abbasi Azhar-Zahoor, Camilla Luccardini, Stephane Gaillard, Jean-Maurice Mallet, Patrick Tauc, Jean-Claude Brochon, Wolfgang J. Parak, Anne Feltz and Martin Oheim. *Langmuir* 2009, *25,* 3232-3239

Polymer coating of quantum dots and modification with different ratios of ATTO-590 dye. UV-Vis spectra of all samples by keeping constant amount of dye/Qdots and steady state fluorescence measurements.

D. "Ion and pH Sensing with Colloidal Nanoparticles: Influence of Surface Charge on Sensing and Colloidal Properties" Feng Zhang, Zulqurnain Ali, Faheem Amin, Anne Feltz, Martin Oheim, and Wolfgang J. Parak. ChemPhysChem 2010, 11, 730 – 735

Synthesis of dye modified nanoparticles, purification and optical characterization

E. "Fluorescent–Magnetic Hybrid Nanoparticles Induce a Dose-Dependent Increase in Proinflammatory Response in Lung Cells in vitro Correlated with Intracellular Localization" Andrea D. Lehmann, Wolfgang J. Parak, Feng Zhang, Zulqurnain Ali, Carlheinz Röcker, G. Ulrich Nienhaus, Peter Gehr, and Barbara Rothen-Rutishauser. small 2010, 6, No. 6, 753–762

Preparation of iron platinum and gold nanoparticles modified with and without dye, purification of samples and optical characterization.

F. "Quantitative Evaluation of Cellular Uptake and Trafficking of Plain and Polyethylene Glycol-Coated Gold Nanoparticles" Christina Brandenberger, Christian Mühlfeld, Zulqurnain Ali, Anke-Gabriele Lenz, Otmar Schmid, Wolfgang J. Parak, Peter Gehr, and Barbara Rothen-Rutishauser. small 2010, 6, No. 15, 1669–1678

Synthesis of different sizes of gold nanoparticles, phase transfer via polymer coating and surface modification with PEG spacers.

G. "Algal toxicity and *in vitro* uptake of polymer coated gold nanoparticles" K. Van Hoecke, A.C. De Schamphelaere, Z. Ali, F. Zhang, A. Elsaesser , P. Rivera Gil, W. J. Parak, G. Smagghe, V. C. Howard and C.R. Janssen. Submitted in Nanotoxicology

Synthesis of gold nanoparticles, phase transfer via polymer coating, purification, modification with Creysel Violet Percholrate dye, poly ethylene glycols and part of characterization.

H. "In vitro and intracellular sensing by using the photoluminescence of quantum dots" Feng Zhang, Zulqurnain Ali, Faheem Amin, Andreas Riedinger &Wolfgang J. Parak. Anal Bioanal Chem

A Review article jointly written by other authors.

9. References

1. Eustis, S. and M.A. El-Sayed, Why gold nanoparticles are more presious than pretty gold: Noble metal surface plasmon resonance and its enhancement of the radiative and nonradiative properties of nanocrystals of different shapes. Chemical Society Reviews, 2006. **35**: p. 209-217.
2. Sperling, R.A. and W.J. Parak, Surface modification, functionalization and bioconjugation of colloidal inorganic nanoparticles. Phil. Trans. R. Soc. A, 2010. **368**: p. 1333 1383.
3. Sperling, R.A., et al., Biological Applications of Gold Nanoparticles. Chemical Society Reviews, 2008. **37**(9): p. 1896 - 1908.
4. Zhang, L., et al., Nanoparticles in medicine: Therapeutic applications and developments. Clinical Pharmacology & Therapeutics, 2008. **83**(5): p. 761-769.
5. Burda, C., et al., Chemistry and Properties of Nanocrystals of Different Shapes. Chem. Rev., 2005. **105**(4): p. 1025-1102.
6. Zawislak, P.A., et al., Technological trajectories and multidimensional impacts: further remarks on the nanotechnology industry. Journal of Business Chemistry, 2010. **7**(1): p. 47-64.

7. Hutchings, G.J., M. Brust, and H. Schmidbaur, Gold - an introductory perspective. Chemical Society Reviews, 2008. **37**(9): p. 1759-1765.
8. Ghosh, P., et al., Gold nanoparticles in delivery applications. Advanced Drug Delivery Reviews, 2008. **60**(11): p. 1307-1315.
9. Bentolila, L.A. and S. Weiss, Biological quantum dots go live. Physics World, 2003. **16**(3): p. 23-24.
10. Alivisatos, A.P., Semiconductor Clusters, Nanocrystals, and Quantum Dots. Science, 1996. **271**(16 February): p. 933-937.
11. Dabbousi, B.O., et al., (CdSe)ZnS Core-Shell Quantum Dots: Synthesis and Characterization of a Size Series of Highly Luminescent Nanocrystallites. Journal of Physical Chemistry B, 1997. **101**(46): p. 9463-9475.
12. Rogach, A.L., et al., Synthesis and Characterization of Thiol-Stabilized CdTe Nanocrystals. Ber. Bunsenges. Phys. Chem., 1996. **100**(11): p. 1772-1778.
13. Peng, Z.A. and X. Peng, Formation of High-Quality CdTe, CdSe, and CdS Nanocrystals Using CdO as Precursor. Journal of the American Chemical Society, 2001. **123**(1): p. 183-184.
14. Frens, G., Controlled Nucleation for Regulation of Particle-Size in Monodisperse Gold Solutions. Nature Physical Science, 1973. **241**(105): p. 20-22.
15. Hirai, H., H. Aizawa, and H. Shiozaki, Preparation of Nonaqueous Dispersion of Colloidal Silver by Phase Transfer. Chem. Lett., 1992. **21**(8): p. 1527-1530.
16. Liz-Marzán, L.M. and I. Lado-Touriño, Reduction and Stabilization of Silver Nanoparticles in Ethanol by Nonionic Surfactants. Langmuir, 1996. **12**: p. 3585-3589.
17. Suslick, K.S., M. Fang, and T. Hyeon, Sonochemical Synthesis of Iron Colloids. J. Am. Chem. Soc., 1996. **118**(47): p. 11960-11961.
18. Sun, S. and C.B. Murray, Synthesis of monodisperse cobalt nanocrystals and their assembly into magnetic superlattices „invited... JOURNAL OF APPLIED PHYSICS, 1999. **85**(8): p. 4325-4331.
19. Daniel, M.C. and D. Astruc, Gold Nanoparticles: Assembly, Supramolecular Chemistry, Quantum-Size-Related Properties, and Applications toward Biology, Catalysis, and Nanotechnology. Chemical Reviews, 2004. **104**(1): p. 293-346.
20. John Turkevich, P.C.S.a.J.H., A study of the nucleation and growth processes in the synthesis of colloidal gold. Discuss. Faraday Soc., 1951. **11**: p. 55 - 75.
21. Weare, W.W., et al., Improved Synthesis of Small (d_{CORE} =1.5 nm) Phosphine-Stabilized Gold Nanoparticles. Journal of the American Chemical Society, 2000. **122**(51): p. 12890-12891.
22. Brust, M., et al., Synthesis of thiol-derivatised gold nanoparticles in a two-phase liquid-liquid system. J. Chem. Soc., Chem. Commun., 1994. **1994**: p. 801-802.
23. Hostetler, M.J., et al., Alkanethiolate Gold Cluster Molecules with Core Diameters from 1.5 to 5.2 nm: Core and Monolayer Properties as a Function of Core Size. Langmuir, 1998. **14**(1): p. 17-30.
24. Fink, J., et al., Self-Organization of Nanosized Gold Particles. Chemistry of Materials, 1998. **10**(3): p. 922-926.
25. Hiramatsu, H. and F.E. Osterloh, A simple large-scale synthesis of nearly monodisperse gold and silver nanoparticles with adjustable sizes and with exchangeable surfactants. Chemistry Of Materials, 2004. **16**(13): p. 2509-2511.
26. Turkevich, J., P.C. Stevenson, and J. Hillier, A study of the nucleation and growth processes in the synthesis of colloidal golde. J. Discuss. Faraday Soc., 1951: p. 55-75.

27. Grabar, K.C., et al., Preparation and Characterization of Au Colloid Monlayers. Analytical Chemistry, 1995. **67**: p. 735-743.
28. Hiramatsu, H. and F.E. Osterloh, A Simple Large-Scale Synthesis of Nearly Monodisperse Gold and Silver Nanoparticles with Adjustable Sizes and with Exchangeable Surfactants. Chem. Mater., 2004. **16**(13): p. 2509-2511.
29. Murray, C.B., C.R. Kagan, and M.G. Bawendi, Synthesis and Characterization of Monodisperse Nanocrystals and Close-Packed Nanocrystals Assembles. Annu. Rev. Mater. Sci., 2000. **30**: p. 545-610.
30. Lemon, B.I. and R.M. Crooks, Preparation and Characterization of Dendrimer-Encapsulated CdS Semiconductor Quantum Dots. Journal of the American Chemical Society, 2000. **122**(51): p. 12886-12887.
31. Talapin, D.V., et al., Highly Luminescent Monodisperse CdSe and CdSe/ZnS Nanocrystals Synthesized in a Hexadecylamine-Trioctylphosphine Oxide-Trioctylphospine Mixture. NanoLetters, 2001. **1**(4): p. 207-211.
32. Rogach, A.L., et al., Colloidally Prepared CdHgTe and HgTe Quantum Dots with Strong Near-Infrared Luminescence. Physica Status Solidi B, 2001. **224**(1): p. 153-158.
33. Murray, C.B., D.J. Norris, and M.G. Bawendi, Synthesis and Characterization of Nearly Monodisperse CdE (E = S, Se, Te) Semiconductor Nanocrystallites. Journal of the American Chemical Society, 1993. **115**: p. 8706-8715.
34. Yang, Y., et al., Preparation, characterization and electroluminescence of ZnS nanocrystals in a polymer matrix. Journal of Materials Chemistry, 1997. **7**: p. 131-133.
35. Schneider, T., et al., Synthesis and Characterization of PbS Nanoparticles in Block Copolymer Micelles. Ber. Bunsen. Phys. Chem., 1997. **101**(11): p. 1654-1656.
36. Arruebo, M., et al., Magnetic nanoparticles for drug delivery. Nano Today, 2007. **2**(3): p. 22-32.
37. Fang, C. and M.Q. Zhang, Multifunctional magnetic nanoparticles for medical imaging applications. Journal of Materials Chemistry, 2009. **19**(35): p. 6258-6266.
38. Hütten, A., et al., New magnetic nanoparticles for biotechnology. Journal of Biotechnology, 2004. **112**: p. 47-63.
39. Pankhurst, Q.A., et al., Applications of magnetic nanoparticles in biomedicine. J. Phys. D: Appl. Phys., 2003. **36**: p. R167-R181.
40. Sun, C., J. Lee, and M. Zhang, Magnetic nanoparticles in MR imaging and drug delivery. ADVANCED DRUG DELIVERY REVIEWS, 2008. **60**(11): p. 1252-1265.
41. McCarthy, J.R. and R. Weissleder, Multifunctional magnetic nanoparticles for targeted imaging and therapy. Advanced Drug Delivery Reviews, 2008. **60**(11): p. 1241.
42. Sun, S. and H. Zeng, Size-Controlled Synthesis of Magnetite Nanoparticles. Journal of the American Chemical Society, 2002. **124**(28): p. 8204-8205.
43. Mornet, S., et al., Magnetic nanoparticle design for medical diagnosis and therapy. Journal of Materials Chemistry, 2004. **14**(14): p. 2161-2175.
44. Puntes, V.F., K.M. Krishnan, and P. Alivisatos, Synthesis, self-assembly, and magnetic behavior of a two-dimensional superlattice of single-crystal ε-Co nanoparticles. Applied Physics Letters, 2001. **78**(15): p. 2187-2189.
45. Liu, Z.L., et al., Synthesis and Magnetic Properties of Fe_3O_4 Nanoparticles. Journal of Materials Synthesis and Processing, 2002. **10**(2): p. 83-87.
46. Wagner, J., T. Autenrieth, and R. Hempelmann, Core shell particles consisting of cobalt ferrite and silica as model ferrofluids [$CoFe_2O_4$ –SiO_2 core shell particles]. Journal of Magnetism and Magnetic Materials, 2002. **252**: p. 4-6.

47. Elkins, K.E., et al., Ultrafine FePt Nanoparticles Prepared by the Chemical Reduction Method. Nanoletters, 2003. **3**(12): p. 1647-1649.
48. Alivisatos, A.P., X. Peng, and L. Manna, Process for forming shaped group III-V semiconductor nanocrystals, and product formed using process. 2001: USA.
49. Algar, W.R. and U.J. Krull, Luminescence and Stability of Aqueous Thioalkyl Acid Capped CdSe/ZnS Quantum Dots Correlated to Ligand Ionization. ChemPhysChem, 2007. **8**(4): p. 561-568.
50. Algar, W.R. and U.J. Krull, Adsorption and Hybridization of Oligonucleotides on Mercaptoacetic Acid-Capped CdSe/ZnS Quantum Dots and Quantum Dot-Oligonucleotide Conjugates. Langmuir, 2006. **22**(26): p. 11346-11352.
51. Uyeda, H.T., et al., Synthesis of Compact Multidentate Ligands to Prepare Stable Hydrophilic Quantum Dot Fluorophores. Journal of the Americal Chemical Society, 2005. **127**(11): p. 3870-3878.
52. Kloepfer, J.A., S.E. Bradforth, and J.L. Nadeau, Photophysical Properties of Biologically Compatible CdSe Quantum Dot Structures. Journal of Physical Chemistry B, 2005. **109**: p. 9996-10003.
53. Aldana, J., Y.A. Wang, and X. Peng, Photochemical instability of CdSe nanocrystals coated by hydrophilic thiols. Journal of the American Chemical Society, 2001. **123**(36): p. 8844-8850.
54. Selvakannan, P.R., et al., Capping of Gold Nanoparticles by the Amino Acid Lysine Renders Them Water-Dispersible. Langmuir, 2003. **19**(8): p. 3545-3549.
55. Zhang, T., et al., A General Approach for Transferring Hydrophobic Nanocrystals into Water. Nano Lett., 2007. **7**(10): p. 3203-3207.
56. Jana, N.R., C. Earhart, and J.Y. Ying, Synthesis of Water-Soluble and Functionalized Nanoparticles by Silica Coating. Chem. Mater., 2007. **19**(21): p. 5074-5082.
57. Ung, T., L.M. Liz-Marzán, and P. Mulvaney, Controlled Method for Silica Coating of Silver Colloids. Influence of Coating on the Rate of Chemical Reactions. Langmuir, 1998. **14**(14): p. 3740-3748.
58. Aliev, F.G., et al., Layer-By-Layer Assembly of Core-Shell Magnetite Nanoparticles: Effect of Silica Coating on Interparticle Interactions and Magnetic Properties. Advanced Materials, 1999. **11**(12): p. 1006-1010.
59. Gerion, D., et al., Synthesis and Properties of Biocompatible Water-Soluble Silica-Coated CdSe/ZnS Semiconductor Quantum Dots. Journal of Physical Chemistry B, 2001. **105**(37): p. 8861-8871.
60. Tan, T.T., et al., Size control, shape evolution, and silica coating of near-infrared-emitting PbSe quantum dots. Chemistry Of Materials, 2007. **19**(13): p. 3112-3117.
61. Alivisatos, A., W. Gu, and C. Larabell, Quantum Dots as Cellular Probes. Annual Review of Biomedical Engineering 2005. **7**: p. 55-76.
62. Dubertret, B., et al., In Vivo Imaging of Quantum Dots Encapsulated in Phospholipid Micelles. Science, 2002. **298**(29 November): p. 1759-1762.
63. Gao, X., et al., In vivo cancer targeting and imaging with semiconductor quantum dots. Nature Biotechnology, 2004. **22**(8): p. 969-976.
64. Wu, M.X., et al., Immunofluorescent labeling of cancer marker Her2 and other cellular targets with semiconductor quantum dots. Nature Biotechnology, 2003. **21**: p. 41-46.
65. Pellegrino, T., et al., Hydrophobic nanocrystals coated with an amphiphilic polymer shell: a general route to water soluble nanocrystals. Nanoletters, 2004. **4**(4): p. 703-707.

66. Corato, R.D., et al., Water solubilization of hydrophobic nanocrystals by means of poly(maleic anhydride-alt-1-octadecene). Journal of Materials Chemistry, 2008. **18**: p. 1991-1996.
67. Yu, W.W., et al., Forming Biocompatible and Nonaggregated Nanocrystals in Water Using Amphiphilic Polymers J. Am. Chem. Soc., 2007. **129**(10): p. 2871-2879.
68. Qian, X., et al., In vivo tumor targeting and spectroscopic detection with surface-enhanced Raman nanoparticle tags. Nat Biotech, 2008. **26**(1): p. 83.
69. Lin, C.-A.J., et al., Design of an amphiphilic polymer for nanoparticle coating and functionalization. Small, 2008. **4**(3): p. 334-341.
70. Petruska, M.A., A.P. Bartko, and V.I. Klimov, An Amphiphilic Approach to Nanocrystal Quantum Dot-Titania Nanocomposites. J. Am. Chem. Soc., 2004. **126**(3): p. 714-715.
71. Luccardini, C., et al., Size, Charge, and Interactions with Giant Lipid Vesicles of Quantum Dots Coated with an Amphiphilic Macromolecule. Langmuir, 2006. **22**(5): p. 2304 - 2310.
72. Kairdolf, B.A., A.M. Smith, and S. Nie, One-Pot Synthesis, Encapsulation, and Solubilization of Size-Tuned Quantum Dots with Amphiphilic Multidentate Ligands. J. Am. Chem. Soc., 2008. **130**(39): p. 12866 - 1286.
73. Nann, T., Phase-transfer of CdSe@ZnS quantum dots using amphiphilic hyperbranched polyethylenimine. Chem. Commun., 2005. **2005**(13): p. 1735-1736.
74. Natarajan, A., et al., NanoFerrite Particle Based Radioimmunonanoparticles: Binding Affinity and In Vivo Pharmacokinetics. Bioconjugate Chem., 2008. **19**: p. 1211–1218.
75. Panchuk–Voloshina, N., et al., Alexa Dyes, a Series of New Fluorescent Dyes that Yield Exceptionally Bright, Photostable Conjugates. Journal of Histochemistry and Cytochemistry, 1999. **47**(9): p. 1179-1188.
76. Shaner, N.C., P.A. Steinbach, and R.Y. Tsien, A guide to choosing fluorescent proteins. Nature Methods, 2005. **2**(12): p. 905-909.
77. Wolff, M., et al., Novel fluorescent proteins for high-content screening. Drug Discovery Today, 2006. **11**(23-24): p. 1054-1060.
78. Charbonniere, L.J. and N. Hildebrandt, Lanthanide complexes and quantum dots: A bright wedding for resonance energy transfer. European Journal Of Inorganic Chemistry, 2008(21): p. 3241-3251.
79. Chandrasekharan, N., et al., Dye-Capped Gold Nanoclusters: Photoinduced Morphological Changes in Gold/Rhodamine 6G Nanoassemblies. Journal of Physical Chemistry B, 2000. **104**(47): p. 11103-11109.
80. Sari, S.M.C., et al., Grafting of colloidal stable gold nanoparticles with lissamine rhodamine B: an original procedure for counting the number of dye molecules attached to the particles. Journal of Materials Chemistry, 2004. **14**(3): p. 402-407.
81. Dulkeith, E., et al., Fluorescence Quenching of Dye Molecules near Gold nanoparticles: radiative and Nonradiative Effects. Physical Review Letters, 2002. **89**(20): p. 203002-1 - 202002-4.
82. Dubertret, B., M. Calame, and A.J. Libchaber, Single-mismatch detection using gold-quenched fluorescent oligonucleotides. Nature Biotechnology, 2001. **19**(4): p. 365-370.
83. Herz, E., et al., Dye structure-optical property correlations in near-infrared fluorescent core-shell silica nanoparticles. Journal of Materials Chemistry, 2009. **19**(35): p. 6341-6347.
84. Bertorelle, F., et al., Fluorescence-modified superparamagnetic nanoparticles: Intracellular uptake and use in cellular imaging. Langmuir, 2006. **22**(12): p. 5385-5391.
85. Schellenberger, E.A., et al., Surface-Functionalized Nanoparticle Library Yields Probes for Apoptotic Cells. ChemBioChem, 2004. **5**: p. 275-279.

86. Banerjee, S.S. and D.H. Chen, A multifunctional magnetic nanocarrier bearing fluorescent dye for targeted drug delivery by enhanced two-photon triggered release. Nanotechnology, 2009. **20**(18).

87. Josephson, L., et al., Near-Infrared Fluorescent Nanoparticles as Combined MR/Optical Imaging Probes. Bioconjugate Chemistry, 2002. **13**(3): p. 554-560.

88. Lehmann, A.D., et al., Fluorescent-Magnetic Hybrid Nanoparticles Induce a Dose-Dependent Increase in Proinflammatory Response in Lung Cells in vitro Correlated with Intracellular Localization. SMALL, 2010. **6**(6): p. 753-762.

89. Röcker, C., et al., A Quantitative Fluorescence Study of Protein Monolayer Formation on Colloidal Nanoparticles. Nature Nanotechnology, 2009. **4**(9): p. 577-580.

90. Buckler, K.J. and R.D. Vaughanjones, Application of a New Ph-Sensitive Fluoroprobe (Carboxy-Snarf-1) for Intracellular Ph Measurement in Small, Isolated Cells. Pflugers Archiv-European Journal of Physiology, 1990. **417**(2): p. 234-239.

91. Zhang, F., et al., Ion and pH Sensing with Colloidal Nanoparticles: Influence of Surface Charge on Sensing and Colloidal Properties. ChemPhysChem, 2010. **11**: p. 730-735.

92. Willard, D.M., et al., CdSe-ZnS Quantum Dots as Resonance Energy Transfer Donors in a Model Protein-Protein Binding Assay. Nanoletters, 2001. **1**(9): p. 469-474.

93. Mattoussi, H., et al., Self-Assembly of CeSe-ZnS Quantum Dot Bioconjugates Using an Engineered Recombinant Protein. J. Am. Chem. Soc., 2000. **122**: p. 12142-12150.

94. Clapp, A.R., et al., Fluorescence Resonance Energy Transfer Between Quantum Dot Donors and Dye-Labeled Protein Acceptors. Journal of the American Chemical society, 2004. **126**(1): p. 301-310.

95. Tran, P.T., et al., Use of Luminescent CdSe-ZnS Nanocrystal Bioconjugates in Quantum Dot-Based Nanosensors. PHYSICA STATUS SOLIDI B-BASIC RESEARCH, 2002. **229**(1): p. 427-432.

96. Medintz, I.L., et al., Self-assembled nanoscale biosensors based on quantum dot FRET donors. Nature Materials, 2003. **2**: p. 630-638.

97. Grecco, H.E., et al., Ensemble and single particle photophysical properties (two-photon excitation, anisotropy, FRET, lifetime, spectral conversion) of commercial quantum dots in solution and in live cells. Microsc Res Tech, 2004. **65**(4-5): p. 169-79.

98. Dennis, A.M. and G. Bao, Quantum Dot-Fluorescent Protein Pairs as Novel Fluorescence Resonance Energy Transfer Probes. Nano Lett., 2008. **8**(5): p. 1439-1445.

99. Peng, H., et al., DNA Hybridization Detection with Blue Luminescent Quantum Dots and Dye-Labeled Single-Stranded DNA. Journal of the American Chemical Society, 2007. **129**(11): p. 3048-3049.

100. Jiang, G., et al., Cascaded FRET in Conjugated Polymer/Quantum Dot/Dye-Labeled DNA Complexes for DNA Hybridization Detection. ACS Nano, 2009. **3**(12): p. 4127-4131.

101. Yakovlev, A.V., et al., Wrapping Nanocrystals with an Amphiphilic Polymer Preloaded with Fixed Amounts of Fluorophore Generates FRET-Based Nanoprobes with a Controlled Donor/Acceptor Ratio. Langmuir, 2009. **25**(5): p. 3232-3239.

102. Niebling, T., et al., Excitation dynamics in polymer-coated semiconductor quantum dots with integrated dye molecules: The role of reabsorption. Journal of Applied Physics, 2009. **106**: p. 104701.

103. Harma, H., et al., Luminescent energy transfer between cadmium telluride nanoparticle and lanthanide(III) chelate in competitive bioaffinity assays of biotin and estradiol. Anal Chim Acta, 2007. **604**(2): p. 177-83.

104. Geissler, D., et al., Quantum Dot Biosensors for Ultrasensitive Multiplexed Diagnostics. Angewandte Chemie International Edition, 2010. **49**(8): p. 1396-1401.

105. Liu, S., Bifunctional coupling agents for radiolabeling of biornolecules and target-specific delivery of metallic radionuclides. Advanced Drug Delivery Reviews, 2008. **60**(12): p. 1347-1370.

106. Vogl, T.J., et al., Superparamagnetic iron oxide-enhanced versus gadolinium-enhanced MR imaging for differential diagnosis of focal liver lesions. Radiology, 1996. **198**(3): p. 881-887.

107. Mewis, R.E. and S.J. Archibald, Biomedical applications of macrocyclic ligand complexes. Coordination Chemistry Reviews, 2010. **254**(15-16): p. 1686-1712.

108. Bottrill, M., L. Kwok, and N.J. Long, Lanthanides in magnetic resonance imaging. Chem. Soc. Rev, 2006. **35**: p. 557-571.

109. Jin, T., et al., Gd3+-functionalized near-infrared quantum dots for in vivo dual modal (fluorescence/magnetic resonance) imaging. Chemical Communications, 2008(44): p. 5764-5766.

110. Bakalova, R., et al., Silica-shelled single quantum dot micelles as imaging probes with dual or multimodality. Analytical Chemistry, 2006. **78**(16): p. 5925-5932.

111. Bakalova, R., et al., Designing quantum-dot probes. Nature Photonics, 2007. **1**(9): p. 487-489.

112. Gerion, D., et al., Paramagnetic silica-coated nanocrystals as an advanced MRI contrast agent. Journal Of Physical Chemistry C, 2007. **111**(34): p. 12542-12551.

113. Marradi, M., et al., Paramagnetic Gd-based gold glyconanoparticles as probes for MRI: tuning relaxivities with sugars. Chem. Commun, 2009. **2009**: p. 3922–3924.

114. Debouttiere, P.J., et al., Design of gold nanoparticles for magnetic resonance imaging. Advanced Functional Materials, 2006. **16**(18): p. 2330-2339.

115. Warsi, M.F., et al., Gd-functionalised Au nanoparticles as targeted contrast agents in MRI: relaxivity enhancement by polyelectrolyte coating. Chemical Communications, 2010. **46**(3): p. 451-453.

116. Md, N.S., et al., Gold Nanoparticles Coated with Gd-Chelate as a Potential CT/MRI Bimodal Contrast Agent. Bulletin of the Korean Chemical Society, 2010. **31**(5): p. 1177-1181.

117. Kim, H.-K., et al., Gold nanoparticles coated with gadolinium-DTPA-bisamide conjugate of penicillamine (Au@GdL) as a T1-weighted blood pool contrast agent. Journal Of Materials Chemistry, 2010. **20**(26): p. 5411-5417.

118. Garanger, E., et al., Simplified syntheses of complex multifunctional nanomaterials. Chem. Commun., 2008. **2008**: p. 4792–4794.

119. Chen, K., et al., Dual-modality optical and positron emission tomography imaging of vascular endothelial growth factor receptor on tumor vasculature using quantum dots. European Journal of Nuclear Medicine and Molecular Imaging, 2008. **35**(12): p. 2235-2244.

120. Schipper, M.L., et al., microPET-Based Biodistribution of Quantum Dots in Living Mice. J Nucl Med, 2007. **48**(9): p. 1511-1518.

121. Stelter, L., et al., Modification of aminosilanized superparamagnetic nanoparticles: feasibility of multimodal detection using 3T MRI, small animal PET, and fluorescence imaging. Mol Imaging Biol, 2009. **12**(1): p. 25-34.

122. Lee, H.-Y., et al., PET/MRI Dual-Modality Tumor Imaging Using Arginine-Glycine-Aspartic (RGD)–Conjugated Radiolabeled Iron Oxide Nanoparticles. J Nucl Med, 2008. **2008**(49): p. 1371.

123. Ting, G., et al., Nanotargeted Radionuclides for Cancer Nuclear Imaging and Internal Radiotherapy. Journal of Biomedicine and Biotechnology, 2010: p. -.

124. Jarrett, B.R., et al., Synthesis of 64Cu-Labeled Magnetic Nanoparticles for Multimodal Imaging. Bioconjugate Chem., 2008(19): p. 1496-1504.

125. Häfelia, U.O., et al., Radiolabeling of magnetic targeted carriers (MTC) with indium-111. Nuclear Medicine and Biology, 2003. **30**(2003): p. 761–769.

126. Huber, M.M., et al., Fluorescently detectable magnetic resonance imaging agents. Bioconjugate Chemistry, 1998. **9**(2): p. 242-249.

127. Roberts, M.J.B., M.D.; Harris, J.M., Chemistry for peptide and protein PEGylation. Advanced Drug Delivery Reviews, 2002. **54**: p. 459 - 476.

128. Brandenberger, C., et al., Quantitative Evaluation of Cellular Uptake and Trafficking of Plain and Polyethylene Glycol-Coated Gold Nanoparticles. SMALL, 2010. **6**: p. 1669-1678

129. Daou, T.J., et al., Effect of Poly(ethylene glycol) Length on the in Vivo Behavior of Coated Quantum Dots. Langmuir, 2009. **25**(5): p. 3040-3044.

130. Boulmedais, F., et al., Water-soluble pegylated quantum dots: From a composite hexagonal phase to isolated micelles. Langmuir, 2006. **22**(23): p. 9797-9803.

131. Acar, H.Y.c., et al., Superparamagnetic nanoparticles stabilized by polymerized PEGylated coatings. Journal of Magnetism and Magnetic Materials, 2005. **293**(1): p. 1.

132. Skaff, H. and T. Emrick, The use of 4-substituted pyridines to afford amphiphilic, pegylated cadmium selenide nanoparticles. Chemical Communications, 2003. **2003**(1): p. 52-53.

133. Hong, R., et al., Surface PEGylation and Ligand Exchange Chemistry of FePt Nanoparticles for Biological Applications. Chemistry of Materials, 2005. **17**: p. 4617-4621.

134. Sakura, T., et al., One-pot preparation of mono-dispersed and physiologically stabilized gold colloid. Colloid & Polymer Science, 2005. **284**(1): p. 97.

135. Wuelfing, W.P., et al., Nanometer Gold Clusters Protected by Surface-Bound Monolayers of Thiolated Poly(ethylene glycol) Polymer Electrolyte. Journal of the American Chemical Society, 1998. **120**(48): p. 12696-12697.

136. Duan, H.W. and S.M. Nie, Cell-penetrating quantum dots based on multivalent and endosome-disrupting surface coatings. Journal Of The American Chemical Society, 2007. **129**(11): p. 3333-3338.

137. Riedinger, A., et al., Ratiometric optical sensing of chloride ions with organic fluorophore - gold nanoparticle hybrids: a systematic study of distance dependency and the influence of surface charge. SMALL, 2010. **accepted**.

138. Sperling, R.A., et al., Electrophoretic separation of nanoparticles with a discrete number of functional groups. Advanced Functional Materials, 2006. **16**(7): p. 943-948.

139. Howarth, M., et al., Monovalent, reduced-size quantum dots for imaging receptors on living cells. Nature Methods, 2008. **5**(5): p. 397-399.

140. Xie, J., et al., Controlled PEGylation of Monodisperse Fe3O4 Nanoparticles for Reduced Non-Specific Uptake by Macrophage Cells. Advanced Materials, 2007. **19**(20): p. 3163-3166.

141. Sun, S., et al., Monodisperse FePt Nanoparticles and Ferromagnetic FePt Nanocrystal Superlattices. Science, 2000. **287**(March 17): p. 1989-1992.

142. Sperling, R.A., et al., Size determination of (bio-) conjugated water-soluble colloidal nanoparticles - a comparison of different techniques. Journal of Physical Chemistry C, 2007. **111**(31): p. 11552 -11559.

143. Bhaskar, S., et al., Multifunctional Nanocarriers for diagnostics, drug delivery and targeted treatment across blood-brain barrier: perspectives on tracking and neuroimaging. Particle And Fibre Toxicology, 2010. **7**.

144. Lee, Y.E., R. Kopelman, and R. Smith, Nanoparticle PEBBLE sensors in live cells and in vivo. Annu Rev Anal Chem, 2009. **2**: p. 57-76.

145. Zhang, F., et al., In vitro and intracellular sensing by using the photoluminescence of quantum dots. Analytical And Bioanalytical Chemistry, 2010. **397**(3): p. 935-942.

146. Niemeyer, C.M., Nanoparticles, Proteins, and Nucleic Acids: Biotechnology Meets Materials Science. Angew. Chem. Int. Ed., 2001. **40**: p. 4128-4158.

147. Green, N.M., Thermodynamics of the Binding of Biotin and some Analogues by Avidin. Biochemical Journal, 1966. **101**: p. 774 - 780.

148. Savage, M.D., et al., Avidin-Biotin Chemistry: A Handbook. 1992: Pierce (downloaded from http://www.piercenet.com/files/Avidin-biotin-book2.zip).

149. Connolly, S. and D. Fitzmaurice, Programmed assembly of gold nanocrystals in aqueous solution. Advanced Materials, 1999. **11**(14): p. 1202-1205.

150. Connolly, S., S.N. Rao, and D. Fitzmaurice, Characterization of Protein Aggregated Gold Nanocrystals. Journal of Physical Chemistry B, 2000. **104**(19): p. 4765-4776.

151. González-García, M.B., C. Fernández-Sánchez, and A. Costa-García, Colloidal gold as an electrochemical label of streptavidin-biotin interaction. Biosensors and Bioelectronics, 2000. **15**(5-6): p. 315-321.

152. Irrgang, J., et al., Analysis of Non-Covalent Bioconjugation of Colloidal Nanoparticles by Means of Atomic Force Microscopy and Data Clustering. Chemphyschem, 2009. **10**(9-10): p. 1483-1491.

153. Hohng, S. and T. Ha, Single-molecule quantum-dot fluorescence resonance energy transfer. Chemphyschem, 2005. **6**(5): p. 956-60.

154. Hildebrandt, N., et al., Quantum dots as efficient energy acceptors in a time-resolved fluoroimmunoassay. Angew Chem Int Ed Engl, 2005. **44**(46): p. 7612-5.

155. Makrides, S.C., C. Gasbarro, and J.M. Bello, Bioconjugation of quantum dot luminescent probes for Western blot analysis. Biotechniques, 2005. **39**(4): p. 501-6.

156. Kim, S. and M.G. Bawendi, Oligomeric Ligands for Luminescent and Stable Nanocrystal Quantum Dots. Journal of the American Chemical society, 2003. **125**: p. 14652-14653.

157. Liu, W., et al., Compact Biocompatible Quantum Dots Functionalized for Cellular Imaging. J. Am. Chem. Soc., 2008. **130**(4): p. 1274-1284.

158. Swift, J.L., R. Heuff, and D.T. Cramb, A two-photon excitation fluorescence cross-correlation assay for a model ligand-receptor binding system using quantum dots. Biophys J, 2006. **90**(4): p. 1396-410.

159. Susumu, K., et al., Design of Biotin-Functionalized Luminescent Quantum Dots. Journal of Biomedicine and Biotechnology, 2007. **2007**(Article ID 90651): p. doi:10.1155/2007/90651.

160. Susumu, K., et al., Enhancing the Stability and Biological Functionalities of Quantum Dots via Compact Multifunctional Ligands. J. Am. Chem. Soc., 2007. **129**(45): p. 13987-13996.

161. Mirkin, C.A., et al., A DNA-Based Method For Rationally Assembling Nanoparticles Into Macroscopic Materials. Nature, 1996. **382**: p. 607-609.

162. He, L., et al., Colloidal Au-Enhanced Surface Plasmon Resonance for Ultrasensitive Detection of DNA Hybridization. Journal of the American Chemical Society, 2000. **122**(38): p. 9071-9077.

163. Zhao, W., et al., DNA Aptamer Folding on Gold Nanoparticles: From Colloid Chemistry to Biosensors. J. Am. Chem. Soc., 2008. **130**(11): p. 3610 -3618.

164. Alivisatos, A.P., et al., Organization of 'nanocrystal molecules' using DNA. Nature, 1996. **382**(15 August): p. 609-611.

165. Fu, A., et al., Discrete Nanostructures of Quantum Dots/Au with DNA. JACS, 2004. **126**: p. 10832-10833.

166. Ghadiali, J.E. and M.M. Stevens, Enzyme-Responsive Nanoparticle Systems. Advanced Materials, 2008. **DOI: 10.1002/adma.200703158**: p. 1-5.

167. Lin, C.A.J., et al., Synthesis, Characterization, and Bioconjugation of Fluorescent Gold Nanoclusters toward Biological Labeling Applications. Acs Nano, 2009. **3**(2): p. 395-401.

168. Krpetic, Z., et al., A Multidentate Peptide for Stabilization and Facile Bioconjugation of Gold Nanoparticles. Bioconjugate Chemistry, 2009. **20**(3): p. 619-624.

169. WILLARD, D.M. and A.V. ORDEN, Resonant energy-transfer sensor. Nature Materials, 2003. **2**: p. 575-576.

170. Clapp, A.R., I.L. Medintz, and H. Mattoussi, Förster Resonance Energy Transfer Investigations Using Quantum-Dot Fluorophores. ChemPhysChem, 2006. **7**: p. 47-57.

171. Ruedas-Rama, M.J., X. Wang, and E.A. Hall, A multi-ion particle sensor. Chem Commun (Camb), 2007(15): p. 1544-6.

172. Callan, J.F., et al., Anion sensing with luminescent quantum dots--a modular approach based on the Photoinduced Electron Transfer (PET) mechanism. J Fluoresc, 2008. **18**(2): p. 527-32.

173. Mulrooney, R.C., et al., An "off-on" sensor for fluoride using luminescent CdSe/ZnS quantum dots. Chem Commun (Camb), 2009(6): p. 686-8.

174. Freeman, R., et al., Biosensing and Probing of Intracellular Metabolic Pathways by NADH-Sensitive Quantum Dots. Angewandte Chemie-International Edition, 2009. **48**(2): p. 309-313.

175. Medintz, I.L., et al., A Fluorescence Resonance Energy Transfer Sensor Based on Maltose Binding Protein. Bioconjugate Chem., 2003. **14**(5): p. 909-918.

176. Shi, L.F., et al., Synthesis and application of quantum dots FRET-based protease sensors. Journal Of The American Chemical Society, 2006. **128**(32): p. 10378-10379.

177. Storhoff, J.J., et al., Sequence-Dependent Stability of DNA-Modified Gold Nanoparticles. Langmuir, 2002. **18**(17): p. 6666-6670.

178. Liu, J.W. and Y. Lu, A colorimetric lead biosensor using DNAzyme-directed assembly of gold nanoparticles. JOURNAL OF THE AMERICAN CHEMICAL SOCIETY, 2003. **125**(22): p. 6642-6642.

179. Hrelescu, C., et al., DNA Melting in Gold Nanostove Clusters. Journal Of Physical Chemistry C, 2010. **114**(16): p. 7401-7411.

180. Reynolds, R.A., C.A. Mirkin, and R.L. Letsinger, A gold nanoparticle/latex microsphere-based colorimetric oligonucleotide detection method. Pure and Applied Chemistry, 2000. **72**(1-2): p. 229-235.

181. Reynolds, R.A., C.A. Mirkin, and R.L. Letsinger, Homogeneous, Nanoparticle-Based Quantitative Colorimetric Detection of Oligonucleotides. JACS, 2000. **122**(15): p. 3795-3796.

182. Aslan, K., C.C. Luhrs, and V.H. Pérez-Luna, Controlled and Reversible Aggregation of Biotinylated Gold Nanoparticles with Streptavidin. Journal of Physical Chemistry B, 2004. **108**: p. 15631-15639.

183. Wang, W., et al., Aptamer biosensor for protein detection using gold nanoparticles. Analytical Biochemistry, 2008. **373**(2): p. 213.

184. Valliant, J.F., A Bridge Not Too Far: Linking Disciplines Through Molecular Imaging Probes. Journal of Nuclear Medicine, 2010. **51**(8): p. 1258-1268.

185. Santra, S., et al., Synthesis and Characterization of Fluorescenct, Radio-Opaque, and Paramagnetic Silica Nanoparticles for Multimodal Bioimaging Applications. Advanced Materials, 2005. **17**: p. 2165-2169.

186. Cherry, S.R., Multimodality in vivo imaging systems: Twice the power or double the trouble? Annual Review Of Biomedical Engineering, 2006. **8**: p. 35-62.

187. Cheon, J. and J.H. Lee, Synergistically Integrated Nanoparticles as Multimodal Probes for Nanobiotechnology. Accounts Of Chemical Research, 2008. **41**(12): p. 1630-1640.

188. Chithrani, D.B., Nanoparticles for Improved therapeutics and Imaging in Cancer Therapy. Recent Pat Nanotechnol, 2010.

189. Tan, W.B. and Y. Zhang, Multi-functional chitosan nanoparticles encapsulating quantum dots and Gd-DTPA as imaging probes for bio-applications. Journal of Nanoscience and Nanotechnology, 2007. **7**(7): p. 2389-2393.

190. Mulder, W.J.M., et al., Quantum dots with a paramagnetic coating as a bimodal molecular imaging probe. Nano Letters, 2006. **6**(1): p. 1-6.

191. van Tilborg, G.A.F., et al., Annexin A5-conjugated quantum dots with a paramagnetic lipidic coating for the multimodal detection of apoptotic cells. Bioconjugate Chemistry, 2006. **17**(4): p. 865-868.

192. Rohrer, M.P., et al., Comparison of Magnetic Properties of MRI Contrast Media Solutions at Different Magnetic Field Strengths. [Article]. 2003: Investigative Radiology November 2005;40(11):715-724.

193. Kircher, M.F., et al., A multimodal nanoparticle for preoperative magnetic resonance imaging and intraoperative optical brain tumor delineation. Cancer Research, 2003. **63**(23): p. 8122-8125.

194. Moore, A., et al., In vivo targeting of underglycosylated MUC-1 tumor antigen using a multimodal imaging probe. Cancer Research, 2004. **64**(5): p. 1821-1827.

195. Devaraj, N.K., et al., 18F labeled nanoparticles for in vivo PET-CT imaging. Bioconjug Chem, 2009. **20**(2): p. 397-401.

196. Cai, W., et al., Dual-Function Probe for PET and Near-Infrared Fluorescence Imaging of Tumor Vasculature. J Nucl Med, 2007. **48**(11): p. 1862-1870.

197. Kobayashi, H., et al., Multimodal nanoprobes for radionuclide and five-color near-infrared optical lymphatic imaging. Acs Nano, 2007. **1**(4): p. 258-264.

198. DeNardo, S.J., et al., Thermal dosimetry predictive of efficacy of In-111-ChL6 nanoparticle AMF-induced thermoablative therapy for human breast cancer in mice. Journal of Nuclear Medicine, 2007. **48**(3): p. 437-444.

199. Choi, J.-s., et al., A Hybrid Nanoparticle Probe for Dual-Modality Positron Emission Tomography and Magnetic Resonance Imaging. Angew. Chem. Int. Ed., 2008. **47**: p. 6259 – 6262.

200. Michalet, X., et al., Quantum Dots for Live Cells, in Vivo Imaging, and Diagnostics. Science, 2005. **307**(5709): p. 538-544.

201. Medintz, I.L., et al., Quantum dot bioconjugates for imaging, labelling and sensing. Nature Materials, 2005. **4**(6): p. 435-446.

202. Larson, D.R., et al., Water-soluble quantum dots for multiphoton fluorescence imaging in vivo. Science, 2003. **300**: p. 1434-1436.

203. So, M.-K., et al., Self-illuminating quantum dot conjugates for in vivo imaging. Nature Biotechnology, 2006. **24**(3): p. 339-343.

204. Alivisatos, P., Colloidal quantum dots. From scaling laws to biological applications. Pure and Applied Chemistry, 2000. **72**(1-2): p. 3-9.

205. Dahan, M., et al., Time-gated biological imaging by use of colloidal quantum dots. Optics Letters, 2001. **26**(11): p. 825-827.

206. Lin, C.-A.J., et al., Quantum Dot Applications in Biotechnology: Progress and Challenges, in Annual Review of Nano Research, G. Cao and C.J. Brinker, Editors. 2006, World Scientific: New Jersey. p. 467-530.

207. Dahan, M., P. Alivisatos, and W.J. Parak, Quantum Dots: Inorganic Fluorescent Probes for Single-Molecule Tracking Experiments in Live Cells, in Single Particle Tracking and Single Molecule Energy Transfer, C. Bräuchle, D.C. Lamb, and J. Michaelis, Editors. 2009, WILEY-VCH: Weinheim.

208. Zrazhevskiy, P. and X. Gao, Quantum dots for cancer molecular imaging. Minerva Biotecnologica, 2009. **21**(1): p. 37-52.

209. Wang, C., X. Gao, and X.G. Su, In vitro and in vivo imaging with quantum dots. Analytical And Bioanalytical Chemistry, 2010. **397**(4): p. 1397-1415.

210. Biju, V., T. Itoh, and M. Ishikawa, Delivering quantum dots to cells: bioconjugated quantum dots for targeted and nonspecific extracellular and intracellular imaging. Chemical Society Reviews, 2010. **39**(8): p. 3031-3056.

211. Su, Y.Y., et al., The cytotoxicity of CdTe quantum dots and the relative contributions from released cadmium ions and nanoparticle properties. Biomaterials, 2010. **31**(18): p. 4829-4834.

212. Limaye, D.A. and Z.A. Shaikh, Cytotoxicity of Cadmium and Characteristics of Its Transport in Cardiomyocytes. Toxicology and Applied Pharmacology, 1999. **154**: p. 59-66.

213. Kirchner, C., et al., Cytotoxicity of Colloidal CdSe and CdSe/ZnS Nanoparticles. Nanoletters, 2005. **5**(2): p. 331-338.

214. Kirchner, C., et al., Cytotoxicity of nanoparticle-loaded polymer capsules. Talanta, 2005. **67**: p. 486-491.

215. Derfus, A.M., W.C.W. Chan, and S.N. Bhatia, Probing the Cytotoxicity of Semiconductor Quantum Dots. NanoLetters, 2004. **4**(1): p. 11-18.

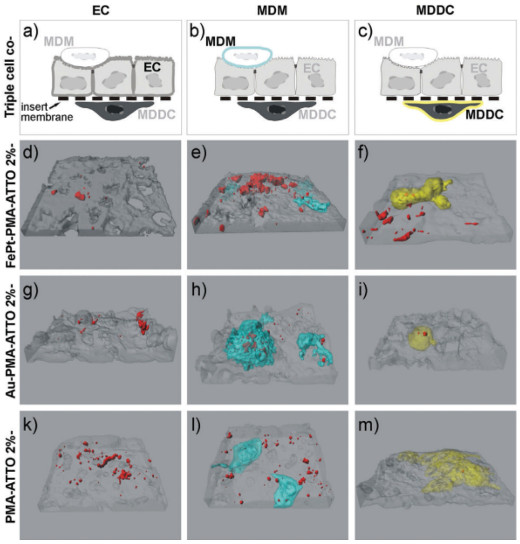

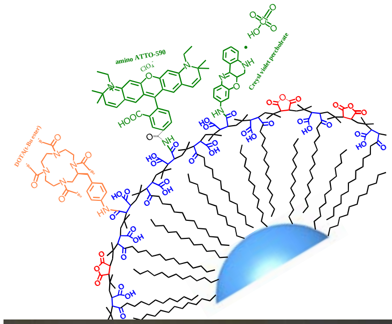

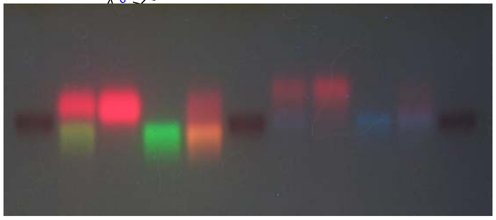

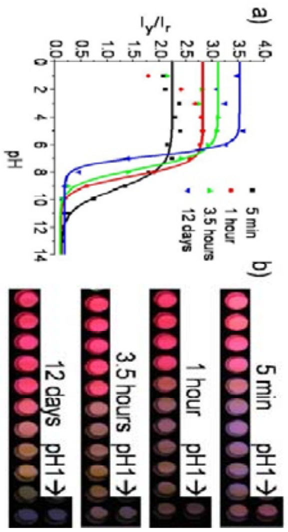

Publications

APPENDIX (A-H)

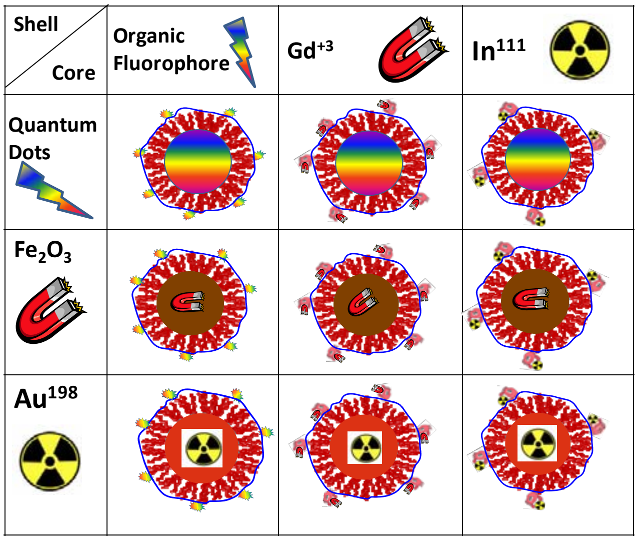

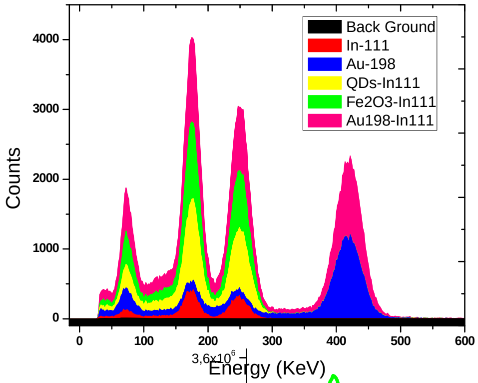

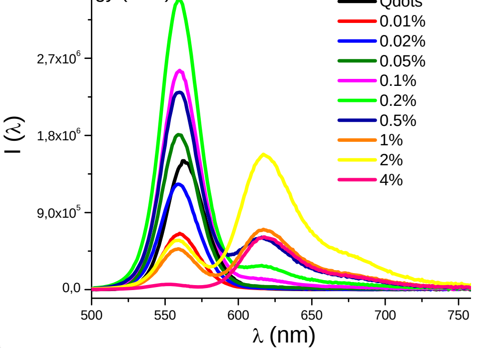

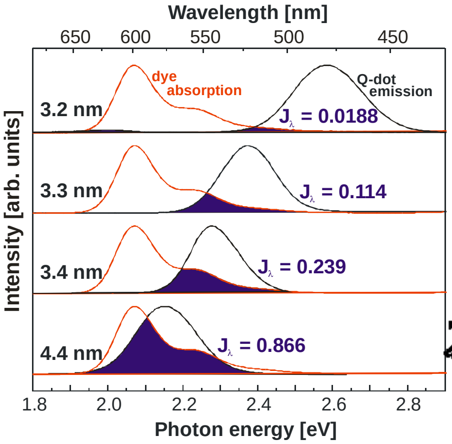

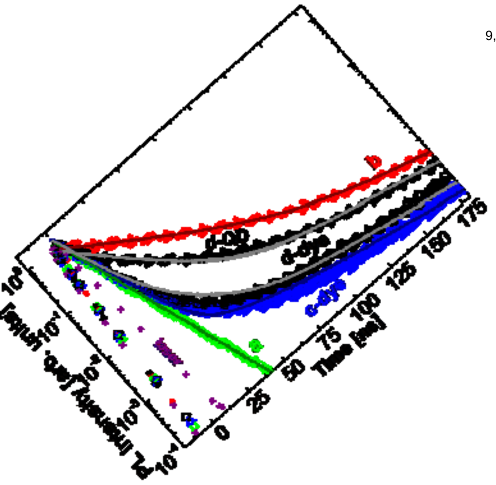

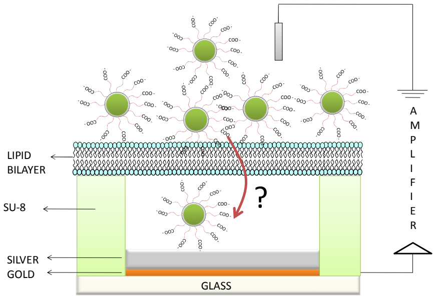

Z. Ali[1], A. Z. Abbasi[1], F. Zhang[1], P. Arosio[2], A. Lascialfari[2, 3], M.F. Casula[4], A. Wenk[5], W. Kreyling[5], R. Plapper[6], M. Seidel[6], R. Niessner[6], J. Knöll[7], A. Seubert[7], W. J. Parak[1,*]

[1] Fachbereich Physik and Wissenschaftliches Zentrum für Materialwissenschaften, Philipps Universität Marburg, Marburg, Germany
[2] Dipartimento di Scienze Molecolari Applicate ai Biosistemi, Università degli studi di Milano, Milano and CNR-Istituto di Nanoscienze, Modena, Italy
[3] Dipartimento di Fisica "A. Volta" and INSTM, Università degli studi di Pavia, Pavia, Italy
[4] Dipartimento di Scienze Chimiche and INSTM, Università di Cagliari, Monserrato, Italy
[5] Comprehensive Pneumology Center - Institute of Lung Biology and Disease, Helmholtz Zentrum München – German Research Center for Environmental Health, Neuherberg / Munich, Germany
[6] Institute of Hydrochemistry, Technische Universität München, München, Germany
[7] Fachbereich Chemie, Philipps Universität Marburg, Marburg, Germany

[*] corresponding author: wolfgang.parak@physik.uni-marburg.de

Multifunctional nanoparticles for dual imaging

Abstract

Colloidal nanoparticles composed out of an inorganic core and a polymer shell have been synthesized. Both, the core and the polymer shell are either fluorescent, magnetic, or radioactive for appropriate imaging / detection. By combining different cores with different polymer shells nine different types of particles for dual imaging have been obtained, as for example fluorescent cores with radioactive polymer shells. In this way a toolkit of nine types of nanoparticles has been created out of which each can be imaged with two different modes. Due to the morphology of the polymer shell all nine different types of particles possess very similar surface chemistry and thus have virtually the same interface for consecutive conjugation with ligands and / or interaction with cells.

Most spatially resolved observations of biological processes inside living cells and organisms required labels which allow for reporting the location of the labelled molecules / entities. The purpose of the labels hereby described is to provide contrast so that the labelled entity can be imaged. Several types of labelling techniques are established in life sciences, like fluorescence, magnetic and radioactive labelling, each of which has its advantages and disadvantages [1, 2]. Fluorescence labelling [3-8] is based on fluorophores that emit fluorescence upon optical excitation, which can be detected with an optical microscope (e.g. fluorescence or laser-scanning microscope). Fluorescence microscopy is very popular for imaging of cellular structures, as it allows for high spatial and temporal resolution. Spatial resolution is classically restricted to the diffraction limit of light, which means in practice a few hundreds of nm. Temporal resolution is limited by the brightness of the fluorophore and the performance of the camera (e. g. the data transfer range). Practically ms time resolution can be easily achieved even with standard set-ups. One problem of fluorescence imaging is the photo-stability of the fluorophores. Photobleaching results in a loss of fluorescence signal in time. In addition imaging of tissues deep inside the animal or human bodies is more complicated. Light in the visible is absorbed by tissue and therefore imaging of structures inside tissue is not possible. As infrared light is absorbed less by tissue for imaging within animals or humans, infrared fluorophores are used. However, the lateral resolution of images within tissue is worse, as it depends for example on the working distance (i.e. the distance between the objective lens and the object). Multiplexed imaging, i.e. visualisation of several structures in parallel with different labels is possible by using fluorophores with different colour. We on purpose do not refer here to transmission electron microscopy (TEM), which allows for even better resolution [9], as TEM is able for *in vivo* imaging. Magnetic labelling [10-14] is based on changes in the nuclear magnetization of nuclei such as ^{1}H or ^{13}C induced by the presence of magnetic particles. Magnetic labels are routinely used for magnetic resonance imaging (MRI) in clinical diagnostics [15]. Spatial resolution allows for contrasting of organ structures, but sub-cellular resolution has not been achieved yet. As magnetic fields are essentially not absorbed by tissue also imaging of structures deep inside bodies is widely used. Multiplexed imaging would be hard to realize with only magnetic particles. On the other hand, MRI is a non-invasive technique as the used rf and static magnetic fields and the magnetic NPs are recognized to not damage the tissues. Radioactive labelling [16] is based on detecting the decay products (most often γ-radiation) of radioactive atoms. Radiation can be detected either with imaging plates which allow for spatial resolution (up to 0.2 mm) or with counters (which do not allow for spatial resolution but have a high sensitivity requiring only pg amounts and have a large dynamic range over 4-5 orders of magnitude of radioactivity) [17-20]. In particular absolute quantification of the number of markers can be done with high precision using radioactivity. As γ-radiation is only weakly absorbed by tissue also imaging of organs deep inside the body is possible. This gives clear advantages to fluorescence detection, as fluorescence emission depends on the local environment (often for example on pH) which in addition to photo-bleaching and light absorption by tissue makes absolute measurements problematic. γ-radiation on the other hand is basically not influenced by tissue. On the other hand γ-radiation counters for animal imaging only have low spatial resolution (hundreds of μm compared to hundreds of nm with optical detection). Problems associated with radiation damage (the tissue is influenced by γ-radiation but not vice versa) automatically reduce the possibilities for using these labels for *in vivo* imaging in humans [21]. Multiplexed imaging is possible by using radioactive molecules / nanoparticles (NPs) with different radiation energies [22-26].

The above mentioned restrictions limit the field of applicability of each label available for *in vivo* imaging purposes. Imaging of an organ deep inside the body of an animal would be for example complicated with fluorescence detection. On the other hand imaging of an *ex vivo* tissue slice taken out of the animal organ with cellular resolution would be complicated with magnetic resonance detection. In an experiment it could be (for example) interesting to first observe to which organs certain administered molecules go and then afterwards to look for their exact cellular distribution with histological techniques on slices taken out from the organs. Here the first part would be preferentially done with magnetic resonance detection in order to avoid loss of the signal by tissue absorption. The second part on the other hand would be best done with fluorescence detection (or with TEM) in order to get high spatial resolution. For this purpose a label which is as well magnetic as fluorescent would be needed [27-33]. Thus, we note the need for labels which can be detected with not only one but with several imaging techniques.

Several approaches have been reported to synthesize materials which can be imaged with two different techniques. This purpose involves for example colloidal hybrid NPs with two different domains as labels [34-36], linkage of two different labels by spacer molecules [37-39], and integration of different labels in a matrix [33, 40, 41]. However, though many different systems for combining two different labels exist, their surface chemistry (as well as their hydrodynamic diameter) and thus their interaction with the environment typically varies from system to system. In this work we report about the synthesis of colloidal NPs in which each NP possesses two different labelling functions. The NPs have an inorganic core that provides the first label. The NPs are then integrated in a polymer shell that comprises the second label. In this way 9 different label combinations are demonstrated. A sketch of the particle geometry is shown in Figure 1. As all NPs are built by embedding an inorganic core in a polymer shell all NPs have highly similar surface chemistry. In this way even different NPs solutions could be easily mixed (without affecting colloidal stability).

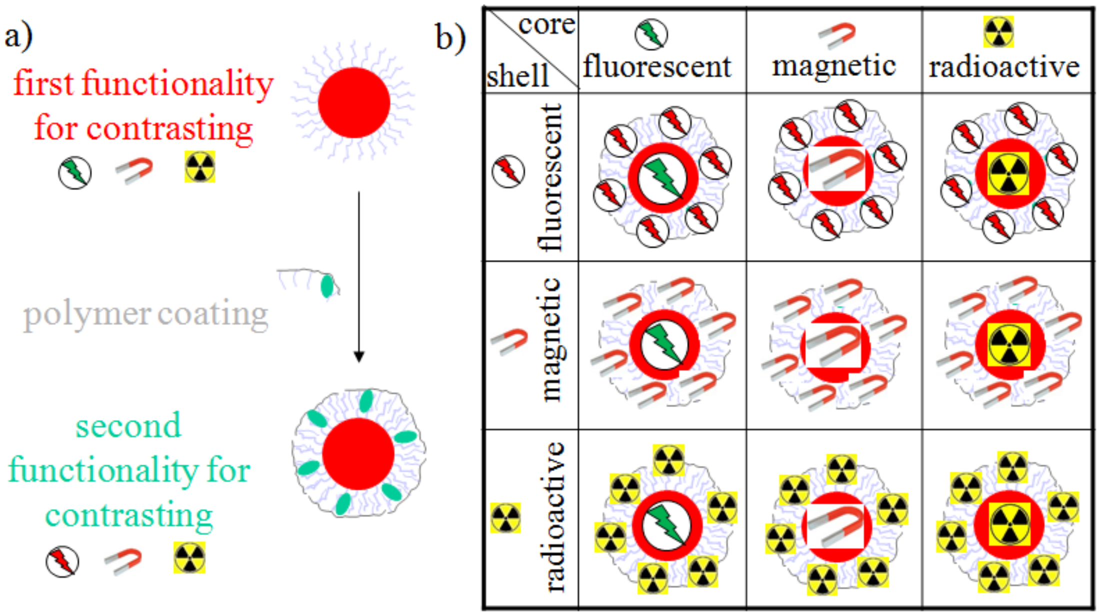

Figure 1: Inorganic colloidal NPs are synthesized from different materials. a) After the synthesis the inorganic cores (drawn in red) are surrounded by organic surfactant molecules (drawn in grey). Depending on the material the cores can be fluorescent, magnetic, or radioactive. The cores are coated with an amphiphilic polymer (drawn in grey) in which a functional organic molecule (drawn in green) has been integrated. This renders the NPs water-soluble. The functional organic molecules can render the polymer shell fluorescent, magnetic, or radioactive. b) By wrapping fluorescent, magnetic, or radioactive polymer shells around fluorescent, magnetic or radioactive cores, NPs with two functionalities are obtained.

Inorganic cores of three different materials were synthesized in organic solvent mixtures. Fluorescent colloidal NPs were based on the well-established CdSe/ZnS system. Using CdSe/ZnS NPs of different sizes all required colours of fluorescence ranging from the blue in the visible to the near infrared (NIR) can be obtained. In this study we used commercial NPs (Evident Technologies) [42]. Magnetic Fe_2O_3 NPs were synthesized according to standard protocols [43]. The NPs and their magnetic properties have been already characterized in detail in literature. Radioactive NPs were based on Au NPs. Au NPs [44] can be radioactivated by neutron irradiation. The resulting NPs contain the ^{198}Au isotope which is a γ- emitter with a photo peak at 315 and 412 keV [45]. As synthesis of the functional cores was performed in organic solvent, the resulting NPs are hydrophobic and have to be rendered hydrophilic before they can be used for biological applications. For this purpose we embedded the hydrophobic cores in an amphiphilic polymer shell, which makes the NPs water-soluble [46-48]. This procedure is very general and allows for embedding of inorganic particles of different materials inside the same type of polymer shell. The amphiphilic polymers were functionalized with organic molecules [49, 50]. In this way the resulting particles have two functionalities: the one of the inorganic core and the one of the organic molecules which are integrated in the polymer shell, see Figure 1. For fluorescent, magnetic, and radioactive polymers organic fluorophores (ATTO-590, ATTO-TEC GmbH), chelator molecules for ions (S-2-(4-Aminobenzyl)-1,4,7,10-tetraazacyclododecane-tetra-tert-butyl acetate, ABz-DOTA, Macrocyclics, loaded with Gd^{3+}), and chelator molecules for In^{3+} ions (ABz-DOTA, loaded with In^{3+}) were used, respectively. Combination of the three different cores and polymer shells led to the 9 different types of NPs as depicted in Figure 1. All NPs were probed for high colloidal stability with gel electrophoresis and size exclusion chromatography according to previously published protocols [51]. The composition of the polymer coated NPs was probed with elemental analysis, in particular with inductive coupled plasma mass spectroscopy (ICP-MS). The fluorescence, magnetic, and radioactive properties of all different 9 NP types were characterized by recording fluorescence spectra, determining r_1 and r_2 relaxivities, and by γ-ray spectroscopy, respectively. All procedures are explained in detail in the Supporting Information.

Fluorescent spectra of all nine different types of NPs were recorded, see Figure 2. From these spectra emission of the organic fluorophore in the polymer shell (ATTO-590) can be clearly seen at 625 nm and emission of fluorescent cores (CdSe/ZnS) at 544 nm. In case the polymer shell with the fluorophore is wrapped around non-fluorescent metal (Au) or metaloxide (Fe_2O_3) cores part of the fluorescence is as expected quenched [31, 52-54]. However, as there are several fluorophores around each core the remaining emission is still enough for imaging. One way to reduce quenching would be the addition of spacers to the fluorophores in order to increase their distance to the surface of cores [55]. In the case of fluorescent cores (CdSe/ZnS) fluorescence resonance energy transfer (FRET) between the cores and the fluorophores in the polymer shell can occur in case emission of one of them matches absorption of the other. This effect is also distance dependent [49]. As a result, in case emissions of cores and fluorophores in the polymer shell are enough spectrally separated, emission originating from the core can be clearly distinguished from emission of the polymer shell.

The relaxometric behaviour of all nine different samples were also characterized to evaluate their contrasting properties for MRI. For this purpose the longitudinal (r_1) and transverse (r_2) relaxivities were calculated, see Figure 2 and the Supporting Information. The relaxometric characterization indicates that when the Gd-containing polymer shells were wrapped around non-magnetic cores (Au or CdSe/ZnS), a significant increase of the relaxation rates is observed. In fact, both Au and CdSe/ZnS core without Gd in their polymer shell exhibit relaxation rates similar to the ones of water, as expected, whereas after the addition of Gd the relaxation rates (and hence the relaxivities) increase. Particularly the longitudinal relaxivity r_1 assumes values comparable to (or higher than) the ones values recorded for positive reference contrast agents such as Omniscan® or Dotarem® (the commercial name of Gd-DOTA). When the Gd-containing polymer shell is added to magnetic cores (Fe_2O_3) the relaxometric behaviour does not vary radically with respect to the one of samples with the original superparamagnetic core. Another useful indicator of the relaxometric properties of a given contrast agent is the ratio between the transverse and longitudinal relaxation rates (r_2/r_1) being 1-2 in the case of traditional paramagnetic (positive) contrast agents and up to 50 in the case of superparamagnetic (negative) contrast agents. The results indicate that the non-magnetic Au and CdSe/ZnS cores mantled with Gd-containing polymer shells have very similar r_2/r_1 values around 2, indicative of a positive contrasting effect which can be ascribed only to the Gd in the polymer shell. On the other hand, the NPs based on a magnetic core (Fe_2O_3) have a r_2/r_1 value indicative of a negative contrasting behaviour irrespective to the presence of Gd in the polymer coating, and behave similarly to reference negative contrast agents such as Endorem®. Though magnetic cores (Fe_2O_3) and polymer shell (with Gd-loaded DOTA) cannot be imaged independently, the choice of having either the core or the polymer shell with magnetic properties allows, in principle to obtain either negative or positive contrasting effects.

Radioactivity of all nine different NP types was detected by γ-ray counters. Energy discrimination hereby allowed for distinguishing between different emitters which in our case were ^{198}Au (as present in neutron-activated Au cores, emitting at 315 and 412 keV) and ^{111}In (as present in In-loaded DOTA in the polymer shell, emitting at 171 and 245 keV). γ-emission of ^{198}Au and ^{111}In is not correlated in any way, which enables parallel detection of both emitters and in this way also discrimination of Au cores and polymer shells containing In. In this way two types of NPs could be imaged in parallel: NPs with ^{198}Au core and regular polymer shell and other cores with ^{111}In-containing polymer shell. In addition, the possibility of recording absolute count rates would for example facilitate experiments which probe whether core and polymer shell are always colocalized or if they are separated, for example when NPs have been taken up by cells.

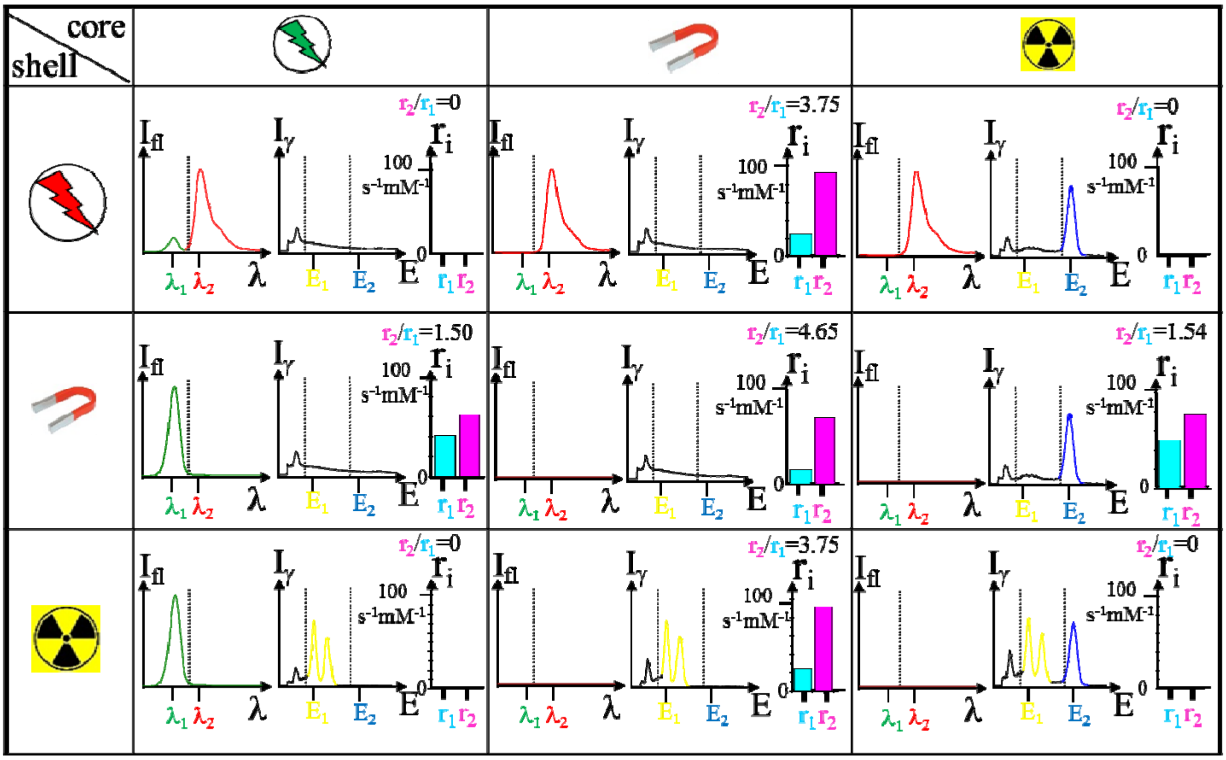

Figure 2: Experimental data obtained for the 9 different types of NPs which are composed out of fluorescent, magnetic, or radioactive cores with a fluorescent, magnetic, or radioactive polymer shell. Each combination performance for imaging with fluorescence microscopy, MRI, and imaging with γ-ray spectroscopy is reported. Concerning fluorescence characterization emission spectra $I_{fl}(\lambda)$ are reported. In all cases of fluorescent core (CdSe/ZnS NPs) and polymer shell (ATTO-590 fluorophore) emission at wavelength λ_1 = 544 nm and λ_2 = 625 nm can be observed. As characterization for MRI the longitudinal (r_1) and transverse (r_2) relaxivities at 20 MHz are depicted. For characterizing the radioactive properties intensity I_γ of γ-ray emission is plotted versus the energy E of γ-rays. With energy discrimination clearly emission from radioactive cores (^{198}Au NPs, 371 keV < E_2 < 464 keV) can be distinguished from emission of radioactive polymer shells (^{111}In-DOTA, 140 keV < E_1 < 200 keV). Emission at lower energies is due to background radiation. Additional information to all experiments can be found in the Supporting Information.

The synthesis procedures as described in this manuscript show a straight-forward way for the creation of a toolkit of NPs which can be simultaneously imaged by two different techniques. This was achieved by combining the properties of inorganic NPs with a modified polymer-coating procedure, in which an additional marker for imaging was integrated. As polymer-coating of NPs has become an established technique we want to point out that with little effort, by incorporation functionalities in the polymer, additional functionalities can be achieved, while retaining the simplicity of the coating procedure. The generality of this approach allows for combination of the properties of a multitude of different cores with polymer shells with different integrated functionalities. In particular these particles allow for dual imaging with two different techniques in parallel. This should also allow for separately tracing the destiny of cores and organic surface on NPs in *in vivo* imaging studies. For *in vivo* experiments PEGylation of the polymer shell of the NPs has been demonstrated to increase the retention time [56]. We however have to critically state that so far no data are available about the integrity of the NPs in *in vivo* studies. In principle as well the inorganic cores, as the polymer shell could be effected. Corrosion of NP cores is well known [57-59]. In the worst case significant amounts of core material could be released as ions to solution. In case of fluorescent and magnetic NPs this would involve only negligible contamination of the label, as for example Cd and Se ions released from fluorescent CdSe NPs are not fluorescent, and the relaxivity of Fe ions is much lower than the one of Fe_2O_3 NPs. In case of radioactivated Au NPs the distribution of radioactive Au isotopes within the Au core should be homogeneous and thus release of Au ions to solution would result to radioactive Au ions in solution, which eventually would no longer colocalize with the Au NPs. A few *percent* loss in Au atoms from the Au cores would thus result in a few *percent* contamination of the label by non-colocalized Au atoms. As Au NPs are quite stable *in vitro* we do not forsee big impact. Also the label of the polymer shell could be lost. The organic fluorophores as fluorescence labels and the chelators for the magnetic and radioactive labels are covalently bound to the polymer and the polymer-coated NPs have been extensively purified with HPLC and gel electrophoresis. Chelators were loaded with Gd and In in case of magnetic and radioactive labels, respectively. Ions might escape from the chelators, which would involve free Gd or In ions in solution. In both cases the magnetic and radioactive label of the NPs would be contaminated due to the relaxivity of the Gd ions and the radioactivity of the In ions, respectively. As there are only few hundred Gd or In ions in the polymer shell around each NP core (see Supporting Information) loss of only few ions would already contaminate the label. The same potential problem applies to all chelator-based labels. However, as explained above, loosely attached ions also have been removed with stringent purification with HPLC and gel electrophoresis. Our toolbox with 9 different NPs will also help to investigate potential disintegration of the labels. As different types of NPs can be mixed due to their similar surface chemistry biodistribution studies correlating the colocalization of the different components can be performed.

Acknowledgements:

This work was supported by the German Research Foundation (DFG, grant 794/11-1 to WJP). Some author (ZA, AZA) acknowledge the Higher Education Commission of Pakistan and the German Academic Exchange Services (DAAD) for funding. The authors are grateful to David Nette for help with ICP-MS measurements.

References:

[1] R. Weissleder, U. Mahmood, *Radiology* **2001**, *219*, 316.
[2] J. Cheon, J. H. Lee, *Accounts Of Chemical Research* **2008**, *41*, 1630.
[3] J. H. Rao, A. Dragulescu-Andrasi, H. Q. Yao, H. Q. Yao, *Current Opinion in Biotechnology* **2007**, *18*, 17.
[4] K. T. Yong, J. Qian, I. Roy, H. H. Lee, E. J. Bergey, K. M. Tramposch, S. He, M. T. Swihart, A. Maitra, P. N. Prasad, *Nano Lett.* **2007**, *7*, 761.
[5] E. I. Altınoğlu, T. J. Russin, J. M. Kaiser, B. M. Barth, B. C. Eklund, M. Kester, J. H. Adair, *ACS Nano* **2008**, *2*, 2075.
[6] W. Liu, M. Howarth, A. B. Greytak, Y. Zheng, D. G. Nocera, A. Y. Ting, M. G. Bawendi, *J. Am. Chem. Soc.* **2008**, *130*, 1274.
[7] A. M. Smith, H. Duan, A. M. Mohs, S. Nie, *Advanced Drug Delivery Reviews* **2008**, *60*, 1226.
[8] B. Ballou, B. C. Lagerholm, L. A. Ernst, M. P. Bruchez, A. S. Waggoner, *Bioconjugate Chemistry* **2004**, *15*, 79.
[9] M. Geiser, W. G. Kreyling, *Particle and Fibre Toxicology* **2010**, *7*.
[10] C. Sun, J. S. H. Lee, M. Zhang, *Advanced Drug Delivery Reviews* **2008**, *60*, 1252.
[11] J. R. McCarthy, R. Weissleder, *Advanced Drug Delivery Reviews* **2008**, *60*, 1241.

[12] S. J. Dodd, M. Williams, J. P. Suhan, D. S. Williams, A. P. Koretsky, C. Ho, *Biophysical Journal* **1999**, *76*, 103.
[13] W. J. M. Mulder, G. J. Strijkers, G. A. F. van Tilborg, A. W. Griffioen, K. Nicolay, *NMR in Biomedicine* **2006**, *19*, 142.
[14] C. A. M. Smith, J. de la Fuente, B. Pelaz, E. P. Furlani, M. Mullin, C. C. Berry, *Biomaterials* **2010**, *31*, 4392.
[15] Y. W. Jun, Y. M. Huh, J. S. Choi, J. H. Lee, H. T. Song, S. Kim, S. Yoon, K. S. Kim, J. S. Shin, J. S. Suh, J. Cheon, *Journal Of The American Chemical Society* **2005**, *127*, 5732.
[16] M. Shokeen, N. M. Fettig, R. Rossin, *Quarterly Journal Of Nuclear Medicine And Molecular Imaging* **2008**, *52*, 267.
[17] R. Singh, D. Pantarotto, L. Lacerda, G. Pastorin, C. Klumpp, M. Prato, A. Bianco, K. Kostarelos, *Proceedings Of The National Academy Of Sciences Of The United States Of America* **2006**, *103*, 3357.
[18] W. Moller, K. Felten, K. Sommerer, G. Scheuch, G. Meyer, P. Meyer, K. Haussinger, W. G. Kreyling, *American Journal Of Respiratory And Critical Care Medicine* **2008**, *177*, 426.
[19] S. Bhaskar, F. R. Tian, T. Stoeger, W. Kreyling, J. M. de la Fuente, V. Grazu, P. Borm, G. Estrada, V. Ntziachristos, D. Razansky, *Particle And Fibre Toxicology* **2010**, *7*.
[20] S. R. Cherry, *Annual Review Of Biomedical Engineering* **2006**, *8*, 35.
[21] E. Bombardieri, A. Coliva, M. Maccauro, E. Seregni, E. Orunesu, A. Chiti, G. Lucignani, *Q J Nucl Med Mol Imaging* **2010**, *54*, 3.
[22] G. Ravizzini, B. Turkbey, T. Barrett, H. Kobayashi, P. L. Choyke, *Wiley Interdiscip Rev Nanomed Nanobiotechnol* **2009**, *1*, 610.
[23] G. Ting, C. H. Chang, H. E. Wang, T. W. Lee, *Journal of Biomedicine and Biotechnology* **2010**.
[24] L. Lacerda, M. A. Herrero, K. Venner, A. Bianco, M. Prato, K. Kostarelos, *Small* **2008**, *4*, 1130.
[25] H. S. Choi, W. H. Liu, F. B. Liu, K. Nasr, P. Misra, M. G. Bawendi, J. V. Frangioni, *Nature Nanotechnology* **2010**, *5*, 42.
[26] H. S. Choi, W. Liu, P. Misra, E. Tanaka, J. P. Zimmer, B. Itty Ipe, M. G. Bawendi, J. V. Frangioni, *Nat Biotechnol* **2007**, *25*, 1165.
[27] J. Kim, H. S. Kim, N. Lee, T. Kim, H. Kim, T. Y. I. C. Song, W. K. Moon, T. Hyeon, *Angewandte Chemie International Edition* **2008**, *47*, 1.
[28] M. Liong, J. Lu, M. Kovochich, T. Xia, S. G. Ruehm, A. E. Nel, F. Tamanoi, J. I. Zink, *ACS Nano* **2008**, *2*, 889.
[29] A. Quarta, R. Di Corato, L. Manna, A. Ragusa, T. Pellegrino, *Ieee Transactions On Nanobioscience* **2007**, *6*, 298.
[30] X. L. Su, Y. Li, *Anal Chem* **2004**, *76*, 4806.
[31] F. Bertorelle, C. Wilhelm, J. Roger, F. Gazeau, C. Menager, V. Cabuil, *Langmuir* **2006**, *22*, 5385.
[32] S. Santra, H. Yang, P. H. Holloway, J. T. Stanley, R. A. Mericle, *J. AM. CHEM. SOC.* **2005**, *127*, 1656.
[33] D. K. Yi, S. T. Selvan, S. S. Lee, G. C. Papaefthymiou, D. Kundaliya, J. Y. Ying, *Journal of the American Chemical Society* **2005**, *127*, 4990.
[34] M. Marradi, D. Alcantara, J. M. d. l. Fuente, M. L. Garcıa-Martın, S. Cerdanb, S. Penades, *Chem. Commun* **2009**, *2009*, 3922–3924.
[35] W. Cai, K. Chen, Z.-B. Li, S. S. Gambhir, X. Chen, *J Nucl Med* **2007**, *48*, 1862.
[36] H.-Y. Lee, Z. Li, K. Chen, A. R. Hsu, C. Xu, J. Xie, S. Sun, X. Chen, *J Nucl Med* **2008**, *2008*, 1371.

[37] J.-s. Choi, J. C. Park, H. Nah, S. Woo, J. Oh, K. M. Kim, G. J. Cheon, Y. Chang, J. Yoo, J. Cheon, *Angew. Chem. Int. Ed.* **2008**, *47*, 6259 –6262.

[38] A. Natarajan, C. Gruettner, R. Ivkov, G. L. DeNardo, G. Mirick, A. Yuan, A. Foreman, S. J. DeNardo, *Bioconjugate Chem.* **2008**, *19*, 1211–1218.

[39] N. K. Devaraj, E. J. Keliher, G. M. Thurber, M. Nahrendorf, R. Weissleder, *Bioconjug Chem* **2009**, *20*, 397.

[40] B. R. Jarrett, B. Gustafsson, D. L. Kukis, A. Y. Louie, *Bioconjugate Chem.* **2008**, 1496.

[41] D. W. Hwang, H. Y. Ko, J. H. Lee, H. Kang, S. H. Ryu, I. C. Song, D. S. Lee, S. Kim, *Journal of Nuclear Medicine* **2010**, *51*, 98.

[42] T. Niebling, F. Zhang, Z. Ali, W. J. Parak, W. Heimbrodt, *Journal of Applied Physics* **2009**, *106*, 104701.

[43] S. Sun, H. Zeng, *Journal of the American Chemical Society* **2002**, *124*, 8204.

[44] F. Zhang, Z. Ali, F. Amin, A. Feltz, M. Oheim, W. J. Parak, *ChemPhysChem* **2010**, *11*, 730.

[45] M. Semmler-Behnke, W. G. Kreyling, J. Lipka, S. Fertsch, A. Wenk, S. Takenaka, G. Schmid, W. Brandau, *Small* **2008**, *4*, 2108.

[46] T. Pellegrino, L. Manna, S. Kudera, T. Liedl, D. Koktysh, A. L. Rogach, S. Keller, J. Rädler, G. Natile, W. J. Parak, *Nanoletters* **2004**, *4*, 703.

[47] T. Liedl, S. Keller, F. C. Simmel, J. O. Rädler, W. J. Parak, *Small* **2005**, *1*, 997.

[48] U. I. Tromsdorf, N. C. Bigall, M. Kaul, O. T. Bruns, M. S. Nikolic, B. Mollwitz, R. A. Sperling, R. Reimer, H. Hohenberg, W. J. Parak, S. Förster, U. Beisiegel, G. Adam, H. Weller, *Nanoletters* **2007**, *7*, 2422.

[49] M. T. Fernández-Argüelles, A. Yakovlev, R. A. Sperling, C. Luccardini, S. Gaillard, A. S. Medel, J.-M. Mallet, J.-C. Brochon, A. Feltz, M. Oheim, W. J. Parak, *NanoLetters* **2007**, *7*, 2613.

[50] C.-A. J. Lin, R. A. Sperling, J. K. Li, T.-Y. Yang, P.-Y. Li, M. Zanella, W. H. Chang, W. J. Parak, *Small* **2008**, *4*, 334.

[51] R. A. Sperling, T. Liedl, S. Duhr, S. Kudera, M. Zanella, C.-A. J. Lin, W. Chang, D. Braun, W. J. Parak, *Journal of Physical Chemistry C* **2007**, *111*, 11552.

[52] G. Schneider, G. Decher, N. Nerambourg, R. Praho, M. H. Werts, M. Blanchard-Desce, *Nano Lett* **2006**, *6*, 530.

[53] L. Josephson, M. F. Kircher, U. Mahmood, Y. Tang, R. Weissleder, *Bioconjugate Chemistry* **2002**, *13*, 554.

[54] N. Hirata, K. Tanabe, A. Narita, K. Tanaka, K. Naka, Y. Chujo, S. Nishimoto, *Bioorg Med Chem* **2009**, *17*, 3775.

[55] E. Dulkeith, M. Ringler, T. A. Klar, J. Feldmann, A. M. Javier, W. J. Parak, *Nanoletters* **2005**, *5*, 585.

[56] M. Lipka, M. Semmler-Behnke, R. A. Sperling, A. Wenk, S. Takenaka, C. Schleh, T. Kissel, W. J. Parak, W. G. Kreyling, *Biomaterials* **2010**, *31*, 6574.

[57] A. M. Derfus, W. C. W. Chan, S. N. Bhatia, *NanoLetters* **2004**, *4*, 11.

[58] C. Kirchner, T. Liedl, S. Kudera, T. Pellegrino, A. M. Javier, H. E. Gaub, S. Stölzle, N. Fertig, W. J. Parak, *Nanoletters* **2005**, *5*, 331.

[59] S. Kittler, C. Greulich, J. Diendorf, M. Koller, M. Epple, *Chemistry of Materials* **2010**, *22*, 4548.

Z. Ali[1], A. Z. Abbasi[1], F. Zhang[1], P. Arosio[2], A. Lascialfari[2, 3], M.F. Casula[4], A. Wenk[5], W. Kreyling[5], R. Plapper[6], M. Seidel[6], R. Niessner[6], J. Knöll[7], A. Seubert[7], W. J. Parak[1,*]

[1] Fachbereich Physik and Wissenschaftliches Zentrum für Materialwissenschaften, Philipps Universität Marburg, Marburg, Germany

[2] Dipartimento di Scienze Molecolari Applicate ai Biosistemi, Università degli studi di Milano, Milano and CNR-Istituto di Nanoscienze, Modena, Italy

[3] Dipartimento di Fisica "A. Volta" and INSTM, Università degli studi di Pavia, Pavia, Italy

[4] Dipartimento di Scienze Chimiche and INSTM, Università di Cagliari, Monserrato, Italy

[5] Comprehensive Pneumology Center - Institute of Lung Biology and Disease, Helmholtz Zentrum München – German Research Center for Environmental Health, Neuherberg / Munich, Germany

[6] Institute of Hydrochemistry, Technische Universität München, München, Germany

[7] Fachbereich Chemie, Philipps Universität Marburg, Marburg, Germany

[*] corresponding author: wolfgang.parak@physik.uni-marburg.de

Multifunctional Nanoparticles for dual imaging

Supporting Information

1 Synthesis of hydrophobic nanoparticles

1.1 General introduction

We selected 3 different types of inorganic cores based on their ability to provide 3 functionalities. Fluorescent colloidal NPs were based on the well-established CdSe/ZnS and CdTe system, which has been extensively described in literature [1-3]. In particular we used commercial CdSe/ZnS NPs from Evident Technologies. Fe_2O_3, FePt, and $CoPt_3$ can be examples of magnetic NPs [4-7]. The NPs and their magnetic properties have been already characterized in detail in literature. In particular iron oxide NPs are known to provide good contrast for T_2 imaging and their use *in vivo* has been approved by the Food and Drug Administration. For this reason in the present study we used in particular Fe_2O_3 NPs which were prepared according to the synthesis described in §1.3. Radioactive NPs were based on Au NPs, as they can be turned radioactive by neutron activation [8]. Synthesis of Au cores is described in §1.2. The neutron activation of Au NPs has to be performed after polymer coating (cfg. §3) in aqueous solution.

1.2 Synthesis of gold nanoparticles

Gold NPs of around 4 nm core diameter were synthesized according to the Brust two-phase method [9, 10], with some modifications. Briefly, an organic phase containing 6.51 g of tetraoctylammonium bromide (TOAB, Sigma-Aldrich #29,413-6) dissolved in 240 mL of toluene (Fluka 89682) and an aqueous phase by dissolving 900 mg hydrogen tetrachloroaurate (III) (99.9%, Alfa Aesar #12325) in 75 mL of Milli-Q water were prepared. The two phases were mixed in a 500 mL separation funnel, whereby the gold precursors (leading to the yellow colour in the aqueous phase) gradually transferred into the organic phase, indicating the formation of tetraoctylammonium-gold pairs (red colour). After discarding the aqueous solution (the bottom part), the organic phase with gold precursors was transferred to a 500 mL round flask. In another beaker, a reduction agent was freshly prepared by dissolving 1.002 g of sodium borohydride (Sigma #452882) in 75 mL of Milli-Q water with stirring. The reduction agent was then added drop-wise within one minute to the gold precursor solution in toluene. Upon vigorous stirring, the colour changed from red to red-violet, indicating the nucleation of gold clusters mediated by reduction of the gold ions by sodium borohydride. Further growth was mediated by the residue of sodium borohydride, which reduced the remaining gold ions. The solution was transferred to a clean separation funnel after one-hour stirring. 75 mL of 0.01 M HCl were added to remove the excess of sodium borohydride. The two-phase solution was shaken for minutes and the aqueous phase was discarded, hereby getting rid of excess sodium borohydride. Again, 75 mL of 0.01 M NaOH were added in order to remove the excess acid by shaking for several minutes and by discarding the aqueous phase. Finally, 75 mL of Milli-Q water were added to remove the excess ions and the aqueous phase was removed after shaking for minutes. This last step was repeated four times. After one day stirring this lead to a solution of Au NPs dissolved in toluene. In order to enhance the stability of the NPs and to provide for a hydrophobic capping with the surfactant pointing towards solution, 30 mL of 1-dodecanethiol (Sigma #471364) were added. The solution was then incubated at 65 °C for 2 hours. The high binding affinity of thiol to gold hereby causes displacement of Br^- ions by alkanethiols and yields dodecanethiol-coated Au NPs. The solution was cooled down to room temperature and larger agglomerates were first removed by centrifuging at 2500 rpm. To the collected supernatant, methanol was added until the solution turned cloudy by precipitation of Au NPs, followed by centrifugation. After discarding the supernatant, the precipitate containing the Au NPs was dissolved in toluene upon vigorous shaking. Again cold methanol was added to the NP solution until it turned cloudy, followed by centrifugation. The supernatant was removed and the precipitate containing the purified Au NPs was re-dissolved in chloroform. The concentration of the resulting Au NP solution was typically in the micro molar range. The average of the inorganic core diameter of the Au NPs was determined by transmission electron microscopy (TEM) and the NP concentration was determined by UV/vis absorption measurements (Agilent 8450 spectrometer). In our case, Au NPs with an average diameter of 4 nm have an extinction coefficient of $8.7\times10^6\ M^{-1}cm^{-1}$ at their plasmon peak at around 518 nm. A typical TEM image and UV/vis absorption spectrum are shown in Figure SI-1.

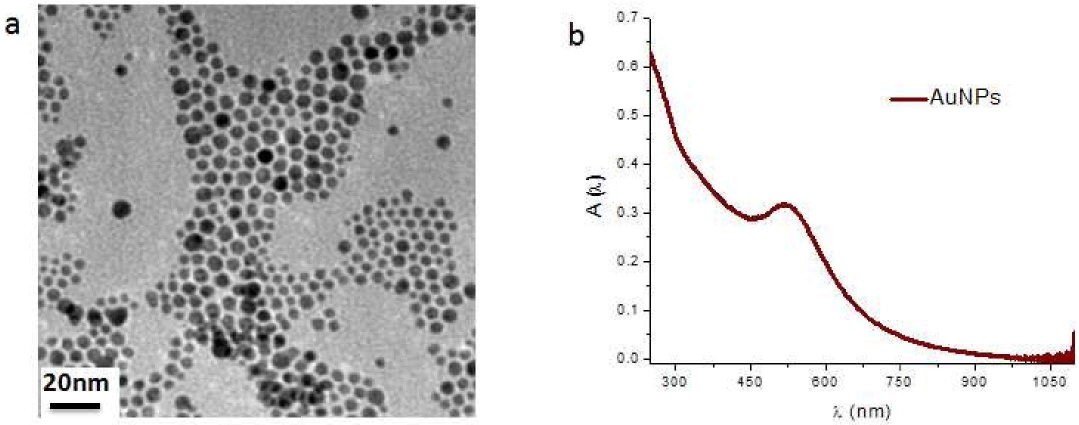

Figure SI-1. a) TEM image of gold nanoparticles. The size distribution of the diameter of the cores (inorganic part without organic capping) was determined as 4.2 ± 0.5 nm. b) UV/vis spectrum of a solution of Au NPs dissolved in chloroform.

1.3 Synthesis of iron oxide nanoparticles

γ-Fe_2O_3 NPs were synthesized using published a protocol by Hyeon [11] and co-workers. Briefly, 10 mL of octyl ether (Sigma #249599) and 1.28 g of oleic acid (Sigma #364525) were mixed and degassed in three-neck flask for 20 min. at 60°C. After 20 minutes temperature was increased to 100°C. At this stage 0.28 mL of iron pentacarbonyl (Sigma #481718) was injected and the temperature was increased up to refluxing temperature (~295-300°C). The solution was kept at this temperature for 1 hour. During this time the initial yellow colour of the solution changed to black. After one hour the solution was cooled to room temperature and 0.34 g of dehydrated trimethylamine oxide (Sigma #T0514) was added. The temperature was increased to 130°C. The solution was kept at this temperature for two hours. During this time the black colour of the solution changed into dark brown. After two hours the solution temperature was again increased to refluxing temperature in steps, each 15°C/min. The solution was kept at refluxing temperature for another hour. During this time the solution colour again changed from dark brown to black. After one hour the reaction was stopped by removing the heating mantel. At room temperature 2-5 mL of toluene (Sigma #244511) was added followed by 25-30 mL of methanol (Sigma #322415). Methanol caused precipitation of the NPs, which were pelleted with centrifugation at a speed of 2800 rpm. The supernatant was removed and the precipitate was washed using toluene and methanol. The precipitate containing the NPs was then redispersed in 10-20 mL of toluene. A TEM image and a UV/vis absorption spectrum of the NPs are shown in Figure SI-2.

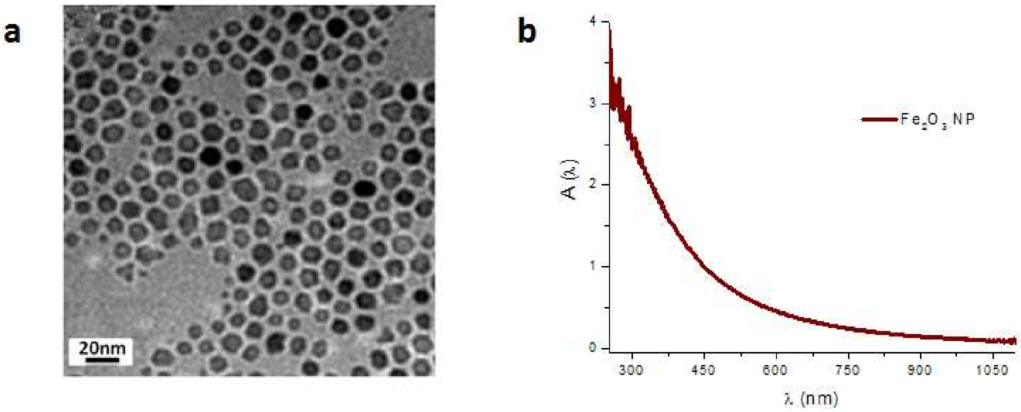

Figure SI-2 a) TEM image of Fe_2O_3 NPs. The size distribution of the inorganic core diameter was determined to be 10.8 ± 0.5 nm. b) UV/vis spectrum of a solution of iron oxide NPs dissolved in toluene.

2 Synthesis of amphiphilic polymer

2.1 General motivation of the polymer coating procedure

As synthesis of the inorganic NPs is performed in organic solvent (see §1) the resulting NPs are hydrophobic and first have to be rendered hydrophilic before they can be used for biological applications. For this purpose procedures exist to embed the hydrophobic cores in an amphiphilic polymer shell, which makes the particles water-soluble [12-14]. This procedure is very general and allows for embedding of inorganic NPs of different materials inside the same type of polymer shell. In this way NPs with a different inorganic core but with virtually the same surface chemistry can be synthesized. Most important, organic molecules such as fluorophores can be directly incorporated into the polymer shell [15, 16]. In this way the resulting NPs have two functionalities: the one of the inorganic core and the one of the organic molecules which are integrated in the polymer shell.

2.2 Synthesis of an amphiphilic polymer for polymer coating of NPs

A convenient way for the synthesis of an amphiphilic polymer (PMA) has been already described earlier [16]. The backbone of this polymer comprises anhydride rings to which hydrocarbon chains with amino-terminal are linked as hydrophobic side-chains, see Figure SI-3 [16]. Other organic molecules bearing amino-groups as the ones described above can be integrated into the amphiphilic polymer by reaction with the anhydride rings (cfg. §2.3).

In practice for the synthesis poly (isobutylene alt- maleic anhydride (Mw ~ 6,000 Da, Sigma #531278)) was reacted with dodecylamine (Sigma #D22220-8). The ratio was chosen in a way that 75% of anhydride rings have dodecylamine as reaction partner. This leaves 25% of anhydride rings intact for further functionalization. For the reaction 2.17 g (15 mmol) of dodecylamine dissolved in 100 mL anhydrous THF were quickly added to 3.084 g powder of poly (isobutylene alt- maleic anhydride) (corresponds to 20 mmol of anhydride rings / monomer units of the polymer, cfg. Figure SI-3) in a round flask. The cloudy mixture was sonicated for several seconds and the solution was refluxed (at the boiling point of THF) for three hours In order to react maleic anhydride with primary amines at high yield, the reaction mixture was afterwards concentrated roughly up to one fifth of the original volume and refluxed overnight. Finally all solvent was evaporated and redissolved in 40 mL anhydrous chloroform to reach a final monomer concentration of the polymer of 0.5 M[1].

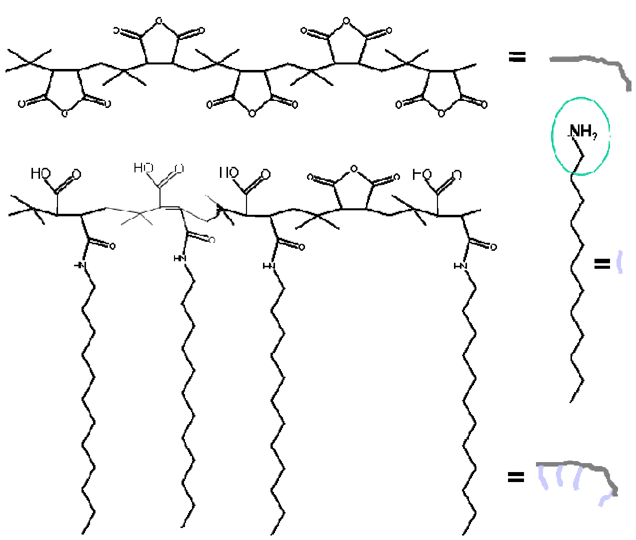

Figure SI-3. Sketch of the synthesis of the amphiphilic polymer from a hydrophilic backbone and hydrophobic sidechains. Amino groups (indicated in green) at the end of the hydrocarbon chains can be directly linked to the anhydride rings of the polymer backbone. In the synthesis around 75% of the anhydride rings are used for linkage to hydrocarbon chains which form the hydrophobic part. Some other anhydride rings can later be used for the linkage of other organic functional amino-modified molecules. The rest of the anhydride rings opens in contact with water to form negatively charged carboxyl groups which warrant for colloidal stability in aqueous solution. Each polymer molecule has around 39 monomer units / anhydride rings[2].

2.3 Synthesis of functionalized amphiphilic polymers

For rendering the amphiphilic polymer functional organic or organo-metallic molecules can be integrated. For this linkage the organic / organo-metallic molecules need to bear a free amino group. Via the amino-group these molecules are then directly attached to the maleic anhydride rings of the amphiphilic polymer.

For the making fluorescence labelled polymers organic fluorophores bearing one amino group can be integrated into the polymer. So far fluoresceinamine, rhodamine 6G, amino

---

[1] 20mmol/40ml = 0.5 M.

[2] The amphiphilic polymer has a molecular weight of $M_w \sim 6000$ g/mol whereby the molecular weight of one polymer unit is $M_w \approx 154$ g/mol. Hence each amphiphilic polymer molecule comprises around 6000 / 154 = 39 monomer units.

modified ATTO 590, amino-modified SNARF, and cresyl violet perchlorate (CVP) have been used for this purpose [10, 15-17]. In the present study ATTO 590 was used (cfg. §2.4)

For adding magnetic labels to the polymer which provide contrast for magnetic resonance imaging (MRI) the following way can be used: Gadolinium ions are known to provide good T_1 contrast with MRI. Several chelator molecules that bind Gd-ions with high affinity are known from literature [18, 19]. For integration into the amphiphilic polymer one therefore needs a Gd-chelator with an available amino group. Gadolinium can be supplied using $GdCl_3$. In the present study S-2-(4-Aminobenzyl)-1,4,7,10-tetraazacyclododecane-tetra-tert-butyl acetate (ABz-DOTA t-Bu ester) was used as chelator (cfg. §2.5)

A similar strategy can be pursued for obtaining radioactive polymer shells. For this Indium ions need to be linked to organic chelator molecules [20, 21] which are modified with amino-groups. In^{111} atoms are γ-emitters at 171 and 245 keV. In this way they can be distinguished from radioactive Au^{198} cores (cfg. §1.2) which emit at 315 and 412 keV by using energy-selective counters. Alternatively to Indium also other radioisotopes such as Tc [22] and corresponding chelators could be used. In the present study we used the same chelator for the incorporation of In as of Gd ions.

2.4 Synthesis of an amphiphilic polymer with integrated fluorescence label

For the fluorescence labelled amphiphilic polymer (PMA-2%ATTO-590), 75% of the anhydride rings were reacted with dodecylamine side chains (cfg. §2.2), 2% were reacted with the amino group of amino-modified ATTO-590, leaving 23% of the anhydride rings intact. ATTO-590 dye (ATTO-TEC Product # AD 590-9, purchased with amino-modification, cfg. Figure SI-4) was firstly dissolved in tetrahydrofurane (THF) in a round flask. All THF was then evaporated and the ATTO-590 powder was redissolved in anhydrous chloroform. A UV/vis absorption spectrum of ATTO-590 in chloroform was recorded. The concentration was determined by using the Lambert Beer law $A = \varepsilon \cdot c \cdot d$. Here A is the optical density at the absorption maximum (597 nm), c is the concentration of ATTO-590, d the path length of the cuvette used for the absorption measurement, and $\varepsilon = 1.2\times10^5\ M^{-1}cm^{-1}$ the extinction coefficient at 597 nm as provided by ATTO-TEC company. 5.0 mL of 1 mM ATTO-590 in anhydrous chloroform were mixed with 500 µL of 0.5 M plain amphiphilic polymer[3] (cfg. §2.2). The mixture was refluxed overnight for a quantitative reaction of amino modified ATTO-590 with the anhydride rings. Finally, all solvent was evaporated and the ATTO-590 modified polymer was redissolved in 5 mL anhydrous chloroform to reach final monomer concentration of 0.05 M of PMA-2%ATTO-590.

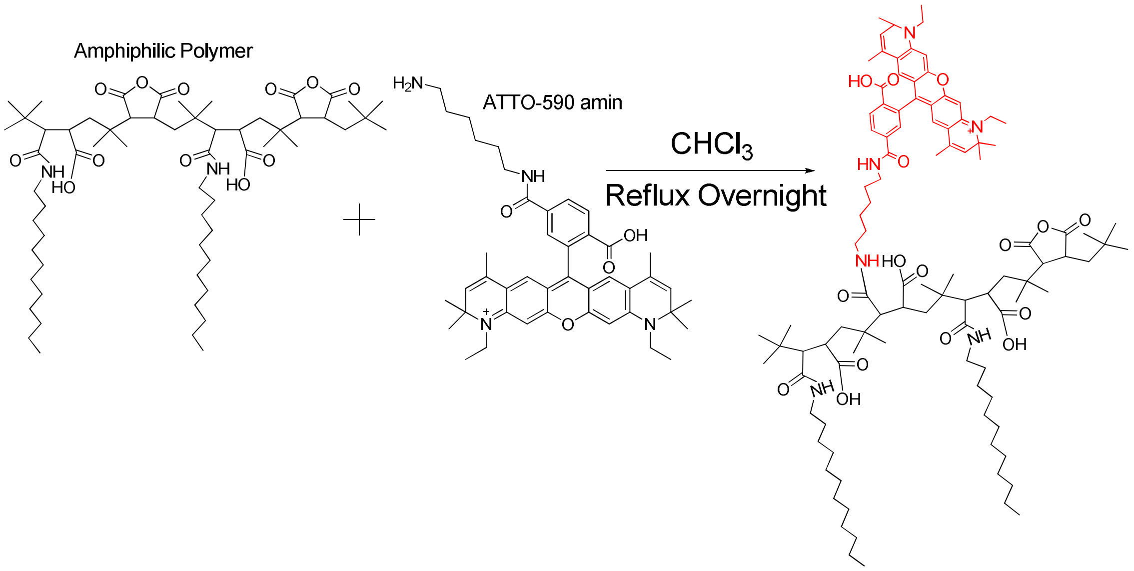

Figure SI-4. Reaction of amino-modified ATTO-590 to the amphiphilic polymer.

2.5 Synthesis of amphiphilic polymers with integrated magnetic or radioactive label

For the chelator-modification of the amphiphilic polymer 75% of the initial anhydride rings of the polymer were reacted with dodecylamine side chains (cfg. §2.2), 3% were reacted with the amino group of the chelators, leaving 22% of the anhydride rings intact. As chelator S-2-(4-Aminobenzyl)-1,4,7,10-tetraazacyclododecane-tetra-tert-butyl acetate (ABz-DOTA t-Bu ester) (Macrocyclics product # B201[4]) was used and the final polymer was called PMA-3%ABz-DOTA. Stock solution was prepared by dissolving 100 mg of ABz-DOTA t-Bu ester in 0.5 mL acetonitrile and 7.4 mL anhydrous THF to have a final concentration of 12.5 mg/mL. Stock solutions could be stored at -20°C. 3.523 mL of ABz-DOTA t-Bu ester stock solution was reacted with 500 µL of 0.5 M amphiphilic polymer (cfg. §2.2; the concentration refers to the concentration of polymer monomers). The reaction mixture was refluxed overnight. All solvents were evaporated and the chelator-modified polymer was redissolved in 2 mL of chloroform. 2 mL of Trifluoroacetic acid (TFA, Sigma #T6508) were added and

---

[3] The concentration hereby refers to the concentrations of monomer units / initial anhydride rings.

[4] This is t-Bu protected chelator. Protection groups improved solubility in organic solvents.

the mixture was stirred for 4-5 hours to deprotect the t-Bu ester end groups [23]. Afterward the solution was heated to 70°C to evaporate TFA by using a Rotavapor. The polymer film was washed 2-3 times with addition and again evaporation of chloroform. Finally the polymer film was redissolved in 5 mL chloroform to get a final concentration of 0.05 M of PMA-3%ABz-DOTA. The whole reaction scheme is shown in Figure SI-5.

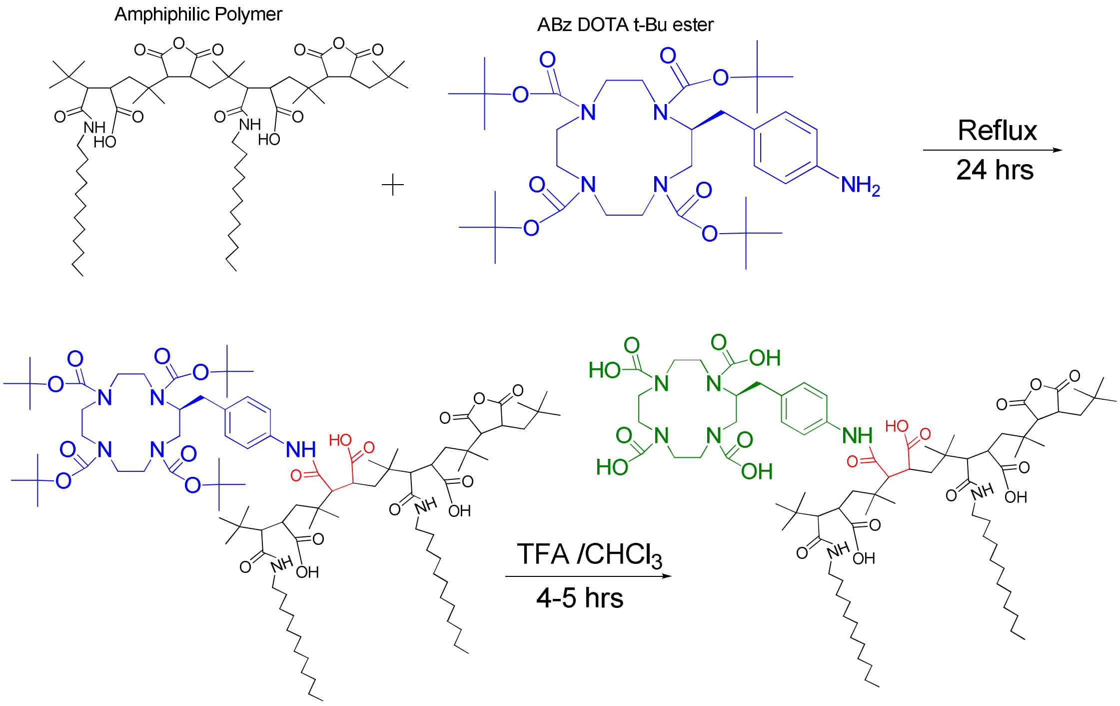

Figure SI-5. Reaction scheme for binding chelator (ABz-DOTA) to the amphiphilic polymer, including deprotection of the chelator.

3 Polymer coating of nanoparticles

Coating of hydrophobic NPs with amphiphilic polymers nowadays has become an established technique [12, 15, 24-30]. However, so far functionalities were added via post-conjugation strategies in which the functional molecule is linked to the surface of the polymer-coated particle. In the present work on the other hand the functionalities are already embedded into the polymer before the particles are coated with the polymer. Though the polymer-coating procedure itself is already established and polymer coating of all kinds of NPs has been achieved according to previously published protocols [16], still only few detailed studies about the actual coating process exist [27]. For this reason the sketches of the polymer coated NPs in the main manuscript have to be interpreted as plausible idealized models.

The amount of amphiphilic polymer required for coating was determined by calculating first the total effective surface area of the hydrophobic NPs. To get this number for a solution of hydrophobic NPs the average diameter d_{core} of the inorganic NP cores was derived from TEM data (such as the ones shown in Figure SI-1 and Figure SI-2) and the concentration c of the NP solution was determined by recording a UV/vis absorption spectrum ((such as the ones shown in Figure SI-1 and Figure SI-2)). The amount of polymer required for coating the NPs of this solution was then determined by Equation SI- 1.

$$V_p = \frac{\pi * c * V * d_{eff}^2 * R_{p/area}}{c_p} \quad \text{……………………………………………………………} \quad \textit{Equation SI-1}$$

Here c and V are the concentration and volume of the NP solution, respectively. $c_{p,}$ and V_p are the monomer concentration and the volume of amphiphilic polymer dissolved in chloroform, respectively. d_{eff} is effective diameter of the NP[5]. $R_{p/area}$ is the number of polymer monomers which need to be added per surface area of nanoparticles (monomer units/nm^2). In this work we used typically $R_{p/area} \approx 100$ nm^{-2}.

The appropriate amount of polymer and NPs solution was mixed in a round flask. After roughly 10 minutes, the solvent was slowly evaporated under reduce pressure (using a

---

[5] $d_{eff} = d_{core} + 2 * l_{surfactant}$ = the sum of the diameter of the inorganic core (d_{core}) plus the assumed thickness of the surfactant shell. In this work we assumed $l_{surfactant} \approx 1.2$ nm.

Rotavapor). The resulting solid film containing the NPs was dissolved in 50 mM sodium borate buffer at pH = 12 (SBB 12). The buffer opened the remaining anhydride rings to lead to negatively charged carboxy groups and thus rendered the NPs water-soluble.

After the polymer-coating the resulting hydrophilic NPs were analysed concerning their colloidal stability based on measurements of the hydrodynamic radii of the NPs. Characterization has been extensively described in previous publications [29] and involved size exclusion chromatography (SEC) and gel electrophoresis (GE). Characterization was performed in different environments, in particular in 150 mM NaCl solution and cell culture media and demonstrated the high colloidal stability of the NPs.

4 Characterization of fluorescent nanoparticles

4.1 Introduction

Fluorescence could either originate from the core or the functionalized polymer shell. As fluorescent cores CdSe/ZnS NPs were used. As fluorescent functionalized polymer shell amphiphilic polymer modified with ATTO-590 (ATTO-TEC GmbH, extinction coefficient $\varepsilon = 1.2\times10^5$ $M^{-1}cm^{-1}$ at 597 nm) was used (cfg. §2.4). In order to quantify the influence of the underlying NPs to the fluorescence properties of the ATTO-590 in the polymer shell also empty micelles with ATTO-590 modified polymer were investigated. They have similar geometry as polymer coated NPs, but without NP inside the polymer shell [15]. Separation between polymer coated NPs and empty polymer micelles was performed by gel electrophoresis (2% agarose gels (Invitrogen #15510027) @ 100 V (Powerpac 1000, Bio-Rad) for 90 minutes) [15], cfg. Figures SI-6, SI-8, SI-10. For characterization of the fluorescence properties of the NPs solutions with 1) NPs coated with amphiphilic polymer without ATTO-590 modification, 2) NPs coated with amphiphilic polymer with ATTO-590 modification, and micelles from amphiphilic polymer without NPs were investigated with fluorescence spectrometry. Hereby the concentrations were adjusted so that in all samples the same amount of NPs and ATTO-590 was present. This was in practice achieved by recording UV/vis absorption spectra of the samples while diluting them to a point that the height of absorption peaks matched [31], cfg. Figures SI-7, SI-9, SI-11. The number of bound ATTO-590 molecules per NP was estimated by deriving the NP and ATTO-590 concentration from the absorption spectra [31].

4.2 Fluorescent cores

CdSe/ZnS NPs (emission @ 544 nm; extinction coefficient 7.78×10^4 $M^{-1}cm^{-1}$, Evident Technologies ED-C11-TOL-0540) were polymer-coated with PMA-2%ATTO-590 (cfg. § 2.4) and plain amphiphilic polymer ($d_{eff} \approx 4.96$ nm; $R_{p/area} = 100\ nm^{-2}$, cfg. §3). In Figure SI-6a a gel is shown on which CdSe/ZnS NPs coated with ATTO-590 modified polymer have been run. This gel shows that besides polymer coated NPs also empty polymer micelles are present after the polymer coating procedure. The faster band on the gel hereby corresponds to empty ATTO-590 modified polymer micelles (PA) and the slower band corresponds to

CdSe/ZnS NPs coated with ATTO-590 modified amphiphilic polymer (EPA). The EPA and PA bands were extracted from the gel by using Dialysis tube (50 kDa, Spectrolabs, 132544) [10]. In a similar way also plain polymer-coated NPs (EP, i.e. CdSe/ZnS NPs coated with polymer without ATTO-590 modification) were also purified by gel electrophoresis. In Figure SI-6b the three resulting samples EP, EPA, PA are compared on a gel. These samples were characterized by UV/vis absorption spectroscopy (Agilent 8450) and fluorescence spectroscopy (Fluorolog®-3 spectrometer, Jobin Yvon, Inc.). Samples were adjusted to equal concentration (Figure SI-7a) and fluorescence spectra were compared (Figure SI-7b).

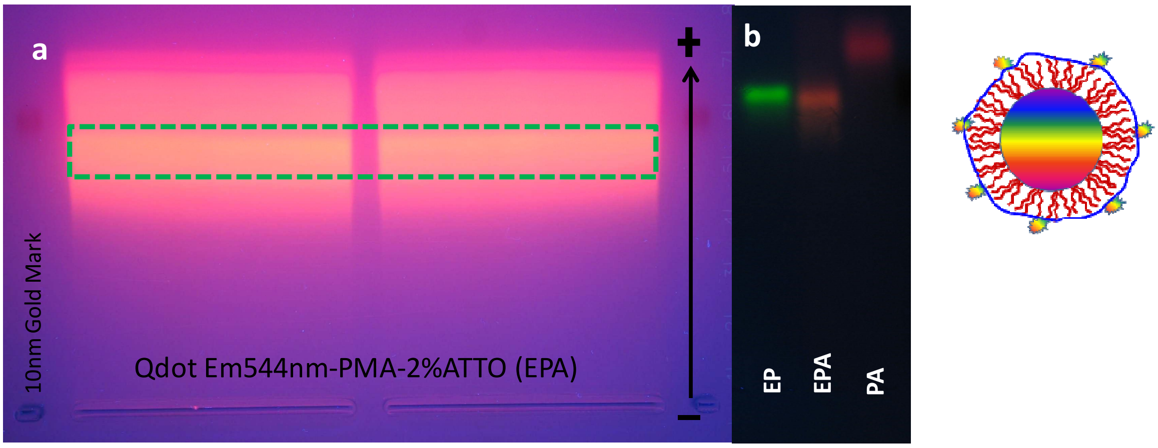

Figure SI-6. Gel electrophoresis of polymer coated NPs a) CdSe/ZnS NPs coated with ATTO-590 modified polymer were run on the gel. This sample consists of actually polymer coated NPs (EPA) and empty polymer micelles (PA). The green dotted rectangle indicates the band on the gel which was identified as EPA and which was cut from the gel. On the left a 10 nm gold marker (phosphine stabilized Au NPs [32]) is shown. b) Final test of the purification showing purified samples of EPA, EPA, and PA which have been run again on a gel.

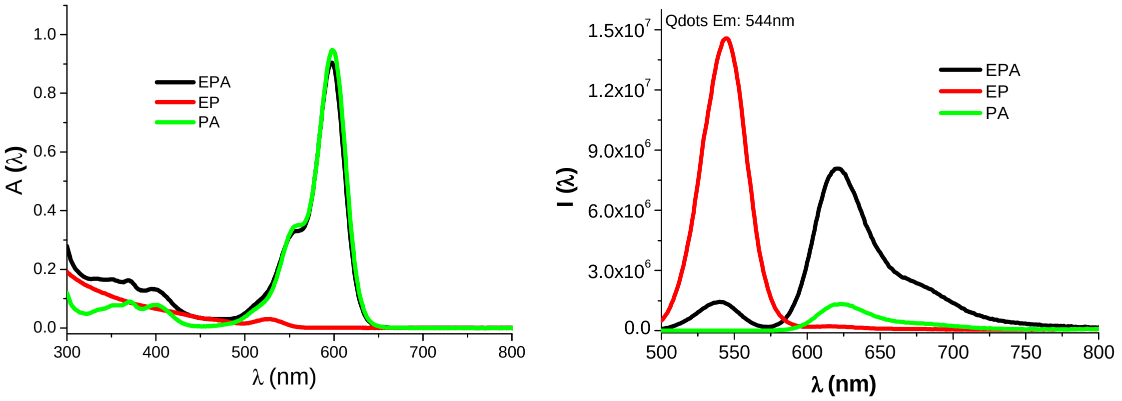

Figure SI-7. a) Absorbance spectra of EPA, EP and PA. Samples were adjusted to the same concentration. b) Fluorescence spectra of EPA, EP and PA under excitation at 450 nm.

By determination of the number of NPs and ATTO-590 molecules in the EPA sample from the absorption spectrum shown in Figure SI-6a (ε_{NP}(@ 527 nm) = 7.78×10^4 $M^{-1}cm^{-1}$,

ε_{ATTO}(@ 597 nm) = 1.2×10^{5} $M^{-1}cm^{-1}$) it was determined that in average around ~19 ATTO-590 molecules are integrated in the polymer shell around each NP. Data from Figure SI-7a demonstrate that both, fluorescence of the core and fluorescence of the dye in the polymer shell can be separated for fluorescent cores coated with a fluorescent polymer shell. In case of appropriate wavelengths for such bi-fluorescent particles fluorescence energy resonance transfer (FRET) can be observed [15, 33]. This is also the case for the combination of CdSe/ZnS NPs emitting at 544 nm and ATTO-590 dye in the polymer shell.

4.3 Magnetic cores

Superparamagnetic iron oxide (Fe_2O_3, estimated extinction coefficient ε_{NP} = 5.07×10^{7} $M^{-1}cm^{-1}$ @ 450 nm [34]) NPs (cfg. §1.3) were polymer coated with PMA-2%ATTO-590 modified polymer (cfg. §2.4). In particular 5.01 nmol of Fe_2O_3 NPs in toluene were polymer coated with 645 µL of 0.05 M polymer solution ($d_{eff} \approx 13.2$ nm; $R_{p/area} = 50$ nm^{-2}, cfg. §3). ATTO-590 modified iron oxide nanoparticles (FPA) were purified by gel electrophoresis from empty polymer micelles (PA) [15]. In Figure SI-8 the slower and faster bands describe the separation of polymer coated NPs and empty polymer micelles (PA), respectively. As control Fe_2O_3 nanoparticles were polymer coated with plain amphiphilic polymer without ATTO-590 modification (FP). In Figure SI-9 absorption and fluorescence spectra of FPA, FP, and PA are shown.

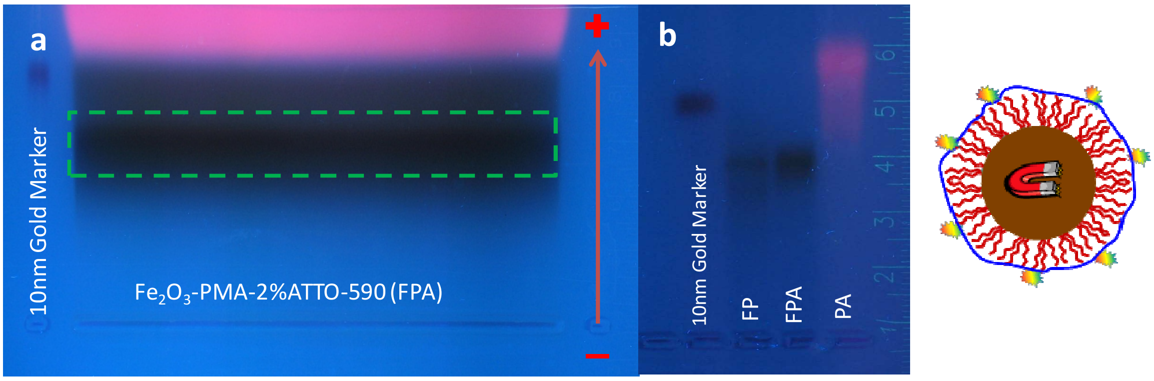

Figure SI-8. a) Iron oxide NPs coated with ATTO-590 modified polymer were run on an agarose gel. The dotted rectangle corresponds to the band of polymer coated NPs and was cut and extracted from the gel as FPA sample. The faster fluorescent band corresponds to empty polymer micelles (PA). On the left as control a 10 nm Au marker is run [32]. b) Gel on which the purified samples FP, FPA, and PA have been run in order to demonstrate their separation.

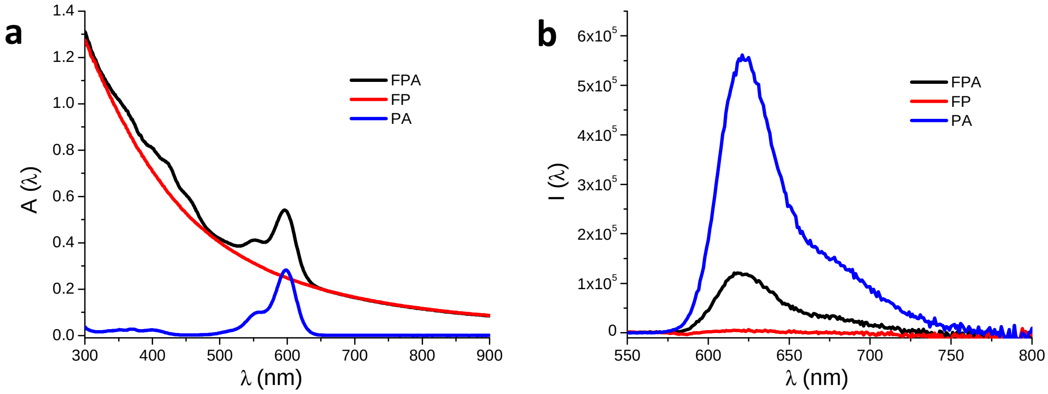

Figure SI-9. a) Absorbance spectra of FPA, FP and PA dissolved in water. Concentrations had been adjusted by dilution to the same amount of NPs and ATTO-590 in each sample. b) Corresponding fluorescence spectra of FPA, FP, PA upon excitation at 500 nm.

Wrapping of fluorescent polymers around inorganic particles has already been demonstrated to affect their fluorescence. This can also be seen in Figure SI-9b. The fluorescence of ATTO-590 integrated to polymer shell around iron oxide NPs is partially quenched (to roughly around 40-60%). However, as there are several ATTO-590 fluorophores around each iron oxide NPs, the overall fluorescent per NP is enough to be imaged. Here we estimate to have around ~74 ATTO-590 molecules integrated in the polymer shell around each iron oxide NP (derived from the absorption spectra shown in Figure SI-9a with ε_{NP}(@ 450 nm = 9.7×10^5 $M^{-1}cm^{-1}$, ε_{ATTO}(@ 597 nm = 1.2×10^5 $M^{-1}cm^{-1}$).

4.4 Radioactive cores

Radioactive Au NPs (cfg. §1.2, §6.1) were coated with ATTO-590 modified polymer. For this 2.02 nmol of 4 nm Au NPs in chloroform (cfg. §1.2, ε_{NP}(@ 518 nm) = 8.7×10^6 $M^{-1}cm^{-1}$) were mixed with 520 µL of PMA-2%ATTO-590 solution of 0.05 M (§2.4) ($d_{eff} \approx 6.4$ nm; $R_{p/area} = 100$ nm^{-2}, cfg. §3). ATTO-590 modified Au nanoparticles (APA) were purified by 2% agarose gel from empty polymer micelles (PA), see Figure SI-10. As control Au NPs coated with a polymer without ATTO-590 (AP) were used. The concentrations of all samples (APA, AP, PA) were adjusted by dilution until their absorption at the ATTO absorption peak and the absorption of the Au cores matched. Afterwards fluorescence spectra of all samples were recorded, see Figure SI-11.

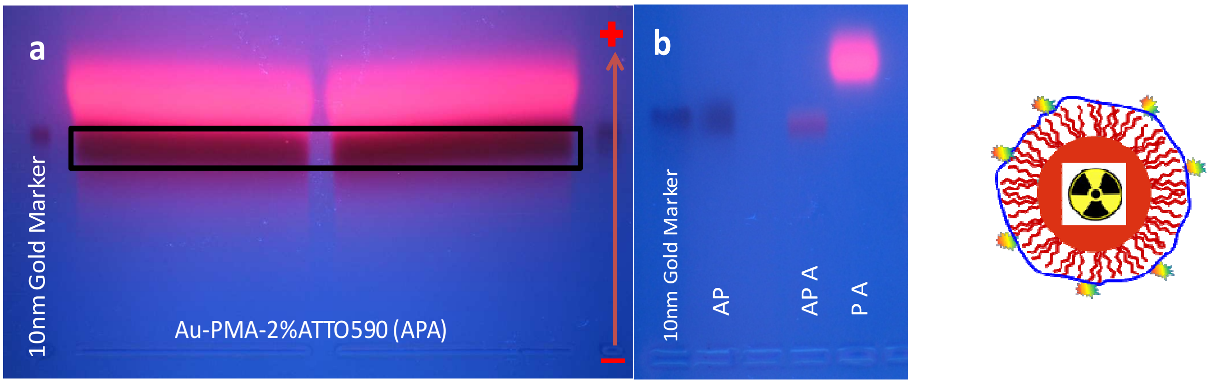

Figure SI-10. a) Au NPs coated with ATTO-590 modified polymer were run on a gel. This sample comprises coated NPs (slower band, indicated by the black frame) and empty polymer micelles (faster band). 10 nm Au NPs were run as control Gold marker [32]. b) Final test for purification, in which AP, APA, and PA samples are run on the same gel. A clear difference between APA and PA can be observed.

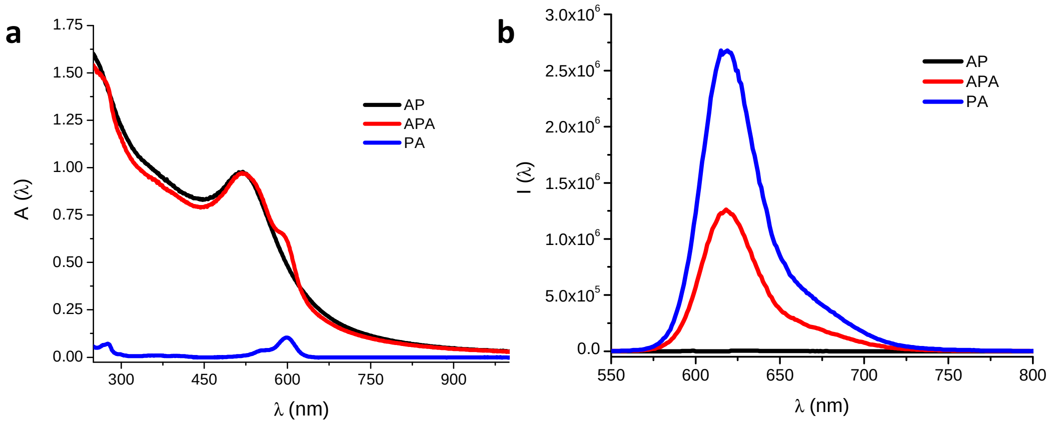

Figure SI-11. a) Absorption spectra of APA, AP, and PA, which had been adjusted to corresponding concentrations of ATTO-590 and Au NPs. b) Fluorescence spectra of the corresponding samples under excitation at 500 nm.

By determination of the number of NPs and ATTO-590 molecules in the APA sample from the absorption spectrum shown in Figure SI-11a (ε_{NP}(@ 518 nm) = 8.7×10^6 $M^{-1}cm^{-1}$, ε_{ATTO}(@ 597 nm) = 1.2×10^5 $M^{-1}cm^{-1}$) it was determined that in average around ~13 ATTO-590 molecules are integrated in the polymer shell around each Au NP. As in the case of ATTO-590 polymer coated iron oxide NPs also Au NPs also quench partly the fluorescence of ATTO-590 in the polymer shell. In this case level of quenching is around 50%. As several ATTO-590 molecules are around each Au NP the overall fluorescence of one NP is still in a range where it can be conveniently detected.

5 Magnetic labelling

5.1 Gadolinium chelation

Magnetic labelling was either achieved from the core (iron oxide NPs) or from Gd ions in the polymer shell. Gd was introduced to the polymer shell via an integrated chelator (cfg. §2.5). NPs were first coated with chelator modified polymer. Then in a next step the chelator was loaded with Gd by adding Gd ions to the NP solution. This sequence had to be used as Gd ions are not soluble in organic solvent in which the chelator modified polymer is synthesized. For loading NPs with Gd a solution of chelator modified NPs was stirred in water and an equivalent amount of $GdCl_3 \cdot H_2O$ (Sigma #G7532) was added. The reaction mixture was stirred at 80^{o}C for 12 hours [35]. Free $GdCl_3$ was removed afterward by a PD-10 column [36]. This purification step was monitored by ICP-MS (cfg. §5.2) and found to be appropriated for removal of free gadolinium ions. Due to the positive charge of the Gd-ions some binding of Gd mediated by electrostatic attraction to the negatively charged polymer shells is expected, even when these polymer shells are not modified with the corresponding chelators. Quantification of specific versus nonspecific electrostatic attachment was done with ICP-MS (cfg. §5.2).

5.2 Elemental analysis (ICP-MS)

The concentration of magnetic and radioactive NP cores and the number of Gd-ions in the polymer shell were determined with inductively coupled plasma mass spectroscopy (ICP-MS). The Gd-ions were quantified by using standards, the cores could be detected after dissolution or as a whole [37, 38]. As the size of cores is known from TEM images, the concentration of cores can be derived from the concentration of ions originating from dissolved cores. For ICP-MS measurements NP samples of micro molar range were diluted thousand times. The ICP-MS instrument (Agilent 7500ce) was calibrated with ICP standards for gold, iron, gadolinium and indium (Sigma). Each measurement was repeated three times. Samples were prepared in water with and without digestion (dissolving in HNO_3). From both methods measured concentrations were the same within 5% difference (Data not shown). The acquisition parameters for the ICP-MS measurements are given in Table SI-1.

===Acquisition Parameters==

Number of Masses: 6

Integration Time [sec]: 1 sec

Mass Element: 57 Fe, 89 Y, 115 In, 157 Gd, 195 Pt and 197 Au

===Plasma Condition===

RF Power: 1500 W

RF Matching: 1.74 V

Sample Depth: 6.4 mm

Torch-H: 0.9 mm

Torch-V: -0.3 mm

Carrier Gas: 0.9 L/min

Makeup Gas: 0.15 L/min

Optional Gas: 0 %

Nebulizer Pump: 0.1 rps

Tubing:1.02 i.d. Tygon

S/C Temp: 2 °C

===Ion Lenses===

Extract 1: 3.4 V

Extract 2: -139.5 V

Omega Bias-ce: -22V

Omega Lens-ce: -2 V

Cell Entrance: -38 V

QP Focus: 4 V

Cell Exit: -54 V

===Octopole Parameters===

OctP RF: 181 V

OctP Bias: -8.4 V

===Q-Pole Parameters===

AMU Gain: 125

AMU Offset: 126

Axis Gain: 0.9996

Axis Offset: -0.02

QP Bias: -5.4 V

===Detector Parameters===

Discriminator: 8 mV

Analog HV: 1810 V

Pulse HV: 1490 V

Table SI-1. Parameters for ICP-MS detection of Gd, In, Au, Fe ions

For determining the amount of Gd ions per NP the concentration of Gd ions and of NPs had to be determined. For CdSe/ZnS NPs the concentration $c_{UV/vis}$(NP) of the NPs was determined by UV/vis absorption measurements, as the extinction coefficient at the first exciton peak is known: $\varepsilon = 3.2\times10^5$ $M^{-1}cm^{-1}$ @ 600 nm for CdSe/ZnS with emission at 610 nm and : $\varepsilon = 7.78\times10^4$ $M^{-1}cm^{-1}$ @ 527 nm for CdSe/ZnS with emission at 544 nm. Also for Au NPs (cfg. §1.2), estimation for their extinction coefficient at the surface plasmon resonance peak exists: $\varepsilon = 8.7\times10^6$ $M^{-1}cm^{-1}$ @ 518 nm. We also determined the concentration of Au ions in a sample of Au NPs (in buffer) by ICP-MS. Assuming a spherical shape of the Au NPs and a density similar with a uniform face-centred cubic the average of gold atoms for each Au NP can be calculated by the Equation SI-2.

$$Number\ of\ Au\ atoms\ per\ NP\ = \frac{{}^{4}/_{3}\pi*({}^{d_{core}}/_{2})^{3}*N_A*\rho}{M} \qquad \text{……………………..Equation SI- 2}$$

Hereby N_A is the Avogadro number, ρ is the density for Au NPs (1.93×10^{-20} g/nm^3), d_{core} is the Au NP diameter, and M stands for atomic weight of gold. [37]. With a core diameter of 4 nm each Au NP contains 1.98×10^3 Au atoms per NP. Finally, by dividing the concentration of Au atoms from ICP-MS by the number of Au atoms per NP the corresponding concentration of Au NPs in solution is derived. Both values show reasonable agreement (cfg. Table SI- 2, Table SI- 4). For iron oxide NPs no extinction coefficients is given in literature, as their absorption spectrum is bare of characteristic features. For this reason concentration of Fe_2O_3 NPs was also determined from ICP-MS. The Fe concentration in a sample of Fe_2O_3 NPs (in buffer) was detected with ICP-MS. Each Fe_2O_3 NP with core diameter of d_{core} = 10.8 nm contains around 13038 atoms (Fe + O) per NP (cfg. Equation SI- 2, d_{core} =10.8 nm, ρ=5.24×10^{-21} g/cm^3). However in this analysis we have only detected Fe atoms (from ICP-MS). Therefore one must still account for the number of oxygen atoms. For every 2 Fe atoms there are 3 O atoms. Therefore each Fe_2O_3 NP core contains 6519 Fe atoms, assuming an oversimplification that Fe and O atoms share equal size in the NP. In this way the Fe_2O_3 NP concentration could be derived from ICP-MS measurements of Fe ions. By recording also the absorption spectrum at 450 nm of the Fe_2O_3 NP a rough estimate for their extinction coefficient was obtained: $\varepsilon_{NP} = 5.07\times10^7$ M^{-1}cm^{-1} @ 450 nm [34]. Both values give quite different concentration of NPs. We decided to use ICP-MS derived concentrations for calculating the number of Gd per Fe_2O_3 NP. The amount of Gd ions in the samples was determined directly via ICP-MS. This finally allowed for calculating the amount of Gd ions per NP. The results are displayed in Table SI-2. They indicate that though there is electrostatic attachment of Gd to the negatively charged polymer shell (NPs without chelator in the polymer) a significant part of the Gd ions is specifically bound to chelator in the polymer shell (compare the APD, EPD, FPD samples versus the AP, EP, FP samples).

NPs	$c_{UV/vis}$(NP) [nM]	$c_{ICP\text{-}MS}$(NP) [nM]	c(^{197}Au) or c(^{56}Fe) [µM]	c(Gd^{3+}) [µM]	c(Gd^{3+})/ c(NP)
AP + Gd[6]	236.74	-	-	-	-
APD	308.83	293.47	580.20	48.27	165
EP + Gd[7]	645.34	-	-	34.23	54
EPD	621.47	-	-	151.15	244
FP + Gd	46.20	121.27	774.56	10.23	84
FPD	44.43	107.68	687.72	61.27	569

Table SI-2. ICP-MS measurement of NPs modified with Gadolinium. APD, EPD, FPD, and AP, EP, FP corresponds to Au, CdSe/ZnS, and Fe_2O_3 NPs which have been coated with a polymer with / without integrated chelator, respectively. Nonspecific binding was observed by addition of Gd to AP, EP and FP at same conditions. Concentration of the NPs c(NP) has been determined with UV/vis absorptions spectroscopy or with ICP-MS. In case of ICP-MS determination also the concentration of the ions from the core (c(Au) in case of Au NPs, c(Fe) in case of Fe_2O_3 NPs) which was the basis for the calculation of the NP concentration c(NP) is given. Gadolinium concentration c(Gd^{+3}) was also determined with ICP-MS. By calculation the ratio the amount of Gd ions per NP was calculated: c(Gd^{3+})/ c(NP).

5.3 Magnetic resonance characterization

^{1}H Nuclear Magnetic Resonance (NMR) relaxometry characterization (NMR-dispersion profile) was performed at physiological (37 °C) and room (25 °C) temperature by measuring the longitudinal and the transverse nuclear relaxation times T_1 and T_2. The NMR signal detection and generation was obtained by a Stelar Spinmaster spectrometer. Standard radio frequency excitation sequences CPMG-like (T_2) and saturation-recovery (T_1) were used [39]. Differences between the results obtained at room and physiological temperatures were within 10%. To determine the efficiency of magnetic resonance imaging (MRI) contrast agents, the

---

[6] When AP was mixed with Gd under the same conditions as APD a complete precipitation of the mixture occured.

[7] For FP and EP mixtures with Gd few aggregates were observed which were removed by purification. However, it has to be noted that after one week both samples were not stable and more precipitates occured.

nuclear relaxivities, both longitudinal, r_1, and transverse, r_2, were calculated according to equation SI- 3.

$$r_i = [\,(1/T_i)_{meas} - (1/T_i)_{dia}\,] / c \qquad i=1,2 \qquad \textit{Equation SI- 3}$$

Where $(1/T_i)_{meas}$ is the value measured for the sample with a concentration c [$mmol \cdot L^{-1}$] of the magnetic centre (i.e. the iron and or Gd in the NPs), and $(1/T_i)_{dia}$ represents the nuclear relaxation rate of the diamagnetic host solution (water in our case). Typically, paramagnetic contrast agents enhance r_1, whereas superparamagnetic contrast agents enhance r_2. The relaxation time of pure water is of the order of few seconds. The longitudinal and the transverse nuclear relaxation times T_1 and T_2 were measured in the frequency range 10 kHz ≤ ν ≤ 200 MHz, in order to gain insights on the mechanisms of nuclear relaxation from the $r_i(\nu)$ curves and to cover the frequencies corresponding to the most used clinical fields, i.e. 0.2 Tesla (~8.5 MHz), 0.5 Tesla (~20 MHz) and 1.5 Tesla (~64 MHz). Commercial negative (Endorem ® from Guerbet Group, Roissy, France, 11.2 mg Fe/mL) and positive (Omniscan® from GE Healthcare, General Electric Company, 0,5 mol Gd/L and Dotarem® from Guerbet Group, Roissy, France, 0.5 mol Gd/L) contrast agents were used as reference compounds without further purification. The ratio between the transverse and longitudinal relaxation rates (r_2/r_1) is typically 1-2 in the case of traditional paramagnetic (positive) contrast agents and up to 50 in the case of superparamagnetic (negative) contrast agents. In particular, the value of 2 is roughly assumed as the threshold value for effective negative contrast. Table SI-3 summarizes the r_2/r_1 ratio for the samples at two frequency values used in clinical imagers (the r_2/r_1 values in the whole investigated frequency range are reported in Figure SI-14).

5.4 Radioactive and fluorescent cores

Au NPs in chloroform (cfg. §1.2) were polymer coated with DOTA-modified polymer (PMA-3%ABz-DOTA, cfg. §2.5) and in this way transferred to aqueous solution (cfg. §3). Purification by gel electrophoresis enabled us to separate Au NPs coated with DOTA-modified polymer (APD) from empty micelles of DOTA-modified polymer (PD). Chelator-modified polymers were then loaded with Gd (cfg. §5.1). As control Au NPs were also polymer coated with plain amphiphilic polymer (AP, cfg. §2.2).

Fluorescent CdSe/ZnS NPs (emission @ 610 nm, Evident Technologies ED-C11-TOL-0610) in toluene were polymer coated with DOTA-modified polymer (PMA-3%ABzDOTA, cfg. §2.5) and in this way made water-soluble (cfg. §3). CdSe/ZnS NPs coated with DOTA-modified polymer (EPD) were separated from empty micelles of DOTA-modified polymer (PD) by gel electrophoresis purification. The chelator molecules in the polymer were loaded with Gd ions (cfg. §5.1). As control CdSe/ZnS NPs were coated with unmodified polymer without chelator (EP, cfg. §2.2).

Results of the relaxometry characterization are shown in Figures SI-12, SI-13, SI-14, and Table SI-3. Addition of Gd-loaded chelator to non-magnetic cores (APD, EPD samples) decreases the ^{1}H relaxation times compared to the samples without Gd in the polymer shell (AP, EP). This clearly indicates presence of Gd in polymer shells with chelator. As a consequence, the r_1 relaxivity of APD and EPD samples is much higher (about ten times) than the one of commercial paramagnetic contrast agents (CA), thus resulting in a very good MRI positive contrast efficiency of our compounds. Interestingly, the r_2 values for both APD and EPD at $\nu>20$ MHz are comparable to the ones of Endorem, thus proposing these systems also as possible negative CAs, to be validated by MR images. The results shown in Table SI-3 indicate that the Gd-loaded Au NPs and CdSe/ZnS NP samples (APD, EPD) have very similar r_2/r_1 values around 2, indicative of a positive contrasting effect which can be ascribed only to the Gd in the outer shell. The relaxation times of the samples without Gd-loaded chelator in the polymer shell (AP, EP) were similar to that of pure water, as expected.

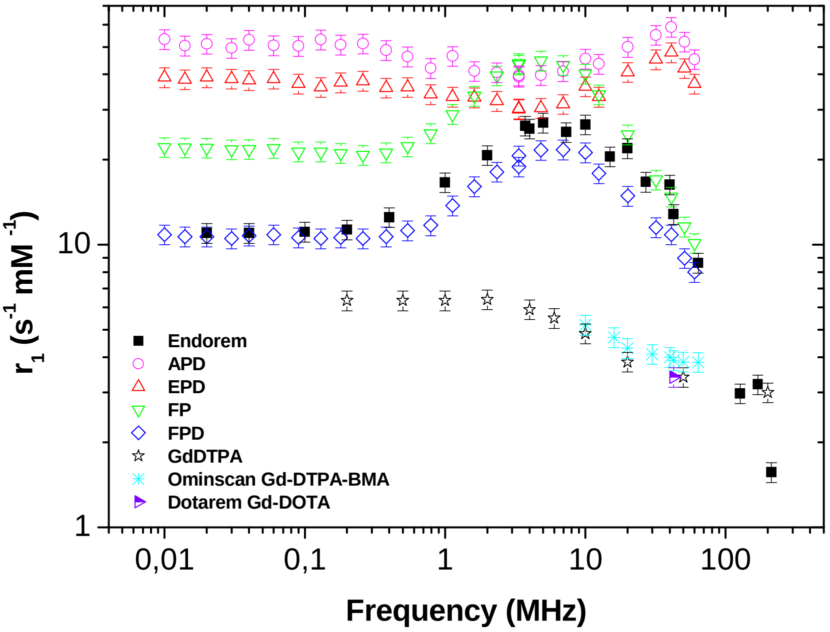

Figure SI-12. Longitudinal relaxation rates r_1 recorded at different frequencies for different NPs and reference samples.

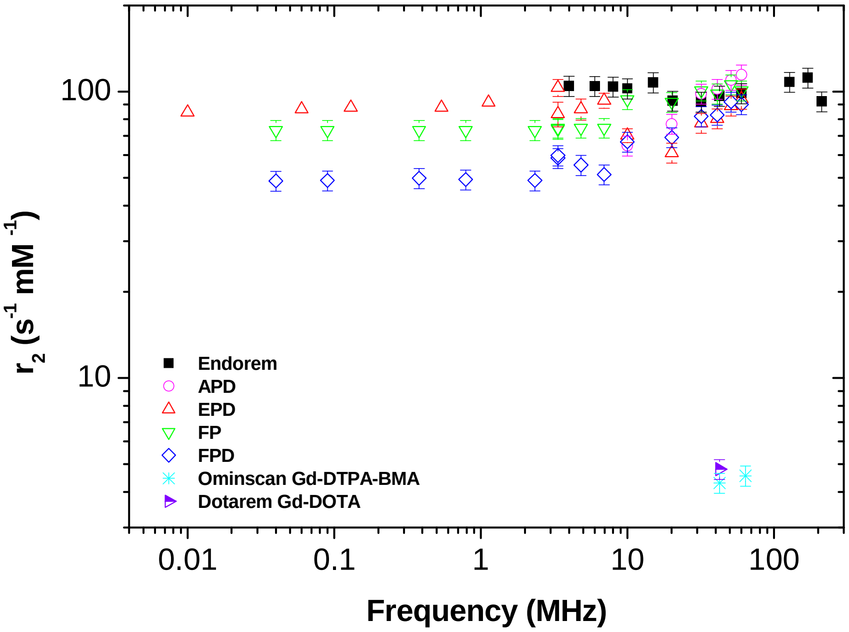

Figure SI-13. Transverse relaxation rates r_2 recorded at different frequencies for different NP and reference samples.

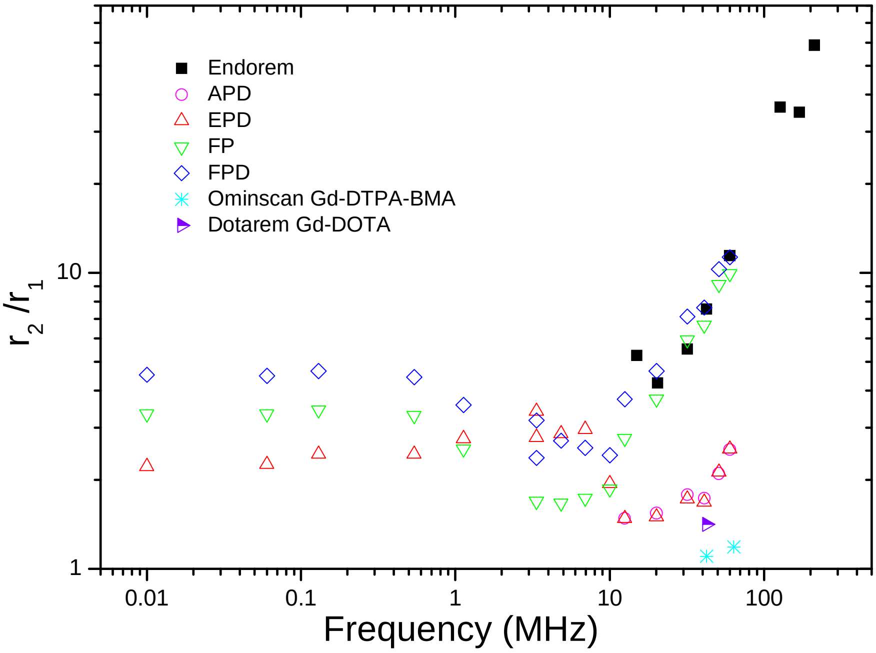

Figure SI-14. r_2/r_1 ratio of the samples displayed in Figures SI-12 and SI-13. The r_2/r_1 ratio is an indicator of the relaxometric properties of a given contrast agent, being 1-2 in the case of traditional paramagnetic ("positive") contrast agents and up to 50 in the case of superparamagnetic ("negative") contrast agents. In particular, the value of 2 is roughly assumed as the threshold value for effective negative contrast.

Sample/ Standard	$(r_1)_{20\,MHz}$ [$s^{-1}mM^{-1}$]	$(r_1)_{60\,MHz}$ [$s^{-1}mM^{-1}$]	$(r_2)_{20\,MHz}$ [$s^{-1}mM^{-1}$]	$(r_2)_{60\,MHz}$ [$s^{-1}mM^{-1}$]	$(r_2/r_1)_{20\,MHz}$	$(r_2/r_1)_{60\,MHz}$
APD	50.01	45.23	77.02	114.46	1.54	2.53
EPD	40.74	37.08	61.11	94.28	1.50	2.54
FP	24.52	10.12	91.86	100.72	3.75	9.95
FPD	14.88	7.99	69.17	90.20	4.65	11.28
FePt					3.47	3.29
FePtD					3.18	3.30
Omsniscan	4.3	3.84	//	4.55	//	1.18
Dotarem	//	3.42	//	4.8	//	1.41

Table SI-3. r_1, r_2 values, and r_2/r_1 ratio for the samples at frequency values used in clinical imagers. APD and AP are Au NPs with and without Gd-loaded chelator in the polymer shell. EPD and EP are CdSe/ZnS NPs with and without Gd-loaded chelator in the polymer shell. FPD and FP are Fe_2O_3 NPs with and without Gd-loaded chelator in the polymer shell. As additional sample also FePt NPs [40] with (FePtD) and without FePt)

5.5 Magnetic cores

Magnetic Fe_2O_3 NPs (cfg. §1.3) in toluene were polymer coated with DOTA-modified polymer (PMA-3%ABzDOTA, cfg. §2.5) in order to make them water-soluble (cfg. §3). Fe_2O_3 NPs modified with DOTA-modified polymer (FPD) were separated from empty micelles of DOTA-modified polymer (PD) by gel electrophoresis. The DOTA-chelator in the polymer was loaded with Gd ions as described in §5.1. As control iron oxide NPs were also coated with polymer without chelator (FP, cfg. §2.2).

The results for the characterization of the nuclear relaxation properties are shown in Figures SI-12, SI-13, SI-14, and in Table SI-3. The r_2 relaxivity of FP, which is more relevant for negative contrast agents, is comparable to Endorem® over the whole frequency range, while in the sample containing both Fe_2O_3 plus Gd (FPD) a small lowering was observed. Moreover, the r_2/r_1 ratio of both samples is very similar at most used clinical frequencies. It can be remarked that when the Gd-containing polymer shell is added to the magnetic NPs

(Fe_2O_3, but also to FePt) the relaxometric behaviour does not vary significantly with respect to the original superparamagnetic core. The dispersion curves indicate that the frequency behaviour $r_1(\nu)$ typical of superparamagnetic contrast agents (see e.g. Endorem®) dominates the overall relaxation mechanism (Figure SI-12) for both Fe_2O_3 original (FP) and Gd-coated (FPD) samples. As the $r_1(\nu)$ behaviour reveals the physical mechanisms that induce the relaxation of the nuclear magnetization, we can infer that in the samples based on Fe_2O_3 core the mechanisms are the same hypothesized for negative commercial contrast agents: the Curie relaxation dominates for frequencies $\nu > 5 \div 20$ MHz, while for lower frequencies the nuclear relaxation is due to the Néel reversal of the particle magnetization, determined by the magnetic anisotropy. The results shown in Table SI-3 indicate that the samples based on a magnetic core (FPD, FP) have an r_2/r_1 value indicative of a negative contrasting behaviour irrespective to the presence of the Gd coating, and behave similarly to the reference negative contrast agent.

6 Radiolabeling

6.1 Neutron activation of gold nanoparticles

Gold NPs were synthesized in organic solution as described in §1.2. The NPs were then polymer coated with unmodified polymer (cfg. §2.2) to make them water-soluble (cfg. §3). Gold NPs (^{197}Au) were transformed to radioactive gold NPs (^{198}Au) by neutron irradiation in a nuclear reactor. The ^{198}Au radioisotope decays with a half-life of 2.7 days to ^{198}Hg by the emission of γ rays among others. In this decay process the mass number remains constant since protons increase by one but neutron decrease by one. A suspension of 0.3 mg gold NPs with a concentration of 0.58 mg/mL[8] were sent for neutron activation to research reactor of the Helmholtz Centre Berlin, Berlin, Germany. After irradiation, Au NPs were labelled with 6.7 MBq of ^{198}Au radio-isotope.

6.2 Indium chelation

Indium-111 chloride ($^{111}InCl_3$) was purchased from Perkin Elmer (Product # NEZ304A000MC). In an Eppendorf vial 1 MBq (1 µL, 5.8×10^{-5} nmol) of $^{111}InCl_3$ in 0.5 M HCl was mixed with 10 µL of 2 mM $InCl_3$ (200 nmol, Sigma #334065) in 0.4 M Ammonium acetate buffer pH 6.0 in order to work with as little amount of radioactive In as possible. To this mixture 60 µL of 5 mM ABz-DOTA (300 nmol, Macrocyclics B200) in 0.4 M Ammonium acetate buffer pH 6.0 was added. The reaction mixture was then heated at 90°C for 35 minutes [23, 41, 42]. In this way the ABz-DOTA chelator is loaded with In, whereby only part of the In (0.0003% molar) is radioactive. The reaction mixture was then diluted to get final volume of 120 µL by adding SBB pH 9 buffer. This solution with In-loaded chelator molecules was divided in three parts for modification of CdSe/ZnS, Au, and Fe_2O_3 NPs. This was done with EDC chemistry which linked the carboxy groups of the polymer shell around NPs with the amino group of the DOTA chelators. Appropriate amount of EDC (N-(3-Dimethylaminopropyl)-N′-ethylcarbodiimide hydro-chloride, Sigma #E7750) was used to

---

[8] $c_{mass} = \frac{c_{molar} * V * N_A * \rho_{gold} * 4\pi r^3}{3}$ Where c_{mass} is mass concentration, c_{molar} = 1.49 µM, V = 1 mL is the volume of the NP solution, N_A is Avogadro number, ρ_{gold}=19.3 gcm^{-3}, r = d_{core}/2 = 2 nm for AuNPs.

activate the carboxyl groups of polymer coated NPs (cfg. §3) in addition with molar equivalent of Sulfo-NHS (N-Hydroxysulfosuccinimide sodium salt, Sigma #56485) for efficient reaction. After 20 min of reaction of the NPs with EDC and Sulfo-NHS excess reagents (i.e. unbound EDC, Sulfo-NHS) were removed by passing the solution mixture through a PD-10 column. The In-loaded DOTA was added and allowed to react for two hours at room temperature. For quantification of the number of EDC needed per NP a test experiment was performed with increasing ratio of EDC per NP [30] by fixing amount of In-loaded DOTA. The estimation of EDC / NP can be found by keeping a constant amount of In / NP (500 In-loaded DOTA in case of Au, CdSe/ZnS and 1000 for Fe_2O_3). The colloidal stability of the NPs before and after attachment of In-loaded DOTA to the polymer shell was observed by dynamic light scattering (DLS) with a Zeta Sizer (Malveren Instruments), see Figure SI-15. Radioactive polymer coated ^{198}Au NPs (AP) were colloidally stable. A slight change in size was observed after coupling ^{111}In-loaded DOTA to the polymer shell (APD). Polymer coated Fe_2O_3 NPs (FP) were also colloidally stable and size increased upon attachment of ^{111}In-loaded DOTA to the polymer shell (FPD).

In the present study for introducing In in polymer shell we used a post modification technique [16]. This was done as when we used chelator modified NPs (preconjugation) then In chelation caused aggregation of the NPs. Efficient In chelation requires acetate buffer at pH ~6.0 [23, 41] but these buffer conditions protonate the carboxylic groups of the polymer and cause aggregation of polymer coated NPs. We have tried other solvents like SBB pH 9, but under these conditions In was not chelated efficiently (cfg. Table SI-3). Before working with radioactive In, series of experiment has been performed for quantification of In chelation efficiency and non-specific binding.

6.4 Radioactive cores

In this case ^{198}Au NPs were supplemented with In-loaded chelator on their polymer shell. In an Eppendorf vial 20 µL ^{198}Au (0.20 MBq, 0.58 mg/mL)[9] with addition of 30 µL AP (0.58 mg/mL) was reacted with 95.4 µL of 50 mM EDC (~60000 EDC / NP) and 50 µL of 200 mM Sulfo-NHS in SBB pH 9. After 20 minutes the NPs were purified from unbound excess

---

[9] 10 µL of Au^{198} NP solution was taken as reference ^{198}Au (APD)

reagents with a PD-10 column. 30 µL of In-loaded DOTA (cfg. §6.2[10]) was added to purified NP solution and allowed to react for two hours at room temperature. Excess unbound chelator and ^{111}In was removed, again with PD-10 column. Results are displayed in Tables SI-5, SI-6, SI-7. The results demonstrate that by energies discrimination, emission from the ^{198}Au cores can be distinguished from emission originating of ^{111}In in the polymer shell.

NPs	Modification	$c_{UV/vis}$(NP) [nM]	c_{ICP-MS}(NP) [nM]	c(^{197}Au) or c(^{56}Fe) [nM]	c(In^{3+}) [nM]	c(In^{3+})/ c(NP)
AP+In	//	0.165	0.154	268.3	8.60	56
APD (SBB9)[11]	Pre	0.141	0.128	253.1	10.37	81
APD	Post	0.154	0.136	268.3	27.76	205
FP+In		0.027	0.174	1112.8	18.37	105
FPD	Post	0.029	0.220	1401.1	144.6	660
EP+In	//	0.048	//	//	4.43	96
EPD	Post	0.046	//	//	15.8	345

Table SI-4. ICP-MS measurement of NPs modified with Indium. APD, EPD, FPD, and AP, EP, FP corresponds to polymer coated Au, CdSe/ZnS, and Fe_2O_3 NPs with / without modification of chelator, respectively. Nonspecific binding was observed by addition of In to AP, EP and FP at same conditions. Concentration of the NPs c(NP) has been determined with UV/vis absorptions spectroscopy or with ICP-MS. In case of ICP-MS determination also the concentration of the ions from the core (c(Au) in case of Au NPs, c(Fe) in case of Fe_2O_3 NPs) which was the basis for the calculation of the NP concentration c(NP) is given. Indium concentration c(In^{+3}) was also determined with ICP-MS. By calculation the ratio the amount of In ions per NP was calculated: c(In^{3+})/ c(NP).

6.5 Fluorescent and magnetic cores

Hydrophobic CdSe/ZnS NPs (emission @ 610 nm; Evident tech ED-C11-TOL-0610; extinction coefficient $\varepsilon_{NP} = 3.2\times10^5$ $M^{-1}cm^{-1}$) were coated with plain amphiphilic polymer

---

[10] One part (40 µL) from the In-loaded DOTA solution as prepared in §6.2 was divided in 10 µL for reference ^{111}In (APD) measurements and 30 µL for coupling to Au^{198} NPs.

[11] In this experiment, SBB pH 9 buffer was used for In chelation.

(cfg. §2.2, §3). The polymer-coated NPs in aqueous phase were purified by gel electrophoresis. Conjugation of In-loaded DOTA was done in the following way: In an Eppendorf vial 100 µL of 2.87 µM NPs solution, 367 µL of 50 mM EDC solution, and 93.2 µL of 200 mM of Sulfo-NHS solution was reacted for 15 minutes at room temperature. 30 µL of In-loaded DOTA (§6.2[12]) were added and the mixture was allowed to react for two hours. The resulting sample was desalted by a PD-10 column in order to remove unbound free In-loaded DOTA from the NPs (EPD) [36].

Hydrophobic Fe_2O_3 NPs (§1.3, $\varepsilon_{NP} = 5.07\times10^7\ M^{-1}cm^{-1}$) were polymer coated with plain amphiphilic polymer (cfg. §2.2 and §3) and purified by gel electrophoresis. For linkage of In-loaded DOTA in an Eppendorf vial 100 µL of 2.64 µM of polymer coated Fe_2O_3 NPs, 340 µL of 50 mM EDC, and 86.1 µL of 200 mM Sulfo-NHS were mixed. After 15 minutes reaction time, the mixture was filtered with a PD-10 column in order to remove EDC and Sulfo-NHS which is not bound to the NPs. The NPs eluent was mixed with 30 µL of In-loaded DOTA (cfg. §6.2[13]) and the mixture was allowed to react for two hours at room temperature. Unbound DOTA was then removed by a PD-10 desalting column.

---

[12] One part (40 µL) from the solution obtains in §6.2 was again divided. 10 µL was kept for reference ^{111}In (EPD) measurements and 30 µL were conjugated with CdSe/ZnS.

[13] One part (40 µL) from the solution obtains in §6.2 was again divided. 10 µL was kept for reference ^{111}In (FPD) measurements and 30 µL were coupled with Fe_2O_3.

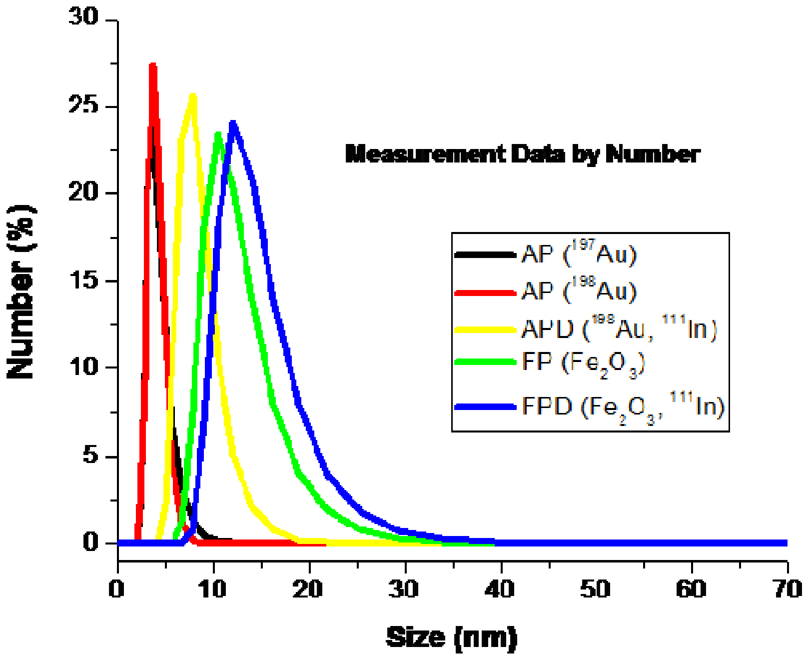

Figure SI-15. Zetasizer measurements of the hydrodynamic diameter of polymer coated NPs. The distribution is plotted according to the number percentage of NPs possessing a certain size.

6.3 Gamma ray spectroscopy

All procedures involving the use of radionuclides were carried out observing As Low As Reasonably Achievable (ALARA) protocols. Characterization of radioactive properties mainly involved the determination of the absolute count rates per NP core and polymer shell. As different emitters (^{198}Au, ^{111}In) were used for the NP core and for the polymer shell count rates of both entities can be distinguished based on energy filters. In this way gamma ray spectroscopy was used for identification and quantification of ^{198}Au, ^{111}In radionuclides by analysis of their gamma-ray energy spectrum as recorded in a gamma-ray spectrometer. Because radioactivity is present everywhere (i.e. background radiation BKG), the spectrum was recorded also when no source was present. This background radiation was then subtracted from the actual measurements. In this work the emission of γ-rays was recorded by a self-made gamma-spectrometer composed of a 5 inch well type NaI detector (*Scionix* Netherlands), a multichannel analyser (MCA), and the appropriated software (Canberra Industries, Inc.). The raw data of γ-rays emission for all NP samples are shown in Figure SI-16.

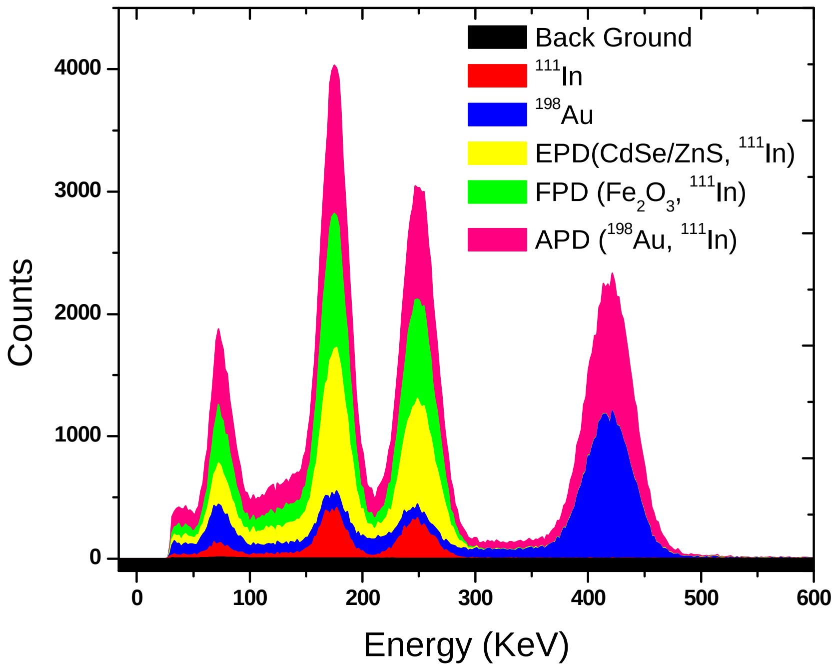

Figure SI-16. Gamma ray emission measurements of NP samples: ^{111}*In loaded DOTA, polymer coated* ^{198}*Au NPs (AP), CdSe/ZnS NPs coated with polymer shell with attached* ^{111}*In loaded DOTA (EPD),* Fe_2O_3 *NPs coated with polymer shell with attached* ^{111}*In loaded DOTA (FPD), and* ^{198Au} *NPs coated with polymer shell with attached* ^{111}*In loaded DOTA (APD).*

In a gamma-ray spectrometer there is a finite processing time required to measure and record each detected gamma ray. During this processing time, the spectrometer is not able to respond to another gamma ray. Thus the processing time is normally regarded as a dead time (T_D). Because gamma-ray photons arrive at the detector with a random distribution in time, some photons will arrive during this dead time and will not be measured or counted. The real time, T_R, is the elapsed time over which the spectrum is accumulated. The residual, after subtracting T_D from T_R, is the total live time, T_L, i.e., the total time during which the spectrometer was able to respond to another gamma ray. In present study ROIs (region of interest) defined as; 200 - 247 (371.25 keV - 463.59 keV) and 82 - 113 (140.51 keV - 200.97 keV) were recorded for the detection of ^{198}Au and ^{111}In, respectively.

Sample	Volume [μL]	ROI	T_R [sec]	Counts	BKG corrected counts[14]	Volume Corrected counts[15]

---

[14] BKG correction = counts – (BKG counts * BKG (T_L / T_R))

BKG	-	82-113	12018.20	13095	-	-
BKG	-	200-247	12018.20	7028	-	-
Reference ^{111}In (FPD)	10	82-113	120.5	6213	6082	18246
FPD (Fe_2O_3, ^{111}In)	30	82-113	121.3	18199	18068	18068
Reference ^{111}In (EPD)	10	82-113	120.6	7479	7348	22044
EPD (CdSe/ZnS, ^{111}In)	30	82-113	121.3	19294	19163	19163
Reference In^{111} (APD)	10	82-113 200-247	120.52 120.52	6635 60	6504 -	19512 -
Reference ^{198}Au (APD)	20	82-113 200-247	121.48 121.48	3855 30962	3724[16] 30892	- 30892
APD (^{198}Au, ^{11}1In)	30 µL ^{111}In + 20 µL ^{198}Au	82-113 200-247	121.52 121.52	21198 28627	21067 28496	17632 28496

Table SI-5: Gamma counts for each NP sample with fixed distance to the detector was 64 cm. Live time T_L is 120 s and Background (BKG) T_L is 12000 sec.

When a gamma ray undergoes Compton interaction, a portion of the energy escapes from the detector volume without being absorbed and the background rate in the spectrum is increased by one count. This count will appear in a channel below the channel that corresponds to the full energy of the gamma ray, hence needs Compton correction. Volume correction accounts the comparison of reference volume to total volume of radioactive sample used in

---

[15] Reference counts correspond to 10µL of initial volume (cfg. §6.4, §6.5) were multiplied by 3 to correct the total volume (30 µL).

[16] These counts were adjusted for Compton correction.

experiment. Finally, total counts have been corrected by BKG counts, volume correction and Compton correction.

The binding efficiency of In-loaded DOTA to the NPs was calculated by gamma ray measurements, in which after linking of In-loaded DOTA to the NPs as described above the count rates of ^{111}In in the NP sample were compared with the total ^{111}In counts[17], cfg. Tables SI-4 and SI-5. The count rates of the ^{111}In-labelled NPs are given in Table SI-6 as derived from the data shown in Figure SI-16. Clearly the ^{111}In in the NP polymer shells could be detected.

Waste materials from NPs	**Detection-distance [cm]**	**ROI**	**T_R [sec]**	**Counts**	**Distance corrected counts**
FPD (Fe_2O_3, ^{111}In)	25	82-113	121.3	717	90
EPD (CdSe/ZnS, ^{111}In)	25	82-113	121.3	2337	337
APD (^{198}Au, ^{111}In)	25	82-113 200-247	121.5 121.5	1926 4066	200 610

Table SI-6. Gamma ray counts for each NP's waste material (include filters, pipette tips, gloves etc.). The counts for the corresponding NP samples (FPD, EPD and APD) are given in Table SI-4. The distance correction factor was 6.55. Distance corrected counts were also account BKG and Compton correction.

Sample	Aliquot %	Total count %
APD	90.36	98.87
EPD	86.93	98.27
FPD	99.02	99.50

Table SI-7. Binding efficiencies of In-loaded DOTA to NPs (FPD, EPD, APD) by aliquot and total count percentage.

---

[17] Total counts involve the counts from all waste material like pipette tips, PD-10 columns and all other waste.

The binding efficiency or the amount of radioactivity effectively bound to the NPs were determined by comparing the initial reference volume (cfg. Footnote 11, 12, 13) to the total radioactivity volume used during experiment or by determining the total radioactivity used including the waste material (cfg. Table SI- 6) to the activity bound to NPs.

$$Aliquot\,\% = (NPs\ counts)/(Reference\ Counts * Volume\ factor) * 100$$

$$Total\ count\,\% = (NPs\ counts)/((NPs\ counts + NPs\ waste\ counts)) * 100$$

Binding efficiencies calculated by Aliquot % is the ratio of total radioactivity (γ counts) bound to NPs to the initial radioactivity. Whereas total count % involves the radioactivity bound to NP divided by sum of radioactivity bound to NP and wasted during experiment. The difference clearly comes from pipetting error or radioactivity lost from waste material.

7 References

[1] D. V. Talapin, S. Haubold, A. L. Rogach, A. Kornowski, M. Haase, H. Weller, *Journal of Physical Chemistry B* 2001, *105*, 2260.

[2] P. Reiss, J. Bleuse, A. Pron, *Nanoletters* 2002, *2*, 781.

[3] B. O. Dabbousi, J. Rodriguez-Viejo, F. V. Mikulec, J. R. Heine, H. Mattoussi, R. Ober, K. F. Jensen, M. G. Bawendi, *Journal of Physical Chemistry B* 1997, *101,* 9463.

[4] M. F. Casula, Y. W. Jun, D. J. Zaziski, E. M. Chan, A. Corrias, A. P. Alivisatos, *Journal of the American Chemical Society* 2006, *128*, 1675.

[5] S. Sun, C. B. Murray, D. Weller, L. Folks, A. Moser, *Science* 2000, *287*, 1989.

[6] A. Figuerola, A. Fiore, R. Di Corato, A. Falqui, C. Giannini, E. Micotti, A. Lascialfari, M. Corti, R. Cingolani, T. Pellegrino, P. D. Cozzoli, L. Manna, *Journal Of The American Chemical Society* 2008, *130*, 1477.

[7] E. V. Shevchenko, D. V. Talapin, A. L. Rogach, A. Kornowski, M. Haase, H. Weller, *JACS* 2002, *124*, 11480.

[8] M. Semmler-Behnke, W. G. Kreyling, J. Lipka, S. Fertsch, A. Wenk, S. Takenaka, G. Schmid, W. Brandau, *Small* 2008, *4*, 2108.

[9] M. Brust, M. Walker, D. Bethell, D. J. Schiffrin, R. Whyman, *J. Chem. Soc., Chem. Commun.* 1994, *1994*, 801.

[10] F. Zhang, Z. Ali, F. Amin, A. Feltz, M. Oheim, W. J. Parak, *ChemPhysChem* 2010, *11*, 730.

[11] T. Hyeon, *Chem. Commun.* 2003, *8*, 927.

[12] T. Pellegrino, L. Manna, S. Kudera, T. Liedl, D. Koktysh, A. L. Rogach, S. Keller, J. Rädler, G. Natile, W. J. Parak, *Nanoletters* 2004, *4*, 703.

[13] T. Liedl, S. Keller, F. C. Simmel, J. O. Rädler, W. J. Parak, *Small* 2005, *1*, 997.

[14] U. I. Tromsdorf, N. C. Bigall, M. Kaul, O. T. Bruns, M. S. Nikolic, B. Mollwitz, R. A. Sperling, R. Reimer, H. Hohenberg, W. J. Parak, S. Förster, U. Beisiegel, G. Adam, H. Weller, *Nanoletters* 2007, *7*, 2422.

[15] M. T. Fernández-Argüelles, A. Yakovlev, R. A. Sperling, C. Luccardini, S. Gaillard, A. S. Medel, J.-M. Mallet, J.-C. Brochon, A. Feltz, M. Oheim, W. J. Parak, *NanoLetters* 2007, *7*, 2613.

[16] C.-A. J. Lin, R. A. Sperling, J. K. Li, T.-Y. Yang, P.-Y. Li, M. Zanella, W. H. Chang, W. J. Parak, *Small* 2008, *4*, 334.

[17] A. Riedinger, F. Zhang, F. Dommershausen, C. Röcker, S. Brandholt, G. U. Nienhaus, U. Koert, W. J. Parak, *SMALL* 2010, *accepted*.

[18] Z. Baranyai, E. Gianolio, K. Ramalingam, R. Swenson, R. Ranganathan, E. Brucher, S. Aime, *Contrast Media Mol Imaging* 2007, *2*, 94.

[19] M. Wolf, W. E. Hull, W. Mier, S. Heiland, U. Bauder-Wust, R. Kinscherf, U. Haberkorn, M. Eisenhut, *J Med Chem* 2007, *50*, 139.

[20] D. A. Westerberg, P. L. Carney, P. E. Rogers, S. J. Kline, D. K. Johnson, *Journal Of Medicinal Chemistry* 1989, *32*, 236.

[21] D. K. Johnson, D. A. Westerberg, P. L. Carney, G. A. Sumerdo, P. E. Rodgers, S. J. Kline, *British Journal Of Cancer* 1987, *56*, 513.

[22] S. Liu, *Advanced Drug Delivery Reviews* 2008, *60*, 1347.

[23] J. K. Sosabowski, S. J. Mather, *Nature Protocols* 2006, *1*, 972.

[24] M. X. Wu, H. Liu, J. Liu, K. N. Haley, J. A. Treadway, J. P. Larson, N. Ge, F. Peale, M. P. Bruchez, *Nature Biotechnology* 2003, *21*, 41.

[25] W. W. Yu, E. Chang, J. C. Falkner, J. Zhang, A. M. Al-Somali, C. M. Sayes, J. Johns, R. Drezek, V. L. Colvin, *J. Am. Chem. Soc.* 2007, *129*, 2871.

[26] W. W. Yu, E. Chang, C. M. Sayes, R. Drezek, V. L. Colvin, *Nanotechnology* 2006, *17*, 4483.

[27] R. E. Anderson, W. C. W. Chan, *ACS Nano* 2008, *2*, 1341.

[28] A. Quarta, R. Di Corato, L. Manna, A. Ragusa, T. Pellegrino, *Ieee Transactions On Nanobioscience* 2007, *6*, 298.

[29] R. A. Sperling, T. Liedl, S. Duhr, S. Kudera, M. Zanella, C.-A. J. Lin, W. Chang, D. Braun, W. J. Parak, *Journal of Physical Chemistry C* 2007, *111*, 11552.

[30] R. A. Sperling, T. Pellegrino, J. K. Li, W. H. Chang, W. J. Parak, *Advanced Functional Materials* 2006, *16*, 943.

[31] A. V. Yakovlev, F. Zhang, A. Zulqurnain, A. Azhar-Zahoor, C. Luccardini, S. Gaillard, J. M. Mallet, P. Tauc, J. C. Brochon, W. J. Parak, A. Feltz, M. Oheim, *Langmuir* 2009, *25*, 3232.

[32] T. Pellegrino, R. A. Sperling, A. P. Alivisatos, W. J. Parak, *Journal of Biomedicine and Biotechnology* 2007, *2007*, article ID 26796.

[33] T. Niebling, F. Zhang, Z. Ali, W. J. Parak, W. Heimbrodt, *Journal of Applied Physics* 2009, *106*, 104701.

[34] A. D. Lehmann, W. J. Parak, F. Zhang, Z. Ali, C. Röcker, G. U. Nienhaus, P. Gehr, B. Rothen-Rutishauser, *SMALL* 2010, *6*, 753.

[35] M. M. Huber, A. B. Staubli, K. Kustedjo, M. H. B. Gray, J. Shih, S. E. Fraser, R. E. Jacobs, T. J. Meade, *Bioconjugate Chemistry* 1998, *9*, 242.

[36] F. M. van de Water, O. C. Boerman, A. C. Wouterse, J. G. P. Peters, F. G. M. Russel, R. Masereeuw, *Drug Metabolism and Disposition* 2006, *34*, 1393.

[37] R. Allabashi, W. Stach, A. d. l. Escosura-Muniz, L. Liste-Calleja, A. Merkoci, *J Nanopart Res* 2008.

[38] A. R. M. Bustos, J. R. Encinar, M. T. Fernandez-Arguelles, J. M. Costa-Fernandez, A. Sanz-Medel, *Chemical Communications* 2009, 3107.

[39] C. P. Slichter, *Principles of Magnetic Resonance*, Springer-Verlag, Berlin, 1990.

[40] M. P. Morales, M. F. Bedard, A. G. Roca, P. de la Presa, A. Hernando, F. Zhang, M. Zanella, A. Z. Abbasi, G. B. Sukhorukov, L. L. del Mercato, W. J. Parak, *Journal of Materials Chemistry* 2009, *19*, 6381.

[41] U. O. Häfeli, J. Yu, F. Farudi, Y. Li, G. Tapolsky, *Nuclear Medicine and Biology* 2003, *30*, 761–769.

[42] S. Liu, Z. He, W.-Y. Hsieh, P. E. Fanwick, *Inorg. Chem.* 2003, 8831.

JOURNAL OF APPLIED PHYSICS **106**, 104701 (2009)

Excitation dynamics in polymer-coated semiconductor quantum dots with integrated dye molecules: The role of reabsorption

Tobias Niebling,[a] Feng Zhang, Zulqurnain Ali, Wolfgang J. Parak, and Wolfram Heimbrodt
Department of Physics and Materials Sciences Center (WZMW), Philipps-University of Marburg,
Renthof 5, D-35032 Marburg, Germany

(Received 30 June 2009; accepted 28 September 2009; published online 19 November 2009)

Inorganic CdSe/ZnS core-shell quantum dots have been coated with amphiphilic polymers in order to enable their transfer to aqueous solutions. Additionally, ATTO-dye molecules have been embedded in the polymer shell. In this geometry ATTO dye acts as acceptor of the quantum dot donors' excitation. The energy transfer dynamics has been investigated in detail within the system by steady state and time-resolved optical spectroscopy. Radiative and nonradiative transfer processes dominate the photoluminescence properties of the quantum dots and dye molecules. Choosing different sizes of the quantum dots allowed for tuning the spectral overlap between the semiconductor dot emission and dye absorption. The experimental results have been described within a kinetic model which enables precisely to reveal the respective contributions of reabsorption and radiationless transfer rates. The distance dependence of quantum efficiencies and transfer rates shows that radiationless transfer is the more dominating the smaller the distance between the core of the nanoparticles and the dye molecules. © *2009 American Institute of Physics*. [doi:10.1063/1.3253762]

I. INTRODUCTION

Colloidal nanoparticles are of current interest in material science and biophysics.[1–4] In particular in the last decade there has been a rapid development of fluorescence-based systems including semiconductor quantum dots (QDs).[5,6] Advantages regarding the photostability[7] and quenching efficiencies[8] have been discussed. QDs can be used for specific cell labeling[7,9–13] and QD based sensors have been suggested using different principles.[14–21] A common sensor principle makes use of Förster resonant energy transfer (FRET) by harnessing changes in the energy transfer process from a donor, e.g., the semiconductor QD to an acceptor, e.g., organic dye molecules on the surface of the QD.[22–27] A major problem in FRET systems is the difficulty to distinguish between the desired real radiationless process and the inevitable reabsorption. To draw a careful distinction between both processes is often neglected but is essential from a physical point of view and to optimize sensor performance. In the present paper the excitation dynamics in polymer-coated QDs with integrated dye molecules will be discussed with special emphasis on the precise separation between the two contributions to the excitation dynamics, the radiative and the nonradiative energy transfer.

II. EXPERIMENTAL DETAILS

A. Sample preparation

For this study, we introduced a FRET geometry in which the acceptor is directly incorporated into the polymer shell to provide colloidal stability for the CdSe/ZnS QD donor. In this way, the linkage of the acceptor to the QD donor is very stable and the whole assembly has excellent colloidal stability. Hydrophobic QDs were purchased from Evident Technologies (see Table I) and transferred to aqueous solution by embedding them in a shell of an amphiphilic polymer.[27–29] The amphiphilic polymer was synthesized by linking amino-functionalized hydrophobic hydrocarbon chains (dodecylamine) to a polar backbone [poly(isobutylene-alt-maleic anhydride], $M_W = 6$ kDa) under reaction of the amino group of the hydrocarbon chain with the anhydride rings of the polymer backbone (reaction in anhydrous tetrahydrofuran).[1,29] The quantity of dodecylamine was chosen in a way that 75% of the anhydride rings inside the hydrocarbon chains react

TABLE I. Properties and determined parameters for the different QD samples. Enlisted are the following values: emission energy E_{em} and wavelength λ_{em} of the QDs, radius $\frac{1}{2}\cdot d_{\mathrm{dot}}$ of the inorganic CdSe/ZnS core, hydrodynamic radius $\frac{1}{2}\cdot d_{\mathrm{eff}}$ of the QDs comprising the inorganic core and the amphiphilic polymer shell, number of ATTO dye molecules N integrated in the polymer shell per QD, overlap integral J_λ, effective decay time of the QDs in solution $\tau^{\mathrm{eff}}_{\mathrm{QD}}$, transfer probabilities w_{FRET}, and determined Förster radius R_0. The decay times of the QDs without the presence of ATTO in the polymer shell was $\tau_{\mathrm{QD}} = 19$ ns. The last rows give the contributions of the reabsorption (a/L) and the nonradiative transfer (f/L) to the total transfer L from the QDs to the dye molecules.

Sample	Evidot® 490	Evidot® 520	Evidot® 540	Evidot® 580
λ_{em} [nm]	480	522	545	579
E_{em} [eV]	2.583	2.375	2.275	2.138
$\frac{1}{2}\cdot d_{\mathrm{dot}}$ [nm]	1.60	1.65	1.70	2.20
$\frac{1}{2}\cdot d_{\mathrm{eff}}$ [nm]	5.0	6.0	6.2	6.7
N	1.8	9.2	17.4	11.7
J_λ	0.0188	0.114	0.239	0.866
$\tau^{\mathrm{eff}}_{\mathrm{QD}}$ [ns]	18.8	12.2	5.6	3.3
w_{FRET} [ns^{-1}]	0.0005	0.03	0.13	0.25
R_0 [nm]	2.07	3.77	4.47	5.74
a/L	0.985	0.75	0.74	0.70
f/L	0.015	0.25	0.26	0.30

---

[a] Electronic mail: tobias.niebling@physik.uni-marburg.de.

B 1

with one dodecylamine molecule each. The acceptor fluorophore (amino-modified ATTO590) was incorporated into the amphiphilic polymer by reaction of the amino group of the dye with the remaining anhydride rings of the polymer backbone (reaction in anhydrous chloroform).[1,29] The quantity of the dye was adjusted so that 2% of the anhydride rings reacted with one dye molecule each. CdSe/ZnS QDs were then coated with the dye (ATTO590)-modified amphiphilic polymer according to a previously published protocol.[28,30] The particles are colloidally stabilized in aqueous solution by negatively charged carboxyl groups originating from opened anhydride rings. As a control, we coated under the same conditions QDs with amphiphilic polymer devoid of ATTO dye. We note that the polymer-coating procedure results in some empty polymer micelles in addition to polymer-coated particles. Size-exclusion chromatography[31] typically failed to separate excess polymer (in form of micelles) from the polymer-coated QDs; however, gel electrophoresis reliably separated the polymer micelles.[28] Additional information about the polymer coating procedure and its characterization can be found in the supporting information (SI).[32]

Four different sample solutions have been investigated: (a) ATTO dye molecules in empty micelles, (b) polymer-coated QDs without dye molecules embedded, (c) a mixture of the solutions (a) and (b), and (d) polymer-coated QDs with dye molecules in their polymer shell.

B. Continuous-wave and time resolved spectroscopy

The different solutions were filled in vessels consisting of fused silica and excited with a pulsed Nd:YAG (yttrium aluminum garnet) laser tripled to a wavelength of 355 nm (3.49 eV) and a temporal full width at half maximum of about 4 ns. The emitted photoluminescence (PL) was collected with a lens system and focused onto the entrance slit of a 0.25 m grating monochromator, where it was dispersed and detected afterwards by a silicon-based intensified charge-coupled device detector system. The temporal resolution was 2 ns given by the integration time window. All time traces are averaged over 200 measured transients. Absorption measurements have been performed in a standard UV/visible spectrometer. All measurements were performed at room temperature.

III. RESULTS AND DISCUSSION

ATTO dye molecules embedded in polymer-micelles exhibit an emission in the spectral range between 1.8 and 2.1 eV with a maximum at about 2 eV (see Fig. 1). The respective absorption band for dye molecules in empty polymer-micelles, i.e., without QD core, is depicted as green line in the inset of Fig. 1. A Franck–Condon blueshift of about 63 meV is seen for the maximum of the absorption band. For comparison the absorption spectrum is depicted for QDs with core diameters $d_{\text{dot}}=3.3$ nm as red line in the inset of Fig. 1. The respective emission wavelength is $\lambda_{\text{em}}=522$ nm (cf. Table I). To study the energy transfer processes and to avoid the strong direct absorption of the dye around 2.1 eV we have chosen $\lambda_{\text{exc}}=400$ nm ($E_{\text{exc}}=3.1$ eV) as excitation wavelength.

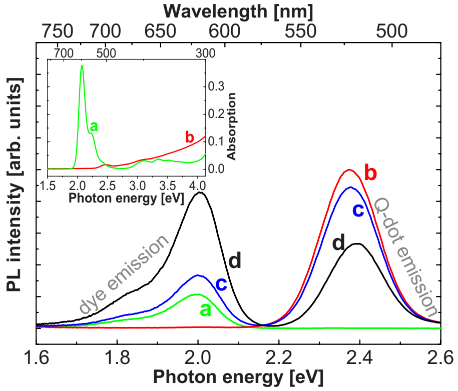

FIG. 1. (Color online) Integrated PL spectra of the different solutions at ambient temperature and an excitation wavelength of 400 nm. (a) ATTO dye molecules in empty micelles, (b) polymer-coated QDs ($d_{\text{dot}}=3.3$ nm) without dye molecules embedded, (c) mixture of the solutions [(a) and (b)], and (d) polymer-coated QDs with dye molecules in their polymer shell. The inset shows the absorption spectra of solutions (a) and (b).

The emission spectra for the different solutions are compared in Fig. 1. The green curve (a) gives the emission of ATTO dye molecules in micelles without semiconductor QDs. Only the orange PL of the dye can be seen. The QD emission without dye is depicted as red curve (b). Now only the green emission band of the 3.3 nm QDs can be seen. The emission of a mixture of solution (a) and (b), i.e., polymer-coated nanoparticles without dye and ATTO dye doped micelles, is depicted as blue curve (c) in Fig. 1. It can be clearly seen, that the integrated ATTO-dye emission is enhanced accompanied by a respective decline of the QD emission. The redistribution of the PL intensity toward the emission of the dye molecules is even more pronounced when the dye molecules are directly linked to the polymer shell of the nanoparticles (black curve (d) in Fig. 1). These results convincingly show that an effective energy transfer takes place from the QDs to the dye molecules, which is the basis for using such systems as FRET sensors. The problem is that just by taking into account the emission spectra it is not possible to draw conclusions from such measurements on the underlying mechanism. It is obvious that the transfer improves if the mean distance between QD and dye is reduced. The radiationless dipole-dipole energy transfer rate w obeys a distance dependence $w \sim r^{-6}$, whereas the reabsorption obeys $w \sim r^{-2}$. Both mechanisms enhance the energy transfer on reduced distance r between QD donor and dye acceptor and it is a real challenge to reveal the respective contributions. Usually, the lack of precise information about dye distribution and number of dye molecules are an additional difficulty. In the following, we provide a way to separate both contributions and draw reliable conclusions on the basis of time-resolved measurements.

The PL decay of dye molecules in empty micelles shows a single exponential decay with a decay time $\tau_{\text{dye}}=4.5$ ns (Fig. 2, green curve a) until the detection limit of 10^{-5} has been reached. This is a clear indication that the excitation is caused by direct intramolecule absorption and feeding processes do not play a significant role in empty micelles without a central QD. The decay of the CdSe/ZnS QD emission coated with polymers gives a weak nonexponential decay

B 2

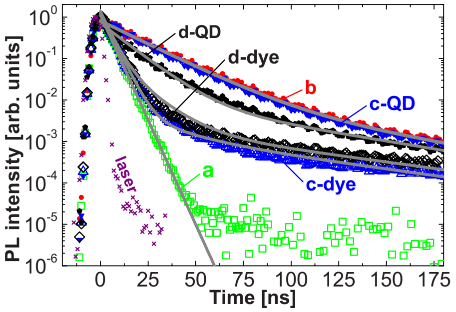

FIG. 2. (Color online) Luminescence transients of different solutions: (a) ATTO dye molecules in empty micelles, (b) polymer-coated QDs ($d_{\mathrm{dot}}=3.3$ nm) without embedded dye, (c) mixture of the solutions [(a) and (b)], and (d) polymer-coated QDs with dye molecules in their polymer shell. Filled symbols show the QD PL decay and open symbols show the temporal behavior of the dye emission. The laser transient is shown for comparison.

behavior (Fig. 2, red curve b), a phenomenon that is often observed in CdSe QDs.[33–35] A feeding mechanism causes the nonexponential decay either from trap states or by a thermal activation of excitons from the lower lying dark triplet-states.

To describe such QD decay one can use a straightforward kinetic model including the QD lifetime as well as an energy transfer channel from feeding states

$$\frac{dn_{\mathrm{QD}}}{dt} = -\frac{n_{\mathrm{QD}}}{\tau_{\mathrm{QD}}} + w_c \cdot n_t. \tag{1}$$

Here n_{QD} and n_t are the occupation numbers of the bright exciton states and the feeding (trap) states, respectively, τ_{QD} is the QD radiative lifetime and w_c is the probability for an excitation transfer from the feeding states to the bright QD states. The solution is a biexponential function with τ_t being the lifetime of the feeding states $[n_t = n_0 \cdot \exp(-t/\tau_t)]$

$$n_{\mathrm{QD}}(t) = n_{\mathrm{QD}}^a \cdot \exp\left(-\frac{t}{\tau_{\mathrm{QD}}}\right) + n_{\mathrm{QD}}^b \cdot \exp\left(-\frac{t}{\tau_t}\right). \tag{2}$$

The weighting factors n_{QD}^a and n_{QD}^b are functions of the initial occupation numbers, decay times as well as the transfer probability w_c (for details see SI).[32]

The fitting of curve b [full line in Fig. 2, $I_{\mathrm{QD}}(t) = -dn_{\mathrm{QD}}/dt$] gives a good agreement using the times $\tau_{\mathrm{QD}} = (19.0 \pm 0.4)$ ns (for Evidot520 QDs) and $\tau_t = (57.7 \pm 1.5)$ ns. It should be mentioned, that the same transient was found for the QD emission in case of a mixture of the QDs without dye in the polymer shell and micelles with embedded ATTO dye molecules but without dot core (curve c-QD). The luminescence of the ATTO dye in such a mixture on the other hand shows an additional slow decay component compared with the exponential emission decay of the pure dye polymer solution (curve a), as can be clearly seen by curve c in Fig. 2. This can be explained only by ATTO dye absorption of QD emission. Such reabsorption does not change at all the temporal behavior of the QD luminescence but reduces of course its integrated intensity as aforementioned (see Fig. 1). The absorbing dye molecules exhibit consequently a decelerated decay which also results in increased emission intensity under steady-state excitation conditions. The respective differential equation for the dye decay including the reabsorption probability w_{reab} by the dye molecules and the number of the excited QDs n_{QD} is given by

$$\frac{dn_{\mathrm{dye}}}{dt} = -\frac{n_{\mathrm{dye}}}{\tau_{\mathrm{dye}}} + w_{\mathrm{reab}} \cdot n_{\mathrm{QD}}. \tag{3}$$

The solution is a sum of three exponential functions

$$n_{\mathrm{dye}}(t) = n_{\mathrm{dye}}^a \cdot \exp\left(-\frac{t}{\tau_{\mathrm{dye}}}\right) + n_{\mathrm{dye}}^b \cdot \exp\left(-\frac{t}{\tau_{\mathrm{QD}}}\right) + n_{\mathrm{dye}}^c \cdot \exp\left(-\frac{t}{\tau_t}\right). \tag{4}$$

The weighting factors $n_{\mathrm{dye}}^{a,b,c}$ are again a complicated interplay of initial occupation numbers, decay times, and w_c, as well as the reabsorption probability w_{reab} (see SI).[32]

The transient (curve c-dye in Fig. 2) can be well fitted (full line) using the same time constants as determined before. The curves d-QD and d-dye also depicted in Fig. 2 give the transients of QD and dye emission in case of solution (d) with the dye molecules in close vicinity to the nanoparticles. An acceleration of the QD decay (curve d-QD) can be seen now. Nonradiative transfer processes (FRET) of the excitation energy from the QD to the dye molecules establish additional relaxation channels, yielding the acceleration of the QD PL decay. With w_{FRET} being the Förster-like dipole-dipole transfer probability the rate equation and respective solution read

$$\frac{dn_{\mathrm{QD}}}{dt} = -\frac{n_{\mathrm{QD}}}{\tau_{\mathrm{QD}}} - w_{\mathrm{FRET}} \cdot n_{\mathrm{QD}} + w_c \cdot n_t = -\frac{n_{\mathrm{QD}}}{\tau^{\mathrm{eff}}_{\mathrm{QD}}} + w_c \cdot n_t, \tag{5}$$

$$n_{\mathrm{QD}}(t) = n_{\mathrm{QD}}^a \cdot \exp\left(-\frac{t}{\tau^{\mathrm{eff}}_{\mathrm{QD}}}\right) + n_{\mathrm{QD}}^b \cdot \exp\left(-\frac{t}{\tau_t}\right). \tag{6}$$

The amplitudes n_{QD}^a and n_{QD}^b are of the same form as used in Eq. (2) but the QD decay time is replaced by the effective decay time

$$\frac{1}{\tau^{\mathrm{eff}}_{\mathrm{QD}}} = \frac{1}{\tau_{\mathrm{QD}}} + w_{\mathrm{FRET}}. \tag{7}$$

The effective decay time of the QDs in solution (d) can be deduced by fitting the curve d-QD (Fig. 2) to be $\tau^{\mathrm{eff}}_{\mathrm{QD}} = (12.2 \pm 0.3)$ ns. The dye emission of sample (d) decreases slightly slower (curve d-dye) due to the extra feeding channel. The decay is then given by Eqs. (3) and (4) but replacing again the QD lifetime τ_{QD} by the effective time $\tau^{\mathrm{eff}}_{\mathrm{QD}}$. As can be seen the respective curve d-dye gives again a remarkable agreement with the experimental data.

To modify the transfer rate from the dots to the dye molecules we investigated QDs with different diameters. In Fig. 3 the luminescence spectra are depicted for QDs with core diameters between $d_{\mathrm{dot}} = 3.2$ nm and 4.4 nm. It can be seen that a reduction in the QD diameter leads to a blueshift of the emission band of the nanoparticles due to the quantum confinement effect. The intensity of the QD emission decreases relatively to the normalized dye emission intensity

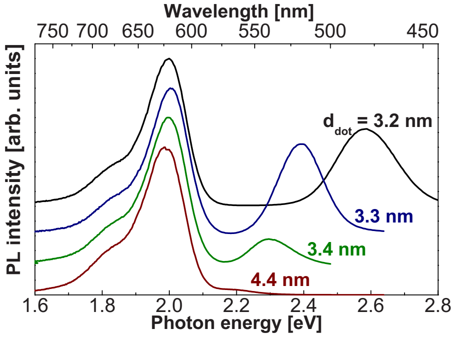

FIG. 3. (Color online) PL spectra of polymer-coated QDs with embedded dye molecules for different diameters of the centered QDs (excitation at 400 nm).

when the QD luminescence approaches the absorption maximum of the ATTO dye. This reduction is obviously caused by an improved energy transfer.

The Förster transfer rate from a donor to an acceptor is determined by

$$w_{\mathrm{FRET}} = \frac{1}{\tau_{\mathrm{QD}}} \cdot \left(\frac{R_0}{r_i}\right)^6, \tag{8}$$

where τ_{QD} is the donor radiative lifetime, r_i is the distance between donor and acceptor, and R_0 is the so-called Förster radius. The Förster radius is defined as distance where the transfer rate equals the radiative transition probability. This radius scales with the spectral overlap between the emission of the donor and the absorption of the acceptor as will be shown later.

In Fig. 4 the QD transients are given for all QD sizes with ATTO molecules in the polymer shell of the nanoparticles. The stronger quenching of the QD luminescence with increasing QD size is clearly observable in the time-resolved measurements. The larger the QDs are the faster the decay is. This is expected by the transfer probabilities of reabsorption and FRET, which are both stronger if the spectral overlap between the QD emission and dye absorption becomes larger. The point is, however, that only the radiationless transfer but not the reabsorption changes the QD decay times, as aforementioned. Real FRET transfer of the excitation energy from the QD to the dye molecules causes the observed acceleration of the QD PL decay and the respective smaller effective lifetime of the QDs.

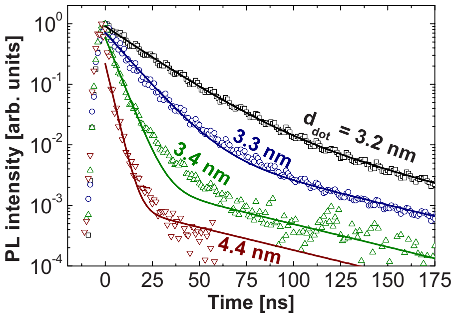

FIG. 4. (Color online) Time-resolved PL intensity of QD solutions with various QD diameters surrounded by a polymer shell with embedded dye molecules.

The full lines in Fig. 4 are calculated using Eq. (5). $\tau^{\mathrm{eff}}_{\mathrm{QD}}$ changes from (18.8 ± 0.4) ns for $d_{\mathrm{dot}}=3.2$ nm QDs to (12.2 ± 0.3) ns for $d_{\mathrm{dot}}=3.3$ nm, (5.6 ± 0.2) ns for $d_{\mathrm{dot}}=3.4$ nm, and (3.3 ± 0.1) ns for $d_{\mathrm{dot}}=4.4$ nm, respectively. The transfer probabilities are $w_{\mathrm{FRET}}=0.0005$ ns^{-1}, 0.03 ns^{-1}, 0.13 ns^{-1}, and 0.25 ns^{-1} according to Eq. (7). It is obvious that for the smallest QDs the transfer probability is almost vanishing, whereas in case of the 4.4 nm dots the radiationless transfer dominates the decay.

Basically, it is also possible to estimate an effective Förster radius R_0 of the various QD-dye systems from the transient results. The total value for the transfer rate is given by the sum over all acceptors $i=1,\ldots,N$ [see Eq. (9)], whereby N is the number of ATTO molecules around each QD

$$w_{\mathrm{FRET}} = \frac{1}{\tau_{\mathrm{QD}}} \cdot \sum_{i=1}^{N} \left(\frac{R_0}{r_i}\right)^6. \tag{9}$$

Neither the exact distance between the dye molecules and the QD (r_i) is known, nor the exact number of dye molecules (N). As a first approximation we assume a mean value $R = \langle r_i \rangle$ between the center of the QD and all surrounding dye molecules and a fixed number N of dye molecules in the polymer shell. We now obtain for the Förster radius

$$R_0 = R \cdot \sqrt[6]{\frac{w_{\mathrm{FRET}} \cdot \tau_{\mathrm{QD}}}{N}}. \tag{10}$$

The average number of dye molecules in the polymer shell of the QDs has been determined spectroscopically (see SI) (Ref. 32) to be about $N=2$, 9, 17, 11 for the 3.2, 3.3, 3.4, and 4.4 nm QDs, respectively.

Using one half of the hydrodynamic diameter d_{eff} of the polymer-coated QDs (see SI) (Ref. 32) as the mean distance R between the QD center and the dye molecules, we determined the effective Förster radii to be about $R_0=2.07$, 3.77, 4.47, and 5.74 nm for $d_{\mathrm{dot}}=3.2$, 3.3, 3.4, and 4.4 nm, respectively, see Table I.

The relation between the Förster radius R_0 and the spectral overlap integral J_λ between the QD emission $F_D(\lambda)$ and the absorption $\varepsilon_A(\lambda)$ of the dye molecules is given by a power of 6 (Ref. 36)

$$R_0^6 = 8.79 \times 10^{-5} \kappa^2 n^{-4} Q_D J_\lambda, \tag{11}$$

with κ^2 being the orientation factor, n the refractive index of the surrounding medium, and Q_D the quantum yield of the donor in absence of an acceptor.

In Fig. 5 the overlap between the QD emission and the absorption of the dye molecules is depicted (blue area). We determined J_λ numerically using

$$J_\lambda = \frac{1}{J_{\max}} \int_0^\infty F_D(\lambda) \varepsilon_A(\lambda) \lambda^4 d\lambda, \tag{12}$$

with $J_{\max}$ being the integral in case of identical emission $F_D(\lambda)$ and absorption $\varepsilon_A(\lambda)$ yielding $J_\lambda=1$.

The values J_λ (also given in Fig. 5) increase by almost two orders of magnitude from about 2% for $d_{\mathrm{dot}}=3.2$ nm to

B 4

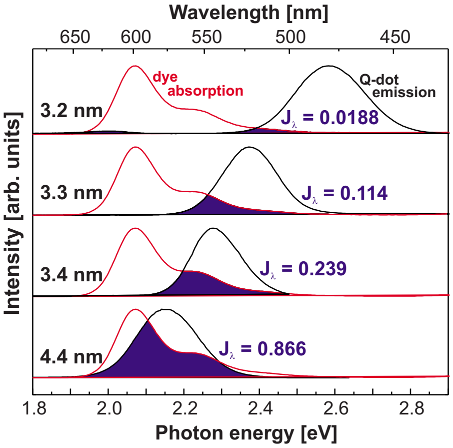

FIG. 5. (Color online) Absorption spectra of ATTO-dye molecules in comparison with the emission bands of polymer-coated QDs with different diameters d_{dot}.

about 87% for $d_{\text{dot}}=4.4$ nm. As can be seen from Fig. 6 the experimental results obey Eq. (11) with $R_0^6 \sim J_\lambda$.

Finally, it should be mentioned that it is also possible to quantify the ratio of reabsorption and FRET. The total transfer L from the QDs to the dye is the sum of absorption a and FRET transfer f and can be determined from the integrated experimental intensities by

$$L = \frac{I_b - I_{d\text{–QD}}}{I_b}, \tag{13}$$

with I_b being the PL intensities of the QDs without dye molecules (solution b) and $I_{d\text{–QD}}$ being the PL intensity of solution d, i.e., QDs with dye molecules embedded in the polymer shell.

L can be expressed by means of the transfer parameters determined before (see also SI) (Ref. 32)

$$L = a + f = \frac{w_{\text{FRET}} \cdot \tau_{\text{QD}} + a}{1 + w_{\text{FRET}} \cdot \tau_{\text{QD}}}. \tag{14}$$

The respective contributions of the reabsorption and FRET can be determined then straightforwardly by the following equations:

$$a = L - w_{\text{FRET}} \cdot \tau_{\text{QD}} + w_{\text{FRET}} \cdot \tau_{\text{QD}} L, \tag{15}$$

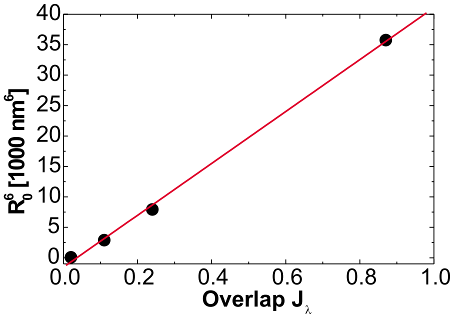

FIG. 6. (Color online) Förster radius R_0^6 as a function of the relative spectral overlap integral J_λ.

$$f = w_{\text{FRET}} \cdot \tau_{\text{QD}} - w_{\text{FRET}} \cdot \tau_{\text{QD}} \cdot L. \tag{16}$$

In case of the 3.2 nm dots about 98.5% of the transfer is caused by reabsorption and FRET is only about 1.5%, whereas in case of the 4.4 nm dots about 30% of the total transfer to the dye molecules is nonradiatively, but still 70% are caused by reabsorption.

IV. CONCLUDING REMARKS

Semiconductor QDs with integrated ATTO dyes in the polymer shell are promising candidates for a new generation of nanobiosensors. To enhance the performance of such a system one has to optimize the energy transfer between the dot and the dye. To do so, it is necessary to distinguish between the radiationless energy transfer and the inevitable reabsorption. It was shown, that reabsorption is significant and has to be taken into account. Time-resolved measurements enable to distinguish between both mechanisms.

In case of a mixture solution with ATTO dye molecules in empty micelles and polymer-coated QDs without dye molecules in the shell the energy transfer is based solely on the reabsorption. Polymer-coated QDs with dye molecules in their polymer shell exhibit a strong decrease in the luminescence lifetime caused by a strong radiationless Förster-like dipole-dipole energy transfer. The efficiency of the transfer depends on the spectral overlap between the dot emission and the dye absorption. The Förster radius increases with enhanced spectral overlap . It was found, that the transfer can be changed from solely reabsorption in case of the 3.2 nm dots to a transfer with a substantial contribution of FRET transfer of about 30% in case of the 4.4 nm dots. The radiationless transfer rate can be of course even more enhanced by further reducing the mean spacing between dye and dot. It was found, that the Förster radius, which is defined as distance where the FRET rate equals the radiative transition probability of the dots, acts also as a kind of borderline for the ratio between reabsorption and FRET. If the mean distance between dye and dot center is comparable to the Förster radius the FRET transfer is a substantial contribution to the total transfer rate. Our results suggest, that the dot dye distance should be smaller than the Förster radius to get an overwhelming FRET transfer.

ACKNOWLEDGMENTS

Part of the project was supported by the German Research Foundation (DFG, SPP 1313 Grant No. PA 794/4-1 and EGC 790—Electron-electron interaction in solids). The authors are grateful for helpful technical discussions to Dr. Martin Oheim, Dr. Niko Hildebrand, Abbasi Azhar-Zahoor, and Faheem Amin.

[1] R. C. Somers, M. G. Bawendi, and D. G. Nocera, Chem. Soc. Rev. **36**, 579 (2007).
[2] C. J. Lin, T. Liedl, R. A. Sperling, M. T. Fernández-Argüelles, J. M. Costa-Fernández, R. Pereiro, A. Sanz-Medel, W. H. Chang, and W. J. Parak, J. Mater. Chem. **17**, 1343 (2007).
[3] A. P. Alivisatos, W. Gu, and C. Larabell, Annu. Rev. Biomed. Eng. **7**, 55 (2005).
[4] P. Alivisatos, Nat. Biotechnol. **22**, 47 (2004).
[5] M. Bruchez, Jr., M. Moronne, P. Gin, S. Weiss, and A. P. Alivisatos,

B 5

Science **281**, 2013 (1998).

[6] U. Resch-Genger, M. Grabolle, S. Cavaliere-Jaricot, R. Nitschke, and T. Nann, Nat. Methods **5**, 763 (2008).

[7] X. Wu, H. Liu, J. Liu, K. N. Haley, J. A. Treadway, J. P. Larson, N. Ge, F. Peale, and M. P. Bruchez, Nat. Biotechnol. **21**, 41 (2002).

[8] A. R. Clapp, I. L. Medintz, J. M. Mauro, B. R. Fisher, M. G. Bawendi, and H. Mattoussi, J. Am. Chem. Soc. **126**, 301 (2004).

[9] J. K. Jaiswal, H. Mattoussi, J. M. Mauro, and S. M. Simon, Nat. Biotechnol. **21**, 47 (2003).

[10] W. C. W. Chan and S. Nie, Science **281**, 2016 (1998).

[11] M. Howarth, W. Liu, S. Puthenveetil, Y. Zheng, L. F. Marshall, M. M. Schmidt, K. D. Wittrup, M. G. Bawendi, and A. Y. Ting, Nat. Methods **5**, 397 (2008).

[12] A. A. Ghazani, J. A. Lee, J. Klostranec, Q. Xiang, R. S. Dacosta, B. C. Wilson, M. S. Tsao, and W. C. W. Chan, Nano Lett. **6**, 2881 (2006).

[13] F. Pinaud and M. Dahan, Science **320**, 187 (2008).

[14] K. E. Sapsford, T. Pons, I. L. Medintz, and H. Mattoussi, Sensors **6**, 925 (2006).

[15] E. R. Goldman, H. Mattoussi, G. P. Anderson, I. L. Medintz, and J. M. Mauro, Methods Mol. Biol. **303**, 19 (2005).

[16] R. Freeman and I. Willner, Nano Lett. **9**, 322 (2009).

[17] R. Gill, L. Bahshi, R. Freeman, and I. Willner, Angew. Chem., Int. Ed. **47**, 1676 (2008).

[18] R. Gill, I. Willner, I. Shweky, and U. Banin, J. Phys. Chem. B **109**, 23715 (2005).

[19] C. Stoll, S. Kudera, W. J. Parak, and F. Lisdat, Small **2**, 741 (2006).

[20] N. Hildebrandt, L. J. Charbonniere, M. Beck, R. F. Ziessel, and H.-G. Lohmannsroben, Angew. Chem., Int. Ed. Engl. **44**, 7612 (2005).

[21] M. T. Fernandez-Argüelles, W. J. Jin, J. M. Costa-Fernandez, R. Pereiro, and A. Sanz-Medel, Anal. Chim. Acta **549**, 20 (2005).

[22] T. Pons, I. L. Medintz, X. Wang, D. S. English, and H. Mattoussi, J. Am. Chem. Soc. **128**, 15324 (2006).

[23] A. R. Clapp, I. L. Medintz, H. T. Uyeda, B. R. Fisher, E. R. Goldman, M. G. Bawendi, and H. Mattoussi, J. Am. Chem. Soc. **127**, 18212 (2005).

[24] A. R. Clapp, I. L. Medintz, and H. Mattoussi, ChemPhysChem **7**, 47 (2006).

[25] W. R. Algar and U. J. Krull, Anal. Bioanal. Chem. **391**, 1609 (2008).

[26] A. M. Dennis and G. Bao, Nano Lett. **8**, 1439 (2008).

[27] A. V. Yakovlev, F. Zhang, A. Zulqurnain, A. Azhar-Zahoor, C. Luccardini, S. Gaillard, J. M. Mallet, P. Tauc, J. C. Brochon, W. J. Parak, A. Feltz, and M. Oheim, Langmuir **25**, 3232 (2009).

[28] C. A. Lin, R. A. Sperling, J. K. Li, T. Y. Yang, P. Y. Li, M. Zanella, W. H. Chang, and W. J. Parak, Small **4**, 334 (2008).

[29] M. T. Fernández-Argüelles, A. Yakovlev, R. A. Sperling, C. Luccardini, S. Gaillard, A. Sanz-Medel, J.-M. Mallet, J.-C. Brochon, A. Feltz, M. Oheim, and W. J. Parak, Nano Lett. **7**, 2613 (2007).

[30] T. Pellegrino, L. Manna, S. Kudera, T. Liedl, D. Koktysh, A. L. Rogach, S. Keller, J. Rädler, G. Natile, and W. J. Parak, Nano Lett. **4**, 703 (2004).

[31] R. A. Sperling, T. Liedl, S. Duhr, S. Kudera, M. Zanella, C.-A. J. Lin, W. H. Chang, D. Braun, and W. J. Parak, J. Phys. Chem. C **111**, 11552 (2007).

[32] See EPAPS supplementary material at http://dx.doi.org/10.1063/1.3253762 for more details about the synthesis of the polymer, polymer coating and purification as well as the determination of the hydrodynamic diameter, the photophysical characterization and details of the kinetic model are available in the supporting information.

[33] O. Labeau, P. Tamarat, and B. Lounis, Phys. Rev. Lett. **90**, 257404 (2003).

[34] G. Schlegel, J. Bohnenberger, I. Potapova, and A. Mews, Phys. Rev. Lett. **88**, 137401 (2002).

[35] A. L. Efros, M. Rosen, M. Kuno, M. Nirmal, D. J. Norris, and M. Bawendi, Phys. Rev. B **54**, 4843 (1996).

[36] J. R. Lakowicz, *Principles of Flourescence Spectroscopy*, 2nd ed. (Kluwer, Dordrecht, 1999).

B 6

Excitation Dynamics in Polymer-Coated Semiconductor Quantum Dots with Integrated Dye Molecules - the Role of Reabsorption

Tobias Niebling, Feng Zhang, Zulqurnain Ali, Wolfgang J. Parak, and
Wolfram Heimbrodt

Department of Physics and Material Sciences Center (WZMW), Philipps-University of Marburg,
Renthof 5, D-35032 Marburg, Germany

Supporting Information

I. Synthesis

a) Amphiphilic polymer

We have synthesized the amphiphilic polymer in the current paper according to previous reports [1-3]. In the following the synthesis protocol is enlisted:

1) 2.70 g (15 mmol) of dodecylamine powder ((#1), 98%, Sigma, #D22,220-8) were dissolved in 100 mL anhydrous tetrahydrofurane (THF, ≥99.9%, Aldrich, #186562) in a round flask.
2) 3.084 g poly(isobutylene-alt-maleicanhydride) powder ((#2), 20 mmol monomer, cfg. Figure 1, average M_w ~ 6,000 g/mol, Sigma, #531278) was weighted in another round flask.
3) As soon as (#1) dissolved completely, all of the solution of (#1) was poured into the round flask containing (#2). This mixture (#3) was sonicated for several seconds (~20 s) and then heated at 55-60°C for 1 hour under stirring conditions.
4) The solution (#3) was concentrated to 30-40 mL by evaporation of the THF solvent in order to enhance the reaction between the maleic anhydride rings and the amino groups. The solution was left stirring overnight.
5) The next day solution (#3) was completely dried by evaporation and the remaining powder of the amphiphilic polymer was redissolved in 40 mL anhydrous chloroform to a final monomer concentration $c_{monomer}$ of 0.5 M (see Figure 1).

All the organic solvents used here were purchased in anhydrous quality in order to keep the maleic anhydride rings active. After the synthesis, the amphiphilic polymer still has 25% of maleic anhydride rings intact (each monomer corresponds to one maleic anhydride ring, see Figure 1), which can react with other molecules such as amino-modified ATTO-590 as will be described in the following.

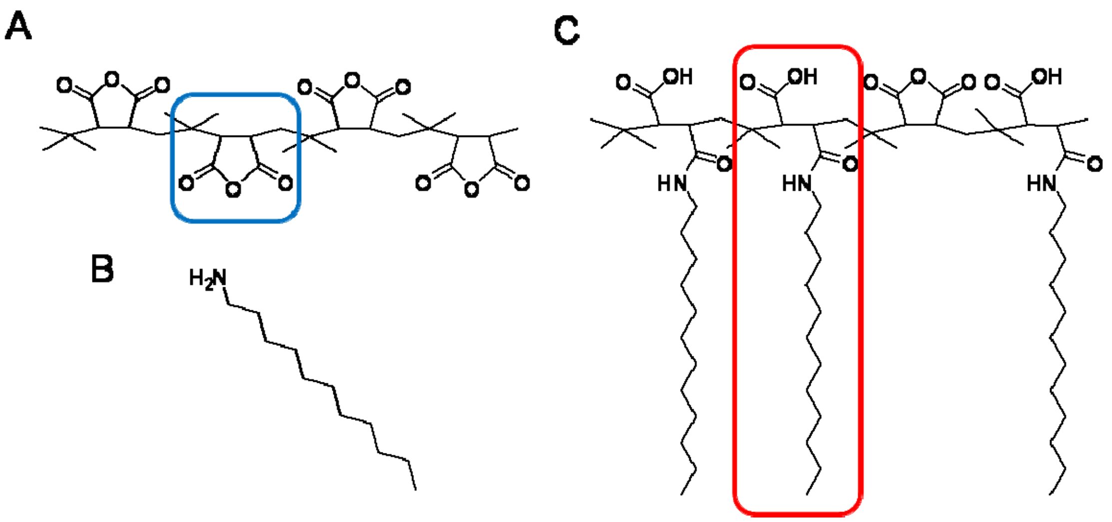

Figure 1. Molecular structure of the amphiphilic polymer. A) Poly(isobutylene-alt-maleic anhydride). The blue box shows one monomer unit which comprises one anhydride ring. B) Dodecylamine. C) Amphiphilic polymer. The red box shows one monomer (or motif) unit. For more information see reference[1].

b) ATTO-590 modified amphiphilic polymer

The method used to modify the amphiphilic polymer with the amine-ATTO-590 dye was according to previous reports [2, 3]. Amine-ATTO-590 is a derivate of ATTO-590 (with a functional amino group, absorption maximum: 597 nm, emission maximum: 615 nm, ATTO-TEC GmbH, Germany). After the synthesis still 25% of the maleic anhydride rings are active[1] and are available for further reactions (cfg. Chapter Ia). The amino group of the amine-ATTO-590 dye molecule was used to link the dye to the amphiphilic polymer by forming a peptide bond with the maleic anhydride ring. For this purpose the ATTO-590 dye was firstly dissolved in THF in a 500 mL round flask[2]. Then all THF was evaporated and afterwards the ATTO-590 powder was redissolved in anhydrous chloroform[3]. The absorption of the ATTO-590 in chloroform solution was measured by recording the UV/vis absorption spectrum. Then the concentration was determined by means of the Lambert-Beer law $A = \varepsilon \cdot c \cdot d$, whereby A is the optical density (absorption) at the absorption maximum (597 nm), c is the concentration of ATTO-590, d is the path length of the cuvette used for the absorption measurement, and $\varepsilon = 120{,}000\ \mathrm{M}^{-1}\mathrm{cm}^{-1}$ is the extinction coefficient at 597 nm as provided by ATTO-TEC company. In the present manuscript we adjusted the ATTO-590 to polymer ratio in a way that 2% of the polymer motifs bind an ATTO-590 dye molecule in average[4]. In practice we mixed ATTO-590 dye and the amphiphilic polymer motifs (cfg. Chap. Ia) in a molar ratio of 2:100 (mol:mol) in anhydrous chloroform and left the mixture overnight at room temperature for reaction. The final concentration of the ATTO-590 modified polymer was derived from the concentration of the unmodified polymer used for the reaction. Alternatively, the concentration of the ATTO-590 modified polymer could also be determined by UV/vis spectrometry. As the extinction of ATTO-590 at 597 nm is not changed by the conjugation to the polymer, the polymer concentration could be determined by measuring the ATTO-590 concentration[5].

---

[1] 75% of the maleic anhydride rings already reacted with dodecylamine. For ease of calculation we assume a reaction efficiency of 100%, which will not be fulfilled in practice.

[2] ATTO-590 dissolves in THF within several minutes, however, the optical absorption in THF is reduced and the extinction coefficient is changed compared to an aqueous solution or a solution in chloroform.

[3] As it turned out to be difficult to dissolve ATTO-590 dye powder directly in anhydrous chloroform (even by sonication) the ATTO-590 was first dissolved in THF before.

[4] The resulting polymer is termed polymer-ATTO 2%´, indicating that 2% of the anhydride rings of the polymer reacted with ATTO-590, and 75% of the anhydride rings reacted with dodecylamine (assuming a reaction efficiency of 100% between the amino-groups and the anhydride rings).

[5] As 2% of the monomer units are modified with ATTO-590 the concentration of monomer units is 50 times the concentration of ATTO-590.

II. Polymer coating and purification.

a) Polymer coating

Four kinds of fluorescent CdSe/ZnS Q-dots (Evidots dispersed in toluene, the product numbers are ED-C11-TOL-0490, ED-C11-TOL-0520, ED-C11-TOL-0540, and ED-C11-TOL-0580 for Evidot® 490, Evidot® 520, Evidot® 540 and Evidot® 580 respectively, Evident Technologies, Inc.) with different colors and diameters were coated with the ATTO-590 modified polymer described in Chapter Ib. The polymer coating procedures was performed according to previous reports [1-3]. Solutions with ATTO-590 modified polymer (dissolved in anhydrous chloroform) were mixed with the different Evidots samples (in the original toluene solvent) in round flasks. The molar ratios are shown in Table 1[6]. Then the solvents were slowly evaporated, and the remaining solid film in the flask was redissolved in SBB buffer (sodium borate, 50 mM, pH 12). A clear solution was formed.

---

[6] At first the amount of Q-dots N_{QD} in the sample was determined. The concentration c_{QD} of the Q-dots was measured via recording the optical density (OD) at the first exciton peak: $OD = \varepsilon \cdot c_{QD} \cdot d$. ε is the extinction coefficient listed in Table 1. $N_{QD} = N_A \cdot c_{QD} \cdot V_{QD}$, with the Avogadro number N_A and the volume of the Q-dot sample V_{QD}. As one Q-dots has an effective surface area A_{eff} (see Table 1) the whole surface of all N_{QD} Q-dots in the sample is $A_{eff,tot} = A_{eff} \cdot N_{QD}$. The number of polymer monomers required per effective particle surface area $N_{monomer}/A_{eff}$ is taken from Table 1. The number of required polymer monomers thus is $N_{monomer} = (N_{monomer}/A_{eff}) \cdot A_{eff,tot}$. If the polymer solution (as prepared in Chapter Ib) has a monomer concentration $c_{monomer}$, then the volume $V_{polymer}$ of this solution has to be added to the volume V_{QD} of the Q-dot solution: $V_{polymer} = (N_{monomer} / N_A) / c_{monomer}$. In total this leads to:

$$V_{polymer} = (N_{monomer} / N_A) / c_{monomer} = ((N_{monomer}/A_{eff}) \cdot A_{eff,tot} / N_A) / c_{monomer}$$
$$= ((N_{monomer}/A_{eff}) \cdot A_{eff} \cdot N_{QD} / N_A) / c_{monomer}$$
$$= ((N_{monomer}/A_{eff}) \cdot A_{eff} \cdot N_A \cdot c_{QD} \cdot V_{QD} / N_A) / c_{monomer}$$
$$= (N_{monomer}/A_{eff}) \cdot A_{eff} \cdot V_{QD} \cdot c_{QD} / c_{monomer}$$

To give an example: how much volume $V_{polymer}$ of a polymer solution with monomer concentration $c_{monomer}$ has to be added to a solution of Q-dots (Evidot 490) with volume V_{QD} and concentration c_{QD}?

$V_{QD} = 1$ mL; $c_{QD} = 1$ µM; $c_{monomer} = 0.5$ M;

$(N_{monomer}/A_{eff}) = 100$; $A_{eff} = 91.6\ \mathrm{nm}^2$ (all from Table 1)

$$\Rightarrow V_{polymer} = (N_{monomer}/A_{eff}) \cdot A_{eff} \cdot V_{QD} \cdot c_{QD} / c_{monomer}$$
$$= 100 \cdot 91.6\ \mathrm{nm}^2 \cdot 1\ \mathrm{mL} \cdot 1\ \mu\mathrm{M} / 0.5\ \mathrm{M} = 18.4\ \mu\mathrm{L}.$$

Sample	**Evidot® 490**	**Evidot® 520**	**Evidot® 540**	**Evidot® 580**
λ_{em} *[nm]*	480	522	545	579
λ_{abs} *[nm]*	456	500	527	544
$\varepsilon\ [M^{-1}cm^{-1}]$	$4.0\cdot10^4$	$5.0\cdot10^4$	$6.7\cdot10^4$	$1.0\cdot10^5$
d_{dot} *[nm]*	3.2	3.3	3.4	4.4
$d_{dot,eff}$ *[nm]*	5.4	5.5	5.6	6.6
$A_{eff}\ [nm^2]$	91.6	95.0	98.5	136.8
$N_{monomer}/A_{eff}\ [nm^{-2}]$	100	100	100	150
d_{eff} *[nm]*	9.9	12.0	12.4	13.3
N	1.8	9.2	17.4	11.7

Table 1. Properties and determined parameters for the different Q-dot samples used in this study. Enlisted are the following values: emission wavelength λ_{em} of the Q-dots, absorption wavelength of the first exciton peak λ_{abs}[7]; extinction coefficient ε at the first exciton peak of the Q-dots[8]; diameter d_{dot} of the inorganic CdSe/ZnS core[9]; effective diameter $d_{dot,eff}$ of the Q-dots including the hydrophobic surfactant shell around the inorganic cores[10]; effective surface area A_{eff} of one Q-dot before polymer coating[11]; number of monomers of amphiphilic polymer added per surface area of the Q-dots for the polymer coating procedure $N_{monomer}/A_{eff}$; hydrodynamic diameter d_{eff} of the Q-dots after the polymer coating comprising the inorganic core and the amphiphilic polymer shell around the surfactant molecules, cfg. Chapter IIc); number of ATTO-590 dye molecules N per Q-dot (cfg. ChapterIIIc).

---

[7] Both λ_{em} and λ_{abs} were determined experimentally in 0.5X TBE buffer after the Q-dot were polymer-coated (with the plain polymer solution (#3) as described in Chapter Ia, i.e. without ATTO-590 in the polymer) and purified by gel electrophoresis.

[8] As provided by Evident Technology. Their data are based on Ref #4.

[9] As provided by Evident Technology http://www.evidenttech.com/products/Evidots/Evidot490nm.html.

[10] This is the diameter before the polymer-coating. It was determined in the following way: $d_{dot,eff} = d_{dot} + 2.2$ nm. From Evident Technologies company, it is suggested that the thickness of the surfactant layer is about 2.0 nm (http://www.evidenttech.com/products/evidots/evidot490nm.html). In contrast we are assuming twice 1.1 nm for the organic ligands around the inorganic CdSe/ZnS cores cfg. Ref #5.

[11] Calculated as $A_{eff} = 4\pi\cdot(d_{dot,eff}/2)^2)$.

b) Purification

All of the polymer-coated samples were purified with gel electrophoresis using 2% agarose gels (UltraPure, Invitrogen #15510027) in 0.5X TBE buffer (Sigma-Aldrich, #T3913). Before the gel electrophoresis, all of the samples were concentrated by ultrafilters[12] (100 kD molecular weight cut off, Millipore). Then the samples were passed through 0.2 micrometer filters (Millipore) to get rid of aggregates[13]. The polymer-coated Q-dots were loaded at concentration of around 15 µM on the gels. Gel electrophoresis (Powerpac 1000, Bio-Rad) was conducted under 100 V for 100 min and the gel pictures were recorded by a digital camera (Canon Digital Ixus IIs) under the UV light illumination. After running the gels the separated bands of both empty micelles (faster bands on the gel, red color, corresponding to ATTO-590 modified) and particles (slower bands on gels, different colors from green to red, ATTO-590 modified polymer-coated Q-dots) were identified by their fluorescence on a UV illuminated table and then cut from the gels [2]. The Q-dots were extracted from the cut gel pieces by sealing the gel pieces in dialysis membrane tubes (50 kD, Spectrolabs, #132544) and putting them back in the gel electrophoresis set-up. The Q-dots ran out of the gel pieces after applying voltage again for around 15 min[14]. The extracted Q-dot solutions were finally concentrated by the 100 kD ultrafilters (Millipore).

For determining the size of the polymer-coated Q-dots with gel electrophoresis we used 10 nm phosphine-coated gold nanoparticles as the standard size markers[15] (cfg. ref [5]).

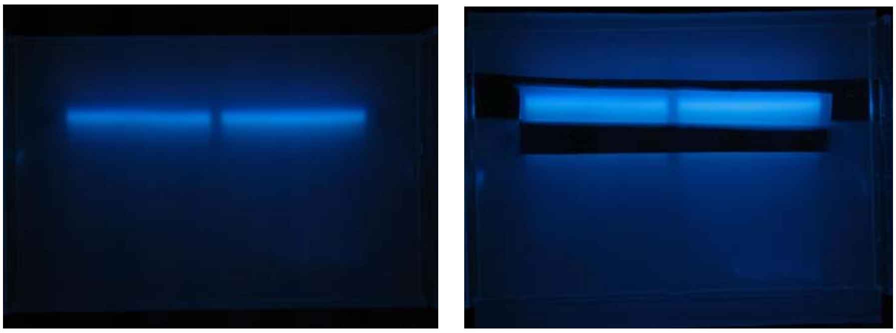

Figure 2. Image of a 2% agarose gel in which polymer-coated Evidot® 490 Q-dots were run (left). The band corresponding to the Q-dots were the cut from the gel (right).

---

[12] Q-dots are too big to pass the semipermeable membrane.

[13] Q-dots can pass the membrane, whereas aggregates are too big to pass, they stick in the filter.

[14] The Q-dots are the trapped in the dialysis membrane tubes as they are too big to pass through the membrane of the dialysis tubes.

[15] The Au samples were prepared as following: commercial gold nanoparticles (British Biocell International) were mixed with triphenyl phosphine (bis(p-sulfonatophenil) phenylphosphine dehydrate, dipotassium salt, (Strem Chemicals 15-0463) by a ratio of 3 mg of triphenyl phosphine molecules per 10 mL gold nanoparticle solution for over 12 hours (ref. #6). The Au nanoparticles were then rinsed and concentrated by using a 100 kD centrifuge filter, whereby 3 mg triphenyl phosphine powder per 50 mL water was used as rinsing-solution.

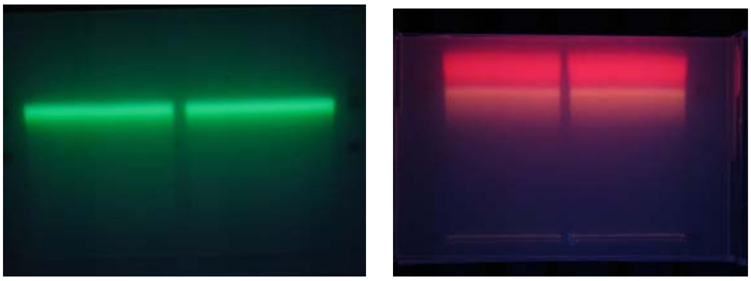

Figure 3. Images of 2% agarose gels in which polymer-coated Evidot® 520 Q-dots (left) and ATTO-590 modified polymer-coated Evidot® 520 Q-dots (right) were run. Due to their negative charge all Q-dots migrate towards to plus-pole. In the right image the 2 bands corresponding to ATTO-590 modified polymer micelles (fast band) and ATTO-590 modified polymer-coated Q-dots (slow band) can be distinguished. For more information see reference[2].

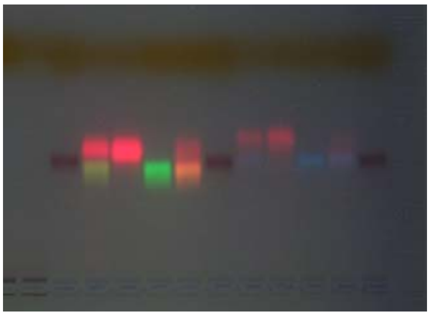

Figure 4: Lanes of different samples on a 2% agarose gel (from left to right): 10 nm phosphine-coated gold, mixture of purified polymer-coated Evidot® 520 Q-dots and purified ATTO-590 modified polymer micelles, purified ATTO-590 modified polymer micelles, purified polymer-coated Evidot® 520 Q-dots, purified ATTO-590 modified polymer-coated Evidot® 520 Q-dots, 10 nm phosphine-coated gold, mixture of purified polymer-coated Evidot® 490 Q-dots and purified ATTO-590 modified polymer micelles, purified ATTO-590 modified polymer micelles, purified polymer-coated Evidot® 490 Q-dots, purified ATTO-590 modified polymer-coated Evidot® 490 Q-dots, 10 nm phosphine-coated gold. The orange band on the top corresponds to orange G, which was added to the loading buffer (glycerol + Orange G).

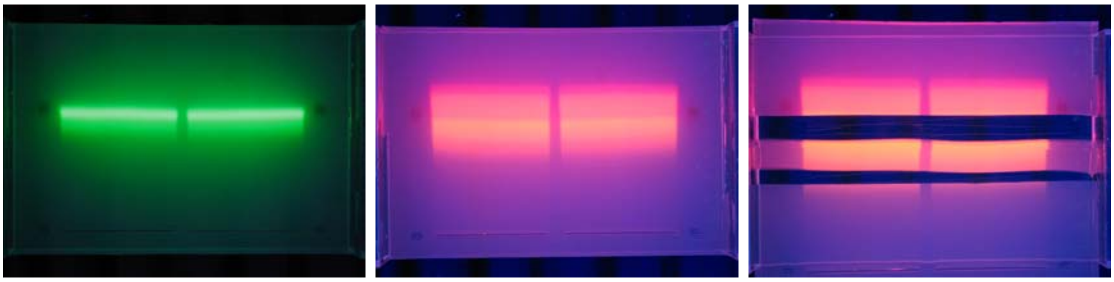

Figure 5. Image of 2% agarose gels in which polymer-coated Evidot® 540 Q-dots (left) and ATTO-590 modified polymer-coated Evidot® 540 Q-dots (middle) were run. In the middle image the 2 bands corresponding to ATTO-590 modified polymer micelles (fast band) and ATTO-590 modified polymer-coated Q-dots (slow band) can be distinguished. In the right image it is shown how the bands were cut out of the gels.

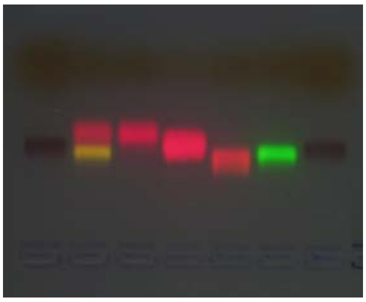

Figure 6: Image of 2% agarose gel in which the purified samples had be run (from left to right): 10 nm phosphine-coated gold, mixture of purified polymer-coated Evidot® 540 Q-dots (EPA band) and purified ATTO-590 modified polymer micelles (PA band), purified ATTO-590 modified polymer micelles (PA band), purified sample cut from the middle between the EPA and PA band, purified ATTO-590 modified polymer-coated Evidot® 540 Q-dots, purified polymer-coated Evidot® 540 Q-dots, 10 nm phosphine-coated gold.

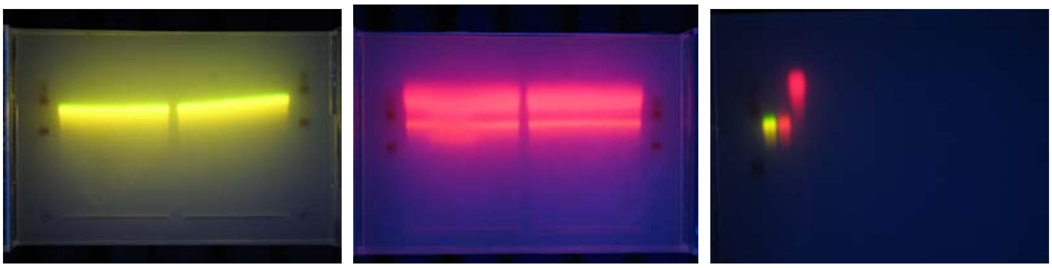

Figure 7. Image of 2% agarose gels in which polymer-coated Evidot® 580 Q-dots (left) and ATTO-590 modified polymer-coated Evidot® 580 Q-dots (middle) were run. In the right image a gel in which purified samples were run on a different gel for a 2nd time is shown (from left to right): 10 nm phosphine-coated gold, purified polymer-coated Evidot® 580 Q-dots, purified ATTO-590 modified polymer-coated Evidot® 580 Q-dots, ATTO-590 modified polymer micelles.

At the end of the purification from each of the Evidot Q-dots (Evidot® 490, Evidot® 520, Evidot® 540, Evidot® 580) four different solutions are available, see Figure 8: a) Polymer-coated Q-dots. This sample is referred to as EP coding for Evidots ("E") with polymer shell ("P"). There is no ATTO-590 dye in the polymer shell. b) ATTO-590 modified polymer-coated Q-dots, i. e. Q-dots with polymer shell in which ATTO-590 is integrated. This sample is referred to as EPA coding for Evidots ("E") with polymer shell ("P") in which ATTO-590 ("A") is integrated. c) ATTO-590 modified polymer micelle. This sample is referred to as PA coding for polymer shell ("P") in which ATTO-590 ("A") is integrated. d) Mix sample: the mixture of polymer-coated Q-dots (EP sample) and ATTO-590 modified polymer micelles (PA sample).

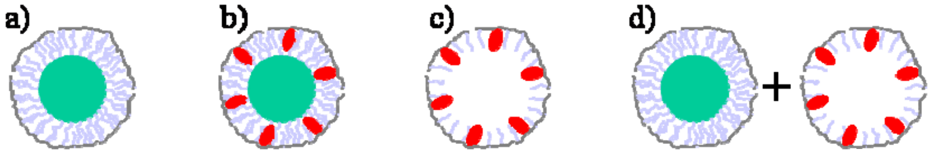

Figure 8. a) Polymer-coated Q-dot (EP sample). b) ATTO-590 modified polymer-coated Q-dot (EPA sample). c) ATTO-590 modified polymer micelle (PA sample). d) Mixture of the EP and PA sample (Mix sample).

c) Determination of the hydrodynamic diameter

The hydrodynamic diameters of the polymer-coated Evidots were determined by gel electrophoresis [5]. Due to their negative charge, the polymer-coated nanoparticles migrate towards the positive electrode. All the samples were run on the same 2% agarose gel with 10 nm phosphine-coated gold nanoparticles as reference. The position of the bands on the gel was then recorded by taking a digital photograph of the gel. For imaging the gels were put on an UV illuminated table during the photographing procedure. Then the running length L_{Evidot} was determined for each sample starting from the position of loading. In previous work we made a calibration curve which relates the relative mobilities ($m_{particle}/m_{10nm}$) to the effective diameters (d_{eff}) for 2% agarose gels [7]:

$$d_{eff} = -37.7 \cdot \ln(m_{Evidot} / m_{10nm} / 1.12) + 6\ nm$$

Hereby the relative mobilities m of the samples were derived from the running lengths L, whereby 10 nm phosphine coated Au was used as reference:

$$m_{Evidot} / m_{10nm} = L_{Evidot} / L_{10nm}$$

In other words: L is the migration length from the final position of the band on the gel to the position where the particles have been loaded into the gel. The relative migration lengths were obtained by normalization with respect to the migration length of 10 nm phosphine-coated Au particles (L_{10nm}).

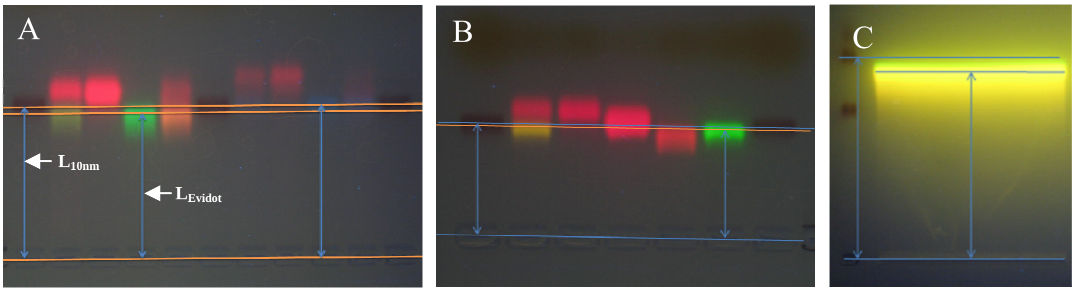

Figure 9. Hydrodynamic diameters derived from gel electrophoresis: A) In the 1st, 6th and 11th lane 10 nm phosphine-coated gold nanoparticles as standard marker are run, 2nd lane: Mix of ATTO-590 modified polymer micelles and polymer-coated Evidot® 520 Q-dots, 3rd lane: ATTO-590 modified polymer micelles (PA sample), 4th lane: polymer-coated Evidot® 520 Q-dots (EP sample), 5th lane: ATTO-590 modified polymer-coated Evidot® 520 A-dots (EPA sample), from 7th lane to 10th lane: Mix, PA, EP and EPA samples of Evidot® 490 Q-dots. B) The 1st and 7th lanes show 10 nm phosphine-coated gold nanoparticles as standard markers, from the 2nd land to 5th lane the following samples are shown: Mix, PA, band between PA and EPA, EPA, EP samples of Evidot® 540 Q-dots. C) The 1st lane (barely visible) shows a mixture of 5 nm, 10 nm and 15 nm phosphine-coated gold particles as standard markers, the 2nd lane displays polymer-coated Evidot® 580 Q-dots (EP sample).

Sample	**Evidot® 490**	**Evidot® 520**	**Evidot® 540**	**Evidot® 580**
L_{Evidot} [cm]	9.1	8.6	3.5	5.9
L_{10nm} [cm]	9.0	9.0	3.7	6.4
L_{Evidot} / L_{10nm}	1.01	0.96	0.95	0.92
d_{eff} [nm]	9.9	12.0	12.37	13.34

Table 2: Calculation of hydrodynamic diameters of polymer-coated Evidot Q-dots, as derived from gel electrophoresis. All of the lengths (L) were measured from data similar shown to the ones in Figure 9.

III. Photophysical characterization

a) Absorption and concentration determination

For a first photophysical characterization UV/vis spectra of the polymer-coated Q-dot samples were recorded. All absorption spectra were obtained from a UV/vis spectrometer (Agilent) by using disposable plastic cuvettes (Eppendorf, #2531). In this work we used 4 kinds of Evidot Q-dots with different diameters as indicated in Table 1. From each of the different Q-dots we have prepared 4 different samples with approximately similar concentrations[16] (cfg. Figure 8).

1) Evidot Q-dots coated with ATTO-590 modified polymer[17] (EPA sample)
2) Evidot Q-dots coated with polymer (EP sample)
3) ATTO-590 modified polymer micelles (PA sample)
4) A mixture of the EP and PA sample (Mix)
Examples are presented in Figures 10 and 11.

The Lambert-Beer law $A = \varepsilon \cdot c \cdot d$ (extinction coefficient $\varepsilon = \varepsilon(\lambda)$, absorption $A = A(\lambda)$) correlates the absorption A with the extinction coefficient ε, which both depend on the wavelength λ. For a sample with concentration c in a cuvette of pathlength d the wavelength-dependent extinction coefficient is given by the measured wavelength-dependent absorption $A(\lambda) = \varepsilon(\lambda) \cdot c \cdot d$. This means:

$$\varepsilon(\lambda_2) = \varepsilon(\lambda_1) \cdot A(\lambda_2)/A(\lambda_1)$$

From the absorption spectrum of the PA sample (see Fig. 11 i), we can see an absorption minimum at 450 nm in the range between 400 nm and 500 nm. For the PA sample shown in Fig. 11-i) A(450 nm) is 0.0054, and A(597 nm) is 0.9431, so the molar extinction coefficient of ATTO-590 at 450 nm can be derived as

$$\varepsilon(450\text{ nm}) = \varepsilon(597\text{ nm}) \cdot A(450\text{ nm})/A(597\text{ nm}) = \varepsilon(597\text{ nm}) \cdot 0.006$$
$$= 120{,}000\ \mathrm{M^{-1}cm^{-1}} \cdot 0.006 \approx 690\ \mathrm{M^{-1}cm^{-1}}.$$

---

[16] Samples were adjusted so that they had similar concentration of Evidot Q-dots and ATTO-590 dye.

[17] In the whole study the ATTO-590 modified polymer contained ATTO-590 dye was synthesized to that 2% of the anhydride rings of the polymer were occupied with ATTO-590, cfg. Chapter Ib.

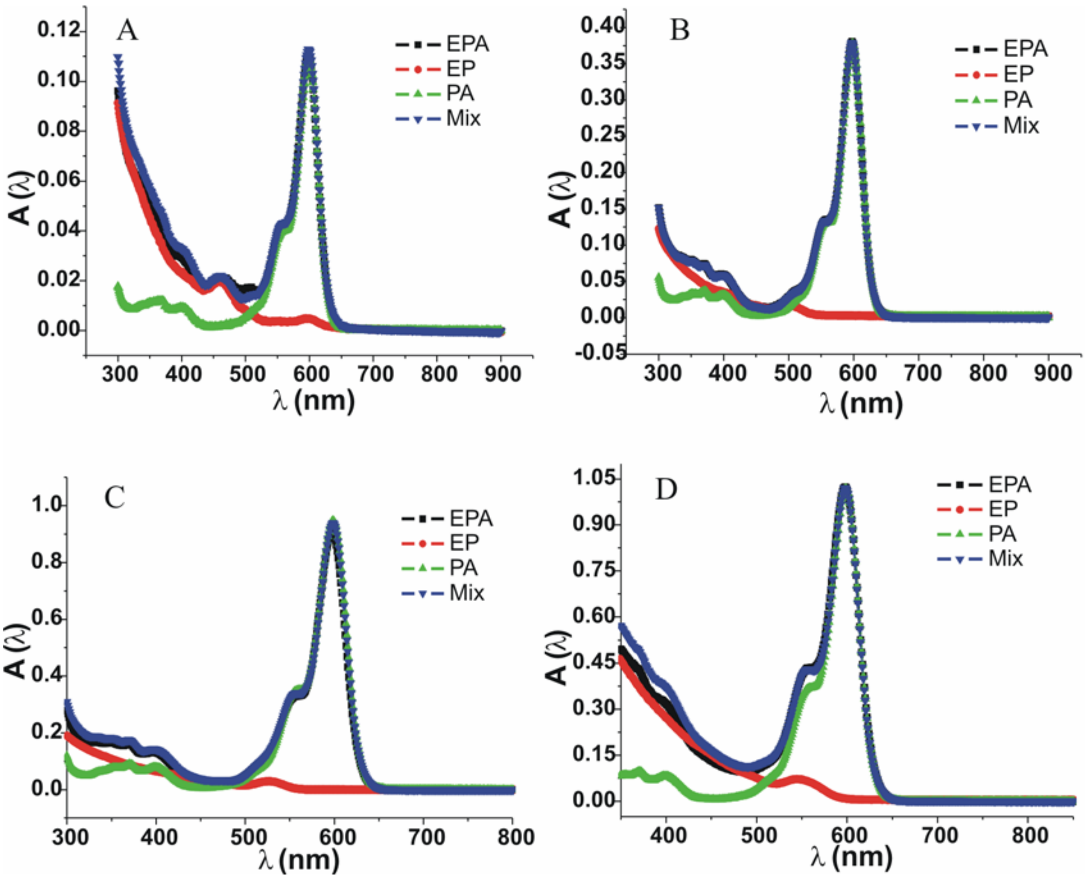

Figure 10. Four sets of Evidot Q-dot samples with the same adjusted concentrations. A) Evidot® 490, B) Evidot® 520, C) Evidot® 540, D) Evidot® 580. EPA: purified ATTO-590 modified polymer-coated Q-dots, EP: purified polymer-coated Q-dots, PA: purified ATTO-590 modified polymer-coated polymer micelles, and Mix: EP mixed with PA. In all of the four sets of samples, the EPA, EP and Mix samples have the same Q-dot concentration and the EPA, PA, and Mix samples have the same ATTO-590 concentration. From all spectra we manually subtracted the mean offset from 850 nm to 900 nm.

In a similar way the absorption for the EP sample (see Fig. 11-ii) is given by A(450 nm) = 0.0339 and A(527 nm) = 0.0303. Therefore the molar extinction coefficient for the Evidot® 540 Q-dots at 450 nm can be derived as

$$\varepsilon(450\text{nm}) = \varepsilon(527\text{ nm}) \cdot A(450\text{ nm})/A(527\text{ nm}) = \varepsilon(527\text{ nm}) \cdot 1.119$$
$$= 6.7 \cdot 10^4\text{ M}^{-1}\text{cm}^{-1} \cdot 1.119 \approx 7.5 \cdot 10^4\text{ M}^{-1}\text{cm}^{-1}.$$

Because of the very different extinction coefficients at 450 nm the absorption of PA (ATTO-590: ε(450 nm) = 690 $\text{M}^{-1}\text{cm}^{-1}$) can be neglected compared to the absorption of the EP and EPA samples (Evidot® 540 Q-dots: ε(450 nm) = $7.5 \cdot 10^4\text{ M}^{-1}\text{cm}^{-1}$). Therefore the EP and EPA samples can be adjusted to have the same Q-dot concentration by diluting them in a way that both samples have the same absorption at 450 nm (cfg. Fig. 11-iv). The contribution of the ATTO-590 dye in the absorption of the EPA sample at 597 nm can be derived by subtracting the absorption A(597 nm) of the EP sample from the absorption of the EPA sample:

$$
\begin{aligned}
A(597\text{ nm, ATTO-590 in EPA}) &= A(597\text{ nm, EPA}) - A(597\text{ m, EP}) \\
&= 0.9049 - 0.0008 = 0.9041.
\end{aligned}
$$

Now the PA sample can be brought to the same ATTO-590 concentration as the EPA sample by diluting the PA sample to have the absorption of A(597 m) = 0.9041 (cfg. Fig. 11-v).

In this way the ATTO-590 concentrations in the EPA and PA sample can be adjusted to be similar within an error of ± 5%. For the Mix sample, the double concentrated PA sample and the double concentrated EP sample are mixed in the ratio 1:1 (vol:vol), cfg. Fig. 11-vi).

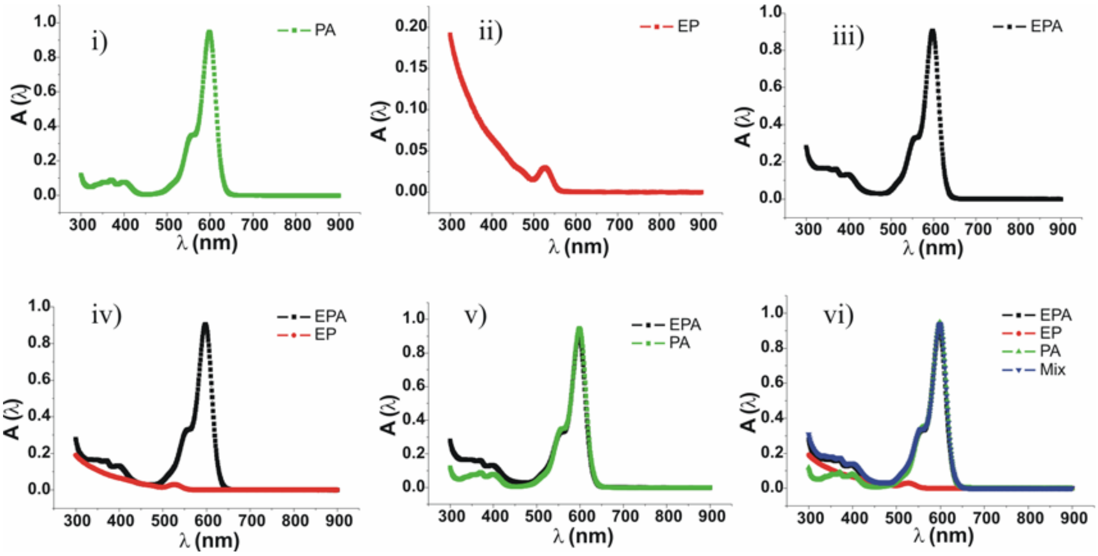

Figure 11. Example for adjusting the concentration of the set of Evidot® 540 Q-dots (4 samples). i) PA sample, ii) EP sample, iii) EPA sample, iv) EPA and EP samples with similar Q-dot concentration (see same absorption for wavelengths < 500 nm), v) EPA and PA samples with similar ATTO-590 concentration (see same absorption at 597 nm), EPA, EP, PA, and Mix samples with same Q-dot and ATTO-590 concentration.

b) Fluorescence measurements

All Q-dot samples (EP, EPA, PA, Mix) were brought to similar concentrations (cfg. Chapter IIIa) and the fluorescence spectra were recorded. The steady fluorescence spectra were obtained on a Fluorolog®-3 spectrometer. Each sample was recorded with excitations at 450 nm and 590 nm, except for the Evidot®490 samples with excitations at 400 nm and 590 nm. The results are shown in Figure 12.

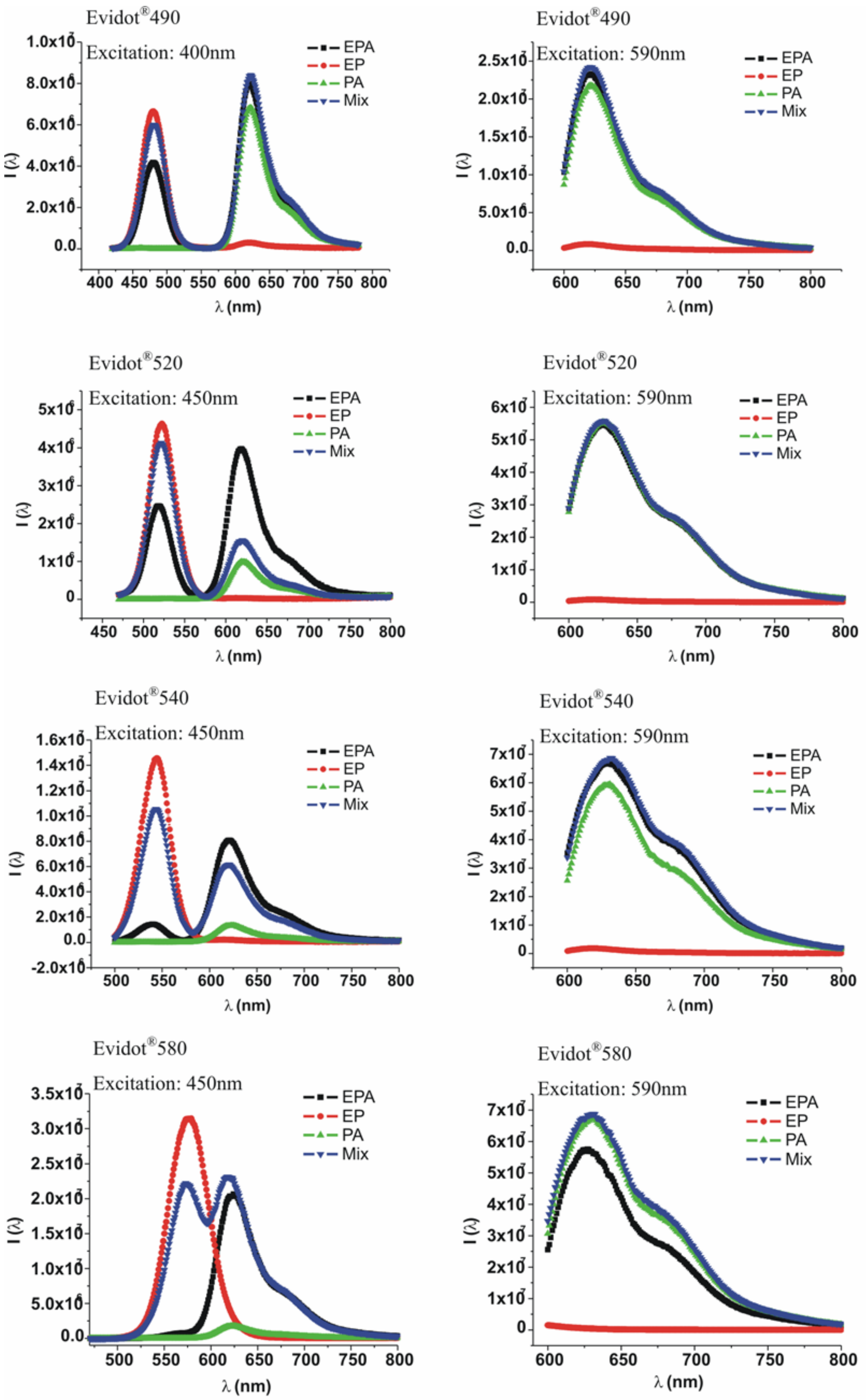

Figure 12. Fluorescence spectra of the different Q-dot samples. The excitation wavelengths are indicated in each graph.

c) Number of ATTO molecules per nanoparticle

For the calculation of the number of ATTO-590 molecules per Evidot Q-dot the absorption spectra shown in Chapter IIIa are used. Each EPA sample contains as much Q-dots as the corresponding EP sample and as much ATTO-590 molecules as the corresponding PA sample, as the PA, EP, and EPA samples for each type of Evidot were adjusted to the same concentration. Therefore the concentrations can be directly determined from the absorption spectra:

N = Number of ATTO-590 molecules per Evidot
= concentration of ATTO-590 in the PA sample divided by the concentration of Q-dots in the EP sample
= c(ATTO-590) / c(Q-dot)

c(ATTO-590) = A(597 nm) / (ε(597 nm) · d)
whereby A(597 nm) is the absorption of the PA sample at 597 nm, ε(597 nm) = 120,000 $M^{-1}cm^{-1}$ the extinction coefficient of ATTO-590 at 597 nm, and d = 1 cm the pathlength of the cuvette.

c(Q-dot) = $A(\lambda_{abs}) / (\varepsilon(\lambda_{abs}) \cdot d)$
whereby $A(\lambda_{abs})$ is the absorption of the EP sample at the first exciton peak λ_{abs} (cfg. Table 1), $\varepsilon(\lambda_{abs})$ the extinction coefficient of the Q-dots at the first exciton peak λ_{abs} (cfg. Table 1), and d = 1 cm the pathlength of the cuvette.

The values are enlisted in Table 3.

Name of sample	Evidot® 490	Evidot® 520	Evidot® 540	Evidot® 580
A(597 nm) of PA	0.11	0.38	0.94	1.01
ε(597 nm) $[M^{-1}cm^{-1}]$ *of PA*	120,000	120,000	120,000	120,000
c(ATTO-590) [µM]	0.90	3.14	7.86	8.45
$A(\lambda_{abs})$ *of EP*	0.0204	0.0170	0.0303	0.0723
$\varepsilon(\lambda_{abs})$ $[M^{-1}cm^{-1}]$ *of EP*	$4.0 \cdot 10^4$	$5.0 \cdot 10^4$	$6.7 \cdot 10^4$	$1.0 \cdot 10^5$
c(Q-dot) [µM]	0.51	0.34	0.45	0.72
N	1.77	9.23	17.4	11.7

Table 3. Calculation of number of ATTO-590 molecules per Q-dot for the 4 types of EPA samples.

IV. Kinetic model

a. CdSe/ZnS dots with polymer shell

To describe the Q-dot decay one can use a straightforward kinetic model including the Q-dot life time as well as an energy transfer channel from feeding states:

$$\frac{dn_{QD}}{dt} = -\frac{n_{QD}}{\tau_{QD}} + w_c \cdot n_t \tag{1}$$

Here n_{QD} *and* n_t are the occupation numbers of the bright exciton states and the feeding (trap) states, respectively, τ_{QD} is the QD radiative life time and w_c the probability for an excitation transfer from the feeding states to the bright quantum dot states. The solution is a bi-exponential function with τ_t being the lifetime of the feeding states ($n_t = n_0 \cdot \exp\left(-t/\tau_t\right)$):

$$n_{QD}(t) = n_{QD}^{a} \cdot \exp\left(-\frac{t}{\tau_{QD}}\right) + n_{QD}^{b} \cdot \exp\left(-\frac{t}{\tau_t}\right) \tag{2}$$

The weighting factors $n_{QD}{}^{a}$ and $n_{QD}{}^{b}$ are:

$$n_{QD}^{a} = n_{QD}^{0} - \frac{n_t^0 \cdot \tau_{QD} \cdot \tau_{trap} \cdot w_c}{\tau_t - \tau_{QD}} \tag{3}$$

$$n_{QD}^{b} = \frac{n_t^0 \cdot \tau_{QD} \cdot \tau_t \cdot w_c}{\tau_t - \tau_{QD}} \tag{4}$$

b. Dot – dye mixture

The respective differential equation for the dye decay including the reabsorption probability w_{reab} by the dye molecules and the number of the excited Q-dots n_{QD} is given by:

$$\frac{dn_{dye}}{dt} = -\frac{n_{dye}}{\tau_{dye}} + w_{reab} \cdot n_{QD} \tag{5}$$

The solution is a sum of three exponential functions

$$n_{dye}(t) = n_{dye}^{a} \cdot \exp\left(-\frac{t}{\tau_{dye}}\right) + n_{dye}^{b} \cdot \exp\left(-\frac{t}{\tau_{QD}}\right) + n_{dye}^{c} \cdot \exp\left(-\frac{t}{\tau_{t}}\right) \tag{6}$$

with the weighting factors $n_{dye}{}^{a,b,c}$:

$$n_{dye}^{a} = n_{dye}^{0} - n_{QD}^{0} \cdot w_{reab} \cdot \frac{\tau_{dye} \cdot \tau_{QD}}{\tau_{QD} - \tau_{dye}} + n_{trap}^{0} \cdot w_{reab} \cdot w_{c} \cdot \frac{\tau_{QD} \cdot \tau_{t} \cdot \tau_{dye}^{2}}{(\tau_{QD} - \tau_{dye})(\tau_{t} - \tau_{dye})} \tag{7}$$

$$n_{dye}^{b} = n_{QD}^{0} \cdot w_{reab} \cdot \frac{\tau_{dye} \cdot \tau_{QD}}{\tau_{QD} - \tau_{dye}} - n_{t}^{0} \cdot w_{reab} \cdot w_{c} \cdot \frac{\tau_{dye} \cdot \tau_{t} \cdot \tau_{QD}^{2}}{(\tau_{QD} - \tau_{dye})(\tau_{t} - \tau_{QD})} \tag{8}$$

$$n_{dye}^{c} = n_{t}^{0} \cdot w_{reab} \cdot w_{c} \cdot \frac{\tau_{dye} \cdot \tau_{QD} \cdot \tau_{t}^{2}}{(\tau_{t} - \tau_{dye})(\tau_{t} - \tau_{QD})} \tag{9}$$

c.Dot – dye hybrids

Non-radiative transfer processes (FRET) of the excitation energy from the Q-dot to the dye molecules establish additional relaxation channels, yielding the acceleration of the Q-dot photoluminescence decay. With w_{FRET} being the Förster-like dipole-dipole transfer probability the rate equation and respective solution read:

$$\frac{dn_{QD}}{dt} = -\frac{n_{QD}}{\tau_{QD}} - w_{FRET} \cdot n_{QD} + w_c \cdot n_t = -\frac{n_{QD}}{\tau_{QD}^{eff}} + w_c \cdot n_t \tag{10}$$

$$n_{QD}(t) = n_{QD}^{a} \cdot \exp\left(-\frac{t}{\tau_{QD}^{eff}}\right) + n_{QD}^{b} \cdot \exp\left(-\frac{t}{\tau_t}\right) \tag{11}$$

with the according weighting factors $n_{QD}{}^{a,b}$:

$$n_{QD}^{a} = n_{QD}^{0} - \frac{n_t^0 \cdot \tau_{QD}^{eff} \cdot \tau_t \cdot w_c}{\tau_t - \tau_{QD}^{eff}} \tag{12}$$

$$n_{QD}^{b} = \frac{n_t^0 \cdot \tau_{QD}^{eff} \cdot \tau_t \cdot w_c}{\tau_t - \tau_{QD}^{eff}} \tag{13}$$

The decay of the dye luminescence is given by Eq. 3 and Eq. 4 but replacing the Q-dot life time τ_{QD} by the effective time $\tau^{eff}{}_{QD}$:

$$\frac{dn_{dye}}{dt} = -\frac{n_{dye}}{\tau_{dye}} + w_{reab} \cdot n_{QD} \tag{14}$$

$$n_{dye}(t) = n_{dye}^{a} \cdot \exp\left(-\frac{t}{\tau_{dye}}\right) + n_{dye}^{b} \cdot \exp\left(-\frac{t}{\tau_{QD}^{eff}}\right) + n_{dye}^{c} \cdot \exp\left(-\frac{t}{\tau_t}\right) \tag{15}$$

And the weighting factors $n_{dye}{}^{a,b,c}$ are:

$$n_{dye}^{a} = n_{dye}^{0} - n_{QD}^{0} \cdot w_{reab} \cdot \frac{\tau_{dye} \cdot \tau_{QD}^{eff}}{\tau_{QD}^{eff} - \tau_{dye}} + n_{trap}^{0} \cdot w_{reab} \cdot w_{c} \cdot \frac{\tau_{QD}^{eff} \cdot \tau_{t} \cdot \tau_{dye}^{2}}{(\tau_{QD}^{eff} - \tau_{dye})(\tau_{t} - \tau_{dye})} \tag{16}$$

$$n_{dye}^{b} = n_{QD}^{0} \cdot w_{reab} \cdot \frac{\tau_{dye} \cdot \tau_{QD}^{eff}}{\tau_{QD}^{eff} - \tau_{dye}} - n_{t}^{0} \cdot w_{reab} \cdot w_{c} \cdot \frac{\tau_{dye} \cdot \tau_{t} \cdot \tau_{QD}^{eff\,2}}{(\tau_{QD}^{eff} - \tau_{dye})(\tau_{t} - \tau_{QD}^{eff})} \tag{17}$$

$$n_{dye}^{c} = n_{t}^{0} \cdot w_{reab} \cdot w_{c} \cdot \frac{\tau_{dye} \cdot \tau_{QD}^{eff} \cdot \tau_{t}^{2}}{(\tau_{t} - \tau_{dye})(\tau_{t} - \tau_{QD}^{eff})} \tag{18}$$

d. Fitting

All time traces in the paper have been fitted by a least square fit of the exponentially weighted data points (using MatLab® 7.0.1).

The dye emission decay in solution a (PA) was fitted according to a single exponential decay:

$$n_{dye}(t) = n_{dye}^{a} \cdot \exp\left(- {t}/{\tau_{dye}} \right) \tag{19}$$

with n^{a}_{dye} and τ_{dye} being free parameters for the fit.

The decay of the Q-dot PL intensity in solution b (EP) was described by Eq. 2 with the fitting parameters τ_{QD}, τ_t, n^{a}_{QD} and n^{b}_{QD}.

Eq. 2 was also used to fit the Q-dot emission decay in solution c (mix) but with fixed τ_{QD} and τ_t values, determined from solution b. The solely fitting parameters are n^{a}_{QD} and n^{b}_{QD}. The dye transient in solution c (mix) was fitted by Eq. 6 with the fitting parameters n^{a}_{dye}, n^{b}_{dye} and n^{c}_{dye}.

The PL decay of the Q-dots in solution d (EPA) was described by Eq. 11 with the fitting parameters n^{a}_{QD}, n^{b}_{QD} and τ^{eff}_{QD}. The respective dye decay of solution d was fitted by means of Eq. 15 with the free parameters n^{a}_{dye}, n^{b}_{dye} and n^{c}_{dye}.

e. Determination of FRET and reabsorption ratio

The total transfer L in the presence of dye molecules in the polymer shell can be determined from the measured PL intensities of the solutions b (EP) and d (EPA):

$$L = \frac{I_b - I_{d-QD}}{I_b} \tag{20}$$

However, the number of photons I_b emitted by the Q-dots without any dye molecules (i. e. EP sample) is also given by:

$$I_b = \int_0^{\infty} \frac{n_{QD}(t)}{\tau_{QD}} dt = n_0 \tag{21}$$

with a single exponential decay of the number of excited states $n_{QD}(t) = n_0 \cdot \exp\left(-{}^{t}\!/_{\tau_{QD}}\right)$.

This number is reduced by embedding ATTO-590 dye molecules into the polymer shell of the Q-dots due to FRET and the absorption factor of the dye molecules:

$$I_{d-QD} = (1-a) \cdot \int_0^{\infty} \frac{n_0}{\tau_{QD}} \cdot \exp\left(-\frac{t}{\tau_{QD}^{eff}}\right) dt = \frac{n_0}{1 + w_{FRET} \cdot \tau_{QD}} \cdot (1-a) \tag{22}$$

The total transfer L is the sum of reabsorption a and radiationless transfer f:

$$L = a + f = 1 - \frac{(1-a)}{1 + w_{FRET} \cdot \tau_{QD}} = \frac{w_{FRET} \cdot \tau_{QD} + a}{1 + w_{FRET} \cdot \tau_{QD}} \tag{23}$$

Now it is possible to extract the contributions of absorption and non-radiative transfer:

$$a = L - w_{FRET} \cdot \tau_{QD} \cdot (1-L) \tag{24}$$

$$f = w_{FRET} \cdot \tau_{QD} \cdot (1-L) \tag{25}$$

References:

1. Lin, C.-A.J., et al., *Design of an amphiphilic polymer for nanoparticle coating and functionalization.* Small, 2008. **4**(3): p. 334-341.
2. Fernández-Argüelles, M.T., et al., *Synthesis and characterization of polymer-coated quantum dots with integrated acceptor dyes as FRET-based nanoprobes.* NanoLetters, 2007. **7**(9): p. 2613-2617.
3. Yakovlev, A.V., et al., *Wrapping Nanocrystals with an Amphiphilic Polymer Preloaded with Fixed Amounts of Fluorophore Generates FRET-Based Nanoprobes with a Controlled Donor/Acceptor Ratio.* Langmuir, 2009. **25**(5): p. 3232-3239.
4. Yu, W.W., et al., *Experimental Determination of the Extinction Coefficient of CdTe, CdSe, and CdS Nanocrystals.* Chemistry of Materials, 2003. **15**(14): p. 2854-2860.
5. Sperling, R.A., et al., *Size determination of (bio-) conjugated water-soluble colloidal nanoparticles - a comparison of different techniques.* Journal of Physical Chemistry C, 2007. **111** (31): p. 11552 -11559.
6. Zanchet, D., et al., *Electrophoretic isolation of discrete Au nanocrystal/DNA conjugates.* Nanoletters, 2001. **1**(1): p. 32-35.
7. Pellegrino, T., et al., *Gelelectrophoresis of Gold-DNA Nanoconjugates.* Journal of Biomedicine and Biotechnology, 2007. **2007**: p. 1-9.

Wrapping Nanocrystals with an Amphiphilic Polymer Preloaded with Fixed Amounts of Fluorophore Generates FRET-Based Nanoprobes with a Controlled Donor/Acceptor Ratio

Aleksey V. Yakovlev,[†,‡,§,||,○] Feng Zhang,[⊥,○] Ali Zulqurnain,[⊥] Abbasi Azhar-Zahoor,[⊥]
Camilla Luccardini,[†,‡,§,||] Stéphane Gaillard,[#] Jean-Maurice Mallet,[#] Patrick Tauc,[∇]
Jean-Claude Brochon,[∇] Wolfgang J. Parak,[*,⊥] Anne Feltz,[*,||] and Martin Oheim[*,†,‡,§]

INSERM, U603, Paris F-75006, France, CNRS UMR 8154, Paris F-75006, France, Laboratory of Neurophysiology and New Microscopies, University Paris Descartes, 45 rue des Saints Pères, Paris F-75006, France, ENS-CNRS, UMR 8544, Laboratoire de Neurobiologie, Département de Biologie, Ecole Normale Supérieure, 46 rue d'Ulm, Paris F-75005, France, Department of Physics, Biophotonics, Philipps University of Marburg, Renthof 7, Marburg D-35037, Germany, ENS-CNRS, UMR 8642, Glycoscience, Département de Chimie, Ecole Normale Supérieure, 24 rue Lhomond, Paris F-75231, France, and ENS-CNRS, UMR 8113, Laboratoire de Biotechnologies et Pharmacologie génétique Appliquée (LBPA), Ecole Normale Supérieure de Cachan, 61 avenue du President Wilson, Cachan F-94235, France

Received November 19, 2008. Revised Manuscript Received December 22, 2008

Colloidal nanocrystal (NC) donors wrapped with a polymer coating including multiple organic acceptor molecules are promising scaffolds for fluorescence resonance energy transfer (FRET)-based nanobiosensors. Over other self-assembling donor−acceptor configurations, our preloaded polymers have the virtue of producing compact assemblies with a fixed donor/acceptor distance. This property, together with the possibility of stoichiometric polymer loading, allowed us to directly address how the FRET efficiency depended on the donor/acceptor. At the population level, nanoprobes based on commercial as well as custom CdSe/ZnS donors displayed the expected dose-dependent rise in transfer efficiency, saturating from about five ATTO dyes/NC. However, for a given acceptor concentration, both the intensity and lifetime of single-pair FRET data revealed a large dispersion of transfer efficiencies, highlighting an important heterogeneity among nominally identical FRET-based nanoprobes. Rigorous quality check during synthesis and shell assembly as well as postsynthesis sorting and purification are required to make hybrid semiconductor−organic nanoprobes a robust and viable alternative to organic or genetically encoded nanobiosensors.

Introduction

With their large absorbance permitting blue-shifted excitation remote from acceptor direct excitation, size-dependent tunable narrow emission, longer excited-state lifetime, and better photostability compared to organic chromophores, semiconductor nanocrystals (NCs) are potent donors for building fluorescence resonance energy transfer (FRET)-based nanoprobes.[1−7] Such nanosensors have been successfully used to detect toxins,[8] probe enzymatic activity,[9] screen for enzyme inhibitors,[10] or measure ion concentration.[11−13] In addition to offering new possibilities for ultrasensitive analyte detection, functionalized NCs provide an ideal platform for the attachment of multiple fluorophores, thereby increasing the FRET efficiency[2,4,12,14−17] or permitting the design of polyvalent sensors through acceptor multiplexing.[8,13,17,18]

In the past, nanoprobe assembly has typically involved a compromise between sensor performance and colloidal stability (reviewed in refs 19 and 20). Compact donor/acceptor assemblies

---

[*] Corresponding authors. E-mail: anne.feltz@ens.fr (A.F.); martin.oheim@univ-paris5.fr (M.O.); wolfgang.parak@physik.uni-marburg.de (W.J.P.)

[†] INSERM, U603.

[‡] CNRS UMR 8154.

[§] University Paris Descartes.

[||] ENS-CNRS, UMR 8544, Laboratoire de Neurobiologie, Département de Biologie.

[⊥] Philipps University of Marburg.

[#] ENS-CNRS, UMR 8642, Glycoscience, Département de Chimie.

[∇] ENS-CNRS, UMR 8113, Laboratoire de Biotechnologies et Pharmacologie génétique Appliquée (LBPA).

[○] These authors contributed equally.

(1) Willard, D. M.; Carillo, L. L.; Jung, J.; Van Orden, A. *Nano Lett.* **2001**, *1*, 469–474.
(2) Tran, P. T.; Goldman, E. R.; Anderson, G. P.; Mauro, J. M.; Mattoussi, H. *Phys. Status Solidi B* **2002**, *229*, 427–432.
(3) Medintz, I. L.; Goldman, E. R.; Lassman, M. E.; Mauro, J. M. *Bioconjugate Chem.* **2003**, *14*(5), 909–918.
(4) Clapp, A. R.; Medintz, I. L.; Mauro, J. M.; Fisher, B. R.; Bawendi, M. G.; Mattoussi, H. *J. Am. Chem. Soc.* **2004**, *126*(1), 301–310.
(5) Alphandéry, E.; Walsh, L. M.; Rakovich, Y.; Bradley, A. L.; Donegan, J. F.; Gaponik, N. *Chem. Phys. Lett.* **2004**, *388*, 100–104.
(6) Fernandez-Arguelles, M. T.; Yakovlev, A.; Sperling, R. A.; Luccardini, C.; Gaillard, S.; Medel, A. S.; Mallet, J. M.; Brochon, J. C.; Feltz, A.; Oheim, M.; Parak, W. J. *Nano Lett.* **2007**, *7*(9), 2613–2617.
(7) Lu, H.; Schöps, O.; Waggon, U.; Niemeyer, C. M. *J. Am. Chem. Soc.* **2008**, *130*, 4815–4827.
(8) Goldman, E. R.; Clapp, A. R.; Anderson, G. P.; Uyeda, H. T.; Mauro, J. M.; Medintz, I. L.; Mattoussi, H. *Anal. Chem.* **2004**, *76*, 684–688.
(9) Xu, C.; Xing, B.; Rao, J. *Biochem. Biophys. Res. Commun.* **2006**, *344*, 931–935.
(10) Shi, F.; Rosenzweig, N.; Roszenzweig, Z. *Anal. Chem.* **2007**, *79*, 208–214.
(11) Snee, P. T.; Somers, R. C.; Nair, G.; Zimmer, J. P.; Bawendi, M. G.; Nocera, D. G. *J. Am. Chem. Soc.* **2006**, *128*(41), 13320–13321.
(12) Pons, T.; Medintz, I. L.; Wang, X.; English, D. S.; Mattoussi, H. *J. Am. Chem. Soc.* **2006**, *128*(47), 15324–15331.
(13) Suzuki, M.; Husimi, Y.; Komatsu, H.; Suzuki, K.; Douglas, K. T. *J. Am. Chem. Soc.* **2008**, *130*(17), 5720–5725.
(14) Patolsky, F.; Gill, R.; Weizmann, Y.; Mokari, T.; Banin, U.; Willner, I. *J. Am. Chem. Soc.* **2003**, *125*(46), 13918–13919.
(15) Kim, J. H.; Stephens, J. P.; Morikis, D.; Ozkan, M. *Sens. Lett.* **2004**, *2*, 85–90.
(16) Levy, M.; Cater, S. F.; Ellington, A. D. *ChemBioChem* **2005**, *6*, 2163–2166.
(17) Medintz, I. L.; Clapp, A. R.; Brunel, F. M.; Tiefenbrunn, T.; Uyeda, H. T.; Chang, E. L.; Deschamps, J. R.; Dawson, P. E.; Mattoussi, H. *Nat. Mater.* **2006**, *5*(7), 581–589.
(18) Clapp, A. R.; Medintz, I. L.; Uyeda, H. T.; Fisher, B. R.; Goldman, E. R.; Bawendi, M. G.; Mattoussi, H. *J. Am. Chem. Soc.* **2005**, *127*, 18212–18221.
(19) Medintz, I. L. *Trends Biotechnol.* **2006**, *24*(12), 539–542.

10.1021/la8038347 CCC: $40.75

favor high FRET efficiencies, but additional coating layers increasing their effective size have to be introduced to preserve solubility and colloidal stability. Also, polyethylene glycol (PEG), which is widely used for this purpose,[21,22] introduces a microenvironment that may restrict the access of the analyte to the acceptor on the NC surface. Conversely, the *post hoc* attachment of the acceptor to the already coated and functionalized NC considerably increases donor/acceptor separation and impairs FRET efficiency.

A factor that has limited sensor performance is that acceptor binding and NC coating have been usually considered as two independent steps. By far, most sensor geometries have in common that FRET is modulated by reversibly or irreversibly displacing the acceptor from the NC donor.[10,17] More recently, a pH sensitive donor/acceptor FRET pair has been described where the acceptor is tethered on the NC surface and analyte binding/unbinding modulates the overlap integral between donor photoluminescence (PL) emission and acceptor excitation and thus modifies the FRET efficiency.[11,13] However, upon analyte binding, most fluorescent indicators change fluorescence through a modulation of their quantum efficiency rather than their absorbance. Thus, in hybrid FRET-based nanoprobes built from such probes, the amount of acceptor fluorescence varies with analyte concentration, but the transfer efficiency is actually constant.

To benefit from the large spectrum of available ion indicators and purpose-tailored fluorescent probes, we designed FRET sensors that incorporate the acceptor directly into an amphiphilic polymer coating. We have previously shown that these probes minimize the acceptor/donor distance, thus permit high transfer efficiencies, and outperform conventional sensors in which the acceptor is added *post hoc*, after synthesis of the amphiphilic coat by surface functionalization.[6]

In the present work, we preloaded the polymer shell with variable amounts of acceptor to study the impact of changing the acceptor/donor ratio (A/D) at a fixed donor/acceptor distance. Taking donor quenching, shortening of the donor lifetime, or an increase in the sensitized acceptor fluorescence as a readout, we demonstrate that the detected transfer efficiency increases with the number of dye molecules but starts to saturate for as little as five acceptor dyes per NC donor. While population measurements closely followed the expected result for a multiple-acceptor transfer mechanism, single-pair FRET (spFRET) recordings revealed a large heterogeneity among nanoprobes, with respect to both their donor quenching and sensitized acceptor fluorescence, and the excited-state lifetime. Our study provides important guidelines for designing FRET-based nanobiosensors and highlights the importance of single-molecule experiments to reveal inner-batch heterogeneity and select for the best FRET sensors.

Materials and Methods

Nanocrystal Synthesis. Four kinds of NCs were used in the current experiments and included Evident NCs (Evidots 560, Evident Technologies, Inc., ED-C11-Tol-0560), Invitrogen NCs (Qdot 565 ITK organic quantum dots, #Q21731MP), and two batches of homemade NCs: one was CdSe without the ZnS shell, and the other was CdSe/ZnS. For Table 1, we determined for each batch the absorption/emission spectra, permitting the direct comparison of the extinction coefficients. Therefore, we could estimate the core size for all four kinds of NCs using the same calibration curve, neglecting the ZnS shell thickness (values in ref 23 are reported for the inorganic core only). Concentrations were determined by absorption measurements, using Beer−Lambert's law.

Table 1. Specifications of the Four Kinds of Nanocrystals Used

	1st peak[a]	$\varepsilon^{(\mathrm{peak})}$	D_i	D_e	A_s
Evident NCs	531	82 325.8	2.7	5.1	177.2
Invitrogen NCs	543	99 040.0	2.9	5.3	186.6
homemade CdSe/ZnS	535	87 334.1	2.8	5.2	180.1
homemade CdSe	523	73 683.1	2.6	5.0	172.0

[a] 1st peak, first exciton absorption peak (nm), obtained by UV−vis spectrometry; $\varepsilon^{(\mathrm{peak})}$, extinction coefficient at its first exciton peak ($\mathrm{cm}^{-1}\ \mathrm{M}^{-1}$), extracted according to ref 23; D_i, diameter of inorganic core (nm), extracted according to ref 23; D_e, effective diameter $= D_i + 2 \times 1.2$ (thickness of TOPO shell) (nm); A_s, surface area of NC $= 4\pi(D_e/2)^2$ (nm^2).

Stoichiometric ATTO−Polymer Embedding. The polymer coating procedure has been described elsewhere.[6,24] Briefly, solutions of different ATTO−polymer ratio were mixed with NC-containing chloroform solution. For the three batches of Evident NCs and the Invitrogen Qdots used, a ratio of 100 polymer motifs per nm^2 of the NC surface was used in the coating process. For the homemade NC batches, we used 50 polymer motifs per nm^2. In contrast to previous protocols,[25] no cross-linker was used in this step. The ATTO−polymer-coated NCs were finally redissolved in borate buffer (sodium borate, 50 mM, pH 12.0).

Donor−Acceptor Ratios. We estimate that 25% of active maleic anhydride rings can react with other molecules containing amino groups. Using a derivate of ATTO with an amino group (abs/em = 597/615 nm, ATTO-TEC GmbH, Germany), the dye was first dissolved in anhydrous chloroform upon sonication, and its concentration was determined by absorption measurements, assuming an extinction coefficient at 597 nm in chloroform of 120 000 $\mathrm{M}^{-1}\ \mathrm{cm}^{-1}$. To obtain different ratios of ATTO dye embedded in polymer, ATTO solution was mixed with polymer solution as detailed in the text in % (mol/mol) of ATTO to maleic anhydride rings. The mixture was left overnight at room temperature and at least three-times concentrated to dryness and redissolved to enhance the reaction efficiency. Finally, the polymer concentration was determined either from the final solvent volume or from the calculated ATTO concentration determined by UV−vis spectrometry. The absorption spectrum of ATTO was not affected by the polymer (data not shown).

Purification. All solutions of the functionalized and assembled NCs were concentrated by ultrafiltering (100 kDa MW cutoff, Millipore) and filtered on 0.2 μm filters (Millipore). Gel electrophoresis on 2% agarose (UltraPure, Invitrogen #15510027) in 0.5× TBE buffer (44.5 mM Tris-borate and 1 mM EDTA, pH 8.3; Sigma-Aldrich, #T3913) was used for purification and run at 100 V for 80−100 min. The separated bands of empty micelles (faster band, red color) and particles (slow band, green or yellow colors) were cut by distinguishing the different colors under the UV lamp.[6] The samples were extracted from the cut bands sealed in dialysis membranes (50 kD, Spectrolabs, #132544) by elution and finally concentrated again by 100 kD ultrafiltration.

Overlap Integrals, Quantum Yields, and Calculated Förster Distances and FRET Efficiencies. We assembled FRET-based nanoprobes by wrapping a central NC donor with an amphiphilic polymer coat into which were included during synthesis ATTO molecules at a stoichiometry ratio (Figure 1A). The choice of these FRET pairs was guided by the requirements (i) to have bright enough NC donors to obtain detectable single-pair FRET (spFRET), (ii) to optimize the overlap between NC photoluminescent emission and ATTO absorption, and (iii) to maximize separation of the donor and acceptor emission spectra to permit dual-color FRET detection.

---

(20) Somers, R. C.; Bawendi, M. G.; Nocera, D. G. *Chem. Soc. Rev.* **2007**, *3*, 579–591.

(21) Ballou, B.; Lagerholm, B. C.; Ernst, L. A.; Bruchez, M. P.; Waggoner, A. S. *Bioconjugate Chem.* **2004**, *15*(1), 79–86.

(22) Yu, W. W. *J. Am. Chem. Soc.* **2007**, *129*(10), 2871–2879.

(23) Yu, W. W.; Qu, L.; Guo, W.; Peng, X. *Chem. Mater.* **2003**, *15*(14), 2854–2860.

(24) Lin, C. A.; Sperling, R. A.; Li, J. K.; Yang, T. Y.; Li, P. Y.; Zanella, M.; Chang, W. H.; Parak, W. J. *Small* **2008**, *4*(3), 334–341.

(25) Pellegrino, T.; Manna, L.; Kudera, S.; Liedl, T.; Koktysh, D.; Rogach, A. L.; Keller, S.; Rädler, J.; Natile, G.; Parak, W. J. *Nano Lett.* **2004**, *4*(4), 703–707.

C2

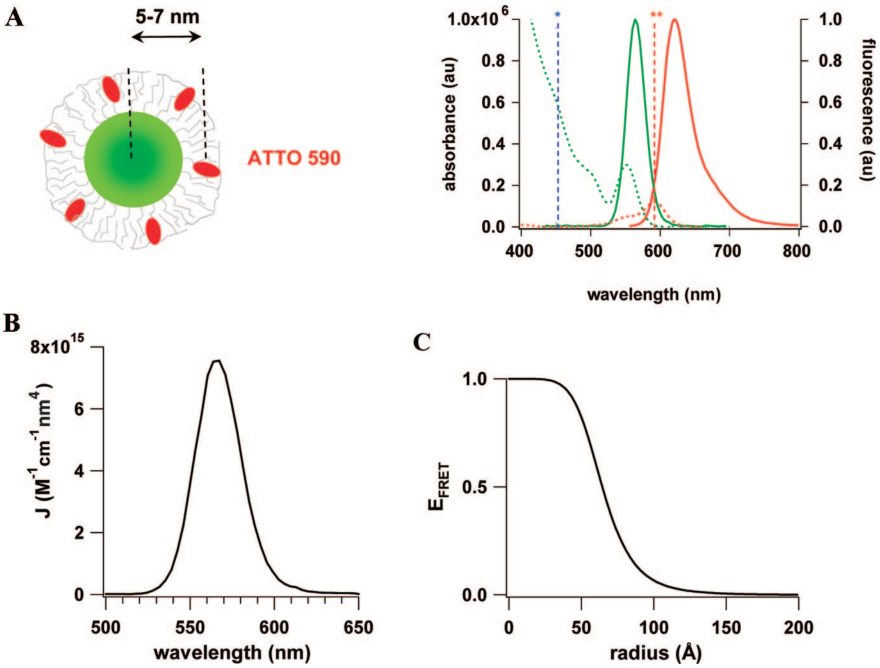

Figure 1. Overlap integrals, quantum yields, and calculated Förster distances and transfer efficiencies between Evident NC donors and ATTO590 dye: (A) Left: Cartoon showing the polymer-wrapped nanocrystal (NC)/ATTO dye assembly. Right: Absorbance (dotted) and normalized emission spectra (solid) of NC donor (green) and ATTO acceptor (red). Asterisk and double asterisk identify 450 and 590 nm wavelengths used for donor and direct (acceptor) excitation. (B) Calculated overlap integral and (C) FRET efficiency, assuming a r^6 dipole−dipole coupling. Förster radius $R_F = 64.5$ Å; $J = 7.75218 \times 10^{15}$ M^{-1} cm^{-1} nm^4.

We note that there is considerable uncertainty in the molar extinction ε of the NC donors, as different sources give different extinction coefficients (e.g., for Invitrogen NC at 543 nm, the manufacturer's data and measured data differ by a factor of 2; and similar discrepancies were observed by others[23,26] and might represent batch-to-batch variability). For consistency, all numbers reported were derived from the same calibration curve.[23,26]

We calculated the overlap integral

$$J = \int \mathrm{d}\lambda\, F_D(\lambda)\, \varepsilon_A(\lambda)\lambda^4 \qquad (1)$$

which quantifies the normalized and dimensionless spectral overlap between donor emission $F_D(\lambda)$ and acceptor absorbance, $\varepsilon_A(\lambda)$, and R_0 the Förster radius, which is defined as the distance between the donor and acceptor that yields 50% energy-transfer efficiency (in Å^6),

$$R_0{}^6 = 8.8 \times 10^{23} \kappa^2 n_D{}^{-4} Q_D J \qquad (2)$$

Here, Q_D is the photoluminescence quantum yield of the NC donor in the absence of an acceptor, n_D is the refractive index of the medium (here, 1.33 for water at ~590 nm), and $\kappa^2 = 2/3$ is the orientation factor, assuming random orientation between the NC and ATTO dipoles.

We derived the transfer efficiency from the quenching of donor photoluminescence, or decrease in donor lifetime in the presence of the acceptor, according to

$$E^{(a)} = 1 - F_{DA}/F_D \qquad (3a)$$

or from the sensitized acceptor fluorescence,

$$E^{(b)} = \frac{\varepsilon_A(\lambda_D)}{\varepsilon_D(\lambda_D)}\left(\frac{F_{DA}(\lambda_A)}{F_A(\lambda_A)} - 1\right) \qquad (3b)$$

where λ_D and λ_A denote the donor and acceptor excitation wavelength, $\varepsilon_D(\lambda)$ is the donor absorbance at wavelength λ (and likewise for the acceptor), and $F_D(\lambda)$ is the donor fluorescence at wavelength λ. We finally used the decrease in donor lifetime in the presence of acceptor,

$$E^{(c)} = 1 - \tau_{DA}/\tau_D \qquad (3c)$$

as a readout for estimating the FRET efficiency.

Finally, assuming a Förster-type (dipole−dipole) interaction between donor and acceptor, and N as the number of acceptors per donor

$$E(N, r) = N/\left(N + (r/R_0)^6\right) \qquad (3d)$$

Estimate of the Donor−Acceptor Ratio. Absorption spectra were obtained on a UV−vis spectrometer (Agilent Technologies). ATTO absorption at 450 nm is negligible to that of the NCs. Conversely, all NC samples hardly absorb at the ATTO absorption peak (597 nm). Thus, measuring the absorbance at 450 and 597 nm, respectively, allowed the determination of [NC] and [ATTO]. All spectra were corrected for background with a blank run.

Fluorescence emission spectra were recorded upon 450 nm (donor excitation) or 590 nm (direct acceptor excitation) on a Fluorolog-3 spectrofluorometer (HORIBA Jobin Yvon, Japan) and were corrected for the instrument response.

After gel electrophoresis, we estimated the number of ATTO dyes per NC donor in the purified samples by the six following steps (Figure 2).

1. The three reference absorption spectra were measured: sample (1), NC−polymer; sample (2), NC−polymer−ATTO 1%; and sample (3), ATTO−polymer 1% in the absence of NC (EP).
2. From Lambert−Beer's law ($A = -\log_{10}(I/I_0) = \varepsilon cL$), using $\varepsilon_{597} = 120\,000$ M^{-1} cm^{-1} of ATTO dye at absorption maximum, the concentration of ATTO in sample (2) was estimated as 1.03 μM.
3. The spectrum of sample (3) was scaled up to match the measured absorption maximum of sample (2) at the ATTO absorption maximum. This scaled spectrum is referred to as sample (3)′ in the following. For the example shown in Figure 2, the scaling factor was 0.9789 (0.12082/0.12342), from the measured absorption of samples (2) and (3) at 597 nm (Figure 2B).

---

(26) Striolo, A.; Ward, J.; Prausnitz, J. M.; Parak, W. J.; Zanchet, D.; Gerion, D.; Milliron, D. J.; Alivisatos, A. P. *J. Phys. Chem. B* **2002**, *106*(21), 5500–5505.

C3

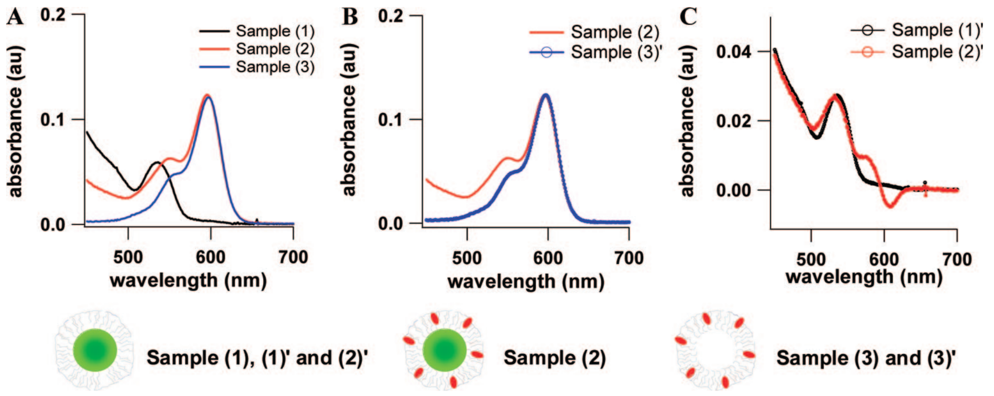

Figure 2. Estimation of the number of ATTO/NC. (A) Samples (1), (2), and (3) indicate absorbance spectra of purified, polymer-coated Evident NC, 1% ATTO−polymer-coated Evident NC, and 1% ATTO−polymer micelles (EP), respectively. (B) and (C) describe the scaling procedure. See text for details.

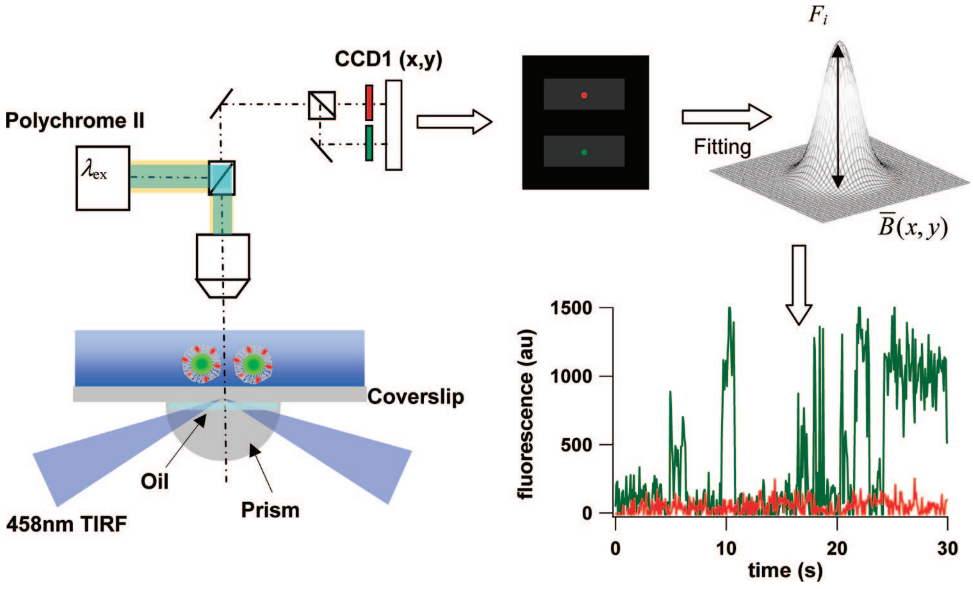

Figure 3. Schematic representation of the setup used for spFRET detection and subsequent data analysis. spFRET was detected on an upright fluorescence microscope fitted for combined epifluorescence and total internal reflection fluorescence (TIRF). We used the “prism-type” configuration, with an external prism and coverslip made of Schott SUPRASIL 311 coupled through a thin layer of ultralow autofluorescence immersion oil. Fluorescence was detected through a water immersion objective and directed, after the splitting of donor (green) and acceptor (red) fluorescence and appropriate filtering, on an electron-multiplying charge-coupled device (CCD) detector. Dual-color images containing a single FRET pair were excised and submitted to a PSF-fitting routine for the measurement of background $\bar{B}(x,y)$and spot *Fi* fluorescence (see Materials and Methods). Traces at the bottom right show blinking fluorescence of a naked NC and the corresponding trace in the red channel.

4. Next, we subtracted the spectrum of sample (3)′ from that of sample (2), thus obtaining a difference spectrum (called (2)′) indicative of the absorption of the NC alone, after subtraction of the ATTO component (Figure 2C). The obtained spectrum compares favorably with a scaled version of spectrum (1), termed sample (1)′ in Figure 2C.
5. From (2)′, the first exciton peak of polymer-coated NCs is measured at 532 nm with an amplitude 0.02731, so that we can calculate the concentration of polymer-coated NCs in sample (2) as 0.33 μM, again using Beer−Lambert’s law and assuming $\varepsilon_{max} \sim 82\,000$ M^{-1} cm^{-1} at the first exciton peak.
6. Finally, the number of ATTO per NC is obtained by dividing the concentrations of ATTO and NCs, 1.03/0.33 = 3.1.

Single-Particle FRET (spFRET) Detection. For spFRET and TSCSPC (time- and space-correlated single-photon counting) measurements, glass coverslips (25 × 10 mm, Menzel, Braunschweig, Germany) were prepared for imaging by successive sonication in absolute ethanol, acetone, HNO_3, and 6 N KOH solutions for 20 min and subsequently washed three times with Milli-Q water. To remove unwanted autofluorescence, they were cured with UV light emitted from a HBO50 lamp during 30 min.

NCs were diluted 100 times from a ~0.2 μM stock in 50 mM borate buffer at pH 9.0. Droplets of 10 μL were dispersed on coverslips and allowed to dry. The coverslips were subsequently washed three times to remove free dye, micelles, and nonattached complexes. NCs remained stably attached to the glass surface in aqueous solution during several hours. For TSCSPC experiments, these coverslips were mounted on microscope slides (76 × 26 × 1 mm LLR2, CML, Nemours, France) and sealed with colorless nail varnish. All samples were stored in the dark at +4 °C until observation.

spFRET measurements were carried out on a custom upright microscope equipped for combined epifluorescence and prism-type evanescent-field excitation (Figure 3, left). Polychrome II (TILL Photonics, Gräfelfing, Germany) provided narrowband (18 nm fwhm intensity) polychromatic epifluorescence excitation which was used for localizing and focusing at the glass surface and for the recording of fluorescence excitation spectra.

For evanescent-field excitation, the beam of a multiline Ar$^+$-ion laser (<5mW at 458 nm impinging on the sample, Reliant 150, Laser Physics, Milton Green, Cheshire, U.K.) was directed at an oblique angle at a ultralow autofluorescence hemicylindrical prism (Suprasil-311, Bernhard Halle Nachfahren, Berlin, Germany).

C4

Penetration depth depended on the angle of incidence of the laser beam and was of the order of 150 nm throughout.

Fluorescence was detected through a LUMFL 60×/1.1-NA water immersion lens (Olympus, Hamburg, Germany) and spectrally separated into a donor and acceptor fluorescence channel (W-view, Hamamatsu, Hamamatsu City, Japan), and directed on a QuantEM 512SC electron-multiplying charge-coupled device (CCD) camera (16 μm × 16 μm pixel size, Photometrics, Tucson, AZ). Images were acquired and analyzed with MetaMorph (Molecular Devices, Sunnyvale, CA). Acquisition rates were 5 or 10 Hz, with exposure times of 75−100 ms for imaging.

For point-spread function fitting and FRET quantification, we first averaged 400−500 image frames of a time-lapse movie and identified regions of interest (ROIs) containing a single NC donor. Individual NCs were recognized by their intensity and blinking; see, for example, Figure 3.

To improve the signal-to-noise ratio, we used a point-spread function (PSF) fitting approach. We used this approach (i) to localize corresponding objects in the donor and acceptor channel and correct for subpixel shift between the color channels, and (ii) to measure the background, amplitude, and width for of spots in the donor and acceptor channel. Image subregions (7 × 7 pixel) were excised from the dual-color fluorescence images and fitted with a two-dimensional (2-D) Gaussian (IGOR, Wavemetrics, Lake Oswego, OR),

$$F(x_i, y_i) = \bar{B}(x, y) + F_i \exp\left[-\frac{1}{2}\left(\left(\frac{x - x_i}{\delta_x}\right)^2 + \left(\frac{y - y_i}{\delta_y}\right)^2\right)\right] \qquad (4)$$

where (x_i, y_i) and δx and δy are the center position and widths of the 2-D Gaussian and $\bar{B}(x,y)$ is the average background in the ROI of interest. For each batch, we report F_i for 20−30 ROIs per coverslip and average over at least three different coverslips.

On 458 nm evanescent-wave excited dual-color fluorescence images of single NCs, we proceeded analogously. We first extracted from the acceptor image ROIs containing a single fluorescent spot and transferred these ROIs onto the donor image. Pairs were retained if they represented detectable acceptor fluorescence as well as donor blinking, indicating a single NC donor at the origin of the detected acceptor fluorescence. Thus, our choice is biased toward bright FRET pairs with negligible donor quenching and moderate duty cycles.

Time- and Space-Correlated Single-Photon Counting (TSCSPC) Measurements. Shortening of the donor fluorescence lifetime in the presence of the acceptor or ingrowth of acceptor lifetime has been used here to quantify FRET efficiencies.[6,12] Lifetime measurements provide an intensity-independent readout of FRET efficiency, which is important when dealing with dim objects as in the present case. Here, we used TSCSPC to reveal the heterogeneity of donor photoluminescence decays within a given batch of NCs. Donor decays were recorded on a Leica SP2 inverted microscope equipped with a Leica TCSP2 confocal scan head (Leica, Solms, Germany). Donor photoluminescence was excited at 802 nm with a femtosecond-pulsed Ti:sapphire laser (100−200 fs, 80 MHz, MaiTai, Spectra Physics, Newport, CA), collected through a HQ 560/40m emission band-pass (Chroma Technology) to reject acceptor fluorescence, and detected on a microchannel plate (MCP) imaging detector (Hamamatsu R3809U-50, Japan). A TCSPC board (SPC-730, Becker & Hickl, Berlin, Germany) was used for the acquisition of both excitation light pulse and fluorescence emission. Typical durations to accumulate enough photons were 2000 s. The time scaling was 37.4 ps/channel, and 4096 channels were used. The instrument response following the laser pulse (100 ps, fwhm) was recorded by detecting the light scattered by a water solution. The large 2PEF cross sections of NC donors permitted the use of low average power (~1 μW). With a 2PEF cross section of ~7000 GM for 525−CdSe−ZnS NCs and ~100 GM for ATTO594, we expect the donor to be the predominantly excited species.[27]

The MCP detector allowed spatially resolved decay measurements (1.5 μm/pixel in the object plane). Binning increased the signal-to-noise ratio, at the expense of spatial resolution. In the later case, the measured decay is the ensemble average of all the NCs present in the binned megapixel. Analysis of the fluorescence decay used either the maximum entropy method[28] or a sum-of-exponentials method implemented in the Becker & Hickl SPCImage software. With the maximal entropy method, we obtained three lifetimes for all samples. Two shorter lifetimes were in the range of 0.2−0.3 ns and 0.8−0.9 ns, and a third longer lifetime component was of the order of 13−21 ns. The sum-of-exponentials method which only gave access to the two shorter lifetimes because of its 10 ns time window is more restrictive, since both χ^2 and the number of exponentials are fixed. We systematically rejected fits with $\chi^2 > 1.2$. The latter approach therefore yields lifetime values similar to those obtained in cuvette measurements, but with the additional information of the spatial distribution. Therefore, histograms of τ values could be obtained by sampling donor lifetimes at different regions of the coverslip.

Results and Discussion

For the synthesis of our NC−ATTO FRET system, an amphiphilic polymer was built by linking a hydrophobic side chain to a backbone of poly(isobutylene-alt-maleic anhydride), as previously described.[6,24] We chose the conditions so that 75% of the anhydride monomers reacted with one dodecyl hydrophobic chain, leaving the remaining 25% vacant for other couplings

As an acceptor fluorophore, we incorporated ATTO590-NH_2 dye (ex/em = 594/624 nm, extinction $\varepsilon_{594} = 120\,000\ M^{-1}\ cm^{-1}$, quantum yield $\phi = 0.8$, fluorescence lifetime $\tau = 3.7$ ns; see Figure 1 for details) by amide linkage to the vacant anhydride monomer positions. By systematically changing the stoichiometric ratio during synthesis, a series of amphiphilic polymers with increasing concentrations of ATTO dye from 0.01% up to 4% (referring to the percentage of anhydride rings in the polymer which are linked to ATTO dye molecules) were preassembled and, upon opening in aqueous medium of the still vacant anhydride which frees negatively charged carboxyl groups, used to colloidally stabilize NCs. We used as donors either EviDots 560 (Evident Technologies), QDot 565 ITK (organic quantum dots, Invitrogen), or homemade CdSe/ZnS and CdSe only nanocrystals.[29,30]

After core−shell assembly, colloidal NCs were purified by gel electrophoresis as described earlier,[31] thereby separating empty polymer micelles (EP) from coated and dye-loaded NCs [6]

Thus, controlling sensor assembly, we investigated how the FRET efficiency varied with the acceptor/donor ratio. Samples synthesized with acceptor varying from 0.01% to 4% were prepared from a *same* batch of NC donors, working either at the same concentration of ATTO dye (Figure 4A, B) or at the same concentration of NCs (Figure 4C, D), adjusting their concentrations so as to obtain identical absorbance at either 597 or 450 nm, respectively (see Materials and Methods). Donor excitation at 450 nm resulted in detectable fluorescence from both Evident NCs and ATTO590, despite the only negligible direct excitation of the acceptor (Figure 4A, C), thus indicating the transfer of excitation from the NC donor to the ATTO acceptor. As expected from a multiple-acceptor system, the yellow-green peak NC

---

(27) Clapp, A. R.; Pons, T.; Medintz, I. L.; Delehanty, J. B.; Melinger, J. S.; Tiefenbrunn, T.; Dawson, P. E.; Fisher, B. R.; O'Rourke, B.; Mattoussi, H. *Adv. Mater.* **2007**, *19*, 1921–1926.

(28) Brochon, J. C. *Numerical computer methods*, Part B; Academic Press: San Diego, CA, 1994; Vol. *240*, pp 262−311.

(29) Dabbousi, B. O.; Rodriguez-Viejo, J.; Mikulec, F. V.; Heine, J. R.; Mattoussi, H.; Ober, R.; Jensen, K. F.; Bawendi, M. G. *J. Phys. Chem. B* **1997**, *101*(46), 9463–9475.

(30) Reiss, P.; Bleuse, J.; Pron, A. *Nano Lett.* **2002**, *2*(7), 781–784.

(31) Parak, W. J.; Gerion, D.; Zanchet, D.; Woerz, A. S.; Pellegrino, T.; Micheel, C.; Williams, S. C.; Seitz, M.; Bruehl, R. E.; Bryant, Z.; Bustamante, C.; Bertozzi, C. R.; Alivisatos, A. P. *Chem. Mater.* **2002**, *14*(5), 2113–211

C5

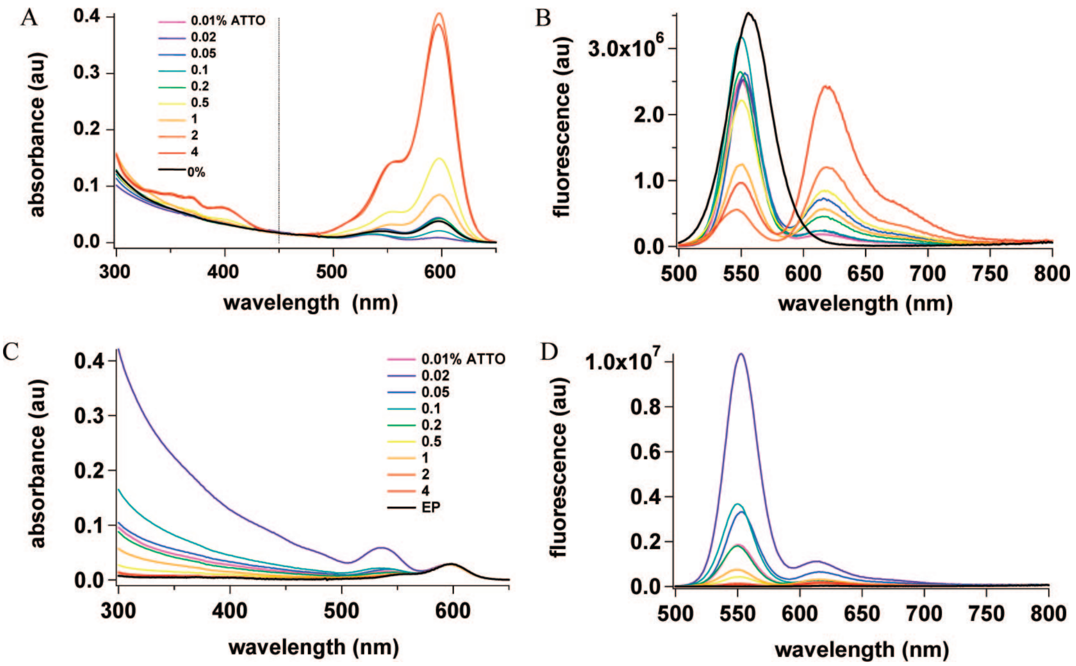

Figure 4. Dependence of normalized absorbance (left) and fluorescence emission (right) on acceptor concentration. A single batch of Evident nanocrystal (NC) donors was coated with ATTO−polymers with an ATTO load increasing from 0.01% to 4%. The percentage refers to the ratio of ATTO molecules to the number of anhydride rings making up the polymer backbone. EPs are empty polymer micelles (2% ATTO) extracted by gel electrophoresis,[6] and Evident NC (0% ATTO) denotes the polymer-coated bare donor, in the absence of acceptor fluorophores. For fluorescence spectra, conditions where adjusted by dilution/concentration of the samples so as to have the same concentration of NCs (absorbance measured at 450 nm, panel (A)) or of ATTO dye (absorbance measurement at 597 nm, panel (C)). (B) and (D) show the corresponding fluorescence emission spectra of the same samples as in (A) and (C) upon donor excitation at 450 nm. Note the increasing transfer of energy from the donor (emission peaking at 560 nm) to the acceptor, ATTO 590 (with 622 nm peak emission) upon increasing the concentration of the later.

emission systematically decreased with increasing ATTO concentration, illustrating the dose-dependent quenching of donor PL emission.[32] We observed a concomitant increase in the ATTO dye emission, indicating the energy absorbed by the donor sensitized acceptor fluorescence in a concentration-dependent manner. Notably, for an equal amount of donor, the total energy that was radiatively emitted as donor PL and acceptor fluorescence (i.e., the area of the spectrum) stayed roughly constant over the entire range of ATTO concentration, indicating that the addition of ATTO does not increase the fraction of dark reactions relaxing NC excitation states compared to bare NCs.

We next experimentally determined the actual acceptor/donor ratio, by successively comparing the absorbance of pairs of polymer−<u>ATTO</u>/NC−polymer−<u>ATTO</u> and <u>NC</u>−polymer/<u>NC</u>−polymer−ATTO. The concentration of ATTO in polymer was directly read off from its absorbance at 594 nm. Since ATTO was preloaded to the polymer before NC coating and NCs only negligibly absorb at 594 nm,[6] the absorbances of ATTO in polymer and in coated NCs could be scaled (see Materials and Methods). Subtracting the two latter spectra generates an artificial compound NC−polymer spectrum that closely reproduces the measured NC−polymer spectrum, with the exception of two small antiphasic deviations suggesting a slight peak shift of the donor or acceptor when conjugated (see Figure 2 in Materials and Methods). Conversely, the amount of NCs included in the NC−polymer−ATTO complexes was directly estimated from absorbance measurements at 450 nm where ATTO absorbance is negligible compared to that of the NCs. The acceptor/donor ratio is then given by the ratio of the measured amounts of ATTO and NCs. From these measurements, we estimate that varying between 0% and 4% the number of monomers building up the polymer resulted in embedding 0−20 molecules of ATTO dye per NC. For example, NCs prepared with "1%" ATTO−polymer contained, on average, five ATTO dye acceptors (see Figure 5A).

Using this stoichiometry calibration, we next quantified these notions by graphing evolution with A/D of the NC peak emission at 565 nm, as well as the sensitized donor fluorescence at 627 nm peak according to eq 3a (Figure 5B, left). From these data, we calculated the FRET efficiency E using either donor quenching or sensitized acceptor fluorescence as a parameter (Figure 5B, right). As expected for multiacceptor FRET, we observe an initial dependence of E on the number of acceptors and a plateau of ~0.65 for >5 acceptors.

How does this observation compare with theory? If we fit eq 3d, $E(N,r) = N/(N+(r/R_0)^p)$ with the experimental data while keeping $p = 6$ fixed, we find $r/R_0 = 1.11 \pm 0.04$, close to 0.77−1.08 predicted from ref 33. Two independent experiments confirmed these bulk cuvette measurements. First, single-pair FRET (spFRET) data obtained from individual NCs images on total-internal reflection fluorescence images (open squares in Figure 5B right) showed the same dependence of donor PL on the A/D ratio ($r/R_0 = 1.09 \pm 0.23$), indicating that our population average was not biased through the existence of bright subpopulations, NC aggregation, or low spectrometer sensitivity. Conversely, the presence of a dielectric interface in evanescent-wave excited fluorescence does only marginally, if at all, affect FRET. Letting both p and r/R_0 run freely in fits of $E(N,r)$ gave 5.6145 ± 1.9 and 1.09 ± 0.34 as best fit parameters. Nevertheless, the dispersion of the data would have allowed other suitable combinations of p and r/R_0 with $p \in (2, 6.5)$ to produce a similar precision (see gray trace in Figure 5B right)

---

(32) Schmelz, O.; Mews, A.; Basché, T.; Herrmann, A.; Müllen, K. *Langmuir* **2001**, *17*, 2861–2865.

(33) Sperling, R. A.; Liedl, T.; Duhr, S.; Kudera, S.; Zanella, M.; Lin, C.-A. J.; Chang, W. H.; Braun, D.; Parak, W. J. *J. Phys. Chem. C* **2007**, *111*, 11552–11559.

C6

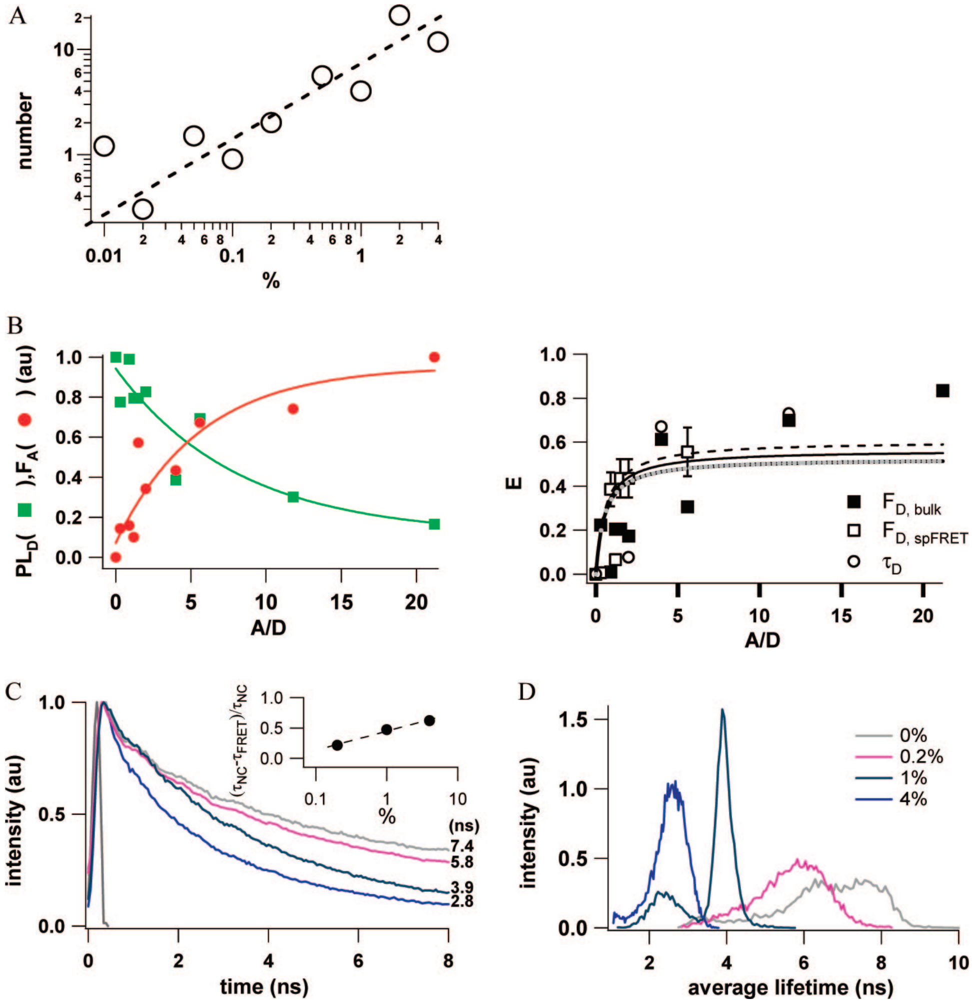

Figure 5. FRET efficiency of the Evident NC/ATTO system as a function of the polymer/ATTO stoichiometry and the number of ATTO molecules actually bound per NC. (A) Log−log plot of the measured relationship between percentages of ATTO included during polymer synthesis and ATTO molecules actually decorating the central NC donor. Points show mean values for three batches. Slope is 4−5. (B) Left: evolution with acceptor/donor ratio (A/D) of donor photoluminescence (PL_D, green rectangles) and sensitized donor fluorescence (F_A, red dots), measured as the peak of spectral donor and acceptor emission at 565 and 627 nm, respectively. Solid lines are to guide the eye. Right: transfer efficiency E as a function of A/D, measured from bulk cuvette photospectrometry, single-donor PL on TIRF images, or average donor lifetime obtained from time- and space-correlated single-photon counting (TSCSPC) measurements. (C) Examples of time-dependent fluorescence recordings for EviDot560 donors with different number of ATTO dye as indicated. Numbers denote average lifetimes calculated according to the maximum-entropy method. Pixel bin was 2 × 2, and total integration time was 2000s. (D) Average lifetime histograms for the different Evident NC samples shown in panel (B). Histograms are normalized to equal area. Note the broad and skewed lifetime distributions, even for bare NCs without ATTO dye.

Second, two-photon excitation time- and space-correlated single-photon counting (TSCSPC) showed a pronounced decrease in donor lifetimes for NC/ATTO assemblies compared with unconjugated NCs (Figure 5C). As expected, excited-state lifetimes dropped with increasing number of ATTO acceptors. Mean average decay times $\langle\tau\rangle$ for bare polymer-coated NCs were around 7 ns, whereas the maximal embedding of 20 dye molecules ("4%") reduced this value to 2.5 ns. Thus, time-resolved fluorescence independently corroborates our bulk and spFRET intensity data that FRET provides an efficient alternative route for donor relaxation, yielding, for $p = 6$ and high N, a limiting $E_{\mathrm{fit}}^{\infty} = 1 - \tau_{DA}/\tau_D = 0.55$, very similar to the 0.51 from bulk and 0.59 TIRF measurements.

Fluorescence lifetime imaging microscopy (FLIM) analysis also allowed us to obtain spatially resolved donor fluorescence decays from FRET nanoprobes immobilized at a low density on a glass coverslip. Figure 5C quantifies the effect of increasing acceptor concentration in terms of distributions of single-pixel donor lifetimes. Even without acceptor, the distribution is relatively large and skewed to the short end. Although the effective pixel size (1.5 × 1.5 μm in the object plane) of our microchannel plate detector prohibited the detection of spFRET from individual nanoprobes (1 pixel containing some 1−5 NCs), the spatial sampling was fine enough to reveal an important heterogeneity of donor lifetimes within a given batch of NC donor and ATTO concentration. The spread of $\langle\tau\rangle$ was not due to pixel noise, because pixel binning resulted in average values reproducing the distribution means of single data (Figure 5C right). Thus, FLIM suggests that donor PL is influenced by factors other than FRET alone and probably linked to sample aging, aggregation, or photodegradation.

In the present work, we stoichiometrically embedded hydrophobic dye molecules in amphiphilic polymer micelles. Using these preassembled micelles to wrap NCs shells, we control the mean number of ATTO acceptor molecules bound per NC donor from 0 to 20. In this range, the intrinsic properties of the NC−ATTO dye complex as measured by the intensity and lifetime of the donor decreased monotonously with ATTO concentration. Our results provide the direct experimental demonstration that, at a fixed A/D distance, multiacceptor FRET provides an efficient means to increasing the sensitivity of FRET-based nanoprobes.

Polymer wrapping is a rigid process, thereby fixing the donor/acceptor distance. However, a narrow distribution of the distances within the polymer shell critically depends on the tight wrapping of the NC central donor with the polymer coat. In this context, it is important to note that our experimental data are the size measurements derived from the hydrodynamic radii.[33] However, we can be sure that the inclusion of ATTO (at any percentage) does not change the geometry of the polymer shell, as the hydrodynamic radii are independent of the ATTO percentage. Also, donor/acceptor distance should fall within the smaller and bigger limits defined by the middle of the polymer shell and the outside of the polymer shell, respectively. However, we cannot exclude that the polymer shell detaches with time, resulting in a potentially larger distribution.

Irrespective of the precise distribution of donor/acceptor distances, our result of a monotonic dependence of the FRET efficiency on the acceptor concentration is different from the bell-shaped dependence of the FRET efficiency on the A/D ratio observed for a CdTe/Rhodamine B system,[5] where the drop in transfer efficiency at acceptor excess may reflect acceptor/acceptor or donor/donor interactions in the densely packed film used, similar to what has been suggested for crowded environments, where significant excitation transfer can occur via states that are optically dark.[34]

Emission-based FRET detection works best within a limited range of molar acceptor/donor ratios.[35] Although FLIM-FRET[36] is less restricted in this respect, the measurement of E and the estimation of interacting versus noninteracting species are simplified when the donor and acceptor are present at fixed molar ratios. Stoichiometric inclusion by preloading polymers permits one to tailor FRET pairs through a chemical variable that can be controlled during synthesis and nanoprobe assembly. It therefore adds a degree of freedom to nanosensor assembly beyond the existing choice of spectrally suitable donors and acceptors and tuning their separation distances through the use of molecular linkers. The capacity to fine tune the transfer efficiency will be of particular importance for sensors that derive their contrast from changes in donor/acceptor spectral overlap, where an E value close to 0.5 would maximize sensitivity, or for ratiometric constant-distance polymer-shell sensors for which one might want to find conditions that go along with incomplete donor quenching yet detectable acceptor fluorescence.

The observed heterogeneity among nominally identical NC donors complicates calibrated analyte sensing and implies that checkpoints need to be introduced at critical points of synthesis and sensor assembly. Alternatively, microfluidic postsynthesis recognition and sorting might provide more homogeneous sensor performance.[37] Thus, although FRET-based hybrid NC/fluorophore assemblies hold important promises for being the next generation of nanobiosensors, to work in nanoscale biological environments, the technique still needs further development.

Acknowledgment. This work was supported by the *Groupement d'intérêt Publique - Agence Nationale de la Recherche Programme Nanosciences et Nanotechnologies* (GIP-ANR PNANO, Grant No. ANR-05-NANO-051 "NanoFRET" to J.-M.M., A.F., M.O., and W.J.P.) and, in parts, by the European Union (Grant Nos. FP6-2004-013880 "Single-motor FLIN", FP6-2005-019481 "From FLIM to FLIN", and FP6-2006-037897 "AUTOSCREEN" to M.O.) and the German Research Foundation DFG (W.J.P., SPP 1313 PA 794/4-1). A.V.Y., C.L., and S.G. were postdoctoral fellows funded by the *Centre National de la Recherche* (CNRS), the *Fondation pour la Recherche Médicale* (FRM), and GIP-ANR, respectively. The authors thank Ralph Sperling and Marco Zanella for discussion.

Supporting Information Available: Synthesis of the polymer and preparation of homemade nanocrystals, estimation of photoluminescence quantum yields of NC donors, electrophoretic purification of NC−ATTO complexes, ensemble FRET measurements in cuvette, FRET efficiency as a function of donor/acceptor ratio, and single-particle FRET (spFRET) data and TSCSPC FLIM data for Invitrogen NCs (Qdot565) and homemade CdSe/ZnS as well as CdSe NCs. This material is available free of charge via the Internet at http://pubs.acs.org.

LA8038347

---

(34) Zimet, D. B.; Thevenin, B. J.-M.; Verkman, A. S.; Shohet, S. B.; Abney, J. R. *Biophys. J.* **1995**, *68*, 1592–1603.

(35) Barney, C.; Danuser, G. *Biophys. J.* **2003**, *84*, 3992–4010.

(36) Becker, W.; Bergmann, A.; Hink, M. A.; König, K.; Benndorf, K.; Biskup, C. *Microsc. Res. Tech.* **2004**, *63*, 58–66.

(37) Chang, J.-Y.; Yang, C.-H.; Huang, K.-S. *Nanotechnology* **2007**, *18*, 305305.

CHEMPHYSCHEM

DOI: 10.1002/cphc.200900849

Ion and pH Sensing with Colloidal Nanoparticles: Influence of Surface Charge on Sensing and Colloidal Properties

Feng Zhang,[a] Zulqurnain Ali,[a] Faheem Amin,[a] Anne Feltz,[b] Martin Oheim,[c] and Wolfgang J. Parak*[a, d]

Ion sensors based on colloidal nanoparticles (NPs), either as actively ion-sensing NPs or as nanoscale carrier systems for organic ion-sensing fluorescent chelators typically require a charged surface in order to be colloidally stable. We demonstrate that this surface charge significantly impacts the ion binding and affects the read-out. Sensor read-out should be thus not determined by the bulk ion concentration, but by the local ion concentration in the nano-environment of the NP surface. We present a conclusive model corroborated by experimental data that reproduces the strong distance-dependence of the effect. The experimental data are based on the capability of tuning the distance of a pH-sensitive fluorophore to the surface of NPs in the nanometer (nm) range. This in turn allows for modification of the effective acid dissociation constant value (its logarithmic form, pK_a) of analyte-sensitive fluorophores by tuning their distance to the underlying colloidal NPs.

Introduction

Ion sensing has applications from analytical chemistry to cellular biology. For example, so as to ascertain drinking water quality, ion concentrations are routinely analysed and the results stated on each bottle.[1] In cell biology, transmembrane ion gradients are at the base of sub-cellular and intercellular signalling, setting transporter activity and providing the driving force for diffusion through ion channels. Perturbed ion homeostasis is a hallmark of disease, as is the typically lower pH of tumor cells. The pH of multi-drug resistant cells is higher by at least 0.4 pH units.[2] Na^+ and Cl^- abnormalities result in cystic fibrosis (CF).[3–5]

Colloidal quantum dots are increasingly being used in a large variety of disciplines, of which ion-sensing applications are a rapidly emerging theme.[6–11] Typically, in these applications, ion sensing is based on changes in the photoluminescence emission subsequent to ion binding. Following excitation, the quantum dots emit light due to the recombination of the generated electron-hole pair. Adsorption of certain ions or ligands to the quantum dot surface can quench this light emission, and the ligand-dependent emission deletion has generally been associated with the generation of surface states.[12–18] Depending on their exact surface chemistry, quantum dots respond differently to different ion species but the ion selectivity is only moderate. Also, at high ionic strength the ions shield the surface charge of the quantum dots and compromise colloidal stability. Similarly, the charged ligands bound to the particle surface detach over time from the quantum dot surface and again affect colloidal stability.[19–21] Thus, although such systems have successfully been used for imaging ionic concentrations in cells,[22] their moderate selectivity and limited colloidal stability are severe obstacles for their practical application. Higher analyte specifity of quantum dots can be achieved by employing the principle of molecular recognition. This involves organic chelators attached to the quantum dot surface that specifically recognize and bind distinct ionic species. In these hybrid sensors, specific ion binding and emission quenching are dissociated and need to be mechanistically linked to provide an ion-sensitive optical readout. Specific binding of ions to chelators on the surface of quantum dots can directly quench their fluorescence upon generation of surface states.[10,23,24] Alternatively, ion binding can lead to a conformation change of the chelator. This can be detected via a quencher attached to the chelator which upon conformation change of the chelator is brought into proximity of the quantum dot surface and thus leads to reduction in fluorescence.

Fluorescence detection of ions by molecular recognition can be also achieved with NPs other than quantum dots, as for example with NPs which are not intrinsically fluorescent. In these cases the main purpose of the NP is to serve as carrier and

---

[a] Dr. F. Zhang, Z. Ali, F. Amin, Prof. Dr. W. J. Parak
Fachbereich Physik
Philipps Universität Marburg, Marburg (Germany)
Fax: (+49) 6421 2824202
E-mail: wolfgang.parak@physik.uni-marburg.de

[b] Dr. A. Feltz
Neurobiology Department
Ecole Normale Supérieure (ENS), Paris
46 rue d'Ulm, 75005 Paris (France)

[c] Dr. M. Oheim
INSERM, U603 and CNRS UMR 8154
University Paris Descartes
Laboratory of Neurophysiology and New Microscopies
45 rue des Saints Pères, 75006 Paris (France)

[d] Prof. Dr. W. J. Parak
Wissenschaftliches Zentrum für Materialwissenschaften (WZMW)
Philipps Universität Marburg, Marburg (Germany)

Supporting information for this article is available on the WWW under http://dx.doi.org/10.1002/cphc.200900849.

D 1

scaffold for up-concentrating ion-sensitive fluorophores in a small analyte volume, beyond the solubility of the probe in the ambient solution. In this case, the readout is directly provided by the ion-sensitive fluorophores, for example, indicator dyes.[25] For the detection of protons an example for such a chelator/fluorophore is sold by Invitrogen under the name seminaphtharhodafluor (abbreviated as SNARF).[26,27] The ion sensitive fluorophore can be either embedded in a porous NP matrix[28] or immobilized on the NP surface. In case the carrier NP is fluorescent (e.g. quantum dots) it can be used for the optical excitation of the ion-sensitive fluorophore via fluorescence energy transfer (FRET).[29–33] For metallic-carrier NPs, the emission of the (ion-sensitive) fluorophore can be quenched, when the fluorophore comes close to the metal surface.[34–38] In either case the fluorescence is influenced by the distance between the NP and the ion-sensitive fluorophore.

However, there is an additional way in which the sheer presence of NPs effects nanoparticle-based sensing of ions. For NPs to be colloidally stable a general strategy involves charging their surface (for example with COO^- groups), so that they repel each other due to equal polarity. From the Debye–Hückel theory[39,40] it is known that charged particles in solution attract a cloud of counter ions. In this way the ion concentration close to the particle surface is modified relative to the one in bulk solution. For negatively charged particle surfaces (such as is the case for COO^- stabilized particles) there is a local depletion of anions (such as OH^-) and a local accumulation of cations (such as H^+). In other words, the local ion concentration close to the particle surface will be different from the bulk concentration. This has severe effects on ion detection with NPs, as they actually measure the local near-surface ion concentration and not the bulk concentration in solution. This fact has to be taken into account for the interpretation of the read-out. We already had previous indications for such a phenomenon: while pH detection around pH 7 with SNARF embedded in the cavity of permeable polyelectrolyte capsules worked as expected,[41,42] we failed when we integrated the same fluorophore in the charged permeable walls of the capsules.

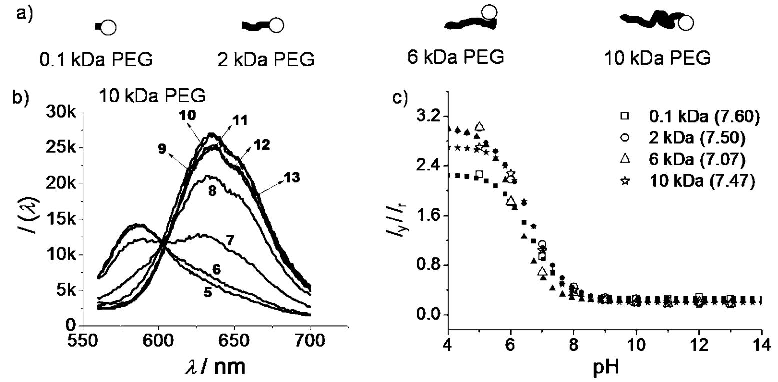

Figure 1. SNARF conjugated to PEG molecules. a) SNARF molecules (drawn as circles) conjugated to PEG molecules of different molecular weights (drawn as thick black lines). The sketches are not drawn to scale. b) Fluorescence spectra $I(\lambda)$ of SNARF conjugated to 10 kDa PEG solubilised in buffers of different pH values as indicated by Arabic numbers near the corresponding curves. The samples were excited with 540 nm. c) For each sample and each pH value the ratio I_y/I_r of the fluorescence intensities I(587 nm)/I(641 nm) is derived from the respective fluorescence spectrum. I_y/I_r vs pH curves are shown for the four different samples. Here pH refers to the bulk pH. Each of the curves is fitted with a sigmoidal function. The pK_a values of samples are indicated in the brackets.

As most colloidal NPs involve charged surfaces we now analyzed this aspect in detail. We are aware that the basic effect, attraction of counter ions, is known since around 100 years.[39,40] It is also well-known that proteins regulate their structure and function by sophisticated interplay of charged domains with adsorbed counter ions. However, to the best of our knowledge, the implications of charged surfaces on ion detection with colloidal NPs have so far not been pointed out in detail and have not been fully characterized. Advanced synthesis methods in colloidal chemistry, bioconjugation, and polymer chemistry nowadays allow for tailored ion-sensitive NPs, in which the distance of the active fluorophore used for detection of the ions to the NP surface can be adjusted with high precision. In this study we want to quantitatively demonstrate and investigate in the case of H^+ how NPs effects on pH-sensing properties in terms of quenching and local charge.

Experimental Section

Based on the commercially available pH indicator SNARF from Invitrogen, we prepared PEG–SNARF conjugates of different molecular weights. Polyethylene glycol (PEG, $M_W = 0.1$, 2, 6, 10 kDa) with amino terminals at both ends (diamino-PEG) was linked to NHS-modified SNARF (SNARF-1 carboxylic acid, acetate, succinimidyl ester, Invitrogen, # S22801). The mixing ratio was adjusted so that linkage of SNARF to both amino terminals of one PEG molecule was unlikely, and the PEG-SNARF conjugates were purified from unbound SNARF with gel electrophoresis. The resulting PEG-SNARF conjugates are depicted in Figure 1 a.

We synthesized negatively and positively charged Au NPs and attached SNARF to their surface using different PEG-spacers. For the negatively charged NPs hydrophobic Au NPs of approximately 4–5 nm core diameter[43] were coated with an amphiphlic polymer,[44] which leads to negatively charged particles rich in COO^- groups. A sketch of the particles is shown in Figure 2 a. Although the polymer coating procedure is established[32,45–50] it has to be pointed out that the exact molecular structure of the polymer around the NPs is not known and the sketches shown in Figure 2 a have to be regarded as plausible idealized models. Diamino-PEG molecules of different molecular weights were bound to the NPs by linking one of the amino terminal of the PEG with the carboxyl groups on the NP surface using EDC (acronyms for 1-ethyl-3-(3-dimethylaminopropyl) carbodiimide) chemistry.[51] The PEG modified Au NPs were firstly purified by gel electrophoresis to get rid of excess PEG. NHS-modified SNARF was then reacted to the amino-terminals on the Au NPs pointing towards solution. The resulting Au NPs conjugated with PEG–SNARF were purified from unbound SNARF with gel electrophoresis and size exclusion chromatography.[32] A sketch of

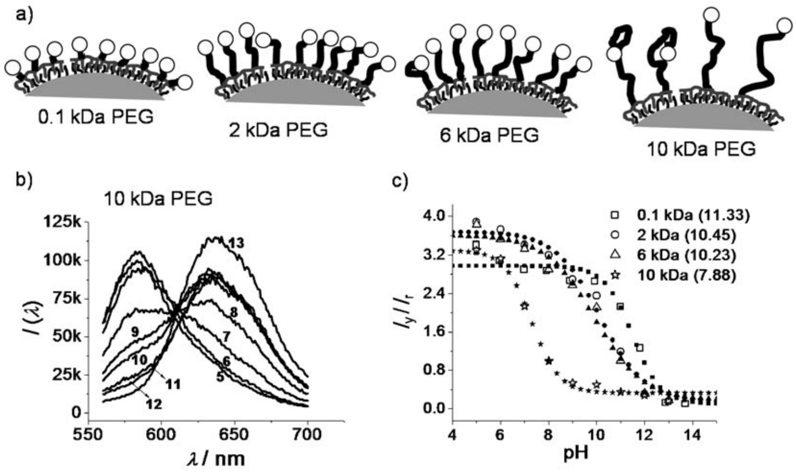

Figure 2. SNARF conjugated to polymer coated gold NPs by different lengths' PEG spacers. a) SNARF molecules (drawn as circles) conjugated to PEG molecules of different molecular weights (drawn as thick black lines) are linked to the surface of polymer-coated (drawn as gray comb-like structures) gold NPs (drawn as gray segmental arch with thin black lines for dodecanthiols). The negatively charged polymer and surfactant layer forms an additional spacer between the Au cores and the PEG ligands. The sketches are plausible idealized models for the conformation of the conjugates and are not drawn to scale. b) Fluorescence spectra $I(\lambda)$ of polymer-coated Au NPs with attached SNARF/10 kDa PEG molecules. The particles were solubilized in buffers with different pH values as indicated by Arabic numbers near the corresponding curves. The samples were excited with 540 nm. c) For each sample and each pH value the ratio I_y/I_r of the fluorescence intensities I(587 nm)/I(641 nm) was derived from the respective fluorescence spectrum. I_y/I_r versus pH curves are shown for the four different samples. Here pH refers to the bulk pH. Each of the curves is fitted with a sigmoidal function. The pK_a values of samples are indicated in the brackets.

the resulting conjugates is shown in Figure 2a. Dependent on the molecular weight of the PEG the size of the particles and thus also the distance of the SNARF to the polymer surface of the particles was adjusted.[52] Negative charge of the particles was verified with gel electrophoresis.

For the positively charged Au NPs, citrate stabilized hydrophilic Au NPs of approximately 10 nm core diameter were coated in a ligand exchange procedure with PEG molecules of different molecular weights which were bearing a thiol on one of their terminals.[51] Alternatively, positively charged Au NPs were directly synthesized in the presence of PEG with one thiol terminal. In both cases the other end of the PEG molecules was either terminated with an amino or a methoxy group. The NPs were firstly purified by centrifuge filters and size-exclusion chromatography in order to remove excess PEG. Then NHS-modified SNARF was linked to the particles by reaction to the amino-terminated PEG. The resulting Au NPs conjugated with PEG-SNARF were purified from unbound SNARF with centrifuge filters and size exclusion chromatography. A sketch of the resulting conjugates is shown in Figure 3a. Positive charge of the particles was verified with gel electrophoresis.

All samples were adjusted to roughly comparable optical densities by using UV/Vis absorption spectroscopy and were diluted in buffers with pH varying between 5 and 13. For each buffer condition a fluorescence spectrum was recorded with a fluorescence spectrometer, see Figures 1b, 2b, and 3b. Ratiometric analysis was performed.[11] The ratio of yellow (excitation at 540 nm, emission at 587 nm) to red (excitation at 540 nm, emission at 641 nm) I_y/I_r emission was derived from each spectrum and this value was plotted for all samples versus the pH of the buffer solution, see Figures 1c, 2c, and 3c. The I_y/I_r versus pH curves were fitted with a sigmoidal function, from which the pK_a value of SNARF in the different samples was determined.

All synthesis protocols and characterization measurements are described in more detail in the Supporting Information (SI). In addition the raw data for all presented results and all control measurements are also provided.

Results and Discussion

Upon varying pH, SNARF conjugated to PEG showed the characteristic pH-dependent fluorescence spectra in response. Colour of emission changed around pH 7 from yellow to red, see Figure 1b and c, allowing for titration of the dye by

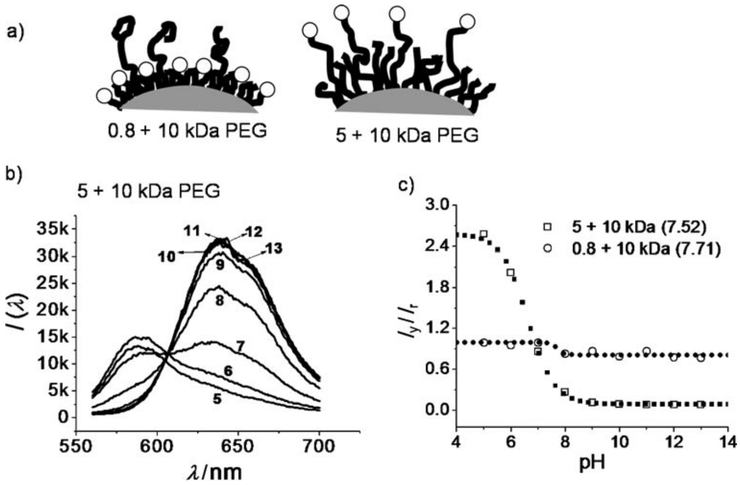

Figure 3. SNARF conjugated to slightly positively charged gold NPs. a) SNARF molecules (drawn as circles) are linked to PEGylated (drawn as thick black lines) slightly positively charged Au NPs (drawn as gray segmental arch). In the first case SNARF is bound to short PEG ($M_W = 0.8$ kDa) in the presence of additional long PEG ($M_W = 10$ kDa). In the second case SNARF is bound to long PEG ($M_W = 10$ kDa) under the presence of additional shorter PEG ($M_W = 5$ kDa). In this way the distance between the SNARF and the Au surface is tuned. The sketches are plausible idealized models for the conformation of the conjugates and are not drawn to scale. b) Fluorescence spectra $I(\lambda)$ of Au NPs protected by PEG molecules (5 kDa + 10 kDa) and modified by SNARF molecules. The particles were solubilised in buffers with different pH values as indicated by Arabic numbers near the corresponding curves. The samples were excited with 540 nm. c) For each sample and each pH value the ratio I_y/I_r of the fluorescence intensities I(587 nm)/I(641 nm) is derived from the respective fluorescence spectrum. I_y/I_r vs pH curves are shown for the 2 different samples. Here pH refers to the bulk pH. Each of the curves is fitted with a sigmoidal function. The pK_a values of samples are indicated in the brackets.

ratiometric measurements. Thus, the conjugation to PEG does not change the pH-sensitivity of SNARF. We are sure that the measured signal derives from PEG-conjugated SNARF and not from contaminating unbound SNARF as the two compounds could be efficiently purified with gel electrophoresis due to their opposite polarity (for data see SI). Thus, the conjugation to PEG does not change the pH-sensitivity of SNARF.

PEG–SNARF conjugates significantly changed their spectral response once they were linked to the surface of negatively charged polymer-coated Au NPs, see Figures 2b and c. Whereas the fluorescence intensity was not appreciably different among the 4 different samples, the colour transition from yellow to red appeared under more basic conditions. The shorter the PEG and thus the closer the SNARF was in the vicinity of the negatively charged polymer surface, the more the I_y/I_r versus pH curve shifted to higher pH values. For the 0.1 kDa PEG the pK_a value was shifted to 11.3 compared to 7.5 of free hydrolyzed NHS-modified SNARF. When long enough PEG ($M_W = 10$ kDa) was used as spacer, the pK_a was back to around pH 7.9 (Figure 2c). We observed the same results when using Au NPs in which PEG–SNARF was directly integrated into the amphiphilic polymer before the polymer-coating procedure[44] and also for empty micelles of the PEG–SNARF modified polymer without embedded Au particles,[15] though for the empty micelles pK_a shift was less, see Table 1 and Supporting Information. This suggests that the polymer/surfactant shell between the Au particle core with a thickness of around 4 nm[52] and the PEG–SNARF is big enough to prevent drastic quenching of the SNARF fluorescence by the underlying gold. However, there is a significant shift in the pH response. We attribute this effect to the presence of the negative charge of the polymer. Gel electrophoresis data clearly demonstrate that despite conjugation with PEG there are still sufficient COO^- groups present on the polymer surface to lead to a negatively charged surface. The lower the molecular weight of the PEG spacer the closer the SNARF is to this negatively charged surface.[52] Hence, in the case of negatively charged Au particles, cations, as H^+, to which SNARF is sensitive to, will be attracted. According to the Debye–Hückel model the concentration of attracted counter cations radially decays with the distance to the particle surface to finally drop off to the bulk concentration at large distances. In this way the local pH at the NP surface is lower than the pH in the bulk solution. SNARF molecules bound with longer PEG spacers are relatively far away from the negatively charged polymer surface (ca. 6–8 nm for PEG of $M_W = 10$ kDa[52]) and thus are basically in contact with bulk pH. Therefore the pK_a as derived from the I_y/I_r versus pH curve is similar to the one of plain SNARF. We point out that the pH on the abscissa of the I_y/I_r versus pH plot refers to the bulk pH of the prepared buffer. Thus, for SNARF molecules linked with only short PEG spacers to the negatively charged polymer surface (< 1 nm for "PEG" of $M_W = 0.1$ kDa) the local pH is significantly lower than the bulk pH. As a result, the I_y/I_r versus (bulk) pH curve appears shifted to higher pH values, as the true local pH the SNARF molecules are exposed to is lower than the bulk pH. In conclusion, depending on their separation from the NP surface, SNARF molecules sense the evolution in pH close to the particle surface, whereas at the distance of a few nm to the surface the bulk pH is detected.

The original Debye model and also the Gouy–Chapman model[53–56] take into account spherical particles, on which the concentration decay of counter ions from the surface scales approximately as $\exp(-r/\kappa)/r$, where, r is the distance from the particle and κ the Debye length. We are aware that this model cannot fully describe our system. First of all, the polymer shell will not be a smooth surface but parts of it might be dangling into solution, thus leading to a complex geometry. Second, the attracted protons can react with the COO^- groups of the particle surface which results in a charged layer directly at the particle surface. This will be of particular importance at pH values lower than the pK_a of the COO^- groups. This has been taken into account for example by the Stern-model[56,57] and elabo-

Table 1. Schematic models for different samples and their corresponding pK_a values. SNARF, PEG, polymer, dodecanethiols and gold NPs are drawn as circles, thick black lines, gray comb-like structure, thin black lines and gray segmental arch, respectively. All of the sketches are plausible idealized models for the conformation of the conjugates and are not drawn to scale. The pK_a values are determined from their I_y/I_r versus pH response curves. The data shown for samples I, IIa, and IVb corresponds to the results shown in Figures 1, 2, and 3, respectively. Sample I refers to SNARF conjugated to PEG. Sample II refers to SNARF conjugated to negatively charged PEG-modified polymer coated Au NPs. The SNARF is conjugated to the PEG-modified polymer coated NP after the polymer-coating (a) or SNARF-PEG conjugates are incorporated into the polymer before using the polymer for coating the NPs (b, c). Purification of the samples is performed using gel electrophoresis (a, c) or size-exclusion chromatography (b). Sample III are the empty micelles of polymers conjugated with SNARF-PEG. Sample IV are SNARF conjugated to slightly positively charged Au particles which are stabilized by PEG. PEG was introduced either by ligand exchange (a) or the particles were directly synthesized in PEG (b). For samples II and III the pK_a is higher for small molecular weights of PEG, whereas for samples I and IV the pK_a does not depend from the M_W of PEG.

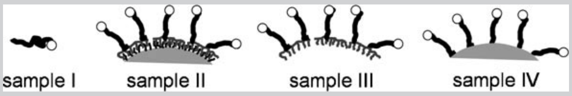

Sample\ M_w (PEG) [kDa]	0.1	1 or 0.8	2	6 or 5	10	20
I	7.6		7.5	7.1	7.4	–
IIa	11.3		10.5	10.2	7.9	–
IIb	–		9.5	8.8	8.7	7.7
IIc	12.0		–	–	9.6	8.9
III	9.8		–	9.2	8.7	8.8
IVa	–		–	7.6	7.1	–
IVb	–	7.7	–	–	7.5	–

rated for the H^+ distribution in the vicinity of H^+-reactive surfaces.[58–60] Above $COO^-/COOH$ pK_a, we can visualize the COO^- groups as local proton buffer maintaining protons in the close vicinity of the SNARF protons sensing radical. Though all serious attempts to model the H^+ distribution around the polymer-coated NPs would have to take into account both effects we believe that our simplistic model still can explain the basic experimental findings.

To check the internal consistency of this interpretation we performed two control experiments. First, given the same valency, to the first approximation the screening effect exerted by a cloud of counter ions is independent of the cationic species. Thus, not only H^+ but, for example, also Na^+ will be attracted. In mixed solutions, for a fixed bulk pH the negative charge of the particles will be screened as well by H^+ as by Na^+ ions with their relative contribution depending on the NaCl concentration. As a consequence, in the presence of Na^+ the pH close to the NP surface should be less affected than without Na^+. In keeping with this idea, we observed a smaller shift ($=11.4$–$9.4=2.0$ units) in the I_y/I_r versus pH curve in the presence of Na^+. However, very high Na^+ concentrations render the NPs less colloidally stable so that we cannot increase NaCl concentration beyond 3.5 M. Corroborating our hypothesis of a surface charge effect no Na^+-dependent change in the pH shift was observed for SNARF in solution (see SI).

As a second control we conjugated SNARF to slightly positively charged Au particles not bearing a (negatively charged) polymer shell, but with only PEG on their surface, which stabilizes the particles by steric repulsion. However, these NPs did not posses the excellent colloidal stability of the negatively charged NPs. The small positive charge of the particles can be verified by gel electrophoresis[51] (see SI). Figures 3 b and c demonstrate that the pH response of SNARF conjugated to the surface of these NPs was similar to that observed for free SNARF in solution, as expected from the negligible repelling force on protons exerted by the slightly positively charged NPs. For this reason the binding equilibrium of protons to SNARF is not changed close to the particle surface. Also, as there is no polymer layer between the PEG spacer and the inorganic Au cores we were able to bring SNARF into very close vicinity of the Au surface of the slightly positive NPs by using short PEG spacers, see Figure 3. In this case the I_y/I_r versus (bulk) pH curve did not shift, but the signal intensity was severely reduced, indicating the efficient quenching of the fluorophore by the gold surface.

Conclusions

By using stringent purification protocols to bind the proton-sensitive fluorophore SNARF at controlled distances to negatively charged NPs, we have demonstrated that the SNARF binding equilibrium is shifted to higher bulk pH values when the fluorophore is bound close to the surface. In this way we can modify the effective pK_a value of SNARF by tuning it's distance to the surface of the NPs. We suggest a model that explains this effect by a reduced local pH value in close vicinity of the negatively charged surface. The screening effect of surface-attracted counter ions was detectable on a length scale compatible with Debye theory. We conclude and alert the user that for ion-sensing applications with ion sensitive fluorophores attached to the NP surface, one has to take into account the influence of charge of the NP on the sensing properties of the fluorophore. This is true both for NPs acting either as a fluorophore carrier or photoluminescence sensor. Besides the possible quenching of fluorescence of surface-proximal fluorophores, the NP surface charge also shifts the ion binding constant, due to the attraction of counter ions to the charged particle surfaces. This in turn could be used to tune the pK_a of fluorophores to the desired value by adjusting their distance to the NP surface.

Acknowledgements

The authors are grateful to Prof. Dr. Uli Nienhaus, Prof. Dr. Jean-Maurice Mallet, Dr. Pilar Rivera Gil, Dr. Loretta del Mercato, Dr. Ralph Sperling, Abbasi Azhar Zahoor, and to Andreas Riedinger for stimulation discussions about the interpretation of our results and for proofreading of the manuscript. The TEM images have been recorded by Abbasi Azhar Zahoor. The German group (W.J.P) was funded by the German Research Foundation (DFG, SPP 1313, grant 794/4-1). A.F. and M.O. acknowledge funding from the Groupement d'intérêt Public—Agence Nationale de la Recherche (GIP-ANR), PNANO, grant 05-NANO-051 NanoFRET). The German and French groups (M.O., W.J.P.) received a Procope grant for travelling from the German Academic Exchange Service (DAAD, grant D/0707567) and the French Ministry of Foreign Affairs (EGIDE).

Keywords: fluorescence · fluorophore · ion sensors · nanoparticles · polymers

[1] M. Chiba, A. Shinohara, M. Sekine, S. Hiraishi, *J. Radioanal. Nucl. Chem.* **2006**, *269*, 519.
[2] B. N. Altan, Y. Chen, M. Schindler, S. M. Simon, *J. Exp. Med.* **1998**, *187*, 1583.
[3] H. Matsui, B. R. Grubb, R. Tarran, S. H. Randell, J. T. Gatzy, C. W. Davis, R. C. Boucher, *Cell* **1998**, *95*, 1005.
[4] M. Mall, A. Hipper, R. Greger, K. Kunzelmann, *FEBS Lett.* **1996**, *381*, 47.
[5] M. J. Stutts, C. M. Canessa, J. C. Olsen, M. Hamrick, J. A. Cohn, B. C. Rossier, R. C. Boucher, *Science* **1995**, *269*, 847.
[6] K. E. Sapsford, T. Pons, I. L. Medintz, H. Mattoussi, *Sensors* **2006**, *6*, 925.
[7] J. M. Klostranec, W. C. W. Chan, *Adv. Mater.* **2006**, *18*, 1953.
[8] N. L. Rosi, C. A. Mirkin, *Chem. Rev.* **2005**, *105*, 1547.
[9] C.-A. J. Lin, T. Liedl, R. A. Sperling, M. T. Fernández-Argüelles, J. M. Costa-Fernández, R. Pereiro, A. Sanz-Medel, W. H. Chang, W. J. Parak, *J. Mater. Chem.* **2007**, *17*, 1343.
[10] R. Freeman, I. Willner, *Nano Lett.* **2009**, *9*, 322.
[11] R. Gill, L. Bahshi, R. Freeman, I. Willner, *Angew. Chem.* **2008**, *120*, 1700–1703; *Angew. Chem. Int. Ed.* **2008**, *47*, 1676–1679.
[12] Y. Chen, Z. Rosenzweig, *Anal. Chem.* **2002**, *74*, 5132.
[13] J. G. Liang, X. P. Ai, Z. K. He, D. W. Pang, *Analyst* **2004**, *129*, 619.
[14] J. L. Chen, C. Q. Zhu, *Anal. Chim. Acta* **2005**, *546*, 147.
[15] M. T. Fernandez-Argüelles, W. J. Jin, J. M. Costa-Fernandez, R. Pereiro, A. Sanz-Medel, *Anal. Chim. Acta* **2005**, *549*, 20.
[16] A. S. Susha, A. Munoz Javier, W. J. Parak, A. L. Rogach, *Colloids Surf. A* **2006**, *281*, 40–43.
[17] C. Bullen, P. Mulvaney, *Langmuir* **2006**, *22*, 3007.
[18] Z. Bin Shang, Y. Wang, W. J. Jin, *Talanta* **2009**, *78*, 364.

[19] J. Aldana, Y. A. Wang, X. Peng, *J. Am. Chem. Soc.* **2001**, *123*, 8844.

[20] K. Boldt, O. T. Bruns, N. Gaponik, A. Eychmüller, *J. Phys. Chem. B* **2006**, *110*, 1959.

[21] W. R. Algar, U. J. Krull, *ChemPhysChem* **2007**, *8*, 561.

[22] Y. S. Liu, Y. Sun, P. T. Vernier, C. H. Liang, S. Y. C. Chong, M. A. Gundersen, *J. Phys. Chem. C* **2007**, *111*, 2872.

[23] M. J. Ruedas-Rama, E. A. H. Hall, *Anal. Chem.* **2008**, *80*, 8260.

[24] M. J. Ruedas-Rama, E. A. H. Hall, *Analyst* **2008**, *133*, 1556.

[25] K. J. Wallace, *Supramol. Chem.* **2009**, *21*, 89.

[26] K. J. Buckler, R. D. Vaughanjones, *Pfluegers Arch.* **1990**, *417*, 234.

[27] S. Bassnett, L. Reinisch, D. C. Beebe, *Am. J. Physiol.* **1990**, *258*, C171.

[28] M. Brasuel, R. Kopelman, J. W. Aylott, H. Clark, H. Xu, M. Hoyer, T. J. Miller, R. Tjalkens, M. A. Philbert, *Sens. Mater.* **2002**, *14*, 309.

[29] P. T. Snee, R. C. Somers, G. Nair, J. P. Zimmer, M. G. Bawendi, D. G. Nocera, *J. Am. Chem. Soc.* **2006**, *128*, 13320.

[30] M. Suzuki, Y. Husimi, H. Komatsu, K. Suzuki, K. T. Douglas, *J. Am. Chem. Soc.* **2008**, *130*, 5720.

[31] J. M. Dubach, D. I. Harjes, H. A. Clark, *J. Am. Chem. Soc.* **2007**, *129*, 8418.

[32] M. T. Fernández-Argüelles, A. Yakovlev, R. A. Sperling, C. Luccardini, S. Gaillard, A. S. Medel, J.-M. Mallet, J.-C. Brochon, A. Feltz, M. Oheim, W. J. Parak, *Nano Lett.* **2007**, *7*, 2613.

[33] A. V. Yakovlev, F. Zhang, A. Zulqurnain, A. Azhar-Zahoor, C. Luccardini, S. Gaillard, J. M. Mallet, P. Tauc, J. C. Brochon, W. J. Parak, A. Feltz, M. Oheim, *Langmuir* **2009**, *25*, 3232.

[34] E. Dulkeith, A. C. Morteani, T. Niedereichholz, T. A. Klar, J. Feldmann, S. A. Levi, F. C. J. M. van Veggel, D. N. Reinhoudt, M. Möller, D. I. Gittins, *Phys. Rev. Lett.* **2002**, *89*, 203002.

[35] E. Dulkeith, M. Ringler, T. A. Klar, J. Feldmann, A. M. Javier, W. J. Parak, *Nano Lett.* **2005**, *5*, 585.

[36] Y. Fu, J. R. Lakowicz, *Laser Photonics Rev.* **2009**, *3*, 221.

[37] S. H. Bae, S. Il Yoo, W. K. Bae, S. Lee, J. K. Lee, B. H. Sohn, *Chem. Mater.* **2008**, *20*, 4185.

[38] T. Ren, P. K. Mandal, W. Erker, Z. H. Liu, Y. Avlasevich, L. Puhl, K. Mullen, T. Basche, *J. Am. Chem. Soc.* **2008**, *130*, 17242.

[39] P. Debye, E. Hückel, *Phys. Z.* **1923**, *24*, 185.

[40] P. Debye, E. Hückel, *Phys. Z.* **1923**, *24*, 305.

[41] O. Kreft, A. Muñoz Javier, G. B. Sukhorukov, W. J. Parak, *J. Mater. Chem.* **2007**, *17*, 4471.

[42] M. Semmling, O. Kreft, A. Muñoz Javier, G. B. Sukhorukov, J. Käs, W. J. Parak, *Small* **2008**, *4*, 1763.

[43] M. Brust, M. Walker, D. Bethell, D. J. Schiffrin, R. Whyman, *J. Chem. Soc. Chem. Commun.* **1994**, 801.

[44] C.-A. J. Lin, R. A. Sperling, J. K. Li, T.-Y. Yang, P.-Y. Li, M. Zanella, W. H. Chang, W. J. Parak, *Small* **2008**, *4*, 334.

[45] M. X. Wu, H. Liu, J. Liu, K. N. Haley, J. A. Treadway, J. P. Larson, N. Ge, F. Peale, M. P. Bruchez, *Nat. Biotechnol.* **2003**, *21*, 41.

[46] T. Pellegrino, L. Manna, S. Kudera, T. Liedl, D. Koktysh, A. L. Rogach, S. Keller, J. Rädler, G. Natile, W. J. Parak, *Nano Lett.* **2004**, *4*, 703.

[47] R. E. Anderson, W. C. W. Chan, *ACS Nano* **2008**, *2*, 1341.

[48] R. D. Corato, A. Quarta, P. Piacenza, A. Ragusa, A. Figuerola, R. Buonsanti, R. Cingolani, L. Manna, T. Pellegrino, *J. Mater. Chem.* **2008**, *18*, 1991–1996.

[49] W. W. Yu, E. Chang, C. M. Sayes, R. Drezek, V. L. Colvin, *Nanotechnology* **2006**, *17*, 4483.

[50] E. E. Lees, T. L. Nguyen, A. H. A. Clayton, P. Mulvaney, *ACS Nano* **2009**, *3*, 1121.

[51] R. A. Sperling, T. Pellegrino, J. K. Li, W. H. Chang, W. J. Parak, *Adv. Funct. Mater.* **2006**, *16*, 943.

[52] R. A. Sperling, T. Liedl, S. Duhr, S. Kudera, M. Zanella, C.-A. J. Lin, W. Chang, D. Braun, W. J. Parak, *J. Phys. Chem. C* **2007**, *111*, 11552.

[53] D. L. Chapman, *Philos. Mag.* **1913**, *25*, 475.

[54] M. Gouy, *J. Phys.* **1910**, *9*, 457.

[55] M. Gouy, *C. R. Hebd. Seances Acad. Sci.* **1909**, *149*, 654.

[56] J. O. M. Bockris, A. K. N. Reddy, *Modern Electrochemistry, Vol. 1, 1st ed.*, Plenum, New York, **1970**.

[57] O. Stern, *Z. Elektrochem. Angew. Phys. Chem.* **1924**, *30*, 508.

[58] S. Levine, A. L. Smith, *Discuss. Faraday Soc.* **1971**, *52*, 290.

[59] N. E. Yates, S. Levine, T. W. Healy, *Faraday Trans. 1* **1974**, *70*, 1807.

[60] L. Bousse, N. F. d. Rooij, P. Bergveld, *Surf. Sci.* **1983**, *135*, 479.

Received: October 30, 2009

D 6

Volume 6 · No. 6 – March 22 2010

D15063

NANO small MICRO

www.small-journal.com

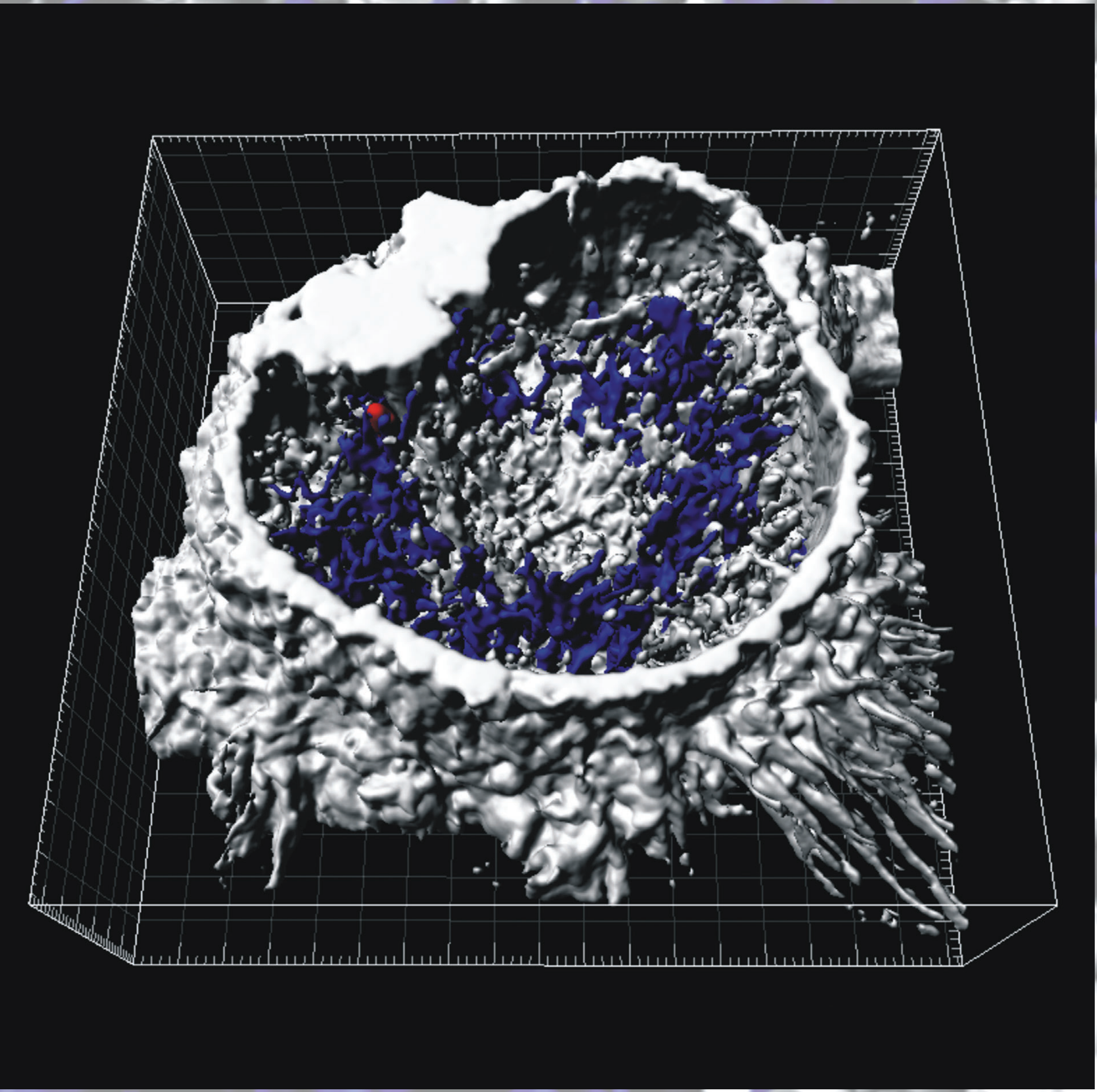

6/2010

WILEY-VCH

Fluorescent–Magnetic Hybrid Nanoparticles Induce a Dose–Dependent Increase in Proinflammatory Response in Lung Cells in vitro Correlated with Intracellular Localization

B. Rothen-Rutishauser et al.

E 1

Fluorescent–Magnetic Hybrid Nanoparticles Induce a Dose-Dependent Increase in Proinflammatory Response in Lung Cells in vitro Correlated with Intracellular Localization

*Andrea D. Lehmann, Wolfgang J. Parak, Feng Zhang, Zulqurnain Ali, Carlheinz Röcker, G. Ulrich Nienhaus, Peter Gehr, and Barbara Rothen-Rutishauser**

Iron–platinum nanoparticles embedded in a poly(methacrylic acid) (PMA) polymer shell and fluorescently labeled with the dye ATTO 590 (FePt–PMA–ATTO-2%) are investigated in terms of their intracellular localization in lung cells and potential to induce a proinflammatory response dependent on concentration and incubation time. A gold core coated with the same polymer shell (Au–PMA–ATTO-2%) is also included. Using laser scanning and electron microscopy techniques, it is shown that the FePt–PMA–ATTO-2% particles penetrate all three types of cell investigated but to a higher extent in macrophages and dendritic cells than epithelial cells. In both cell types of the defense system but not in epithelial cells, a particle-dose-dependent increase of the cytokine tumor necrosis factor alpha (TNFα) is found. By comparing the different nanoparticles and the mere polymer shell, it is shown that the cores combined with the shells are responsible for the induction of proinflammatory effects and not the shells alone. It is concluded that the uptake behavior and the proinflammatory response upon particle exposure are dependent on the time, cell type, and cell culture.

Keywords:
- dendritic cells
- epithelial lung cells
- macrophages
- magnetic–fluorescent-hybrid nanoparticles
- proinflammatory response

1. Introduction

The rapid expansion of nanotechnology has resulted in the production of a huge variety of nanoparticles (NPs), which are defined as objects with all three spatial dimensions on the nanometer scale, of different sizes, shapes, charges, chemistries, coatings, and solubilities. Many of these NPs are already in use for consumer products. For example, magnetic NPs are interesting as contrast agents in magnetic resonance imaging (MRI), in particular for transverse (or spin–spin) relaxation

---

[*] A. D. Lehmann, Prof. P. Gehr, Dr. B. Rothen-Rutishauser
Institute of Anatomy, University of Bern
Bern 3012 (Switzerland)
E-mail: rothen@ana.unibe.ch

Prof. W. J. Parak, Dr. F. Zhang, Z. Ali
Philipps Universität Marburg, Fachbereich Physik
Marburg 35032 (Germany)

Supporting Information is available on the WWW under http://www.small-journal.com or from the author.

DOI: 10.1002/smll.200901770

Dr. C. Röcker
Institute of Biophysics, University of Ulm
Ulm 89081 (Germany)

Prof. G. Ulrich Nienhaus
Institute of Applied Physics and Center for Functional Nanostructures
Karlsruhe Institute of Technology
Karlsruhe 76128 (Germany)

Prof. G. Ulrich Nienhaus
Department of Physics
University of Illinois at Urbana-Champaign
Urbana, IL 61801 (USA)

E 2

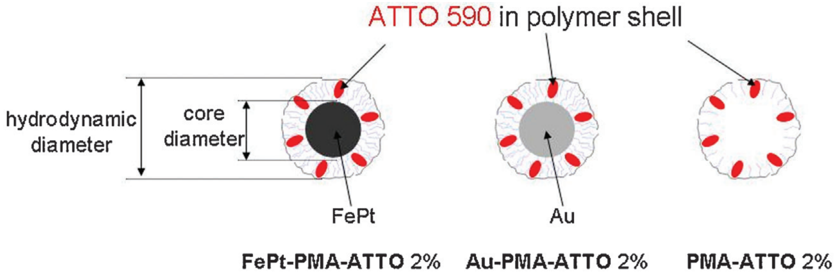

Figure 1. Geometry of the FePt–PMA–ATTO-2% NP, Au–PMA–ATTO-2% NP, and PMA–ATTO-2% micelle samples. The micelles are only drawn schematically and may also be oval shaped.

time (T_2) imaging.[1,2] By additionally endowing these particles with fluorescence, they can be monitored simultaneously by optical means.[3–9] Originally hydrophobic NPs can be dispersed in an aqueous solution by encapsulating them within an amphiphilic polymer shell.[10] Despite the potential benefits of nanomaterials, there is increasing concern that intentional or unintentional human exposure to some types of NPs may cause significant adverse health effects.[11] Issues regarding the size effects of NPs compared to the bulk material are important since the potential of their exposure will increase as the quantities and types of NP used in technological applications continues to grow. As an outcome of all these debates and concerns, nanotoxicology has emerged as a branch in toxicology research that aims to investigate the possible harmful effects of exposure to nanomaterials.[12,13] There is a great deal of ongoing research into the mechanism of the toxic effects of NPs. One important question is how the reactive surface of a NP interacts with the environment in the body. A number of recent in vitro and in vivo studies on NP uptake and intracellular trafficking demonstrate that there is probably no single uptake mechanism for NPs.[14,15]

Before the designed core–shell particles described previously can be used as pharmaceuticals and drug-delivery agents, their possible adverse effects in cell-culture experiments, which may be the basis for adverse health effects,[16,17] need to be carefully investigated. In the present study, polymer-coated iron–platinum NPs with ATTO 590 dye embedded in a poly(methacrylic acid) (PMA) polymer shell (FePt–PMA–ATTO-2%)[18] were included to investigate their intracellular particle localization in monocultures of different lung cells. Their potential to induce a proinflammatory response dependent on particle concentration and incubation time was determined. Colocalization of the particles with lysosomes and mitochondria was assessed by laser scanning microscopy (LSM) combined with digital image restoration. To determine which component of the particles (i.e., the core or the shell) induces a proinflammatory response, several experiments were also performed with particles containing a gold core (Au–PMA–ATTO-2%) and with empty polymer shells (PMA–ATTO-2% micelles) in both monocultures and the more realistic triple-cell coculture model of the human epithelial airway barrier.[19]

2. Results

2.1. Determination of Hydrodynamic Radii and Aggregation Assay

Hydrodynamic radii of 5.6 ± 0.4 nm for FePt–PMA–ATTO-2% NPs, 6.4 ± 0.4 nm for Au–PMA–ATTO-2% NPs, and 9.8 ± 0.8 nm for PMA–ATTO-2% micelles were determined by fluorescence correlation spectroscopy (FCS) measurements in phosphate-buffered saline (PBS) buffer.[20–22] After 24-h incubation in PBS or in medium, the hydrodynamic radii were unchanged for both core–shell particles. A slight size increase was noticed for the empty micelles, however, which also appeared less homogeneous. After 24-h incubation and subsequent filtering, a loss of single particles or micelles was not noticeable, indicating that the formation of larger NP assemblies during incubation was essentially absent. A schematic drawing of the particles is shown in Figure 1. The micelles are presented only schematically and could also be oval in shape. The exact shell shape could not be determined because LSM lacks the required resolution and transmission electron microscopy (TEM) cannot visualize the shells because they do not have sufficient electron density.

2.2. NP Penetration into Cells Visualized by TEM

When particles are added to cell cultures in suspension, it is important to show whether the particles are inside the cells or whether they are attached to the cell surface. Since the particles have an electron-dense core and a fluorescent dye embedded in the shell, different microscopic techniques, such as conventional TEM and LSM, can be applied to visualize the particles.[23–25]

16HBE14o- epithelial cells (EC) were analyzed by conventional TEM after exposure to FePt–PMA–ATTO-2% and Au–PMA–ATTO-2% NPs. Both FePt–PMA–ATTO-2% (Figure 2a and a′) and Au–PMA–ATTO-2% NPs (Figure 2b and b′) were found within the cells. A detailed view is shown in Figure 2a′ and b′, respectively, with an 80000-fold magnification. Single particles as well as aggregates are visible. Most of the particles were found in vesicles. In Figure 2a″ and b″, an image of the particle solution is shown. The PMA–ATTO-2% micelles could not be visualized with TEM as their electron density was too low, as mentioned above.

2.3. Detection of the Intracellular FePt–PMA–ATTO-2% NPs by LSM and Their Colocalization with Lysosomes

We visualized the FePt–PMA–ATTO-2% NPs intracellularly by LSM. We included monocyte-derived macrophages (MDM), monocyte-derived dendritic cells (MDDC), and EC. To address the question of whether the particles can be found inside lysosomes, organelles that digest macromolecules transferred from phagocytic or endocytotic pathways, monocultures of MDM were incubated for 24 h with FePt–PMA–ATTO-2% NPs and then stained for 30 min with a cell-labeling dye and Lysotracker to specifically stain lysosomes. The unfixed cells were then imaged by LSM. Intracellular NPs

E 3

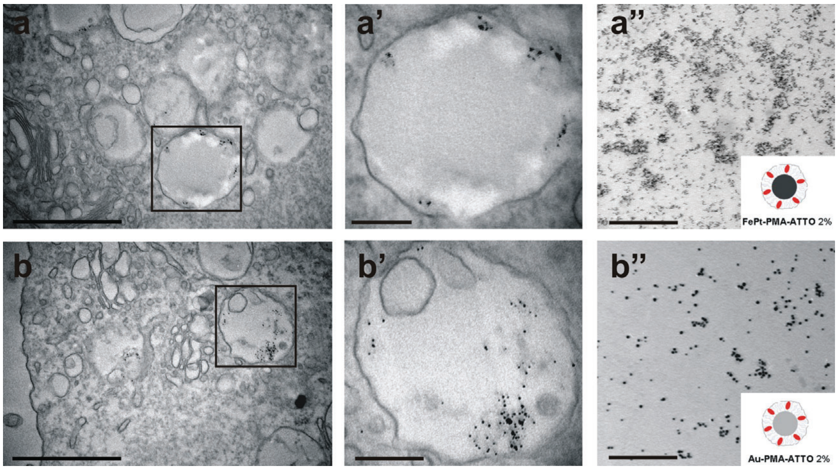

Figure 2. Internalized NPs visualized by TEM. a) FePt–PMA–ATTO-2% NPs and b) Au–PMA–ATTO-2% NPs in vesicles of EC. Scale bars are 1 μm. a′,b′) Detailed view of the squares with an 80000-fold magnification. Scale bars are 200 nm. a″,b″) Particle solutions only with an 80 000-fold magnification. Both particle types were present as single or agglomerated particles.

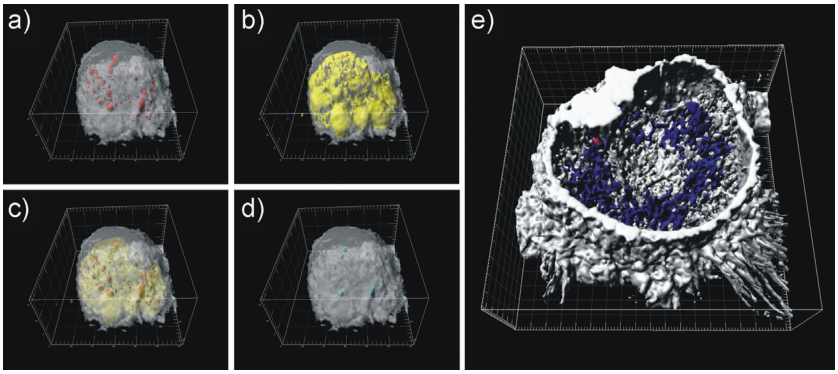

Figure 3. Visualization of FePt–PMA–ATTO-2% NPs with LSM. a) Internalization of FePt–PMA–ATTO-2% NPs (red) in MDM monocultures (light gray) shown in a 3D reconstruction. a–d) Localization and colocalization (turquoise) of the particles with lysosomes (yellow) are shown. c) By making the cell-body channel (light gray) transparent as well as the lysosome channels, the particles colocalized with the lysosomes become visible. d) The colocalization of particles in lysosomes. e) Mitochondria staining (blue) and particles (red) in a MDM.

and NP agglomerates, which we define as particles, events are shown in a reconstructed 3D illustration of a single MDM that was made transparent (Figure 3a). The lysosomes (Figure 3b and c) and the particle events colocalized with lysosomes are also presented (Figure 3d). The same experiment was done with MDDC and EC monocultures resulting in similar pictures. In order to detect any possible colocalization of the NPs with mitochondria, the mitochondria were labeled with MitoTracker, as shown in Figure 3e. However, there was no colocalization of the NPs with the mitochondria in either the presented MDM or the other examined cell types, MDDC and EC.

2.4. Approximate Quantification of Intracellular FePt–PMA–ATTO-2% NPs and Their Colocalization with Lysosomes

We counted the intracellular particle events using specific software to determine the extent to which the particles were taken up, where one particle event refers to one individual particle-filled vesicle, as well as the lysosomal colocalization events. Monocultures of MDM, MDDC, as well as EC, were exposed to different particle concentrations (3.6×10^{10}, 18×10^{10}, 36×10^{10}, 180×10^{10} particles per surface area of culture dish in cm^2). The number of particles and colocalization events were quantified using specific software (see Experimental Section). This quantitative analysis has already been used successfully for micro- and nanometer-sized particles.[26] Since the resolution of light microscopy is limited to approximately 200 nm in the lateral dimensions and 500 nm in the axial dimension,[27] and therefore single NPs and small aggregates cannot be distinguished, only the number of voxels which gave a signal could be counted. However, since the same method was used for all applied concentrations and cell types, the approach of counting events seems reasonable.

The FePt–PMA–ATTO-2% NPs penetrated into all three cell types, but into MDM and MDDC to a higher extent than into EC (Figure 4). The number of particle events in MDM represented a nonlinear dose-dependent uptake and increased faster than in EC and MDDC. The increase of intracellular particles was linear in EC and MDDC. Using the same technique, an approximate quantification of the colocalized particle events with lysosomes was performed. The number of colocalization events was very low at each concentration in EC and, interestingly, also in MDDC. In contrast, the number of colocalized events with lysosmes in MDM increased even at low particle concentrations.

2.5. Proinflammatory Response Upon Particle Exposure

Since a dose-dependent increase of intracellular FePt–PMA–ATTO-2% NP events was observed in all cell types, the potential of those NPs to induce a proinflammatory response was investigated. The concentration of proinflammatory cytokine tumor necrosis factor alpha (TNFα) in the supernatants was determined by enzyme-linked immunosorbent assay (ELISA) after particle exposure for 1 h and 24 h. As a positive control, the inflammatory stimulus lipopolysaccharide (LPS) was added during both incubation times. In the EC monocultures, no increase in TNFα secretion was found (Figure 5a), and the exposure to LPS did not stimulate TNFα production. In both cell types of the defense system, a particle-dose-dependent increase of TNFα was found after 24 h but not after 1 h of exposure to particles (Figure 5b and c). The highest

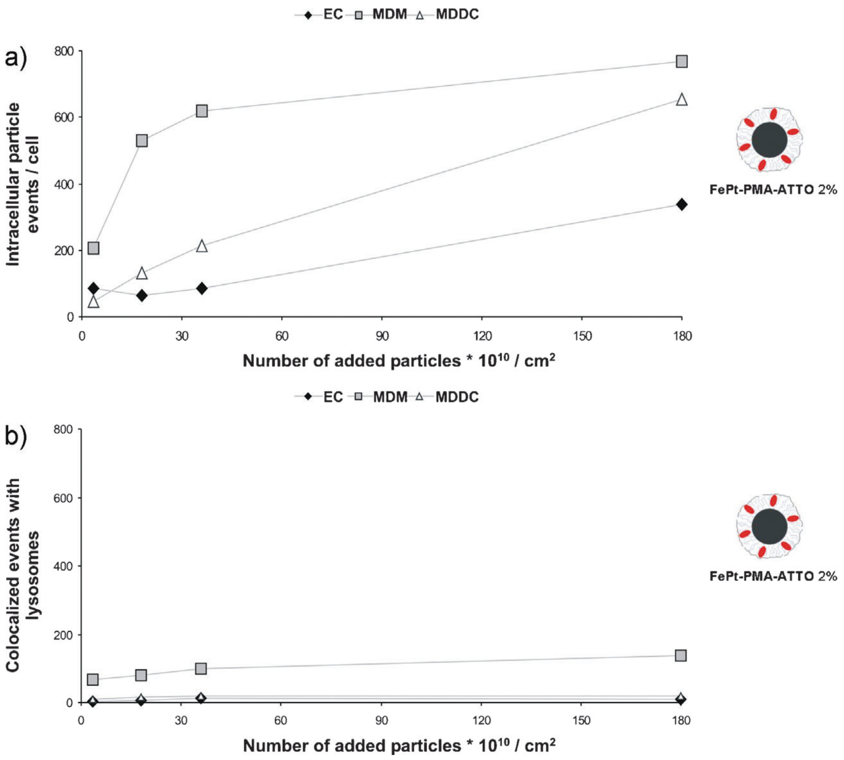

Figure 4. Number of intracellular and colocalized particle events correlated to the applied NP concentration. The number of particles added ($\times 10^{10}$ cm^{-2}) is plotted for each cell type, EC (black rhombus), MDM (gray quad), and MDDC (white triangle), against a) the number of intracellular particle events and b) the number of colocalized events.

NP concentration induced a similar proinflammatory reaction in MDM as LPS. In MDM and MDDC, LPS stimulation had already increased the TNFα level after 1 h. In MDM, exposure of LPS exhibited equal levels of TNFα as exposure for 24 h. However, in MDDC, the LPS stimulation for 24 h led to a higher TNFα release as compared to 1 h.

2.6. Proinflammatory Response of EC, MDM, and MDDC Monocultures to Different Core Particles of the Same NP Type and Comparison with Mere Shells

The dose-dependent proinflammatory reaction of MDM and MDDC to FePt–PMA–ATTO-2% NPs raises the question of which component of the NP, that is, the core, the shell, or a combination of both, is responsible for this reaction. Therefore, we compared the FePt–PMA–ATTO-2% NPs to the same particle type but with a gold core, that is, Au–PMA–ATTO-2% NPs. To compare those NPs with the polymer shell only, PMA–ATTO-2% micelles were also included in the experiments. In the first step, the induction of TNFα release upon adding the different particles was compared in different monocultures. In EC, there was no increase in TNFα concentration in either case (Figure 6a). In MDM as well as in MDDC, an increase in TNFα was observed for both NP types (Figure 6b and c).

The results for MDM highlighted that both NP types showed a similar dose-dependent induction of TNFα release. The latter was observed for all examined concentrations. The PMA–ATTO-2% micelles showed no dose dependent TNFα release and, compared to the complete particles (core plus shell), the induction was always lower (Figure 6b).

In MDDC, a dose dependence was found for the FePt–PMA–ATTO-2% NPs. Au–PMA–ATTO-2% NPs showed a slight dose-dependence but the results were not significant. Interestingly, the PMA–ATTO-2% micelles induced a significant TNFα release at the highest concentration. By comparing the three particle types for each concentration, no significant differences in the TNFα level were observed (Figure 6c).

When the experimental data of the three cell types with respect to one particle type was compared, it was observed that in MDM and MDDC the FePt–PMA–ATTO-2% NPs as well as the Au–PMA–ATTO-2% NPs showed a similar and a dose-dependent effect on TNFα release and that the values were higher than in EC. The Au–PMA–ATTO-2% NPs showed the highest TNFα response in MDM, whereas the PMA–ATTO-2% micelles showed the highest response in MDDC. To exclude any possible influence on the proinflammatory response of the fluorescent dye, ATTO-590, embedded in the shells, MDM and MDDC were exposed to the lowest and highest concentration of pure fluorescent dye as well as to the FePt–PMA and Au–PMA NPs without fluorescent dye. Whereas no proinflammatory response was determined upon exposure to the fluorescent dye, the level of the response in both cell types, MDM and MDDC, to the FePt–PMA and Au–PMA NPs was comparable to that obtained by the fluorescently labeled NPs (see Supporting Information).

2.7. Localization of the Particles in an Epithelial Airway Barrier Model and Proinflammatory Response

Following experiments with the monocultures, we examined whether the various particles also penetrated into all three cell types when these were combined in the triple-cell coculture model.[19,28] Schematic views of the model are shown in Figure 7a–c for EC, MDM, and MDDC, respectively, each with an emphasis on the respective cell type. All three particle types could be visualized with LSM and image-restoration techniques. Figure 7d–m gives an overview of the particles localized in the triple-cell cocultures. All three particle types (FePt–PMA–ATTO-2% NPs, Au–PMA–ATTO-2% NPs, and PMA–ATTO-2% micelles) were found in all three cell types, in EC (Figure 7d, g, and k), in MDM (Figure 7e, h, and l), and in MDDC (Figure 7f, i, and m). Furthermore, we examined whether there was a different proinflammatory response upon exposure to the particle types in the more realistic triple-cell coculture model compared to the monocultures.

The data for the upper-chamber supernatant showed that the two core particles (FePt–PMA–ATTO-2% and Au–PMA–

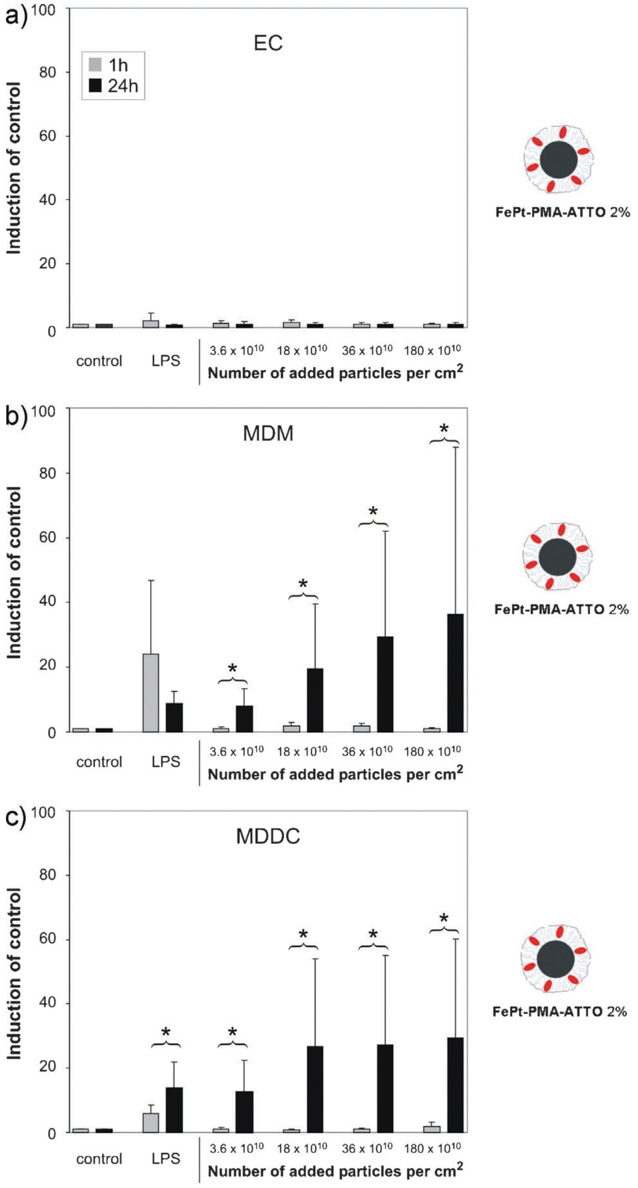

Figure 5. Time-dependent TNFα release upon exposure to FePt–PMA–ATTO-2% NPs. For each particle concentration, the TNFα value is plotted for monocultures of a) EC, b) MDM, and c) MDDC for exposure times of 1 h (gray bars) and 24 h (black bars). All values were normalized to the untreated control. Alterations were expressed as induction of the control (*y* axis). Values are presented as means ± SD; * indicates $p \leq 0.05$. All experiments were independently performed between 3 and 11 times.

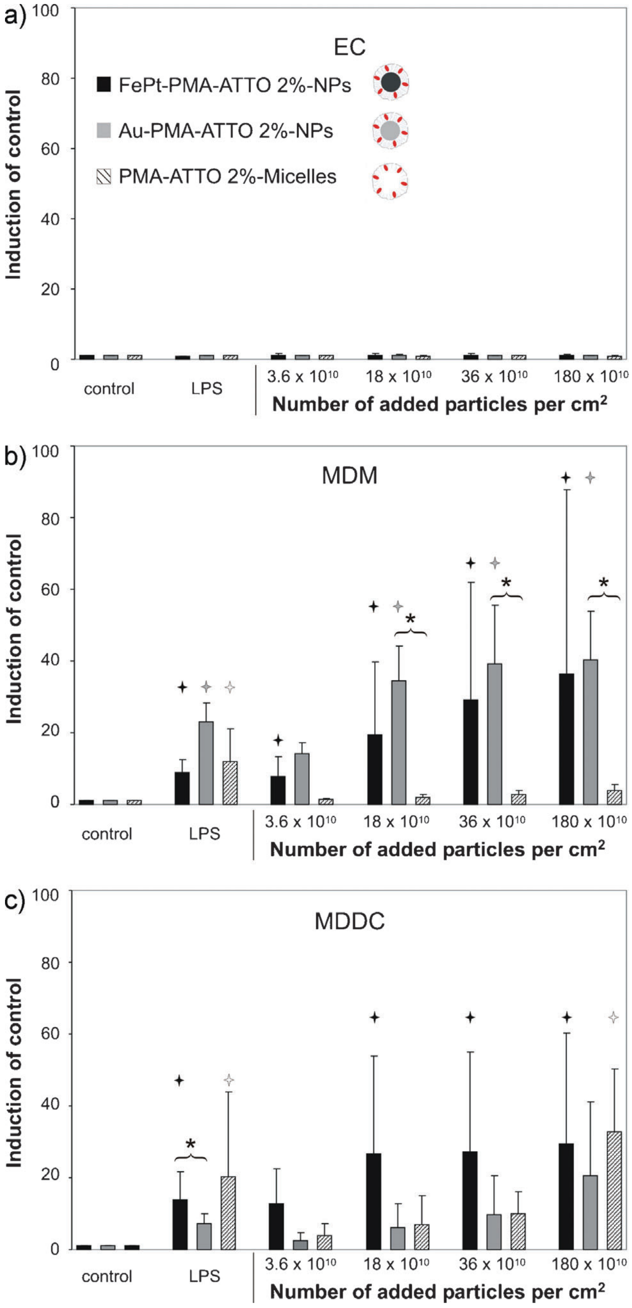

Figure 6. Dose-dependent TNFα release upon exposure of monocultures to different NPs for 24 h. TNFα release upon exposure to the three different particles, FePt–PMA–ATTO-2% NPs (black bars), Au–PMA–ATTO-2% NPs (gray bars), and PMA–ATTO-2% micelles (striped bars), are presented as the induction of the control for each monoculture: a) EC, b) MDM, and c) MDDC. Values are presented as means ± SD. Significance was determined with $p \leq 0.05$. Significant dose dependence of particle type versus control is indicated by a black + for FePt–PMA–ATTO-2% NPs, a gray + for Au–PMA–ATTO-2% NPs, and a white + for PMA–ATTO-2% micelles. Differences between particle type for each concentration are marked with *. All experiments were independently performed between 3 and 11 times.

ATTO-2% NPs) induced a dose-dependent increase in TNFα release (Figure 8a). Again, no effect was found for the PMA–ATTO-2% micelles. Interestingly, no differences in TNFα release for the different particle types and concentrations could be found in the lower chamber (Figure 8b).

3. Discussion

NPs offer new approaches in diagnostics, due to their small size, high surface-to-volume ratio, stability in solvents, and ability to modify their surface.[29] As an example, hybrid magnetic-core–shell NPs are of high interest because their application field includes imaging by TEM, fluorescence, and also MRI, and/or a combination of these techniques. However, as yet, these NPs are rarely used because of uncertainties

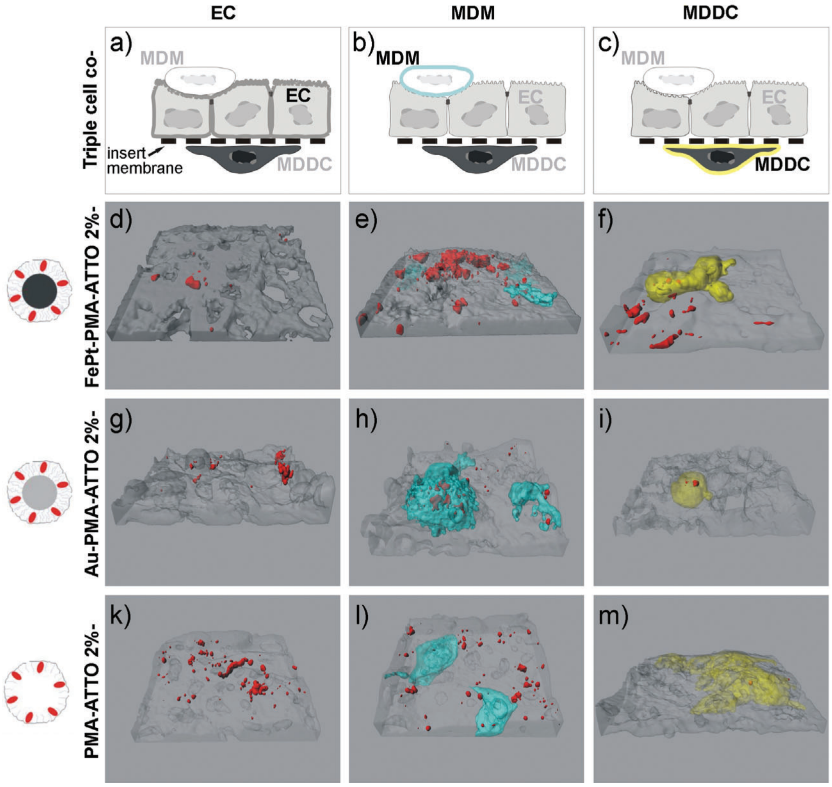

Figure 7. Visualization of the different particles in the triple-cell coculture model. a–c) Schematic views of the triple-cell coculture model in which the corresponding examined cell type is highlighted in color. Columns present results for a,d,g,k) EC (gray), b,e,h,l) MDM (light blue), and c,f,i,m) MDDC (yellow). All visualized particles and micelles, FePt–PMA–ATTO-2% NPs (d–f), Au–PMA–ATTO-2% NPs (g–i), PMA–ATTO-2% micelles (k–m), are shown in red.

concerning the fate of the NPs after being internalized in the human body and possible health effects. The development of novel, inhalable nanomaterial-based therapeutic and diagnostic applications in the respiratory tract requires a careful examination of possible toxic effects.

The aim of this study was to determine the localization and colocalization of a specifically designed magnetic core–shell NP[30] in relation to the dose-dependent proinflammatory response in different monocultures of lung cells. as well as in a more realistic triple-cell coculture model of the epithelial airway barrier.[19] Two NP types with different cores but the same shell were examined and compared to the shells only to investigate which part of the magnetic core–shell particle induces a proinflammatory response in lung cells.

Data obtained with TEM as well as LSM imaging techniques confirmed the uptake and intracellular localization of the FePt–PMA–ATTO-2% and Au–PMA–ATTO-2% NPs in all culture and cell types investigated here. This is in agreement with other studies where polystyrene NPs, titanium dioxide, gold NPs,[31] diesel-exhaust particles, or carbon nanotubes[32] were detected in all cell types of monocultures and triple-cell co-cultures.

Since a dose-dependent proinflammatory response was measured, the colocalization of NPs with intracellular structures, such as lysosomes or mitochondria, was studied as both organelles are important for the induction of an inflammatory signal. All NPs used in the current investigations were detected inside vesicles by TEM and inside lysosomes, which were stained with Lysotracker, by LSM. In other studies, NPs with electron-dense cores have been detected using TEM in lysosomal vesicles in monocultures of murine-bone-marrow-derived dendritic cells of mice and HeLa cells, respectively.[33–35] Other studies have shown NPs colocalized with lysosomes.[33,34,36,37] In vitro experiments have revealed the penetration of combustion-derived NPs into the mitochondria of macrophages and epithelial cells. This process was associated with oxidative stress and mitochondrial damage.[38] In the current experiments, colocalization of NPs with mitochondria was not observed. However, as the particles carry no signaling sequences, such as a mitochondrial import sequence, for example, it might be impossible for the NPs to be imported into the mitochondria. Quantum dots coupled to a nuclear or mitochondrial targeting ligand could be directed to the nuclear compartment and mitochondria, respectively.[39] A recent study investigated the localization of negatively charged, carboxylated polystyrene particles (20 nm in diameter) in primary and hepatocyte cell lines in vitro.[40] No colocalization of the NPs either with early endosomes or with lysosomes was found but a colocalization with mitochondria was reported. A similar staining and visualization procedure was used but neither deconvolution nor a quantitative colocalization was performed as we have done in our study.

The amount of particles incorporated per cell was approximated by LSM combined with digital-image restoration. The authors are aware that the resolution limit of light microscopy prevents distinguishing between single particles and small NP agglomerates. It is also well known that particles inside cells are clustered in small vesicular structures, whereby each vesicle can contain multiple particles.[41] Therefore, ''particle events'' were counted, where one particle event corresponds to an individual vesicular structure containing NPs. Thus, relative differences in the amount of incorporated particles per cell could be quantified. It was found that only 1% of the added particles penetrated into cells (data not shown). This could be due to the fact that the particles in suspension behave in a diffusion rather than sedimentation manner.[42] The aggregation assay showed that the NPs were present as single particles during the 24-h incubation time. Within the cells, however, large aggregates were found in vesicles of the endosomal pathway.

Based on the analysis of the dose-dependent amount of particles in the three cell types (EC, MDM, and MDDC), a different uptake pattern in the various cell types was inferred. By considering the cell function in the human epithelial airways,

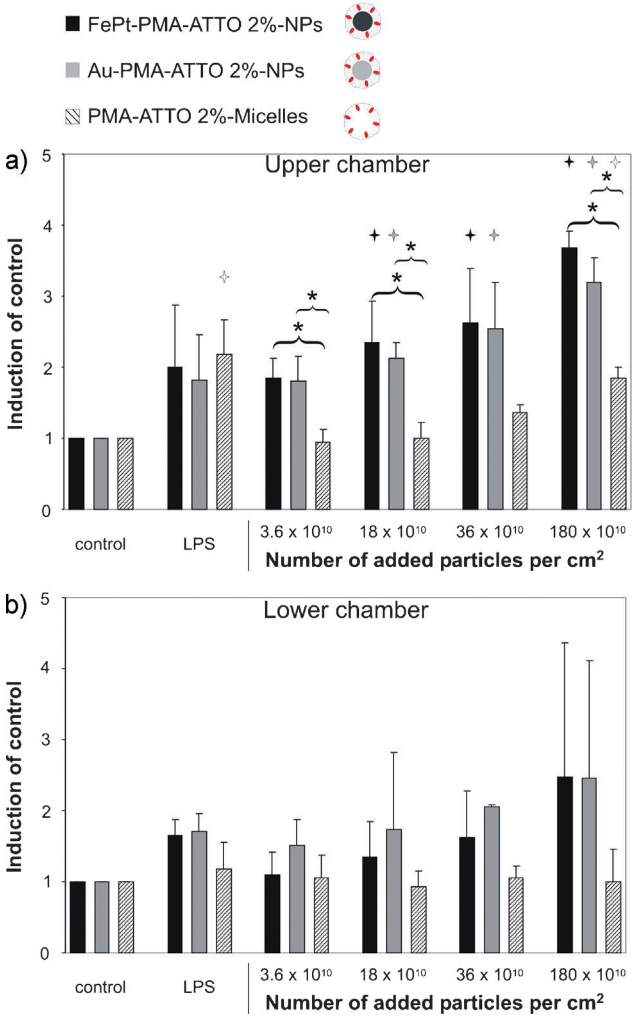

Figure 8. Dose dependence of TNFα release upon exposure of the triple-cell coculture model to different NPs for 24 h. TNFα release upon exposure to the three different particles, FePt–PMA–ATTO-2% NPs (black bars), Au–PMA–ATTO-2% NPs (gray bars), and PMA–ATTO-2% micelles (striped bars), are presented as the induction of the control in a) the upper chamber and b) the lower chamber. Values are presented as means ± SD. Significance was determined with $p \leq 0.05$. Dose dependence of particle type versus control is expressed with a black + for FePt–PMA–ATTO-2% NP, a gray + for Au–PMA–ATTO-2% NP, and a white + for PMA–ATTO-2% micelles. Differences between particle type for each concentration are marked with *. All experiments were independently performed in triplicate.

it is reasonable that more particle events were counted in MDM and MDDC than in EC. The macrophages reside on top and the dendritic cells at the base, with the epithelial cell layer in between. They act as professional phagocytes and professional antigen-presenting cells, respectively.[43,44] The latter show a high phagocytotic activity in the immature state but lose this function with maturation.[45,46] The EC showed enhanced particle uptake per cell in a dose-dependent manner, which is in agreement with the study of Qaddoumi et al.,[47] who showed that primary air-interface cultures of rabbit conjunctival epithelial cells take up fluorescently labeled poly-(D,L-lactide-*co*-glycolide) NPs (100 nm). Previously, it has also been described that, in the triple-cell coculture model, which mimics the airway barrier, only a few 1-μm as well as nanometer-sized polystyrene beads were detected in EC compared to MDM and MDDC after 24-h incubation.[31] These findings support the differences in uptake behavior of the same three cell types in this study. We could show that macrophages in monoculture, as well as in the triple-cell coculture model, take up NPs to a high extent, in contrast to that reported before.[48] A dose- and time-dependent uptake of Fe_3O_4 magnetic NPs was shown in another study using the HeLa cell line.[49] At lower particle concentrations, MDM showed a higher particle uptake than MDDC. This is based on the finding that immature MDDC possess a phagocytotic capacity that is lower than that of peripheral blood monocytes and alveolar macrophages but higher than that of mature dendritic cells.[45] Another study revealed a difference in the phagocytic activities of MDM and MDDC after exposure to surface-modified polystyrene particles of a different size and charge,[50] suggesting that the phagocytic activity of both cells is dependent on particle size and surface charge. Interestingly, the two cell types of the defense system showed distinctly different uptake behaviors. While the MDDC exhibited a linear dose-dependent particle uptake, the MDM showed a faster initial uptake that saturated at higher concentrations. For dendritic cells, a dose-dependent linear NP uptake has already been shown by Demento and coworkers.[51] They localized the internalized particles by means of channel fluorescence. Sallusto and coworkers[52] found that MDDC use two distinct mechanisms for capturing antigen: one is fluid-phase uptake via macropinocytosis, which showed a constitutive manner, and the other is a receptor-mediated mechanism. The first is thought to be unsaturable with respect to the capture of any soluble antigens and the latter showed a selective and saturable way of taking up antigens. Due to the small size of our particles, the current findings could be compared to the cell dye Lucifer yellow,[52] which exhibited a nonsaturating uptake.

Interestingly, only a small percentage of the particle events were localized in lysosomes. Steinman and Swanson[53] have already found that dendritic cells do not readily accumulate solutes and particles in lysosomes, which would support the current findings. The TEM images of the EC showed that the particles are mostly localized in vesicles. However, it might be possible that single particles or small aggregates in other compartments could not be detected.

In addition to observing the cellular uptake of the FePt–PMA–ATTO-2% NPs and colocalization with lysosomes, we performed experiments to determine whether the particles can induce a proinflammatory response. No TNFα release was found in EC, neither upon export to NPs nor LPS. This is in agreement with other studies, in which proinflammatory release of TNFα in EC was absent.[54,55] In MDM and MDDC, the particles caused a dose-dependent proinflammatory response after incubation for 24 h but not after 1 h. Additionally, NPs prepared with a gold core but with the same shell and also the shells only were included to determine which part of the particle may cause the proinflammatory response. A gold core was chosen because gold NPs are already used in nanomedical applications[56] and because several publications have highlighted gold as a nonproinflammatory agent.[57,58] Until now, no study has been reported that investigates exactly the same particle type as used here. However, an enhanced TNFα response has been reported after exposure of human primary monocytes and macrophages to quantum dots or magnetic NPs, with similar incubation times as used in the current study.[37,59] Similar findings were also shown by Guildord et al. with iron NPs.[60] A study examined the TNFα release after exposure to nanometer- and micrometer-sized silicon particles in RAW 264.7 macrophages. The nanometer-sized particles showed no dose-dependent enhanced release of TNFα but the micrometer-sized particles did.[61]

Similar to the NP uptake of the three cell types in monoculture, the proinflammatory response to the different NPs was cell specific. EC alone showed no increased TNFα release, whereas MDM and MDDC did. When EC, MDM, and MDDC were combined in the triple-cell coculture model, a TNFα release was observed already at lower NP doses but the TNFα concentrations were always less than in the monocultures. This difference can be explained by the amount of MDM and MDDC, which is remarkably reduced in the triple-cell coculture model compared to the monocultures. MDM monocultures showed a dose-dependent TNFα response after exposure to FePt–PMA–ATTO-2% NPs and Au–PMA–ATTO-2% NPs but not to the PMA–ATTO-2% micelles. The same was found in the supernatant of the upper chamber in the triple-cell coculture system, which actually consists of a combination of the EC and MDM.

Interestingly, the micelles used as the shell material induced no proinflammatory response in MDM but did in MDDC. Therefore, it is thought that each cell type reacts in a different way to the different particle types. The fluorescent dye embedded in the shell does not have an influence on the proinflammatory response. Moreover, in some cases, a combination of the core and shell material is responsible for the release of a proinflammatory reaction, as seen for MDDC, but in other cases the proinflammatory reaction could be mainly due to the core particle, as was found for MDM.

4. Conclusions

We may conclude that particle uptake as well as the proinflammatory response after exposure to a specifically designed core–shell NP for nanomedical applications is cell-type and cell-culture-type dependent and that the incubation time plays an important role. Moreover, very similarly designed NPs exhibit different proinflammatory responses in a particular cell type or cell-culture type. The core–shell particles seem to be more proinflammatory reactive than the shell only, indicating that the choice of the core is very important. Although the magnetic and fluorescent functionality would be practical in the field of biomedical applications, the observed proinflammatory potential shown upon particle exposure demands further basic experiments with these NPs to further investigate their toxic potential. Furthermore, the fate of the internalized particles has to be considered as well as long-term exposure.

5. Experimental Section

16HBE14o- monocultures: The 16HBE14o- bronchial epithelial cell line was used as described in earlier studies[28] and in the Supporting Information. The 16HBE14o- cells were kindly provided by Dr. Gruenert (University California, San Francisco).

MDM and MDDC monocultures: MDM and MDDC were obtained from human peripheral blood monocytes as described in Reference [52]. Further details are given in the Supporting Information. When the cells were used for live-cell image experiments, adhered MDM and MDDC were removed carefully with a cell scraper (Sarstedt, Sevelen, Switzerland) and 2 mL of each cell suspension was transferred into two-chambered cover-glass slides (Nunc, Fisher Scientific AG, Wohlen, Switzerland) at least 24 h prior to particle exposure.

Triple-cell cocultures: The triple-cell cocultures were prepared as previously described.[28] Details are provided in the Supporting Information.

Particle preparation and characterization: Detailed information about the preparation and characterization of the particles have been given by Lin et al.[30] A sketch of the three different samples is shown in Figure 1. At this point, it should be noted that the determination of the concentration of the particles is not trivial and is subject to significant errors. A detailed discussion of the synthesis and the concentration determination can be found in the Supporting Information.

Determination of the hydrodynamic radius and the aggregation assay of the different NP types: Hydrodynamic radii were determined by FCS using a home-built instrument, as previously described,[62] with minor adaptations to the spectral properties of the particles used here. Briefly, the 532-nm excitation light of a DPSS laser (Excelsior 532, Newport Spectra Physics, Mountain View, CA) was delivered to the back port of an epifluoresence microscope (Axiovert 200, Carl Zeiss, Göttingen, Germany). The light emitted from the sample was collected by a water-immersion objective (UPLAPO 60×/1.2w, Olympus, Hamburg, Germany), passed through a dichroic mirror (z 532 RDC, AHF, Tübingen, Germany) and a band-pass filter (HQ 545 LP, AHF), and focused onto a 62.5-μm-diameter gradient-index fiber (Thorlabs, Newton, NJ, USA), which acts as a confocal pinhole. The fluorescence signal was detected by an avalanche photodiode (SPCM-CD3017, Perkin Elmer, Fremont, CA) and processed by a digital correlator (ALV-5000/E, ALV, Langen, Germany). All measurements were performed in a temperature-controlled laboratory at 22 °C using an excitation power of ≈10 μW. Rhodamine 6G (Invitrogen, Karlsruhe, Germany) in water at 22 °C was used as a reference standard with a diffusion coefficient of 3.82×10^{-10} m^2 s^{-1}, which was calculated from the recently determined value at 25 °C.[63]

For aggregation studies, samples were incubated for 24 h in PBS or medium and subsequently passed through centrifugation filters (300 kDa, Pall Nanosep, Ann Arbor, MI) and gel-filtration cartridges (Edge BioSystems, Gaithersburg, MD) for removal of large aggregates and buffer exchange, respectively. By comparison with freshly prepared, but otherwise identically treated samples, the particle loss due to the formation of large aggregates during incubation was characterized by FCS.

Particle exposure of cell cultures of MDM, MDDC, and EC: All cell cultures were exposed to either different particle concentrations or 10 μg mL^{-1} LPS (Sigma, Buchs Switzerland) directly diluted in culture medium.

Prior to particle exposure, the culture medium was removed and 400 μL of fresh, prewarmed culture medium without serum, in which the different particles as well as the fluorescence dye only were diluted from the stock solution of 67 nM to the final concentrations of 8×10^{10}, 40×10^{10}, 80×10^{10}, and 400×10^{10} particles mL^{-1} (corresponding to 3.6×10^{10}, 18×10^{10}, 36×10^{10}, and 180×10^{10} particles per unit surface area of the culture dish in cm^2), was added to the cells. Prior to the incubation, all particle solutions were sonicated for 2 min to avoid aggregation. An incubation time of either 1 h or 24 h was chosen for all particles and cell cultures.

Cell fixation and labeling for LSM: After the exposure, the cells were fixed and stained as described in Reference [64] and the Supporting Information. Antibodies were diluted in PBS as follows: mouse anti-human CD14 1:20 (Clone UCHM-1, C 7673, Sigma), mouse anti-human CD86 1:20 (Clone HB15e, 36931A, PharMingen, BD Biosciences), goat anti-mouse cyanine 5 1:50 (AP124S, Chemicon, VWR International AG, Life Sciences, Lucerne, Switzerland), and phalloidin rhodamine 1:100 (R-415, Molecular Probes, Invitrogen AG, Basel, Switzerland).

Unfixed cells were used for visualization of the particles and cell imaging of EC, MDM, and MDDC monocultures with Mitotracker and Lysotracker staining. They were stained and examined immediately in two-chamber coverglass slides. For the labeling of mitochondria and lysosomes, the commercial dyes Mitotracker Deep Red 633 (Invitrogen AG, Basel, Switzerland) and Lysotracker Yellow-HCK-123 (Invitrogen AG, Basel, Switzerland) were used. For staining the cells, Vybrant cell-labeling solutions were used according to the manufacturer's protocol. After removing the cell medium, the prewarmed staining solutions were added to the adhered cells. They were incubated for 15 min at 37 °C in a 5%-CO$_2$-humidified atmosphere. Afterwards, the staining solution was removed and the monocultures were washed twice with prewarmed PBS. Cell imaging was performed after adding prewarmed PBS to the cells.

LSM and image restoration: Optical sections were taken on a Zeiss LSM 510 Meta with an inverted Zeiss microscope (Axiovert 200M; Lasers: 633-nm HeNe, 543-nm HeNe, and 488-nm Ar) using a Plan-Apochromat 63 ×/1.4 objective and a digital zoom. The resulting voxel size was 0.07 μm × 0.07 μm × 0.25 μm. For image processing of unfixed cells, visualization and colocalization of particles either with lysosomes or with mitochondria was performed using IMARIS, a 3D multichannel image processing software for confocal microscopy images (Bitplane AG, Zurich, Switzerland). The same methods were used for fixed-cell examinations. For particle localization, visualization, and colocalization at high resolution, a deconvolution algorithm was applied using the Huygens 2 software (Scientific Volume Imaging B. V., Hilversum, Netherlands) in order to increase the axial and lateral resolutions and to decrease noise.[27]

Particle quantification: After image acquisition, the total particle number and the number of particles colocalized with lysosomes and mitochondria were counted with the particle-tracking software Diacount (Semasopht, Lausanne, Switzerland). In each experimental sample, the cells were randomly scanned by LSM. Experiments were performed in triplicate or quadruplicate, and 10–12 cells were scanned for each data point. The particles were counted within individually defined cell types. All counted particles and colocalization were expressed as particle events and colocalized events, respectively, because the resolution limit was lower than the particle size. Actually, the events referred to the number of voxels.

Cytokine detection: Following particle incubation, supernatants of the cell cultures from the two-chamber slides (EC, MDM, and MDDC monocultures) and from the upper and lower chamber (triple-cell cocultures) were collected separately and stored at −70 °C. After centrifugation, the TNFα concentration was quantified by a commercially available DuoSet ELISA, as described in Reference [32] and the Supporting Information.

TEM: For TEM analysis, cells were fixed and prepared as described in Reference [28] and in the Supporting Information.

Statistics: ELISA results were normalized to the untreated control cells and are expressed as mean values with the standard deviation of the mean (SD). The statistical analysis was performed using SigmaStat for Windows (version 3.10, Systat Software, Inc., Richmond, California, USA) statistical software. For internal group comparison, an ANOVA with a Bonferroni posthoc test (compared to the untreated control cells) was performed if the data was normally distributed. If the distribution was not normal, an ANOVA on ranks with a Dunn's posthoc test (compared to the untreated control cells) was performed. For comparing the data of the three particle types in a cell culture, an ANOVA on ranks with the Dunn's posthoc with a pairwise comparison was run. In all cases, $p < 0.05$ was considered significant.

Acknowledgements

We are grateful to Abbasi Azhar Zahoor for the synthesis of the FePt NPs cores and thank Barbara Tschirren, Andrea Stokes, and Mohammed Ouanella for their excellent technical assistance. We thank Kirsten Dobson for comments on the manuscript. The project was funded by the German Research Foundation (DFG SPP 1313) and the Swiss National Foundation (Nr. 3100A0_118420). We also thank Bitplane AG, Switzerland, for covering partial cost of the inside cover image.

---

[1] U. I. Tromsdorf, N. C. Bigall, M. G. Kaul, O. T. Bruns, M. S. Nikolic, B. Mollwitz, R. A. Sperling, R. Reimer, H. Hohenberg, W. J. Parak, S. Forster, U. Beisiegel, G. Adam, H. Weller, *Nano Lett.* **2007**, *7*, 2422–2427.
[2] O. T. Bruns, H. Ittrich, K. Peldschus, M. G. Kaul, U. I. Tromsdorf, J. Lauterwasser, M. S. Nikolic, B. Mollwitz, M. Merkel, N. C. Bigall, S. Sapra, R. Reimer, H. Hohenberg, H. Weller, A. Eychmuller, G. Adam, U. Beisiegel, J. Heeren, *Nat. Nanotechnol.* **2009**, *4*, 193–201.
[3] W. J. Mulder, G. J. Strijkers, G. A. van Tilborg, A. W. Griffioen, K. Nicolay, *NMR Biomed.* **2006**, *19*, 142–164.
[4] M. Ettenauer, T. Posnicek, M. Brandl, V. Weber, D. Falkenhagen, *Biomacromolecules* **2007**, *8*, 3693–3696.

[5] A. Quarta, R. Di Corato, L. Manna, A. Ragusa, T. Pellegrino, *IEEE Trans. Nanobiosci.* **2007**, *6*, 298–308.
[6] A. Quarta, R. Di Corato, L. Manna, S. Argentiere, R. Cingolani, G. Barbarella, T. Pellegrino, *J. Am. Chem. Soc.* **2008**, *130*, 10545–10555.
[7] J. Kim, H. S. Kim, N. Lee, T. Kim, H. Kim, T. Yu, I. C. Song, W. K. Moon, T. Hyeon, *Angew. Chem. Int. Ed.* **2008**, *47*, 8438–8441.
[8] M. Liong, J. Lu, M. Kovochich, T. Xia, S. G. Ruehm, A. E. Nel, F. Tamanoi, J. I. Zink, *ACS Nano* **2008**, *2*, 889–896.
[9] R. E. Anderson, W. C. Chan, *ACS Nano* **2008**, *2*, 1341–1352.
[10] T. Pellegrino, L. Manna, S. Kudera, T. Liedle, D. Koktysh, A. L. Rogach, S. Keller, J. Rädler, G. Natile, W. J. Parak, *Nano Lett.* **2004**, *4*, 703–707.
[11] G. Oberdorster, E. Oberdorster, J. Oberdorster, *Environ. Health Perspect.* **2007**, *115*, A290.
[12] G. Oberdorster, A. Maynard, K. Donaldson, V. Castranova, J. Fitzpatrick, K. Ausman, J. Carter, B. Karn, W. Kreyling, D. Lai, S. Olin, N. Monteiro-Riviere, D. Warheit, H. Yang, *Part. Fibre Toxicol.* **2005**, *2*, 8.
[13] A. Nel, T. Xia, L. Madler, N. Li, *Science* **2006**, *311*, 622–627.
[14] C. Muhlfeld, B. Rothen-Rutishauser, F. Blank, D. Vanhecke, M. Ochs, P. Gehr, *Am. J. Physiol. Lung Cell. Mol. Physiol.* **2008**, *294*, L817–L829.
[15] K. Unfried, U. Sydlik, K. Bierhals, A. Weissenberg, J. Abel, *Am. J. Physiol. Lung Cell. Mol. Physiol.* **2008**, *294*, L358–L367.
[16] B. Rothen-Rutishauser, L. Mueller, F. Blank, C. Brandenberger, C. Muehlfeld, P. Gehr, *ALTEX* **2008**, *25*, 191–196.
[17] B. Rothen-Rutishauser, F. Blank, C. Muhlfeld, P. Gehr, *Expert Opin. Drug Metabol. Toxicol.* **2008**, *8*, 1075–1089.
[18] M. T. Fernandez-Arguelles, A. Yakovlev, R. A. Sperling, C. Luccardini, S. Gaillard, A. S. Medel, J. M. Mallet, J. C. Brochon, A. Feltz, M. Oheim, W. J. Parak, *Nano Lett.* **2007**, *7*, 2613–2617.
[19] B. M. Rothen-Rutishauser, S. G. Kiama, P. Gehr, *Am. J. Respir. Cell Mol. Biol.* **2005**, *32*, 281–289.
[20] L. Zemanova, A. Schenk, M. J. Valler, G. U. Nienhaus, R. Heilker, *Drug Discov. Today* **2003**, *8*, 1085–1093.
[21] R. Rieger, C. Röcker, G. U. Nienhaus, *Am. J. Phys.* **2005**, *73*, 1129–1134.
[22] C. Rocker, M. Potzl, F. Zhang, W. J. Parak, G. U. Nienhaus, *Nat. Nanotechnol.* **2009**, *4*, 577–580.
[23] B. D. Chithrani, A. A. Ghazani, W. C. Chan, *Nano Lett.* **2006**, *6*, 662–668.
[24] P. Nativo, I. A. Prior, M. Brust, *ACS Nano* **2008**, *2*, 1639–1644.
[25] J. M. de la Fuente, C. C. Berry, *Bioconjug. Chem.* **2005**, *16*, 1176–1180.
[26] *The Toxicology of Particles* (Eds.: K. Donaldson, P. Borm), CRC Press, Boca Raton, FL **2007**.
[27] B. Rothen-Rutishauser, S. D. Kramer, A. Braun, M. Gunthert, H. Wunderli-Allenspach, *Pharm. Res.* **1998**, *15*, 964–971.
[28] F. Blank, B. M. Rothen-Rutishauser, S. Schurch, P. Gehr, *J. Aerosol Med.* **2006**, *19*, 392–405.
[29] P. R. Gil, W. J. Parak, *ACS Nano* **2008**, *2*, 2200–2205.
[30] C. A. Lin, R. A. Sperling, J. K. Li, T. Y. Yang, P. Y. Li, M. Zanella, W. H. Chang, W. J. Parak, *Small* **2008**, *4*, 334–341.
[31] B. Rothen-Rutishauser, C. Muhlfeld, F. Blank, C. Musso, P. Gehr, *Part. Fibre Toxicol.* **2007**, *4*, *9*.
[32] L. Muller, M. Riediker, P. Wick, M. Mohr, P. Gehr, B. Rothen-Rutishauser, *J. R. Soc. Interface* **2010**, *S1*, S27–S40.
[33] D. Sen, T. J. Deerinck, M. H. Ellisman, I. Parker, M. D. Cahalan, *PLoS One* **2008**, *3*, e3290.
[34] H. Y. Nam, S. M. Kwon, H. Chung, S. Y. Lee, S. H. Kwon, H. Jeon, Y. Kim, J. H. Park, J. Kim, S. Her, Y. K. Oh, I. C. Kwon, K. Kim, S. Y. Jeong, *J. Controlled Release* **2009**, *135*, 259–267.
[35] K. Muller, J. N. Skepper, M. Posfai, R. Trivedi, S. Howarth, C. Corot, E. Lancelot, P. W. Thompson, A. P. Brown, J. H. Gillard, *Biomaterials* **2007**, *28*, 1629–1642.
[36] M. S. Cartiera, K. M. Johnson, V. Rajendran, M. J. Caplan, W. M. Saltzman, *Biomaterials* **2009**, *30*, 2790–2798.
[37] H. M. Lee, D. M. Shin, H. M. Song, J. M. Yuk, Z. W. Lee, S. H. Lee, S. M. Hwang, J. M. Kim, C. S. Lee, E. K. Jo, *Toxicol. Appl. Pharmacol.* **2009**, *238*, 160–169.
[38] N. Li, C. Sioutas, A. Cho, D. Schmitz, C. Misra, J. Sempf, M. Wang, T. Oberley, J. Froines, A. Nel, *Environ. Health Perspect.* **2003**, *111*, 455–460.
[39] A. Hoshino, K. Fujioka, T. Oku, S. Nakamura, M. Suga, Y. Yamaguchi, K. Suzuki, M. Yasuhara, K. Yamamoto, *Microbiol. Immunol.* **2004**, *48*, 985–994.
[40] H. J. Johnston, M. Semmler-Behnke, D. M. Brown, W. Kreyling, L. Tran, V. Stone, *Toxicol. Appl. Pharmacol.* **2010**, *242*, 66–78.
[41] W. J. Parak, R. Boudreau, M. Le Gros, D. Gerion, D. Zanchet, C. M. Micheel, S. C. Williams, A. P. Alivisatos, C. A. Larabell, *Adv. Mater.* **2002**, *14*, 882–885.
[42] L. K. Limbach, P. Wick, P. Manser, R. N. Grass, A. Bruinink, W. J. Stark, *Environ. Sci. Technol.* **2007**, *41*, 4158–4163.
[43] L. P. Nicod, *Eur. Respir. Rev.* **2005**, *95*, 45–50.
[44] F. Blank, Ch. von Garnier, C. Obregon, P. Gehr, L. P. Nicod, *Expert Rev. Resp. Med.* **2008**, *2*, 215–233.
[45] S. G. Kiama, L. Cochand, L. Karlsson, L. P. Nicod, P. Gehr, *J. Aerosol Med.* **2001**, *14*, 289–299.
[46] E. S. Trombetta, I. Mellman, *Annu. Rev. Immunol.* **2005**, *23*, 975–1028.
[47] M. G. Qaddoumi, H. Ueda, J. Yang, J. Davda, V. Labhasetwar, V. H. Lee, *Pharm. Res.* **2004**, *21*, 641–648.
[48] M. Geiser, M. Casaulta, B. Kupferschmid, H. Schulz, M. Semmler-Behnke, W. Kreyling, *Am. J. Respir. Cell Mol. Biol.* **2008**, *38*, 371–376.
[49] S. Shen, Y. Liu, P. Huang, J. Wang, *J. Nanosci. Nanotechnol.* **2009**, *9*, 2866–2871.
[50] L. Thiele, B. Rothen-Rutishauser, S. Jilek, H. Wunderli-Allenspach, H. P. Merkle, E. Walter, *J. Controlled Release* **2001**, *76*, 59–71.
[51] S. L. Demento, S. C. Eisenbarth, H. G. Foellmer, C. Platt, M. J. Caplan, S. W. Mark, I. Mellman, M. Ledizet, E. Fikrig, R. A. Flavell, T. M. Fahmy, *Vaccine* **2009**, *27*, 3013–3021.
[52] F. Sallusto, M. Cella, C. Danieli, A. Lanzavecchia, *J. Exp. Med.* **1995**, *182*, 389–400.
[53] R. M. Steinman, J. Swanson, *J. Exp. Med.* **1995**, *182*, 283–288.
[54] C. Obregon, B. Rothen-Rutishauser, P. Gerber, P. Gehr, L. P. Nicod, *Am. J. Pathol.* **2009**, *175*, 696–705.
[55] T. Krakauer, *Immunopharmacol. Immunotoxicol.* **2002**, *24*, 113–119.
[56] E. Boisselier, D. Astruc, *Chem. Soc. Rev* **2009**, *38*, 1759–1782.
[57] R. Shukla, V. Bansal, M. Chaudhary, A. Basu, R. R. Bhonde, M. Sastry, *Langmuir* **2005**, *21*, 10644–10654.
[58] C. Brandenberger, B. Rothen-Rutishauser, C. Muhlfeld, O. Schmid, G. A. Ferron, K. L. Maier, P. Gehr, A. G. Lenz, *Toxicol. Appl. Pharmacol.* **2010**, *242*, 56–65.
[59] J. K. Hsiao, T. I. Weng, M. F. Tai, Y. F. Chen, Y. H. Wang, C. Y. Yang, J. L. Wang, H. M. Liu, *J. Nanosci. Nanotechnol.* **2009**, *9*, 1388–1393.
[60] A. L. Guildford, T. Poletti, L. H. Osbourne, A. Di Cerbo, A. M. Gatti, M. Santin, *J. R. Soc. Interface* **2009**, *6*, 1213–1221.
[61] J. Choi, Q. Zhang, V. Reipa, N. S. Wang, M. E. Stratmeyer, V. M. Hitchins, P. L. Goering, *J. Appl. Toxicol.* **2009**, *29*, 52–60.
[62] C. Röcker, M. Pötzl, F. Zang, W. J. Parak, G. U. Nienhaus, *Nat. Nanotechnol.* **2009**, *4*, 577–580.
[63] C. T. Culbertson, S. C. Jacobson, R. J. Michael, *Talanta* **2002**, *56*, 365–373.
[64] F. Blank, B. Rothen-Rutishauser, P. Gehr, *Am. J. Respir. Cell Mol. Biol.* **2007**, *36*, 669–677.

Received: September 21, 2009
Revised: December 21, 2009

NANO MICRO small

Quantitative Evaluation of Cellular Uptake and Trafficking of Plain and Polyethylene Glycol-Coated Gold Nanoparticles

*Christina Brandenberger, Christian Mühlfeld, Zulqurnain Ali, Anke-Gabriele Lenz, Otmar Schmid, Wolfgang J. Parak, Peter Gehr, and Barbara Rothen-Rutishauser**

This study addresses the cellular uptake and intracellular trafficking of 15-nm gold nanoparticles (NPs), either plain (i.e., stabilized with citrate) or coated with polyethylene glycol (PEG), exposed to human alveolar epithelial cells (A549) at the air–liquid interface for 1, 4, and 24 h. Quantitative analysis by stereology on transmission electron microscopy images reveals a significant, nonrandom intracellular distribution for both NP types. No particles are observed in the nucleus, mitochondria, endoplasmic reticulum, or golgi. The cytosol is not a preferred cellular compartment for both NP types, although significantly more PEG-coated than citrate-stabilized NPs are present there. The preferred particle localizations are vesicles of different sizes (<150, 150–1000, >1000 nm). This is observed for both NP types and indicates a predominant uptake by endocytosis. Subsequent inhibition of caveolin- and clathrin-mediated endocytosis by methyl-β-cyclodextrin (MβCD) results in a significant reduction of intracellular NPs. The inhibition, however, is more pronounced for PEG-coated than citrate-stabilized NPs. The latter are mostly found in larger vesicles; therefore, they are potentially taken up by macropinocytosis, which is not inhibited by MβCD. With prolonged exposure times, both NPs are preferentially localized in larger-sized intracellular vesicles such as lysosomes, thus indicating intracellular particle trafficking. This quantitative evaluation reveals that NP surface coatings modulate endocytotic uptake pathways and cellular NP trafficking. Other nonendocytotic entry mechanisms are found to be involved as well, as indicated by localization of a minority of PEG-coated NPs in the cytosol.

Keywords:
- cells
- coatings
- gold
- nanoparticles
- stereology

[*] Dr. B. Rothen-Rutishauser, Dr. C. Brandenberger, Prof. P. Gehr
Institute of Anatomy
University of Bern
Bern 3012 (Switzerland)
E-mail: rothen@ana.unibe.ch

Dr. C. Mühlfeld
Institute of Anatomy and Cell Biology
Justus-Liebig-University Giessen
Giessen 35385 (Germany)

Supporting Information is available on the WWW under http://www.small-journal.com or from the author.

Z. Ali, Prof. W. J. Parak
Fachbereich Physik
Philipps Universität Marburg
Marburg 35032 (Germany)

Dr. A.-G. Lenz, Prof. O. Schmid
Comprehensive Pneumology Center
Institute of Lung Biology and Disease
Helmholtz Zentrum München
Neuherberg 85764 (Germany)

DOI: 10.1002/smll.201000528

F 1

1. Introduction

Nanoparticles (NPs; <100 nm in all three dimensions, ISO/TS 27687:2008) show promising features for pharmaceutical applications,[1,2] especially for targeted drug delivery,[3,4] biomedical imaging,[5] or biosensing.[6] However, biomedical applications require a detailed understanding of interactions between NPs and biological systems. Upon exposure, NPs may interact with cells and enter them by different mechanisms dependent on their size, material, and surface characteristics.[7] The pathways of entry and the subsequent intracellular particle distribution influence the biological effects caused by particles.[8] To understand a possible relationship between intracellular distribution and induced effects, it is important to investigate the processes involved in cellular uptake of NPs and their intracellular trafficking.

Quantitative uptake studies with different well-characterized NPs indicate that size, shape, surface charge, and coating modify the amount of cellular particle uptake.[9–12] The mechanisms by which particles of different physical and chemical properties enter the cells has also been the subject of diverse investigations, and there is convincing evidence that different mechanisms are involved, such as phagocytosis, macropinocytosis, clathrin-mediated endocytosis, caveolae-mediated endocytosis, and direct entering mechanisms summarized by the term adhesive interactions (reviewed in References [7,13,14]). Besides quantitative and mechanistic uptake studies, there are reports on intracellular particle localizations. Most frequently, NPs have been reported to be found in intracellular vesicles including early and late endosomes, lysosomes, or phagosomes.[15,16] Some studies also report the presence of NPs in the cytosol,[17–19] in mitochondria,[20] and in the nucleus.[18,21] However, so far no quantitative study on relative intracellular particle localization has been performed, with regard to the number of particles associated with intracellular compartments relative to their size. Therefore this study aimed to quantify the relative intracellular distribution of gold NPs over time.

Gold NPs have a broad spectrum of applications in nanomedicine[22] as they are supposedly nontoxic,[23] suitable for biomedical imaging,[5] and they can be coated with medical substrates.[24] Coatings with polyethylene glycol (PEG) are quite often used in nanomedical applications since this material is biocompatible, stabilizes the particles, and reduces their reactivity.[25] Furthermore, it has been shown that PEG coatings can decrease the toxicity of potentially harmful NP materials and simplify particle engineering.[26] However, it is known that surface coatings modify targeting[27] and cellular uptake of gold NPs.[28] For this reason, the study also aimed to compare uptake mechanisms and intracellular trafficking of gold NPs, either coated with PEG or plain (i.e., stabilized in citrate buffer). The gold NPs had a core 15 nm in diameter, since different studies have used similar-sized gold NPs as carriers for drugs or DNA.[3,24,29] In addition, these particles were easily detectable by transmission electron microscopy (TEM) within the cells.

The particles were deposited onto human alveolar epithelial cells (A549 cell line) at the air–liquid interface of the cell culture, by using a recently developed cell exposure system.[30] This system has many advantages compared to suspension experiments. Air–liquid interface cell exposure (ALICE) mimics the physiological conditions of aerosol inhalation in the lungs more realistically and offers a beneficial system for pharmacological and toxicological in vitro studies. The human A549 lung cell line used in this study is well established and can be cultured at the air–liquid interface. After a few hours of maintenance at the air–liquid interface, the cells start producing and secreting surfactant, thus lowering the surface tension and providing a similar microenvironment to that found in pulmonary alveoli.[31] In addition, the ALICE system allows an exact dosimetry and minimizes inadvertent particle effects such as agglomeration and diffusional loss, as it occurs under submerged exposure conditions.[32] Following NP deposition, the cells were exposed to the particles for 1, 4, and 24 h, which allowed the analysis of intracellular NP distribution over time. Since different endocytotic uptake mechanisms were assumed to be involved in cellular NP entry, partial inhibition of endocytotic pathways, such as caveolin- and clathrin-mediated endocytosis, was induced by methyl-β-cyclodextrin (MβCD).[33] For analyzes of intracellular NP distribution, the cells were fixed and processed for TEM. The compartmental localization of the NPs was determined relative to the size of the intracellular compartment by the method of the relative deposition index (RDI).[34] This approach is based on the principles of stereology and enables the identification of preferentially occupied cell compartments as well as the intracellular trafficking of gold NPs.

2. Results

2.1. Relative Particle Distribution within the Cells

The relative intracellular particle distribution of 15-nm gold NPs, plain (i.e., citrate-stabilized) and PEG-coated, was evaluated after particle exposure times of 1, 4, and 24 h by means of stereology on TEM images. The cell compartments that were included in the study were intracellular vesicles, cytoplasm, nucleus, mitochondria, endoplasmic reticulum (ER) or golgi, and residual, defined as the locations that could not be assigned to one of the other compartments. A functional vesicle categorization on the TEM level could not be used for a quantitative approach, due to difficulties in specifically marking all intracellular vesicles. Therefore, we used size-dependent categories (<150, 150–1000, >1000 nm) referring to the size of primary endocytotic vesicles (<150 nm), medium-sized vesicles (between 150 and 1000 nm) such as endosomes or multivesicular bodies, and larger-sized vesicles (>1000 nm) such as phagosomes or lysosomes.[35]

Both plain and PEG-coated NPs were found in vesicles of different sizes (Figure 1A and B), in residual compartments (data not shown), or in the cytoplasm (Figure 1B). With the quantitative analysis described in the Experimental Section, RDI and χ^2 values were obtained for each experimental setting. An RDI > 1 indicates a preferentially populated compartment, that is, more NPs were found than expected for random intracellular NP distribution; an RDI < 1 represents a compartment that contains fewer NPs than expected solely from its size. Using the χ^2 test, it was statistically analyzed whether the

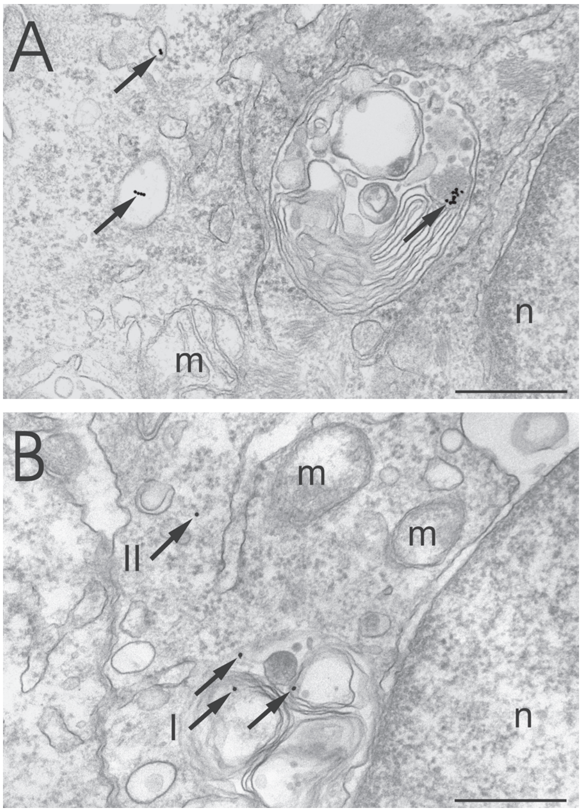

Figure 1. Intracellular compartments where particles were encountered with A) plain gold NPs and B) PEG-coated gold NPs. In (A), the particles (see arrows) are localized within vesicles of different size categories (<150, 150–1000, >1000 nm) and in (B) within a lysosome (arrows I) and in the cytosol (arrow II). n = nucleus, m = mitochondria; scale bars: 500 nm.

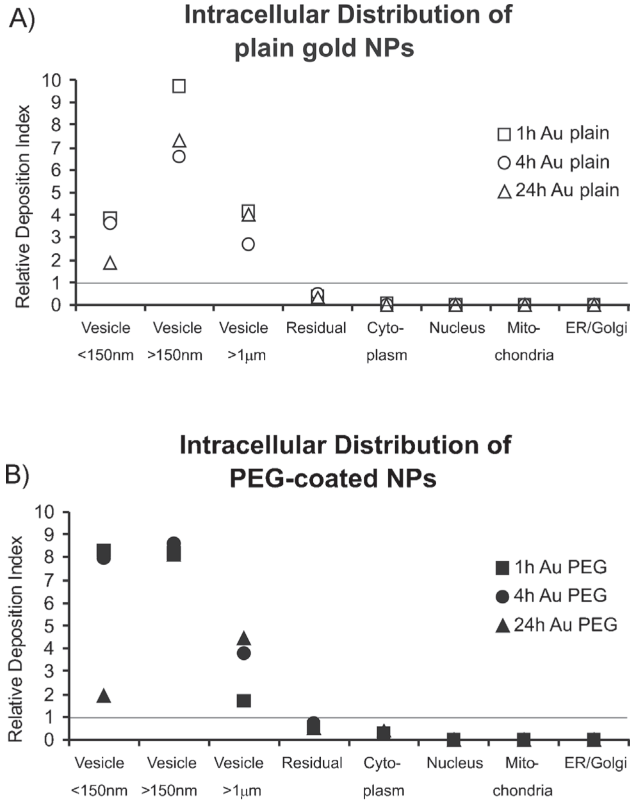

Figure 2. Intracellular particle distribution of A) plain gold (Au) NPs and B) PEG-coated Au NPs after 1, 4, and 24 h post-exposure incubation time. Both particle types showed a significant nonrandom distribution ($p < 0.05$) within the cells with a preference for intracellular vesicles of all three sizes (RDI > 1). A minor fraction of NPs (RDI < 1) was localized in the cytosol and in residual compartments, which could not be assigned to any of the other compartments. No particles were found in the nucleus, mitochondria, and ER/golgi.

particles were equally distributed within the compartments. An example of how the calculations were performed, including the results of intracellular distribution for plain NPs with 1 h exposure time, can be found in the Supporting Information. The total RDI values of all compartments and incubation time points of plain and PEG-coated NPs are shown in Figure 2. Statistical analysis revealed a significant ($p < 0.05$), nonrandom distribution of plain and PEG-coated NPs in the cells. Preferentially targeted compartments (RDI > 1) were vesicles of all sizes, whereas all other compartments such as residuals and cytoplasm showed an RDI < 1. No particles were encountered in the nucleus, mitochondria, and ER or golgi. Table 1 summarizes the RDI and χ^2 values of all compartments and experimental time points.

A further comparison between the relative number of events of plain and PEG-coated NPs and the temporal development of the particle distribution within the cells was statistically analyzed with the χ^2 test (Figure 3A). The plain gold NPs showed no significant change of particle distribution between 1 and 4 h, but a major shift of particles localized in the smallest vesicle fraction (<150 nm) towards the largest (>1000 nm) occurred between 4 and 24 h. A major shift was also observed for the PEG-coated NPs both between 1 and 4 h and also between 4 and 24 h. The middle-sized vesicle fraction (150–1000 nm) remained almost constant over time for both NP types. A comparison between PEG-coated and plain particles is shown in Figure 3B. The distribution of the two NP types after 1 h exposure time differed within all three vesicle sizes and the cytoplasm. However, after 4 and 24 h significantly more plain NPs were localized in the middle-sized vesicle fraction and more PEG-coated NPs were located in the cytoplasm.

2.2. Effects of NP Agglomerates on Uptake and Intracellular Distribution

The largest diameter (henceforth referred to as size) of each particle event (either single NP or agglomerate) was measured and the particle size distribution of single particles and agglomerates was evaluated in terms of the size frequency and how this affected intracellular particle distribution. The relative frequency of agglomerate sizes shows different intracellular agglomeration behavior between the two particle types (see the Supporting Information). At least 94% of the PEG-coated NPs remained as single particles at all time points and no agglomerates >100 nm were detected, whereas an increasing intracellular agglomeration with time was observed for plain NPs: 22% of agglomerates of plain NPs were in the size range of >100 nm in diameter after 1 h incubation time and this

Table 1. RDI and χ^2 test values of all compartments at incubation times of 1, 4, and 24 h for plain NPs (A) and PEG-coated NPs (B).

A: Cell compartments	1 h RDI	1 h χ^2	4 h RDI	4 h χ^2	24 h RDI	24 h χ^2
vesicle <150 nm	3.83	111	3.61	115	1.87	10
vesicle >150 nm	9.71	2882	6.62	1545	7.29	1703
vesicle >1000 nm	4.19	187	2.69	48	4	155
ER/golgi	0	20	0	14	0	14
cytoplasm	0.03	171	0.01	160	0.01	156
nucleus	0	176	0	135	0	119
mitochondria	0	20	0	15	0	15
residual	0.41	21	0.49	12	0.34	19
Total	18.17	3588	13.42	2044	13.51	2191

B: Cell compartments	1 h PEG RDI	1 h PEG χ^2	4 h PEG RDI	4 h PEG χ^2	24 h PEG RDI	24 h PEG χ^2
vesicle <150 nm	8.30	578	7.98	482	1.91	11
vesicle >150 nm	8.20	848	8.60	1499	8.11	1583
vesicle >1000 nm	1.72	4	3.79	92	4.46	204
ER/golgi	0	11	0	14	0	19
cytoplasm	0.30	37	0.27	84	0.39	45
nucleus	0	109	0	142	0	152
mitochondria	0	14	0	16	0	18
residual	0.53	13	0.71	4	0.50	16
Total	19.05	1614	21.35	2333	15.37	2048

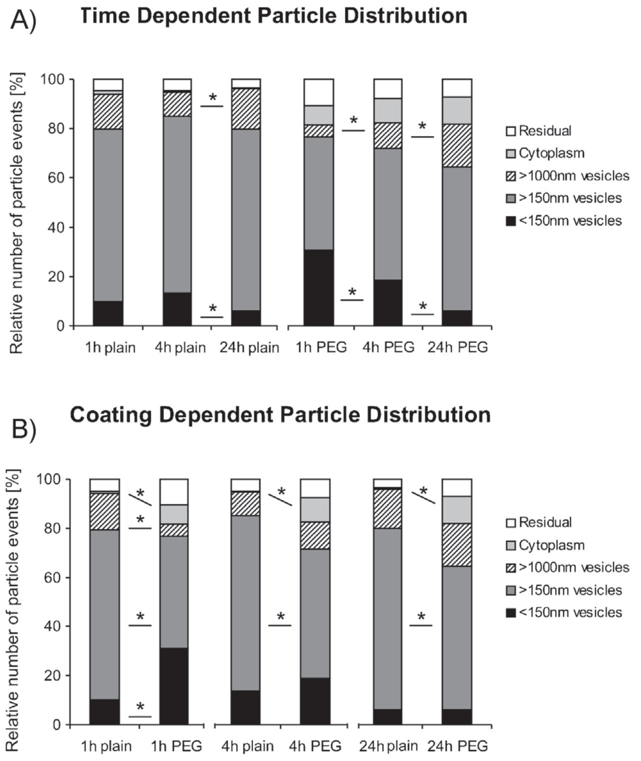

Figure 3. A) Time- and B) coating-dependent intracellular distribution of gold NPs. The time-dependent intracellular distribution (A) of plain NPs revealed a significant ($p < 0.05$) difference between 4 and 24 h, which resulted in a decrease of the smallest vesicle fraction (<150 nm) and an increase in the largest vesicle fraction (>1000 nm). The same shift from smallest towards largest vesicle fraction was observed between all time points for PEG-coated NPs. The surface-coating-dependent intracellular particle distribution (B) revealed a major increase of PEG-coated NPs localized in the cytoplasm and a decrease in the middle-sized vesicle fraction at all time points. There is also a reduced localization in the largest vesicle fraction and an increase in the smallest vesicle fraction of PEG-coated NPs at 1 h. ($* = \chi^2 \geq 10\%$ of total χ^2 value).

fraction increased to 27% after 4 h and to 39% after 24 h. Comparing the relative intracellular distribution of single NPs and small agglomerates (≤100 nm in diameter) with bigger agglomerates (>100 nm in diameter) within the different cellular compartments, it was confirmed that agglomerates >100 nm were predominantly localized in the middle- and larger-sized vesicles (data not shown).

Further experiments were performed to compare the effects of particle agglomeration and diffusion under submerged exposure conditions with those in the ALICE system. Plain particles were mainly present as single particles if suspended in 10 mM citrate buffer, whereas when dissolved in cell culture medium (RPMI 1640 without fetal calf serum) they formed large agglomerates (see Supporting Information). An exposure with particles suspended in cell culture medium, at the same particle number concentration as in the ALICE experiments, resulted in a significant reduction of particles per cell compared to particle uptake in the ALICE. After 4 h of NP exposure in suspension, only 527 (standard deviation (SD) 307) particles/cell were counted, whereas significantly more (i.e., 3575 (SD 689) particles cell^{-1}) could be estimated after using the ALICE system. An increased intracellular particle agglomeration was further observed after submerged exposure. In suspension experiments, only 10.2% single NPs and 36.7% small agglomerates <100 nm were found to be intracellular, whereas in ALICE experiments 22.7% were present as single NPs and 73.2% as agglomerates <100 nm (see the Supporting Information). Hence, suspension experiments with plain NPs lead to an increased formation of agglomerates, which might influence particle uptake mechanisms, as well as a decrease in NP uptake rates due to diffusional NP loss in suspension.

2.3. Endocytosis Inhibition Study

NP-containing vesicles of different sizes were further analyzed qualitatively. As shown in Figure 4, particles were found in lysosomes (Figure 4A), caveosomes (Figure 4B), and

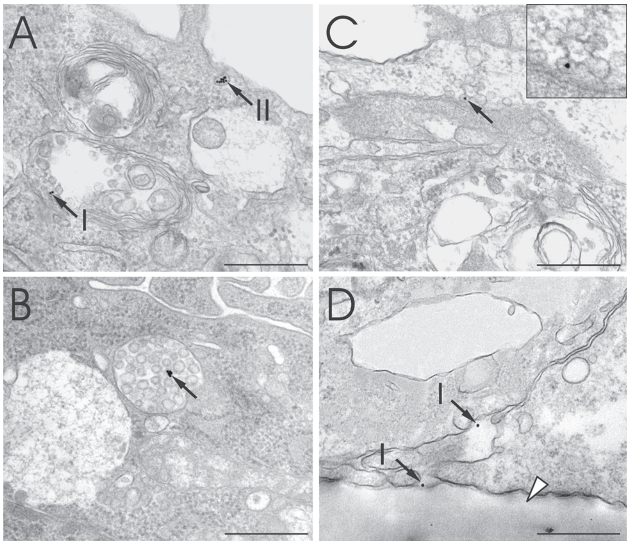

Figure 4. Different intracellular vesicles that can be identified by their morphology. These images are representative for both NP types. A) A small agglomerate of plain NPs in a lysosome (arrow I) and another one in a clathrin-coated pit (arrow II). B) A small particle agglomerate is localized in a multivesicular body (arrow). C) A single plain NP can be found in a caveosome (highlighted by an arrow and at a higher magnification in the inset). D) PEG-coated NPs are located in the intercellular space (black arrows I) at the basal side of the cells (white arrowhead points to the insert membrane on which cells are cultured). Most possibly, NPs have been translocated through the cells by transcytosis. Scale bars: 500 nm.

multivesicular bodies (Figure 4C). Invaginations of the apical plasma membrane, most possibly involved in the process of caveolin- or clathrin-mediated endocytosis (Figure 4A), as well as particle transcytosis through the cell (Figure 4D), were observed. These qualitative observations were confirmed for all time points and both NP types. The particle identification inside vesicular structures was assumed to result from endocytotic uptake processes and the different intracellular vesicles can also be related to specific endocytotic pathways (Figure 5). For this reason, partial inhibition of endocytosis was performed by cholesterol extraction with MβCD.[28] The particle uptake as well as the intracellular distribution of particles was subsequently analyzed by stereological means after 1 and 4 h of incubation. Figure 6 shows the evaluation of the total number of particles taken up per cell. At 1 h, we found 362 (SD 184) compared to 2591 (SD 506) plain NPs taken up per cell with and without inhibition, respectively, and 15 (SD 6) compared to 526 (SD 61) PEG-coated NPs per cell with and without inhibition. At 4 h, the values were 1831 (SD 169) compared to 3575 (SD 689) with and without inhibition, respectively, for the plain NPs and 38 (SD 23) and 1068 (SD 424) for the PEG-coated NPs. Statistical analysis revealed a significantly enhanced uptake rate for plain NPs compared to PEG-coated NPs. This was observed in MβCD-treated and untreated cells. While particle uptake of plain gold NPs significantly increased after 4 h, uptake of PEG-coated NPs was still blocked at 4 h.

The RDI and intracellular distribution with and without inhibition were evaluated, but since the uptake of PEG-coated gold NPs was almost completely blocked, the number of counted intracellular particle events was too small to perform

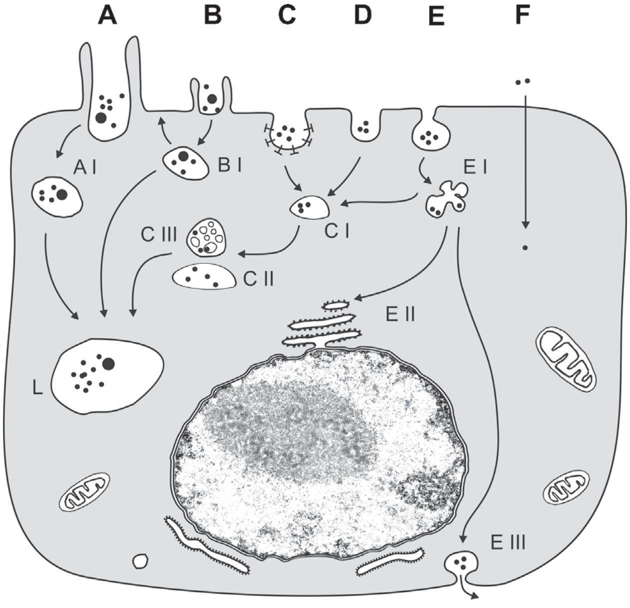

Figure 5. Cellular uptake mechanisms of NPs and related intracellular trafficking. A: Phagocytosis, occurring primarily in professional phagocytes, leading to phagosomes (AI) and phago-lysosomes (L). B: Macropinocytosis, engulfing NPs with poor selectivity, leading to macropinosomes (BI) which might be exocytosed or fused with lysosomes (L). C: Clathrin-mediated endocytosis, forming primary endosomes (CI) and late endosomes (CII) including multivesicular bodies (CIII). D: Clathrin- and caveolae-independent endocytotic pathways. E: Caveolae-mediated endocytosis, forming caveosomes (EI) which fuse with the ER (EII) or translocate through the cell (EIII). F: Particle diffusion/transport through the apical plasma membrane, resulting in particles located freely in the cytosol. The figure and descriptions are adapted from Mühlfeld et al. 2008[39] and Hillaireau and Couvreur 2009,[7] respectively.

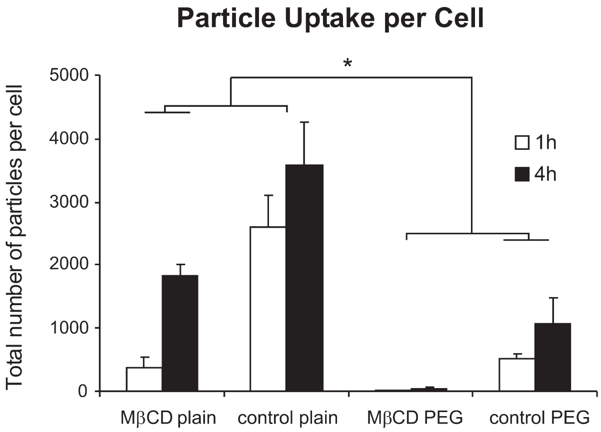

Figure 6. Cellular uptake of plain and PEG-coated NPs with and without inhibition of endocytosis by MβCD. The uptake of plain NPs was significantly increased compared to that of the PEG-coated NPs at both time points, with and without endocytotic inhibition. A significant increase between 1 and 4 h was further observed for plain NPs after endocytotic inhibition and PEG-coated NPs without inhibition. The inhibition resulted in a significantly reduced particle uptake for both particle types; however, it was stronger for PEG-coated NPs (86 and 49% reduction at 1 and 4 h, respectively, for the plain NPs and 97 and 96% reduction at 1 and 4 h, respectively, for the PEG-coated NPs). ($* = p < 0.05$).

statistics. However, the uptake of plain gold NPs was not entirely blocked and intracellular particle distribution was compared with the values without inhibition (Figure 7). A significantly different distribution was found in MβCD-treated cells compared to control cells at both time points. The inhibition resulted in an increase of particles localized in the largest vesicle fraction (>1000 nm), and a decrease in deposition in the middle- and smallest-sized vesicle fractions (<1000 nm).

3. Discussion

Within this study, we analyzed the uptake mechanisms and the intracellular trafficking of either plain (i.e., stabilized with citrate buffer) or PEG-coated (5 kD) 15-nm gold NPs. The particle exposure was performed at the air–liquid interface of cultured human alveolar epithelial cells (A549 cell line). This allowed an exact particle exposure dosimetry and enabled us to directly study and quantify particle–cell interactions. The spatial uniform dispersal of gold NPs onto the cells in the ALICE system was evaluated and diffusional particle loss or increased formation of agglomerates, as occurs under submerged exposure conditions,[32] could be excluded (Supporting Information). Diverse previous studies investigating size- and coating-dependent particle uptake in submerged exposure conditions have not addressed this issue.[9,11,36,37] However, this is of major importance since diffusional particle loss as well as increased particle agglomeration leads to a size-biased particle deposition which influences particle uptake mechanisms and rates.

The quantification of total particle uptake per cell was performed after 1 and 4 h of exposure, since particle uptake was shown to occur mainly within the first 4 h.[23] The later time point, 24 h, was only used to study subsequent intracellular NP distribution. The evaluation of NP uptake rates showed that significantly more plain NPs than PEG-coated NPs enter the cells. Although this was, in part, due to a slightly reduced deposition of the PEG-coated particles in the ALICE system ($16.1 \times 10^9 \pm 1.5 \times 10^9$ plain NPs cm^{-2} and $14.1 \times 10^9 \pm 1.6 \times 10^9$ PEG-coated NPs cm^{-2}), decreased uptake of PEG-coated NPs was still significant after correcting for the reduced deposition. The effect of decreased uptake of PEG-coated particles has also been shown previously.[28] It is further known that PEG-coated particles can remain in the blood circulation for a longer time after intravenous injection, which also indicates reduced cellular uptake from circulation.[38]

The intracellular NP distribution in relation to the relative intracellular compartment size was further assessed with a new quantitative approach, based on stereology, which allows the estimation of three-dimensional structures (number, length, surface, volume) from two-dimensional sections. This approach has been shown to be very beneficial for the intracellular quantification of NPs.[19] However, further analysis with alternative detection methods, such as inductively coupled plasma mass spectrometry (ICP-MS), might also be valuable for a particular understanding of the mechanisms involved in NP uptake and trafficking.

We showed that both plain and PEG-coated 15-nm gold NPs were nonrandomly distributed in the cells, with preference for vesicles of all sizes (82–96% of both NP types). In accordance with other reports on intravesicular particle localization, it has been suggested that NP uptake by cells mainly occurs by endocytotic processes (reviewed in References [7,13,39]). Our findings also indicate that different endocytotic uptake mechanisms are responsible for the observed intravesicular particle localization, since both particle types were found in a variety of vesicular structures that are associated with different endocytotic pathways, such as clathrin- or caveolin-mediated endocytosis (e.g., caveosomes, clathrin-coated pits, multivesicular bodies, or particle transcytosis as shown in Figure 4). A functional characterization of all vesicle types for the quantitative evaluation was not possible on the TEM level. Therefore, vesicles were categorized by size into small-sized endocytotic vesicles (<150 nm), medium-sized vesicles (150–1000 nm) such as endosomes or multivesicular bodies, and larger-sized vesicles (>1000 nm) such as lysosomes or macropinosomes.[35] It has to be noted that in two-dimensional image evaluation the true vesicle size is underestimated, and thus the categories cannot be interpreted as absolute values. However, since underestimation of vesicle size can be assumed to be equal in all experiments, a relative comparison within different experimental conditions is still possible.

The relative comparison within 1, 4, and 24 h exposure time revealed time-dependent particle localization in differently sized vesicles. A significant decrease of particles in the smallest vesicle fraction and an increase of particles in the largest fraction was found with time, thus inferring intracellular trafficking such as from primary endocytotic vesicles towards late endosomes and finally lysosomes[7] (Figure 5). The effect was stronger for PEG-coated particles (significant

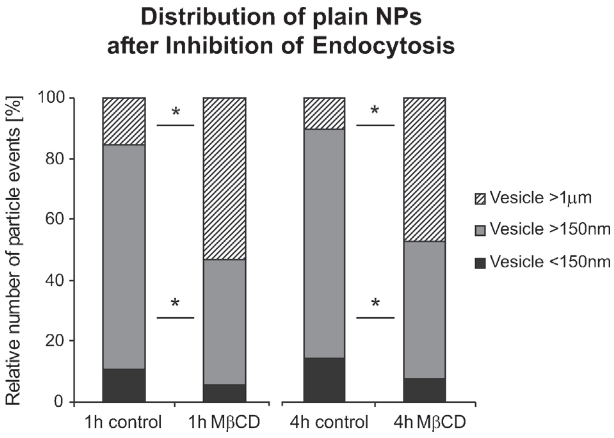

Figure 7. Effects on intracellular particle distribution after inhibition of endocytosis of plain gold NPs. While uptake of PEG-coated NPs was almost completely blocked and no statistics on intracellular distribution could therefore be performed, plain gold NPs were still taken up to a certain extent. However, intracellular particle distribution after MβCD inhibition was significantly different ($p < 0.05$) and resulted in a major particle localization in the largest vesicle fraction (>1000 nm), whereas particle deposition in the middle- and smallest-sized fractions (<1000 nm) was dramatically decreased. This might infer particle uptake via macropinocytosis, thus resulting in particle deposition in larger-sized vesicles compared to primary endocytotic vesicles as from clathrin- or caveolin-mediated endocytosis. ($* = \chi^2 \geq 10\%$ of total χ^2 value).

between 1, 4, and 24 h) than for the plain particles (significant between 4 and 24 h). This might be explained by the different agglomerate size of both particle types. The PEG-coated NPs mostly occurred as single particles in the cells whereas the plain NPs tended to form agglomerates, although they were initially shown to deposit homogeneously onto the cells (see Supporting Information). Regarding the cellular particle entry, it is therefore possible that larger agglomerates of plain particles are taken up by the cells via macropinocytosis, thus being localized in larger-sized vesicles such as macropinosomes after 1 h of exposure.

To further study endocytotic particle uptake and intracellular particle trafficking, we inhibited the endocytotic processes of caveolin- and clathrin-mediated endocytosis by cholesterol extraction via MβCD. Cholesterol extraction mainly acts on caveolin-mediated endocytosis, but was also shown to inhibit clathrin-mediated endocytosis.[33] This inhibition resulted in a significant reduction of the number of particles per cell: 86 and 49% reduction at 1 and 4 h, respectively, for the plain particles and 97 and 96% reduction at 1 and 4 h, respectively, for the PEGylated particles. In particular, the PEG-coated NP uptake was almost completely blocked, which means that either caveolin- or clathrin-mediated endocytosis, or both pathways, are the main mechanisms of internalization for this NP type. We assume that caveolin-mediated endocytosis, which is known to be associated with transcytosis,[35] is mainly involved in PEG-coated NP trafficking, since an increased number of PEGylated NPs were observed between cells or at the basal extracellular side (Figure 4D). The low number of intracellular PEG-coated NPs after inhibition did not allow any further statistical evaluation of their intracellular localization. However, it should be mentioned that not only the vesicular but also the cytosolic localization of PEG-coated NPs was relatively decreased. This implies that either endocytosis is involved in cytoplasmic particle transport or that the changes of apical plasma membrane composition due to cholesterol depletion further affected the cytosolic passage of PEG-coated NPs.

Since the uptake of plain gold NPs was less affected by the inhibition and resulted in a predominant localization in large vesicles, we assume that other uptake mechanisms are involved, such as macropinocytosis or phagocytosis as discussed before. When the total number of plain particles per cell was considered, 14.0 times fewer particles were found in the smallest vesicles, 12.9 times fewer in middle-sized vesicles, but only 2.1 times fewer particles in the largest vesicles of MβCD treated cells (at 1 h). This finding indicates that gold NP localization in the largest vesicle fraction was only marginally affected by MβCD treatment and plain intracellular NPs resulted from macropinocytotic uptake. This would be consistent with the observation of an increased number of plain NPs, localized in larger-sized vesicles such as macropinosomes after 1 h exposure time, compared to PEG-coated NPs as discussed before. Besides the different abilities to form agglomerates, we assume that the potential of protein binding to NPs was responsible for the different cellular uptake and the different distribution of citrate-stabilized and PEG-coated particles. Size, surface charge, and coatings of NPs have been shown to influence particle–protein interactions.[40,41] These interactions might play a key role in the regulation of endocytotic internalization pathways, since many different proteins are associated with a specific uptake mechanism.[42] Plain gold NPs or other charged NPs show a broad spectrum of potential particle–protein interaction,[43,44] whereas PEGylated particles were shown to interact with proteins to a lesser extent.[45] Hence, reduced protein binding could explain the reduced cellular uptake of PEG-coated gold NPs.

A further interesting difference between plain and PEG-coated NPs was the NP localization in the cytosol. Although the cytosol was not the major target compartment (RDI $<$ 1), there was a significantly increased number of PEG-coated NPs localized free in the cytosol compared with plain NPs. While the cytosolic presence of the plain particles can be considered to happen accidentally due to its very rare occurrence (RDI $<<$1), there seems to be a coating-dependent entry pathway to the cytosol for the PEGylated particles. It has previously been reported that PEG-coated particles have the potential to avoid vesicular trafficking and enter the cytosol.[18] The possible explanation for their cytosolic uptake is that PEG can dissolve in both polar and nonpolar solvents, and has a high solubility in cell membranes.[28] Therefore, a transmembrane passage of PEG-coated particles may be considered**.** However, the entry mechanism is not yet entirely understood and needs further investigation.

The other cellular compartments such as nucleus, mitochondria, or ER/golgi that were included in this study did not contain any NPs of either particle type. However, other reports found NPs to be localized in the nucleus[18,21] or in mitochondria.[20] Since their evaluation was not quantitative, it is possible that particles detected in these compartments might be the results of a single observation. Nevertheless, it has been shown that the surface coatings on the particles are responsible for intracellular targeting to cellular compartments, such as the cytosol[17] and the nucleus.[21] It is therefore not surprising that reports of particles entering the nucleus relate to NPs coated with nuclear tracer molecules.[21] This observation could not be confirmed with the 15-nm gold NPs used in the current study; however, no NP coating with nuclear tracers was used.

4. Conclusions

The quantitative evaluation of the intracellular localization of NPs revealed that particle modifications such as PEGylation can influence particle agglomeration, cellular entry mechanisms, and intracellular trafficking. Plain and PEG-coated NPs were found to enter the cells by different endocytotic mechanisms and to be transported over time into larger-sized vesicles such as lysosomes, as described in Figure 5. Plain gold NPs were shown to be taken up by macropinocytosis as well as by clathrin- and caveolin-mediated endocytosis. This might be due to interactions with different proteins or lipids, related to one of the uptake mechanisms, and their increased ability to form agglomerates. The PEG-coated NPs were shown to enter the cells by caveolin- and/or clathrin-mediated endocytosis, but not by macropinocytosis. An increased transcytosis of PEG-coated NPs was further observed and a significant number of PEG-coated NPs were measured free within the cytosol. The latter suggests an endocytosis-independent cellular entry mechanism. These findings show the influence of NP coatings, such as particle PEGylation, on cellular entry mechanisms and subsequent intracellular trafficking. This is of particular importance for the design of new pharmaceutical NPs and their targeting to specific intracellular locations. This study has also demonstrated that the ALICE system and stereological analysis are ideal tools for the evaluation of NP–cell interactions.

5. Experimental Section

Cell cultures: The A549 cell line was obtained from American Tissue Type Culture Collection (LGC Promochem, Molsheim, France). Cells from passage number 5 to 30 were maintained in RPMI 1640 medium (w/25 mM 4-(2-hydroxyethyl)-1-piperazine-ethanesulfonic acid (HEPES), Invitrogen, Karlsruhe, Germany) supplemented with 1% L-glutamine (Invitrogen, Germany), 1% penicillin/streptomycin (Biochrom, Berlin, Germany), and 10% fetal calf serum (FCS; Superior Biochrom, Berlin, Germany). The cells were seeded at a density of 0.5×10^6 cells mL^{-1} on BD Falcon six-well plate cell culture transwell inserts (high-pore-density poly(ethylene terephthalate) (PET) membranes with a growth area of 4.2 cm^2 and 3.0 μm pore diameter; Omnilab GmbH, Munich, Germany). Inserts were placed in BD Falcon six-well tissue culture plates with 2 mL medium in the upper and 3 mL in the lower transwell chamber. The medium was changed twice a week. Cells were grown on transwell inserts under submerged conditions in medium for 7 days to grow to confluence. Twenty-four hours before exposure, the cells were exposed to the air–liquid interface[31] and the medium in the lower chamber was replaced by fresh RPMI (1.8 mL) with supplements.

Particles: Commercially available plain 15-nm gold NPs stabilized with citrate buffer from British Biocell International (BBI; Plano GmbH, Wetzlar, Germany) were used in this study. The BBI gold suspension had a molar concentration of 2 nM. The molarity refers to the number of particles per mole and was determined by UV/Vis spectroscopy using the molecular extinction coefficient of their absorption at the plasmon peak: 3.64×10^8 $M^{-1}cm^{-1}$ as provided by BBI. In this study, exposures with a tenfold higher concentration (20 nM) were performed, which was reached for plain gold NPs by centrifugation of the original BBI solid suspension at 19 RCF (relative centrifugal force) for 20 min and removal of 90% of the citrate buffer. PEGylation of the particles was performed by ligand exchange: replacement of the citrate molecules on the surface of the gold NPs by thiolated PEG molecules due to the stronger and more stable bond between thiol groups and gold NPs. Thiolated PEG ($SH\text{-}PEG_{(5kD)}\text{-}OCH_3$, Rapp Polymere Company, Tübingen, Germany) was dissolved in Millipore water to make a stock solution with a molar concentration of 2 mM. A ratio of 50 PEG molecules per 1 nm^2 surface area of the gold NPs was used to mix the solution with the 2 nM colloidal gold suspension. The mixture was vigorously stirred with a magnetic stirring bar for 12 h. After the ligand exchange, the PEG-coated gold NP solution was rinsed three times with Millipore water with ultrafiltration (Viva Spin Ultrafiltration, 100 000 molecular weight cutoff (MWCO) PES, Sartorius Stedim, VS2042) to eliminate the excess PEG and to replace the original buffer of the BBI gold NPs with Millipore water. The final molar concentration of the solution was determined by UV/Vis spectroscopy using the extinction coefficient of the plain gold NPs. Gel electrophoresis was conducted by using 2% agarose gel (UltraPure, Invitrogen, Germany) under a constant voltage of 100 V for 50 min, which showed that the PEG-coated gold NPs have a small positive charge. Before particle exposure, the PEG-coated gold NPs were diluted with citrate buffer to a nominal concentration of 20 nM. The hydrodynamic diameter of the PEG-coated particles was estimated by gel electrophoresis to be around 25 nm.[46]

Cell exposure and particle deposition: A recently developed exposure system was used for the air–liquid interface exposure of the cell cultures (ALICE) with the particles.[30] The exposure procedure of gold NPs has previously been described.[23,30] Briefly, micrometer-sized droplets were generated from the 20 nM particle suspension (1 mL) with a vibrating membrane droplet generator (investigational eFlow, PARI Pharma GmbH, Munich, Germany) and were deposited via cloud settling and single-particle sedimentation onto the cells in an exposure chamber. The NP deposition lasted 20 min followed by a particle exposure time of 1, 4, or 24 h. NP deposition and distribution at the air–liquid interface was analyzed as described previously[23] and resulted in deposition of 16.1×10^9 (SD 1.5×10^9) citrate-stabilized gold particles cm^{-2} and 14.1×10^9 (SD 1.6×10^9) PEG-coated particles cm^{-2}. It could also be shown that plain particles, which are only stabilized by citrate buffer and not by a PEG shell, were predominantly deposited onto the cells as single particles or small agglomerates (see the Supporting Information). Additional experiments were also performed to compare cellular NP deposition and uptake in the submerged exposure with those in the ALICE. The same number of plain particles as deposited on the cells per six-well insert (6.8×10^{10}) was dissolved in 1 mL cell culture medium (plain RPMI without FCS) and exposed to the cells for 4 h. The effects of diffusion and agglomeration of plain particles in suspension were subsequently analyzed and compared with the ALICE.

To investigate different endocytotic mechanisms of NP uptake, inhibition of caveolin- and clathrin-mediated endocytosis was performed with MβCD (Sigma Aldrich, Buchs, Switzerland).[33] The cells were therefore incubated with 10 mM MβCD in phosphate-buffered saline for 30 min and washed with RPMI medium before the exposure. Each experiment was repeated three times.

Preparation for TEM: The cells on the insert membrane were fixed with 2.5% glutaraldehyde in 0.03 M potassium phosphate buffer for at least 24 h. The cells were then washed with buffer, post-fixed with 1% osmium tetroxide in sodium cacodylate buffer, washed with maleate, and stained en bloc with 0.5% uranyl acetate in maleate buffer. After additional washing, the cells were dehydrated in an ascending ethanol series, and embedded in epon.[47] From the embedded cells, semi- and ultrathin sections were cut parallel to the vertical axis of the cells. Ultrathin sections were mounted on copper grids, stained with lead citrate and uranyl acetate, and were investigated with TEM.

Relative particle distribution within the cells: The method describing the RDI[34] was designed to test whether intracellular NPs are localized randomly in all cellular compartments or if they

F 8

show any preferences for specific compartments. The observed particle density for each cellular compartment was estimated by relating the number of particle events in a given compartment to the corresponding fractional volume of the compartment.

All particle events (an event is defined as the intracellular occurrence of a single particle or agglomerate) were sampled by systematic uniform random sampling (reviewed in Reference [48]). This is fundamental for the acquisition of unbiased data in stereological image analysis. Details on sampling of particle events and sample preparations are given in the Supporting Information. Screening was performed on ultrathin TEM sections, with a Philips CM12 transmission electron microscope (FEI Co. Philips Electron Optics, Zürich, Switzerland) at a primary magnification of 25 000 ×. Each time a particle event was encountered, the cell compartment of its localization was reported and the largest diameter and the number of particles per particle event were recorded. Approximately 150 particle events were reported per experiment and the results of all three repetitions were pooled. The relative size of each cellular compartment was estimated by randomly superimposing a grid of test points over randomly located test fields (cells imaged at a magnification of 11 500 ×) and simply counting the number of points, *P*(comp), hitting each cellular compartment. More details on data acquisition are given in the Supporting Information.

The number of expected particles for each compartment, N_E(comp), assuming a purely random particle distribution within the cell, can be calculated from the total number of observed particles, N_O(total), and the numbers of observed points, *P*(total) and *P*(comp), by the following equation:

$$N_E(\mathrm{comp}) = N_O(\mathrm{total})\frac{P(\mathrm{comp})}{P(\mathrm{total})} \tag{1}$$

From the observed N_O(comp) and expected N_E(comp) particle distributions, the RDI was calculated for each compartment:

$$\mathrm{RDI} = \frac{N_O(\mathrm{comp})}{N_E(\mathrm{comp})} \tag{2}$$

An $\mathrm{RDI} > 1$ indicates a preferentially populated compartment, that is, more NPs were found than expected for random intercellular NP distribution; an $\mathrm{RDI} < 1$ represents a compartment that contains fewer NPs than expected solely from its size. An example of the calculation is given in Table 1. The observed and expected distributions were then statistically analyzed by the χ^2 test. A similar approach was used to compare observed distributions between two or more experimental groups, such as different time points, partial endocytotic inhibition, or different particle types. From the number of observed particles within each group, the number of expected particles was calculated for each compartment. This is the number of particles that would be expected if the distributions between the groups were equal. Again, the observed and the expected distributions of the different groups were statistically analyzed by the χ^2 test. If the total χ^2 value reached the significance level, the null hypothesis (“the particles are equally distributed among the cellular organelles” or “the intracellular particle distribution is equal among different experimental groups”) was rejected. A contribution of >10% of the partial χ^2 value to the total χ^2 value indicated those compartments that contributed substantially to the nonrandom distribution or the intergroup differences, respectively.

Total particle uptake per cell: The total cellular NP uptake, with and without inhibition of clathrin- and caveolin-mediated endocytosis by MβCD treatment, was evaluated by quantifying the number of intracellular NPs. This was performed by estimating the intracellular particle density and multiplying the result by the average estimated cell volume. Particle events were counted for the distribution of the particles within the cells, whereas in this evaluation the total number of particles per cell was considered.

The intracellular particle density, N_V, defined as the ratio of the number of intracellular NPs per sampling volume, was estimated by applying an unbiased counting frame with defined test field area on TEM images obtained by systematic uniform random sampling (magnification 25 000 ×) and counting the number of NPs (*N*) in all test fields (*n*). An average number of 200–300 test fields per TEM section were evaluated with three independent sections per experiment and three repetitions per experimental condition (see systematic uniform random sampling in the Supporting Information). In this case, the total number of particles was counted, not the number of particle events. The volume was obtained by multiplying the test field area (*A*) by the section thickness (*d*), estimated by the method of the smallest fold,[49] which is half of the diameter of the smallest fold in the ultrathin section (average section thickness: 50–80 nm).

$$N_V = \frac{N}{n\,A\,d} \tag{3}$$

For estimation of the mean cellular volume of cells, $\overline{V}_N$ (cell), a number-weighted sampling procedure was used by application of the single-section disector. Thus, every time a nucleolus was observed in an A549 nucleus this cell was sampled for cell volume estimation by the vertical rotator.[50] The rotator is a local stereological tool used to estimate the volume of a biological particle from a two-dimensional section. The sampling was performed on toluidene blue stained semithin sections with a conventional light microscope coupled to a CAST system (CAST 2.0, Olympus, Ballerup, Denmark) at an objective lens magnification of 60 ×. From these results the number-weighted mean cell volume, $\overline{V}_N$ (cell), was estimated for each experiment. The average number of particles per cell, $\overline{N}$ (cell), was obtained by:

$$\overline{N}(\mathrm{cell}) = N_V\overline{V}_N(\mathrm{cell}) \tag{4}$$

Statistics: To test if the intracellular particles were randomly distributed, the expected versus the counted particles were statistically analyzed with a χ^2 test and considered significant if the resulting χ^2 values exceeded the χ^2 values given in the tables of statistical analysis ($f = n-1$; $p \leq 0.05$). Furthermore, the intracellular particle distributions of different experimental setups, such as particle coating, incubation times, or partial inhibition of endocytosis, were also compared and analyzed with the χ^2 test.

The nonparametric Kruskal–Wallis One-Way Analysis of Variance (ANOVA) on Ranks was used to test if cellular particle uptake was reduced in MβCD-treated cells. If $p < 0.05$, the Mann–Whitney *u*-test was further performed for comparison of two groups. Differences were considered significant at $p < 0.05$.

Acknowledgements

The authors would like to thank Mr. Bukalis and Mrs. Alber for performing the neutron-activated gamma spectroscopic determination of the mass of the gold nanoparticles and Barbara Krieger, Andrea Stokes, and Mohamed Ouanella for their excellent technical assistance, Kirsten Dobson for English proofreading, and Dr. Feng Zhang for the helpful discussions. This study was supported by grants of the Animal Free Research Foundation, the Doerenkamp-Zbinden Foundation, the Deutsche Forschungsgemeinschaft (DFG, SPP 1313), the Swiss National Science Foundation (3100A0_118420), and the Helmholtz Association.

[1] Y. Y. Liu, H. Miyoshi, M. Nakamura, *Int. J. Cancer* **2007**, *120*, 2527–2537.

[2] J. Peteiro-Cartelle, M. Rodríguez-Pedreira, F. Zhang, P. Rivera Gil, L. del Mercato, W. J. Parak, *Nanomedicine* **2010**, *4*, 967–979.

[3] S. Dhar, E. M. Reddy, A. Shiras, V. Pokharkar, B. L. Prasad, *Chem. Eur. J.* **2008**, *14*, 10244–10250.

[4] H. M. Joshi, D. R. Bhumkar, K. Joshi, V. Pokharkar, M. Sastry, *Langmuir* **2006**, *22*, 300–305.

[5] P. K. Jain, X. Huang, I. H. El-Sayed, M. A. El-Sayed, *Acc. Chem. Res.* **2008**, *41*, 1578–1586.

[6] L. Olofsson, T. Rindzevicius, I. Pfeiffer, M. Kall, F. Hook, *Langmuir* **2003**, *19*, 10414–10419.

[7] H. Hillaireau, P. Couvreur, *Cell. Mol. Life Sci.* **2009**, *66*, 2873–2896.

[8] L. W. Zhang, J. Yang, A. R. Barron, N. A. Monteiro-Riviere, *Toxicol. Lett.* **2009**, *191*, 149–157.

[9] J. Rejman, V. Oberle, I. S. Zuhorn, D. Hoekstra, *Biochem. J.* **2004**, *377*, 159–169.

[10] K. Yin Win, S. S. Feng, *Biomaterials* **2005**, *26*, 2713–2722.

[11] B. D. Chithrani, A. A. Ghazani, W. C. W. Chan, *Nano Lett.* **2006**, *6*, 662–668.

[12] C. Brandenberger, B. Rothen-Rutishauser, F. Blank, P. Gehr, C. Mühlfeld, *Respir. Res.* **2009**, *10*, 22.

[13] K. Unfried, C. Albrecht, L.-O. Klotz, A. Von Mikecz, S. Grether-Beck, R. P. F. Schins, *Nanotoxicology* **2007**, *1*, 52–71.

[14] B. Rothen-Rutishauser, S. Schuerch, P. Gehr, in: *The Toxicology of Particles* (Eds: K. Donaldson, P. Borm), CRC, Boca Raton **2007**, pp. 139–160.

[15] A. Lehmann, F. Zhang, Z. Ali, C. Röcker, G. U. Nienhaus, P. Gehr, B. Rothen-Rutishauser, *Small* **2010**, *6*, 753–762.

[16] M. Geiser, M. Casaulta, B. Kupferschmid, H. Schulz, M. Semmler-Behnke, W. Kreyling, *Am. J. Respir. Cell. Mol. Biol.* **2008**, *38*, 371–376.

[17] A. Verma, O. Uzun, Y. Hu, Y. Hu, H. S. Han, N. Watson, S. Chen, D. J. Irvine, F. Stellacci, *Nat. Mater.* **2008**, *7*, 588–595.

[18] Y. J. Gu, J. Cheng, C. C. Lin, Y. W. Lam, S. H. Cheng, W. T. Wong, *Toxicol. Appl. Pharmacol.* **2009**, *237*, 196–204.

[19] B. Rothen-Rutishauser, C. Mühlfeld, F. Blank, C. Musso, P. Gehr, *Part. Fibre Toxicol.* **2007**, *4*, 9.

[20] H. J. Johnston, M. Semmler-Behnke, D. M. Brown, W. Kreyling, L. Tran, V. Stone, *Toxicol. Appl. Pharmacol.* **2010**, *242*, 66–78.

[21] P. Nativo, I. A. Prior, M. Brust, *ACS Nano* **2008**, *2*, 1639–1644.

[22] R. A. Sperling, P. Rivera Gil, F. Zhang, M. Zanella, W. J. Parak, *Chem. Soc. Rev.* **2008**, *37*, 1896–1908.

[23] C. Brandenberger, B. Rothen-Rutishauser, C. Mühlfeld, O. Schmid, G. A. Ferron, K. L. Maier, P. Gehr, A. G. Lenz, *Toxicol. Appl. Pharmacol.* **2010**, *242*, 56–65.

[24] Y. H. Chen, C. Y. Tsai, P. Y. Huang, M. Y. Chang, P. C. Cheng, C. H. Chou, D. H. Chen, C. R. Wang, A. L. Shiau, C. L. Wu, *Mol. Pharm.* **2007**, *4*, 713–722.

[25] S. M. Ryan, G. Mantovani, X. X. Wang, D. M. Haddleton, D. J. Brayden, *Expert Opin. Drug Delivery* **2008**, *5*, 371–383.

[26] A. Jain, S. K. Jain, *Crit. Rev. Ther. Drug Carrier Syst.* **2008**, *25*, 403–447.

[27] S. D. Perrault, C. Walkey, T. Jennings, H. C. Fischer, W. C. W. Chan, *Nano Lett.* **2009**, *9*, 1909–1915.

[28] Y. Zhang, N. Kohler, M. Zhang, *Biomaterials* **2002**, *23*, 1553–1561.

[29] N. L. Rosi, D. A. Giljohann, C. S. Thaxton, A. K. R. Lytton-Jean, M. S. Han, C. A. Mirkin, *Science* **2006**, *312*, 1027–1030.

[30] A. G. Lenz, E. Karg, B. Lentner, V. Dittrich, C. Brandenberger, B. Rothen-Rutishauser, H. Schulz, G. A. Ferron, O. Schmid, *Part. Fibre Toxicol.* **2009**, *6*, 32.

[31] F. Blank, B. M. Rothen-Rutishauser, S. Schurch, P. Gehr, *J. Aerosol Med.* **2006**, *19*, 392–405.

[32] L. K. Limbach, Y. Li, R. N. Grass, T. J. Brunner, M. A. Hintermann, M. Muller, D. Gunther, W. J. Stark, *Environ. Sci. Technol.* **2005**, *39*, 9370–9376.

[33] S. K. Rodal, G. Skretting, O. Garred, F. Vilhardt, B. van Deurs, K. Sandvig, *Mol. Biol. Cell* **1999**, *10*, 961–974.

[34] C. Mühlfeld, T. M. Mayhew, P. Gehr, B. Rothen-Rutishauser, *J. Aerosol Med.* **2007**, *20*, 395–407.

[35] S. D. Conner, S. L. Schmid, *Nature* **2003**, *422*, 37–44.

[36] D. Mandal, A. Maran, M. Yaszemski, M. Bolander, G. Sarkar, *Mater. Sci. Mater. Med.* **2009**, *20*, 347–350.

[37] B. D. Chithrani, W. C. W. Chan, *Nano Lett.* **2007**, *7*, 1542–1550.

[38] B. Ballou, B. C. Lagerholm, L. A. Ernst, M. P. Bruchez, A. S. Waggoner, *Bioconjugate Chem.* **2004**, *15*, 79–86.

[39] C. Mühlfeld, P. Gehr, B. Rothen-Rutishauser, *Swiss Med. Wkly.* **2008**, *138*, 387–391.

[40] R. Gref, M. Luck, P. Quellec, M. Marchand, E. Dellacherie, S. Harnisch, T. Blunk, R. H. Muller, *Colloids Surf. B Biointerfaces* **2000**, *18*, 301–313.

[41] M. Lundqvist, J. Stigler, G. Elia, I. Lynch, T. Cedervall, K. A. Dawson, *Proc. Natl. Acad. Sci. USA* **2008**, *105*, 14265–14270.

[42] C. Tekle, B. van Deurs, K. Sandvig, T. G. Iversen, *Nano Lett.* **2008**, *8*, 1858–1865.

[43] M. A. Dobrovolskaia, A. K. Patri, J. Zheng, J. D. Clogston, N. Ayub, P. Aggarwal, B. W. Neun, J. B. Hall, S. E. McNeil, *Nanomedicine* **2009**, *5*, 106–117.

[44] C. Röcker, M. Potzl, F. Zhang, W. J. Parak, G. U. Nienhaus, *Nat. Nanotechnol.* **2009**, *4*, 577–580.

[45] M. S. Ehrenberg, A. E. Friedman, J. N. Finkelstein, G. Oberdörster, J. L. McGrath, *Biomaterials* **2009**, *30*, 603–610.

[46] R. A. Sperling, T. Liedl, S. Duhr, S. Kudera, M. Zanella, C. A. J. Lin, W. H. Chang, D. Braun, W. J. Parak, *J. Phys. Chem. C* **2007**, *111*, 11552–11559.

[47] C. Mühlfeld, B. Rothen-Rutishauser, D. Vanhecke, F. Blank, P. Gehr, M. Ochs, *Part. Fibre Toxicol.* **2007**, *4*, 11.

[48] T. M. Mayhew, *Placenta* **2008**, *29*, 1–14.

[49] J. V. Small, in *Proc. 4th European Regional Conf. Electron Microscopy* (Ed: D. S. Bocciarelli), Tipografisa Poliglotta Vaticana, Rome **1968**, pp. 609–610.

[50] E. B. V. Jensen, H. J. G. Gundersen, *J. Microsc.* **1993**, *170*, 282–282.

Received: April 1, 2010

F10

Algal toxicity and *in vitro* uptake of polymer coated gold nanoparticles

K. Van Hoecke[a,*], K.A.C. De Schamphelaere[a], Z. Ali[b], F. Zhang[b], A. Elsaesser[c], P. Rivera Gil[b], W. J. Parak[b], G. Smagghe[d], V. C. Howard[c] and C.R. Janssen[a]

[a]: Laboratory of Environmental Toxicology and Aquatic Ecology, Faculty of Bioscience Engineering, Ghent University, Jozef Plateaustraat 22, B-9000 Gent, Belgium.

[b]: Fachbereich Physik and Wissenschaftliches Zentrum für Materialwissenschaften, Philipps Universität Marburg, Renthof 7, 35037 Marburg, Germany

[c]: University of Ulster, Coleraine BT52 1SA, Co. Londonderry, United Kingdom

[d]:Laboratory of Agrozoology, Faculty of Bioscience Engineering, Ghent University, Coupure Links 653, B-9000 Gent, Belgium

* Corresponding author:
Karen Van Hoecke
Phone: +32 – 9 – 264 3710
Fax: +32 – 9 – 264 3766
Email: karen.vanhoecke@ugent.be

Email addresses of co-authors: karel.deschamphelaere@ugent.be, ali@Physik.Uni-Marburg.DE, fengzhang1978@googlemail.com, a.elsaesser@ulster.ac.uk, pilar.riveragil@physik.uni-marburg.de, wolfgang.parak@physik.uni-marburg.de, v.howard@ulster.ac.uk, guy.smagghe@ugent.be, colin.janssen@ugent.be.

Abstract - Gold NPs are used in many pharmaceutical applications. However, their ecotoxicity has not been determined. We investigated the uptake/adsorption and ecotoxicity of two types of polymer coated (amphiphilic (AP) and amphiphilic + 10 kDa polyethylene glycol (PEG) (APma10kPEG) coated) NPs comprising a 4-5 nm Au core.

In 72h algal growth inhibition tests APma10kPEG NPs were found less toxic compared to AP particles, with 72h-E_rC_{10} values (std.dev.) of 5.1(0.3) and 1.2(0.1) mgAu/l, respectively. From 46 mgAu/l, algal growth was decreased due to light limitation caused by light absorption by the particles.

In 24h cytotoxicity assays with cell line RTGill-W1 24h-EC_{20} values (std.dev.) of 15(5) and 54(18)mg Au/l were obtained.

No particle uptake in algal cells was observed. However, uptake/adsorption of fluorescently labeled AP in fish gill cells reached $>10^6$ particles/cell after 1h and particles were eliminated for ≥96% after 24h. Both particles were found within membrane enclosed vesicles in the cytoplasm.

Keywords – gold, nanoparticles, algae, RTGill-W1

1 Introduction

Colloidal gold NPs have been used since ancient times, among others as a staining component in glass. Faraday was the first to scientifically report the synthesis and optical characteristics of gold colloids (Faraday, 1857). However, only in the last few years have gold NPs gained interest regarding their potential catalytic and bionanotechnological applications.

In addition to their flexible use as a catalyst (Han et al., 2009; Li et al., 2009; Tsunoyama et al., 2004), the optical properties of gold NPs make them an interesting tool in various fields of biological research. Traditionally, gold NPs are used as a contrast agent for labelling purposes. Because of their strong visible light absorbing and scattering ability, a variety of detection techniques can be used, like dark field microscopy, photothermal imaging, photo-acoustic imaging and fluorescence microscopy (Sperling et al., 2008). Gold NPs also exhibit high contrast in transmission electron microscopy (TEM) and X-ray imaging. Besides biological labelling, gold NPs can be used as a carrier of DNA and drugs for specific and non-specific delivery into cells. The molecules of interest are adsorbed to the NP surface and once taken up in the cells, the molecules detach from the surface. A similar strategy is of particular interest for cancer therapy. For example, gold NPs can be covered with ligands specifically binding to receptors predominantly present in the membrane of cancer cells. After uptake, any drugs attached to the surface can be released into the intracellular environment (Jain et al., 2007).

Besides their intrinsic characteristics useful in the above-mentioned and many other applications, the most important reason for their use arises from the possibility to synthesize, stabilize and modify gold NPs with application-specific tailored properties. First, gold NPs can be synthesized in aqueous and organic media through reduction of gold salts, like $AuCl_3$ (Sperling et al., 2007). Often the particles are stabilized by a surfactant. The surface of gold NPs can then be modified in subsequent reactions aimed at producing a NP with the ligand of choice. Typically, molecules containing a thiol functional group are anchored to the gold surface through formation of Au-S bonds (Brust et al., 1994). If desired, these molecules can serve as a template for the attachment of other molecules (Woehrle et al., 2005).

Despite the high potential gold NPs offer for biomedical applications, concerns have been raised regarding their biocompatibility and the potential risks to human health and the environment (Murashov, 2009; Ray et al., 2009). Although gold is an inert material, size reduction towards the nanoscale can cause increased reactivity and toxicity. Due to their expected increased use, especially in pharmaceutical formulations, man and the environment may be exposed to a wide variety of functionalized Au NPs. Therefore, their (eco-)toxic effects need to be addressed.

In this study, the ecotoxicity of two types of polymer coated gold NPs used as a precursor in biological applications was assessed using an algal species (*Pseudokirchneriella subcapitata*) and a rainbow trout gill cell line. Toxicity data were corrected for the interference caused by the optical properties of the particles. Furthermore, uptake of the particles in both cell types was investigated using transmission electron microscopy (TEM) and confocal laser scanning microscopy.

2 Materials and methods

2.1 *Polymer coated gold nanoparticles*

Gold nanoparticles (NPs) were synthesized according to previously published protocols (Lin et al., 2008; Zhang et al., 2010). The inner gold core of the NPs was around 4.5 nm in diameter and the surface was capped with dodecanethiol. One batch (AP) was coated with an amphiphilic polymer, consisting of a hydrophobic part (dodecylamine) and a hydrophilic part, poly-(isobutylene-alt-maleic anhydride) (PMA). Following the coating procedure with the amphiphilic polymer (Lin et al., 2008; Zhang et al., 2010), another batch (APma10kPEG) was prepared through post modification of the amphiphilic polymer with polyethylene glycol (PEG) molecules with a molecular weight (MW) of 10000 g/mol (Sperling et al., 2006), each containing a methyl and an amino group at the outer ends, whereby the amine functional group served as an anchor point for attachment to the functionalized NP surface. Both particle types are presented in **Figure 1**. Size determination of the gold core, the amphiphilic coated gold NPs and the pegylated (i.e. post-modified with 10 kDa PEG) amphiphilic coated gold NPs was performed immediately after synthesis. The TEM derived size of the gold core was 4.6 nm. The particles were stored in 10 mM $NaHCO_3$ and 100 mM NaCl solution at pH 10 and 4 °C. Gold particle stock concentrations were 6.4 µM and 3.8 µM of AP and APma10KPEG particles, respectively. This corresponded to an estimated mass concentration of 2.5 and 1.5 g/l, respectively. More details on the synthesis and purification procedure and on the calculation of mass concentration are given in the **Supporting information**. After purification, reaction by-products such as excess precursor molecules or empty polymer micelles were removed and the solution only contained the NPs (Sperling et al., 2007). More details on the characterization studies performed after synthesis are given in the **Supporting information** section. In the following paragraphs, amphiphilic coated gold NPs are referred to as 'AP particles' and the pegylated amphiphilic coated particles as 'APma10kPEG'.

The polymer coating of the NPs was optionally modified with a fluorophore, cresyl violet, for confocal microscopy experiments (Zhang et al., 2010).

2.2 *Characterization in test media used for in vitro experiments*

The actual hydrodynamic size of both gold NP types was determined at 0.13 μM Au NP concentration (~50 mg Au/l) and 25 °C in the two ecotoxicity test media used in this study, i.e. the OECD algal medium (OECD, 2006) supplemented with 3.6 mM 3-(N-Morpholino)propanesulfonic acid (MOPS) buffer at pH 7.4 and the Leibovitz's L15 medium (Leibovitz, 1963), using a PCS 4700 SM (Malvern Instruments, Worcestershire, UK) dynamic light scattering device. Incident light was produced by a 5 mW HeNe laser and scattered light was detected at an angle of 150 °. A 7032 CN correlator (Malvern Instruments) was used for data processing. Monomodal analysis was performed to determine particle size distributions, whereas the harmonic intensity weighed average hydrodynamic diameter was obtained by the cumulant analysis option of the automeasure software (Malvern Instruments). All samples were analyzed in triplicate.

The light absorbance spectrum of 0.05 μM Au NPs (~20 mg Au/l) particle suspensions in Leibovitz's L15 test medium was recorded using an Aquamate spectrophotometer (Thermo Electron Corporation, Waltham, MA, US) between wavelengths of 315 and 900 nm.

2.3 *Ecotoxicity testing*

2.3.1 Algal assays

The alga *Pseudokirchneriella subcapitata* was obtained from the Culture Collection of Algae and Protozoa (CCAP 278/4, 121 Oban, Scotland) and was cultured at Ghent University in ES-medium at 1/2 strength (Provasoli, 1968) which was added to carbon filtered aerated tap water, supplemented with 1.4 mg/l $FeSO_4.7H_2O$, 15 mg/l $NaH_2PO_4.2H_2O$, 150 mg/l $NaNO_3$ and 2.35 mg/l $MnCl_2.4H_2O$. Four days prior to the start of 72 h algal growth inhibition experiments, a new algal culture was prepared and allowed to grow on a shaking table at 20 ± 1 °C in continuous light (70 $\mu E/(m^2s)$). This new culture was subsequently used to inoculate each replicate of a growth inhibition experiment with 10000 cells/ml.

Test concentrations, which were prepared in OECD algal test medium supplemented with 3.6 mM MOPS buffer at pH 7.4 one day in advance of the test and equilibrated at 25 °C, varied between 0.0012 and 0.12 µM Au NPs (~0.46 to 46 mg Au/l). Both NP types were tested twice according to the standard OECD guideline No. 201 (OECD, 2006). For each test concentration three replicates and one blank correction (no inoculation with algae) were included. During the 72 h test, all flasks were incubated at a temperature of 25 °C under continuous illumination (70 μE/(m^2s)) and were shaken manually three times a day. Every 24 h, the fluorescence of extracted chlorophyll in a sample from each replicate was measured. To this end, 3 ml extraction mixture (dimethylsulfoxide (DMSO): acetone (1:1)) was added to a 0.75 ml sample, vortexed and allowed to stand in the dark for at least 20 minutes. Chlorophyll fluorescence was recorded with a spectrophotometer (LS50B, Perkin Elmer, Zaventem, Belgium) in a 1 cm quartz cuvette at a wavelength of 671 nm, using an excitation wavelength of 431 nm (Mayer et al., 1997). The fluorescent signal of each sample was subsequently converted to an algal cell density using chlorophyll fluorescence measurements of algal concentration series prepared in the control medium and in each Au NP test concentration ≥ 0.0057 µM Au NPs (~2.2 mg Au/l), of which the algal cell densities had been determined using a cell counter (Beckman Coulter Counter, Ghent, Belgium). The concentration series were prepared from algal cells originating from the same culture used for the tests and that were incubated in standard OECD test medium containing 3.6 mM MOPS buffer at pH 7.4 under the same conditions as the Erlenmeyer flasks of the test. Every day, new concentration series were prepared for chlorophyll extraction and measurement. The average specific growth rate μ (d^{-1}) was calculated for each concentration as the slope of a linear regression of the natural logarithm of the measured cell density versus time. The necessity of preparing an algal concentration series in each Au NP test concentration ≥ 2.2 mg Au/l arose from the interference on chlorophyll fluorescence caused by the light absorbing characteristics of the Au NPs. Indeed, **Figure 2 shows** shows a gradual decrease of the slope of the linear regression between algal cell concentration and detected chlorophyll fluorescence. The slope of the linear regression decreased from 3.29 in the control to 2.79 in 22 mg/l Au NP suspensions. By preparing a concentration series in each concentration ≥ 2.2 mg Au/l, we could correct for this interference.

A possible shading effect caused by the gold NPs was investigated using the approach outlined by Hund-Rinke and Simon (2006). Briefly, the chlorophyll contents upon spatially separating Au NPs and algal cells in two different 96 well plates, one transparent plate positioned on top of a white plate, was compared to the chlorophyll contents when algal cells and NPs were added to the same well and allowed to stand for 3 days at 25 °C under continuous illumination. The initial cell density in the wells was 10000 cells/ml and the plates were shaken manually three times a day. Again, algal cell densities were determined relative to a concentration series prepared in the control medium or in the corresponding Au NP concentration.

2.3.2 Assays with the fish gill cell line RTGill-W1

The RTGill-W1 cell line was first developed and described by Bols *et al.* in 1994. The cell line originated from a primary culture of gill epithelial cells of the rainbow trout (*Oncorhynchuss mykiss* (Walbaum)). The cells exhibit epithelial morphology and are believed to have derived from undifferentiated precursor gill stem cells. The cells were a gift from Dr. Kristin Schirmer (Eawag, Dübendorf, Switzerland) and were routinely cultured at 20 °C in 75 cm^2 tissue culture flasks with 10 ml of L15 supplemented with 10 % (v/v) heat inactivated fetal bovine serum (FBS).

In vitro cytotoxicity tests were performed with 25000 cells/well attached overnight to the surface of an opaque 96 well plate. Before exposure, the cell layers were washed with 100 µl L15 medium. The cells were subsequently exposed for 24 h to a 100 µl gold NP suspension in L15 medium, following colorimetric measurement of cell metabolic activity using the resazurine dye (O'Brien et al., 2000). The tests involved 5 replicates of each test concentration (including control) containing cells and one no-cell treatment for each test concentration (including control). Following the 24 h exposure period, 10 µl of a 500 µM resazurin solution in phosphate buffered saline (PBS) was spiked to each well and allowed to react for 3.5 h at 20 °C. Ninety microliter reaction product from each well was subsequently transferred to a white 96-well plate. Finally, immediately before measurement, 20 µl AP or APma10kPEG suspension in L15 medium was added in order to set the final Au NP concentration in each well to the highest test concentration used, i.e. 0.12 µM Au NPs (~46 mg Au/l). In this way, the decrease in fluorescent signal of resorufin was equal for each replicate. Resorufin fluorescence was recorded using the LS50B device, adopting excitation and emission wavelengths of 560 and 590 nm, respectively.

The need to adjust the final Au NP concentrations in each well to the maximum test concentration arose from the interference of the Au NPs with the fluorescent detection of resorufin (Sigma Aldrich, No. R3257), which is shown in **Figure 3**. In presence of 0.026 and 0.26 µM (~10 and 100 mg Au/l) AP Au NPs, the detected fluorescence of resorufin strongly decreased, resulting in a decrease of the slope of the linear regression from 40.8 to 31.4 and 7.2, respectively.

2.3.3 Statistical data treatment

In algal assays, concentration-response curves of AP and APma10kPEG particles were fitted to the log-logistic and modified log-logistic model, respectively. Because of the appearance of a horizontal plateau in the concentration-response curves of AP particles, the modified log-logistic equation better described the experimental data of AP than the log-logistic equation (Van Hoecke et al., 2008). In fish gill cell assays, effect concentrations were determined using the log-logistic model. The description of both models can be found in supporting information. Effect concentrations of AP and APma10kPEG established in the algal growth inhibition assays and in the cytotoxicity tests were compared using *t*-tests for dependent samples ($\alpha = 0.05$). To assess importance of shading, Jonckheere-Terpstra step down trend tests were used to identify treatments that showed a significant difference compared to the control (Jonckheere, 1954; Terpstra, 1952).

2.4 Cellular uptake studies

2.4.1 Fluorescently labeled gold NPs

Uptake of gold NPs by RTGill-W1 cells, both qualitatively and quantitatively, was studied using the same two types of gold NPs to which a cresyl violet perchlorate fluorescent label was attached (Zhang et al., 2010).

Uptake and/or strong adsorption to the cell membrane was qualitatively detected using a confocal laser scanning microscope (LSM 510 META, Carl Zeiss MicroImaging GmbH, Göttingen, Germany) with excitation at 543 nm with a helium-neon laser and selection of emission wavelength with a 560 nm long pass filter. The images were taken with an 100x immersion oil objective (N.A. 0.55). Samples were prepared by exposing ~80 % confluent cell layers in 75 cm^2 culture flasks for 24 h to 10 ml L15, L15 + 0.013 µM (~5 mg Au/l) AP and APma10KPEG particles. After exposure, the medium was poured off and the cell layer was treated with 5 ml trypsine working solution (Invitrogen, Merelbeke, Belgium, No. 25300). Cells were then transferred to 50 ml centrifugation tubes containing 10 ml L15 medium, followed by centrifugation for 5 minutes at 150x*g*. The pellet was resuspended in 1.5 ml L15 medium and transferred to an Eppendorf tube, after which a second five minute centrifugation at 150x*g* was performed. The pellet was resuspended in formalin (Sigma Aldrich No. HT501128), followed by centrifugation (150x*g*, 5 minutes). Again, the pellet was resuspended in formalin. The fixed samples were used for confocal laser scanning microcopy.

Uptake of AP particles was quantified using a short exposure time (1 h), after which the cells were still intact and apoptosis did not yet result in a substantial loss of cells. Exposure concentrations used were 0.0026, 0.0057, 0.012, 0.026, 0.057, 0.12, 0.26 µM Au NPs (~1.0, 2.2, 4.6, 10, 22, 46 and 100 mg Au/l). In 24 well plates, 200000 cells/well were allowed to attach overnight and were rinsed with L15 medium. The cell layer was subsequently exposed to 1 ml medium with or without fluorescently labeled gold particles. For each treatment, 6 replicates containing cells and 6 replicates without cells were included. After 1 h exposure, the medium was removed and all wells were rinsed three times with phosphate buffered saline (PBS) at 4 °C. Then, 250 µl L15 medium and 60 µl 1 % Triton X-100 was added to each well in order to lyse the cells. The cell homogenate was transferred to a 0.5 ml Eppendorf tube and centrifuged for 2 minutes at 1000x*g*. Finally, 200 µl of the supernatant was used for fluorescent detection in a white 96 well plate, using an excitation wavelength of 600 nm and an emission wavelength of 630 nm. The concentration of Au NPs in both the cell homogenates and in identically treated no cell controls was calculated relative to a standard series in the same matrix (L15 + 0.2 % Triton X-100) and finally the concentration in cell homogenates was corrected for the Au NPs still present in the no cell controls.

In a separate experiment, the elimination of AP particles by the RTGill-W1 cells over a 24 h period post exposure to 46 mg/l Au NPs was investigated. An identical procedure was used, except that after the 1 h exposure to AP particles rinsing of the cell layer was performed with PBS at 20 °C instead of at 4 °C, in order not to induce any changes due to a temperature decrease. Elimination was allowed in 1 ml L15 medium/well. After 4 and 20 h, the L15 medium was renewed in each well.

2.4.2 Transmission electron microscopy

Transmission electron microscopy was used to investigate uptake of the two gold NP types in both the algae and the fish cells. The exposure conditions were identical to the cytotoxicity experiments, except for the fact that fish cells were exposed in a 75 cm^2 culture flask. Algal cells and RTGill-W1 cells were exposed to AP particles at concentrations of 0.0026 µM (~1.0 mg Au/l) and 0.0057 µM (~2.2 mg Au/l), respectively and to APma10kPEG particles at concentrations of 0.012 µM (~4.6 mgAu/l) and 0.0057 µM, respectively. Sample pre-treatment was performed as described in Van Hoecke et al., 2009. Ultrathin sections (100 nm) were cut using an ultramicrotome (RMC, PowerTomeXL, Tucson, Arizona, USA) with a diamond knife (Diatome, Biel, Switzerland). These samples were imaged with an FEI Tecnai G2 Spirit Biotwin TEM (Fei, Hillsboro, OR, USA) at an operating voltage of 120 kV.

3 Results

3.1 Characterization in test media

Gold NP suspensions were stable under experimental conditions in both test media. The intensity-weighted particle size distributions of both AP and APma10KPEG indicated small aggregates up to 150 nm, however, less than 2 % of the signal arose from aggregates > 100 nm. Average diameters (std.dev.) and polydispersity indexes are given in **Table 1**. Particle size distributions are presented in **Figure 4**. Data correspond reasonably with previous studies which had been performed in different media (Sperling et al., 2007).

The absorbance spectra of both Au NP types in L15 medium are given in **Figure 5**. These particles absorb over the entire visible light spectrum with a peak maximum around

515 nm, which corresponds to the plasmon peak (Sperling et al., 2007). The absorbance spectrum between 315 and 900 nm in L15 was similar to that obtained immediately after synthesis (**Supporting information**). This indicates that the NPs were well dispersed.

3.2 Effects on the alga Pseudokirchneriella subcapitata

In the algal growth inhibition tests, 10, 20 and 50 % effect concentrations were established in the low milligram per liter range. Mean values and standard deviations obtained in the two experiments are given in **Table 2**. Based on 72 h-E_rC_{10} and E_rC_{20} values, *t*-tests for dependent samples ($\alpha = 0.05$) indicated that the amphiphilic coated Au NPs were more toxic than the pegylated amphiphilic coated particles. For E_rC_{10} and E_rC_{20} p-values of the *t*-tests were 0.037 and 0.045, respectively. However, no significant difference between 72 h-E_rC_{50} values was identified by the *t*-test for dependent samples ($p = 0.071$). **Figure 6** presents the concentration-response curves obtained in the two experiments.

In addition, it was investigated if light limitation might have contributed to the observed reduction in algal growth rate. The 96-well plate experiment showed that algal cells directly exposed to gold NPs, i.e. in which light first crossed OECD medium without NPs, were more severely affected than algal cells in control medium that were not directly exposed to Au NPs, i.e. whereby light first had to cross a gold NP suspension. Only after passage of light through a gold NP concentration of 0.12 µM (~46 mg/l), was a significant decrease in chlorophyll fluorescence relative to the control found. This indicated that the decrease in algal growth in the latter case was due to decreased light availability. The results of this experiment with both Au NP types are given in **Figure 7**. The results demonstrate that Au NPs have the potential to cause a decrease in algal growth due to their light absorbing characteristics. However, the shading effect cannot explain the observed decrease in growth of the algal cells, since it was only relevant at the highest test concentration of 46 mg Au/l. In addition, the shading effect cannot explain why the AP particles induced a more severe decrease in algal growth rate compared to the APma10kPEG particles.

3.3 In vitro cytotoxicity assays with the gill cell line RTGill-W1

In four separate 24 h resazurin assays with both particle types, mean EC_{10} values (std.dev.) of 0.012 (0.009) and 0.039 (0.025) µM Au NPs (or ~4.7 (3.3) and 15 (10) mg/l) were calculated for amphiphilic and pegylated amphiphilic coated Au NPs, respectively. Mean EC_{20}s (std.dev.) were 0.039 (0.015) and 0.14 (0.05) µM Au NPs (~15 (6) and 54 (18) mg/l), respectively. The 24 h-EC_{10} values obtained for both NP types were not significantly different ($p = 0.135$). However, based on the 24 h-EC_{20} values the AP particles were more toxic than the pegylated APma10KPEG particles ($p = 0.010$). Concentration-response curves for both NP types are given in **Figure 8**. The latter figure presents data points as overall mean values (std.dev.) of individual replicates assessed in 4 separate experiments. The four individual concentration-response curves of each experiment are shown in the **supporting information**. In **Figure 9**, morphology of the cell layer exposed to both types of Au NPs and in the control is shown.

3.4 Cellular uptake

3.4.1 Qualitative and quantitative uptake using fluorescently labeled particles

The images in **Figure 10** represent the RTGill-W1 control and gill cells exposed to both fluorescently labeled AP and APma10KPEG Au NPs. Uptake of amphiphilic coated gold NPs (AP) was detected using confocal laser scanning microscopy (Figure 10, panels B and C). The particles were found distributed all over the cytoplasm, but no internalization into the cells' nuclei was observed. The pegylated amphiphilic coated particles (APma10kPEG) were taken up to a much lesser extent (Figure 10, Panel D). However, the labelling efficiencies of the NPs with fluorophores varied from batch to batch. For this reason the difference in fluorescence observed in the cells does not directly relate to the difference in amount of particles taken up. In the shown images the fluorescent signal of the cresyl violet label was weaker for the pegylated particles (factor 8) compared to the non pegylated particles. In Panel D of Figure 10, it was difficult to distinguish the fluorescence with the naked eye. However, observation of the fluorescence image in the dark confirmed the uptake of the pegylated particles in the cells.

In the quantitative study, the concentration of AP particles in the cell homogenate of cells exposed to 0.0026, 0.0057 and 0.012 µM NPs (~1.0, 2.2 and 4.6 mg Au/l) was lower than the method detection level (< 1.2×10^{-4} µM Au NPs or < 0.048 mg Au/l). However, cells exposed to 0.026, 0.057, 0.12 and 0.26 µM NPs (~10, 22, 46 and 100 mg Au/l) suspensions increasingly sequestered the particles up to 0.0078 µM Au NPs (~3.1 mg Au/l) in the cell homogenate (concentration corrected for no cell controls) of cells exposed to 0.26 µM (~100 mg Au/l) AP particles. **Table 3** lists the results of the uptake study in RTGill-W1 cells, with quantities expressed as concentration, as absolute mass and as an estimation of the amount of particles/cell. The amount of particles/cell was estimated in the order of 10^6.

In a separate experiment, the elimination of AP particles was studied: cells were exposed for 1 h to 0.12 µM (~46 mg Au/l) suspensions followed by a 24 h depuration period. The concentration of AP particles in the cell homogenate was lower than the method detection level. Hence, it can be concluded that at least 96 % of the particles initially taken up were eliminated within the 24 h depuration period.

3.4.2 Transmission electron microscopy

Exposure to AP and APma10kPEG particles did not affect the algal cell morphology, as can be observed from the TEM images in **Figure 11**. Moreover, no particles were observed in the intracellular environment, attached to the cell membrane or closely surrounding the cells. Algal cell walls were intact.

No effect on fish gill cell morphology could be observed. **Figure S6 in supporting information** shows a cross section of both a cell in the control and a cell exposed to APma10kPEG particles. Only when using higher magnifications, could Au NPs be observed inside the cellular environment (**Figure 12**).

All particles taken up in the cells could be visualized in the dark shaded cellular vesicles to which the OsO_4 bound. No large aggregates could be observed in the vesicle and the particles appeared as single spheres or as clusters of a few particles. The size of the gold core of individual particles inside the vesicle shown in panel C of Figure 12 ranged between 3.19 and 7.97 nm. Furthermore, no change on cellular arrangement could be detected at the low NP concentrations used in the TEM study.

4 Discussion

Amphiphilic and PEG + amphiphilic coated Au NPs were stable under experimental conditions. The DLS derived average hydrodynamic sizes were larger compared to the TEM observed particle sizes. This is due to the fact that the TEM shows contrast only for the inorganic particle core but not for the surrounding polymer coating. In addition, a solvent layer is expected to be associated with the coated Au NPs, which can also explain the larger hydrodynamic size. A similar observation was made by Uboldi et al. (2009).

So far, only three other ecotoxicity studies used gold NPs, however, those studies were not performed according to standard test protocols. One study reported the absence of effects on *in vitro* metabolic activity in a rainbow trout primary hepatocyte culture exposed to 5-10 nm citrate coated Au NPs at a maximum test concentration of 17.4 mg/l. However, a threefold increase in cellular ROS levels was observed (Farkas et al., 2010).

The other studies involved *in vivo* tests on soil micro-organisms, lettuce seeds, green algae and a benthic bivalve. Shah and Belozerova (2009) were unable to detect any significant effect on a soil microbial community exposed for 15 days to dodecanethiol functionalized gold NPs of undefined size spiked to the soil at 0.013 and 0.066 % (w/w). On the other hand, increase in the shoot/root ratio of germinated lettuce seeds was observed relative to the control after a 15 day exposure in soil, indicating that the Au NPs indirectly affected growth of lettuce plants.

Mortality of the green alga *Scenedesmus subspicatus* during exposure to 10 nm Au NPs saturated with a 1.7 kDa polymer coating containing a positively charged amine group at the outer end, was studied by Renault et al. (2008). At the highest test concentration of $1.6x10^5$ Au NPs/algal cell, 50 % algal mortality was observed after 24 h. Furthermore, the Au NPs were found to strongly adsorb to the cell wall, including the cellulosic layer after penetration into the trilaminar layer of the cell wall. However, no uptake was observed into the intracellular environment. The contaminated algae were subsequently fed to the benthic mollusc *Corbicula fluminea*. Despite the detectable uptake of Au NPs in various tissues of the digestive tract, the uptake was limited to the epithelial layer and did not cause any morphological damage. A TEM analysis revealed the presence of the particles in lysosomal vesicles inside the cells, but not freely in the cytoplasm or the cells' nucleus.

Because of the diversity regarding size and surface coating of Au NPs used in these studies, the different (non standardized) experimental approaches and species used, it is difficult to compare these results with those obtained in the present study. In the present study, the metabolic activity of the RTgill-W1 cell line was significantly impaired at the low milligram per liter concentration. This is in contrast with the results obtained by Farkas et al. (2010), which could be due to the different size and/or surface coating of the Au NPs, or to the sensitivity of the cell culture.

The high affinity of the amine coated Au NPs for the *Scenedesmus subspicatus* algal cell wall can be explained by the electrostatic attraction between the negatively charged cell surface and the positively charged amine groups (Renault et al., 2008). This situation is clearly different from our experiments with *Pseudokircheriella subcapitata*, in which the Au NPs had a coating with uncharged organic functional groups at the outer ends (APma10kPEG) or with negatively charged carboxyl groups (AP). Therefore, the particles were not electrostatically attracted to the algal cells and perhaps the bulky organic PEG coating might even have caused steric repulsion in our experiments. Furthermore, the experimental approach in our study and in the study by Renaultt et al. is completely different. Renault et al. (2008) studied algal cell mortality in a dense algal suspension ($30x10^6$ algal cells/ml), while in our study algal growth inhibition of a starter culture of $1.0x10^4$ cells/ml was the endpoint, which is a standard toxicity endpoint. However, when expressing exposure concentrations of both studies as number of NPs/l, it becomes clear that the amine coated Au NPs used by Renault et al. (2008) caused the 50 % decrease in algal cell survival at a concentration of $4.8x10^{15}$ NPs/l, while only 10 % decrease in algal growth rate was observed in our study at AP and APma10kPEG particle concentrations of $1.9x10^{15}$ NPs/l and $7.9x10^{15}$ NPs/l, respectivley. Hence, for a similar Au NP concentration, the observed effect on algal cell mortality was much more severe for the amine coated Au NPs compared to the amphiphilic and pegylated amphiphilic coated particles.

Likewise, *in vitro* toxicity studies with Au NPs in the context of human toxicology have used diverse NP sizes, coatings and cell types. Triphenylphosphine stabilized Au NPs of different sizes were found to exhibit a size dependent cellular toxicity in various cell line types (Pan et al., 2007). The smallest 1-2 nm particles induced cell death, while the largest 15 nm particles had no effect up to a 60 fold higher concentration. Furthermore, two types of cell death, necrosis and apoptosis, were identified for the range of Au NPs tested. Citrate coated 14 nm Au NPs, on the other hand, caused cell growth and proliferation impairment in human dermal fibroblast cells (Pernodet et al., 2006).

In contrast with those studies, several papers report no or limited toxicity of Au NPs with various sizes and coatings. For example, Connor et al. (2005) did not detect cytotoxicity of 18 nm Au NPs towards the human leukemic cell line K562. Even smaller non coated Au NPs (3 tot 8 nm) were non toxic to RAW 264.7 macrophage cells exposed to 100 µM concentrations for 72 h (Shukla et al., 2005) and showed anti-oxidant behaviour through reduction in ROS and reactive nitrogen species (RNS) after a 48 h exposure to 100 µM Au NP suspensions. Wang et al. (2008) reported absence of cytotoxicity towards the human keratinocyte skin cell line HaCaT for a Au NP size range between 5 and 70 nm. The Au particles had been synthesized through reduction by citrate, nonetheless, the citrate remaining on the surface of the particles was unable to stabilize the suspensions. Hence, aggregation processes might have played a role in the outcome of the assays. Uboldi et al. (2009) furthermore demonstrated that effects on cell viability and cell proliferation of human alveolar type II cell lines exposed to 9.5-25 nm citrate coated Au NPs was dependent on the amount of sodium citrate residues remaining in suspension and/or anchored to the Au NP surface. Here, the most severe effect observed was a 30-40 % decrease in cell viability after 72 h exposure to a high concentration of 700 µM Au NPs, while no effect was observed for the most purified suspensions. In addition, Au nanorods stabilized by the positively charged hexadecylcetyltrimethylammonium bromide (CTAB) caused a 30-40 % decrease in HaCaT cell viability, which could be attributed to the CTAB present at the NP surface. Indeed, upon changing the coating with negatively charged polystyrene sulfonate, the effects were no longer observed (Wang et al., 2008). Likewise, Goodman et al. (2004) demonstrated that a positively charged monolayer coating increased Au NP toxicity compared to a negatively charged monolayer in Cos-1 cells, red blood cells and *E. coli*. Resulting LC_{50} values for the positively charged coating were 1-3 µM particles. Finally, Gu et al. (2009) did not observe significant morphological changes or cytotoxicity in human adenocarcinoma HeLa cells exposed to 10 µM 3 - 5 nm gold particles post modified with 3-mercaptoproprionic acid and conjugated with di-amine PEG polymer.

The combined results of these *in vitro* toxicity studies point out that predominantly only minor effects were observed following exposure of various cell lines to Au NPs. Differences in toxicity can be due to differences in NP size, whereby smaller NPs were found to be more toxic (Pan et al., 2007). Importantly, toxicity can specifically be due to the stabilizing coating used and in general, positively charged coatings induced a more severe effect compared to negatively charged coatings. In comparison, the RTGill-W1 cells were found to be relatively sensitive to both types of Au NPs, since concentrations used in the present study were 0.0026 µM to 0.12 µM Au NPs, whereas some of the above-mentioned studies used much higher test concentrations of up to 100 µM Au NPs. However, for some studies the actual test concentrations used had not been clearly defined.

Despite the large variety in toxicity study outcomes, most studies agree on the cellular uptake and intracellular behaviour of Au NPs. Every study, which so far investigated uptake, confirmed that Au NPs with different coatings were readily taken up by a large variety in cell types. For example, Chithrani et al. (2006) established uptake half lives of about 2 h of 14, 50 and 74 nm particles. Furthermore, several studies concluded that endocytic pathways were responsible for Au NP uptake in cells, since particles were mostly observed in the cytoplasm encapsulated by membrane surrounded vesicles (Shukla et al., 2005; Uboldi et al., 2009). Shukla et al. (2005) reported intracellular movement of lysosomes containing Au NPs towards the nucleus and subsequent perinuclear arrangement without internalization into the cell's nucleus. In contrast, Gu et al. (2009) convincingly demonstrated the affinity of di-amine PEG coated Au NPs towards the HeLa cells' nuclei.

Both NP types used in our study were not freely dispersed into the cytoplasm, but were encapsulated by closed membrane vesicles, in agreement with Shukla et al. (2005) and with Uboldi et al. (2009). In the quantitative uptake study, more than 10^6 amphiphilic coated Au NPs were found strongly adsorbed or taken up by each cell after 1 h. The same order of magnitude was reported by Gu et al. (2009) for pegylated Au NPs with a 3.7 nm Au core after 6 h treatment. After 24 h, the amount of cells taken up reached a plateau. Nevertheless, the amounts taken up in our study seem to exceed the ones reported by Gu et al. (2009). Possible explanations include the fact that our experimental approach reflects the sum of particles strongly attached to the cell wall and particles taken up into the intracellular environment. Possibly, the amount of particles adsorbed to the cell wall represent a substantial fraction of the final result. In addition, pegylation was found to decrease cellular uptake in the present study, which can also explain the discrepancy between both studies.

Furthermore, it should be mentioned that bioconjugation of Au NPs can be performed in such a way that makes them specifically tailored to target nuclei. Kang et al. (2010) for example, published the cancer cell nucleus specific targeting of pegylated 30 nm Au NPs bioconjugated with both arginin-glycin-aspartic acid peptide (RGD) and a nuclear localization signal peptide. First, particles are taken up in the cells by receptor-mediated endocytosis, followed by translocation to the nucleus.

In total, about a dozen of *in vitro* studies have shown the absence or only moderate toxicity of surface modified Au NPs, which increases their value as a potential candidate in advanced pharmaceutical applications. Likewise, in the present study, only moderate toxicity was observed. Indeed, no more than 60 % decrease in algal growth rate and 40 % decrease in RTGill-W1 cell survival and proliferation was detected at ~46 mg/l (0.12 µM Au NPs) concentrations.

In comparison, organic polymer NPs like polyethylene imine (PEI), which have similar medicinal applications, have been shown to be less efficient (factor 8) than functionalized Au NPs in e.g. mediating DNA translocation across the cellular membrane (Goodman et al., 2004). In addition, PEI as free polymer and as polyplex with DNA, was found to be highly toxic towards *Pseudokirchneriella subcapitata,* with 72 h E_rC_{10} values of 41 and 67 µg PEI/l. From 220 µg PEI/l on, algal cells were deteriorated (Robbens et al., 2010).

Acknowledgement

This work was supported by the European Union Sixth Framework Programme NanoInteract (NMP4-CT-2006-033231) and the Agency for Innovation through Science and Technology (IWT, Belgium). Parts of this work were supported by BMBF (WJP, project UMSICHT). Furthermore, we thank Dr. Kristin Schirmer and Myriam Claeys.

References

Brust, M., Walker, M., Bethell, D., Schiffrin, D.J., Whyman, R., 1994. Synthesis of thiol-derivatized gold nanoparticles in a 2-phase liquid-liquid system. *Journal of the Chemical Society – Chemical Communications* 7, 801-802.

Chithrani, B.D., Ghazani, A.A., Chan, W.C.W., 2006. Determining the size and shape dependence of gold nanoparticles uptake into mammalian cells. *Nano Letters* 6(4), 662-668.

Connor, E.E., Mwamuka, J., Gole, A., Murphy, C.J., Wyatt, M.D., 2005. GNPs are taken up by human cells but do not cause acute cytotoxicity. *Small* 1:325–327.

Faraday, M., 1857. The Bakerian Lecture: experimental relations of gold (and other metals) to light. *Philosophical Transactions of the Royal Society of London*, 147, 145-181.

Farkas, J., Christian, P., Urrea, J.A.G., Roos, N., Hassellöv, M., Tollefsen, K.E., Thomas, K.V., 2010 Effects of silver and gold nanoparticles on rainbow trout (*Oncorhynchus mykiss*) hepatocytes. *Aquatic Toxicology* 96, 44–52.

Goodman, C.M., McCusker, C.D., Yilmaz, T., Rotello, V.M., 2004. Toxicity of Gold Nanoparticles Functionalized with Cationic and Anionic Side Chains. *Bioconjugate Chemistry 15,* 897-900.

Gu, Y.J., Cheng, J., Lin, C.C., Lam, Y.W., Cheng, S.H., Wong, W.T., 2009. Nuclear penetration of surface functionalized gold nanoparticles. *Toxicology and Applied Pharmacology* 237, 196–204.

Han, J., Liu, Y., Guo, R., 2009. Reactive Template Method to Synthesize gold nanoparticles with Controllable Size and Morphology Supported on Shells of Polymer Hollow Microspheres and Their Application for Aerobic Alcohol Oxidation in Water. *Advanced Functional Materials* 19(7), 1112-1117.

Hund-Rinke, K., Simon, M., 2006. Ecotoxic effect of photocatalytic active nanoparticles (TiO_2) on algae and daphnids. *Environmental Science and Pollution Research* 13, 225–232.

Jain, P.K., El-Sayed, I.H., El-Sayed, M.A., 2007. Au nanoparticles target cancer. *NanoToday* 2(1), 18-29.

Jonckheere, A.R., 1954. A distribution-free k-sample test against ordered alternatives. Biometrika 41, 133–145.

Kang, B., Mackey, M.A., El-Sayed, M.A., 2010. Nuclear Targeting of Gold Nanoparticles in Cancer Cells Induces DNA Damage, Causing Cytokinesis Arrest and Apoptosis. *Journal of the American Chemical Society* 132, 1517–1519.

Bols, N.C., Barlian, A., Chirinotrejo, M., Caldwell, S.J., Goegan, P., Lee, L.E.J., 1994. Development of a cell-line from primary cultures of rainbow-trout, Oncorhynchus mykiss (Walbaum), gills.

Leibovitz, A., 1963. The growth and maintenance of tissue cell culture in free gas exchange with the atmosphere. *American Journal of Hygiene* 78, 173-180.

Li, L., Ji, W., Au, C.T., 2009. Gold nanoparticles Supported on Mesoporous Silica and Their Catalytic Application. *Progress in Chemistry* 21(9), 1742-1749.

564 Lin, C.-A.J., Sperling, R.A., Li, J.K., Yang, Z.-Y., Li, P.-Y., Zanella, M., Chang, W.H., Parak, W.J., 2008. Design of an amphiphilic polymer for nanoparticle coating and functionalization. *Small* 4, 334-341.

567 Mayer, P., Cuhel, R., Nyholm, N., 1997. A simple *in vitro* fluorescence method for biomass measurements in algal growth inhibition tests. *Water Research* 31, 2525-2531.

569 Murashov, V., 2009. Occupational exposure to nanomedical applications. Wiley interdisciplinary reviews – nanomedicine and nanobiotechnology 1(2), 203-213.

571 O'Brien, J., Wilson, I., Orton, T., Pognan, F., 2000. Investigation of the Alamar Blue (resazurin) fluorescent dye for the assessment of mammalian cell cytotoxicity. *European Journal of Biochemistry* 267, 5421-5426.

574 OECD, 2006. Freshwater alga and cyanobacteria, growth inhibition test. Guideline 201. Organization for Economic Cooperation and Development, Paris, France.

576 Pan, Y., Neuss, S., Leifert, A., Fischler, M., Wen, F., Simon, U., Schmid, G., Brandau, W., Jahnen-Dechent, W., 2007. Size-dependent cytotoxicity of gold nanoparticles. *Small* 3(11), 1941-1949.

579 Pernodet, N., Fang, X., Sun, Y., Bakhtina, A., Ramakrishnan, A., Sokolov, J., Ulman, A., Rafailovich, M., 2006. Adverse effects of citrate/GNPs on human dermal fibroblasts. *Small* 2, 766–773.

582 Provasoli, L., 1968. Media and prospects for the cultivation of marine algae. 63-75. In: Watanabe, A. and Hattori, A. (Eds.) Cultures and Collections of Algae. Proc. US-Japan Conf. Hakone, Japan, September 1966. Publ. by the J. Am. Soc. Plant. Physiol.

Ray, P.C., Yu, H., Fu, P.P., 2009. Toxicity and Environmental Risks of Nanomaterials: Challenges and Future Needs. *Journal of environmental science and health part C – environmental carcinogenesis & ecotoxicology reviews* 27(1), 1-35.

Renault, S., Baudrimont, M., Mesmer-Dudons, N., Gonzalez, P., Mornet, S., Brisson, A., 2008. Impacts of gold nanoparticle exposure on two freshwater species: a phytoplanktonic alga (*Scenedesmus subspicatus*) and a benthic bivalve (*Corbicula fluminea*). *Gold bulletin 41*(2), 116-126.

Robbens, J., Vanparys, C., Nobels, I., Blust, R., Van Hoecke, K., Janssen, C., De Schamphelaere, K., Roland, K., Blanchard, G., Silvestre, F., Gillardin, V., Kestemont, P., Anthonissen, R., Toussaint, O., Vankoningsloo, S., Saout, C., Alfaro-Moreno, E., Hoet, P., Gonzalez, L., Dubruel, P., Troisfontaines, P., 2010. Eco-, geno- and human toxicology of bio-active nanoparticles for biomedical applications. *Toxicology* 269, 170–181.

Shah, V., Belozerova, I., 2009. Influence of Metal Nanoparticles on the Soil Microbial Community and Germination of Lettuce Seeds. *Water air and soil pollution* 197:143–148.

Shukla, R., Bansal, V., Chaudhary, M., Basu, A., Bhonde, R.R., Sastry, M., 2005. Biocompatibility of Gold Nanoparticles and Their Endocytotic Fate Inside the Cellular Compartment: A Microscopic Overview. *Langmuir* 21, 10644-10654.

Sperling, R.A., Pellegrino, T., Li, J.K., Chang, W.H., Parak, W.J., 2006. Electrophoretic separation of nanoparticles with a discrete number of functional groups. *Advanced Functional Materials* 16, 943-948.

Sperling, R.A., Liedl, T., Duhr, S., Kudera, S., Zanella, M., Lin, C.A.J., Chang, W.H., Braun, D., Parak, W.J., 2007. Size determination of (Bio)conjugated water-soluble colloidal nanoparticles: A comparison of different techniques. *Journal of Physical Chemistry* 111, 11552-11559.

Sperling, R.A., Gil, P.R., Zhang, F., Zanella, M., Parak, W.J., 2008. Biological applications of gold nanoparticles. *Chemical Society Reviews* 37, 1896-1908.

Terpstra, T.J., 1952. The asymptotic normality and consistency of Kendall's test against trend, when ties are present in one ranking. Proceedings of the Section of Sciences, Koninklijke Nederlandse Akademie van Wetenschappen 55 (Series A), 327–333.

Tsunoyama, H., Sakurai, H., Ichikuni, N., Negishi, Y., Tsukuda, T., 2004. Colloidal gold nanoparticles as catalyst for carbon-carbon bond formation: Application to aerobic homocoupling of phenylboronic acid in water. *Langmuir* 20(26), 11293-11296.

Uboldi, C., Bonacchi, D., Lorenzi, G., Hermanns, M.I., Pohl, C., Baldi, G., Unger, R.E., Kirkpatrick, C.J., 2009. Gold nanoparticles induce cytotoxicity in the alveolar type-II cell lines A549 and NCIH441. *Particle and Fibre Toxicology*, 6(18).

Van Hoecke, K., De Schamphelaere, K.A.C., Van der Meeren, P., Lucas, S., Janssen, C.R., 2008. Ecotoxicity of silica nanoparticles to the green alga *Pseudokirchneriella subcapitata*: importance of surface area. *Environmental Toxicology and Chemistry* 27(9), 1948-1957.

Van Hoecke, K., Quik, J.T.K, Mankiewicz-Boczek J., De Schamphelaere, K.A.C, Elsaesser, A., Van der Meeren, P., Barnes, C., McKerr, G., Howard, C.V, Van de Meent, D., Rydzynski, K., Dawson, K.A., Salvati, A., Lesniak, A., Lynch, I., Silversmit, G., De Samber, B., Vincze, L., Janssen, C.R., 2009. Fate and effects of CeO_2 nanoparticles in aquatic ecotoxicity tests. *Environmental Science and Technology* 43, 4537–4546.

Wang, S., Lu, W., Tovmachenko, O., Rai, U.S., Yu, H., Ray, P.C., 2008. Challenge in understanding size and shape dependent toxicity of gold nanomaterials in human skin keratinocytes. *Chemical Physics Letters* 463, 145–149.

Woehrle, G.H., Brown, L.O., Hutchison, J.E., 2005. Thiol-Functionalized 1.5-nm Gold Nanoparticles through Ligand Exchange Reactions: Scope and Mechanism of Ligand Exchange. *Journal of the Americal Chemical Society* 127, 2172-2183.

Zhang, F., Ali, Z., Amin, F., Feltz, A., Oheim, M., Parak, W.J., 2010. Ion and pH Sensing with Colloidal Nanoparticles: Influence of Surface Charge on Sensing and Colloidal Properties. *Chemical Physics and Physical Chemistry* 11, 730-735.

Table 1 - Mean particle sizes and polydispersity indexes (PI) determined by DLS in OECD algae medium and in Leibovitz's L15 medium.

	AP		**APma10kPEG**	
Medium	**Diameter** (std.dev.) (nm)	**PI** (std.dev.)	**Diameter** (std.dev.) (nm)	**PI** (std.dev.)
OECD	17.6 (3.8)	0.293 (0.155)	35.6 (0.7)	0.354 (0.048)
L15	21.5 (0.7)	0.415 (0.025)	37.3 (1.3)	0.292 (0.064)

639 **Table 2 -** Effect concentrations (std.dev.) (n = 2) of AP and APma10KPEG particles

640 obtained in 72 h algal growth inhibition tests.

	AP	**APma10KPEG**
E_rC_{10} (µM)	0.0031 (0.0003)	0.013 (0.001)
E_rC_{20} (µM)	0.0049 (0.0005)	0.028 (0.003)
E_rC_{50} (µM)	0.019 (0.006)	0.10 (0.02)
E_rC_{10} (mg/l)	1.2 (0.1)	5.1 (0.3)
E_rC_{20} (mg/l)	1.9 (0.2)	11 (1)
E_rC_{50} (mg/l)	7.5 (2.3)	39 (7)

Table 3 - Quantitative uptake of AP particles in RTGill-W1 cells exposed to various concentrations during 1 h.

Exposure concentration	**concentration in cell homogenate**	**mass taken up by cell layer**	**Number of particles/cell**
mg/l	mg/l	µg	(x10^6)
10	0.05 (0.10)	0.02 (0.03)	0.13 (0.24)
22	0.29 (0.12)	0.09 (0.04)	0.69 (0.29)
46	1.2 (0.1)	0.38 (0.04)	2.9 (0.3)
100	3.1 (0.1)	0.94 (0.04)	7.3 (0.3)

Figure legends

Figure 1 - 4-5 nm Au NPs capped with dodecanethiol, coated with an amphiphilic polymer, consisting of dodecylamine and poly-(isobutylene-alt-maleic anhydride) (PMA) (A), to which 10000 MW polyethylene glycol (PEG) molecules are attached (B).

Figure 2 - Chlorophyll fluorescence of algal concentration series in standard OECD medium supplemented with amphiphilic coated Au NPs (AP) in various concentrations. Straight lines are linear least squares regressions.

Figure 3 - Resorufin fluorescence in L15 medium + 45 µM resazurin without and with 10 and 100 mg/l amphiphilic coated Au NPs (AP).

Figure 4 - Particle size distributions of AP and APma10KPEG particles in L15 and in OECD medium.

Figure 5 - Light absorbance spectrum of 20 mg/l AP and APma10KPEG particles in L15 medium.

Figure 6 - Concentration-response curves of AP and APma10KPEG particles obtained in 2 independent 72 h algal growth inhibition tests.

Figure 7 - Results of 96 well plate experiment to assess the shading effect induced by AP (part A) and APma10KPEG (part B) particles. The white bars indicate algal cells directly exposed to Au NPs in the same well, while the black bars indicate algal cells spatially separated from the particles. Treatments significantly different from the control are indicated by an asterisk (*).

Figure 8 – Concentration-response curves of AP and APma10KPEG Au NPs obtained in 24 h resazurin cytoxicity assays with RTGill-W1 cells. Data points present mean values (std.dev.) assessed in 4 separate experiments.

Figure 9 – RTGill-W1 cell morphology in the control (A) and exposed to 0.12 µM (~46 mg Au/l AP (B) and APma10KPEG (C) particles after 24 h.

Figure 10 - Overlap laser scanning microscopy images of RTGill-W1 cells in the control (A) and exposed to AP (B, C) and APma10KPEG (D) particles. The height of the Z plane where the fluorescence was registered is given in parts B, C and D.

Figure 11 - TEM images of *Pseudokirchneriella subcapitata* cross sections in the control (A, B, C), exposed to APma10KPEG (D) and to AP particles (E, F). In panel F initiation of cell division can be observed. chl = chloroplast; p = polyphosphate; s = starch; va = vacuole.

Figure 12 - TEM images of RTGill-W1 cells in the control (A) and exposed to 0.0057 µM (~2.2 mg Au/l) AP (B, C) and APma10KPEG (D, E) particles.

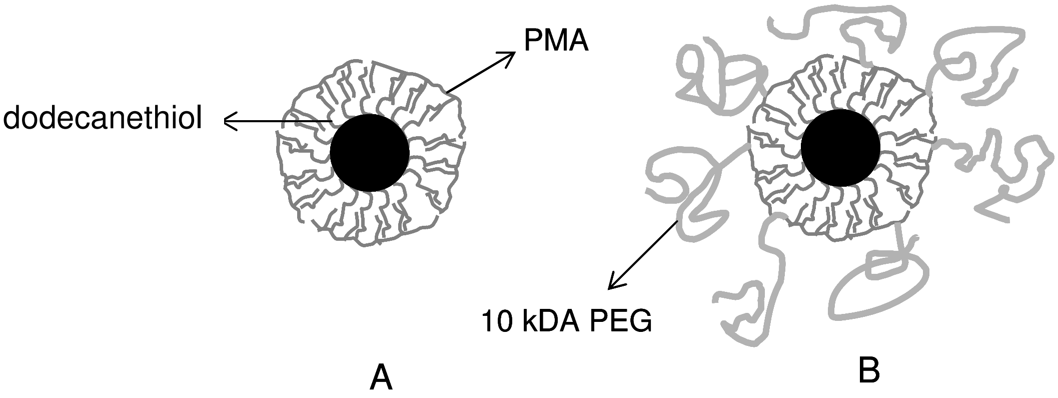
PMA
dodecanethiol
10 kDA PEG
A
B

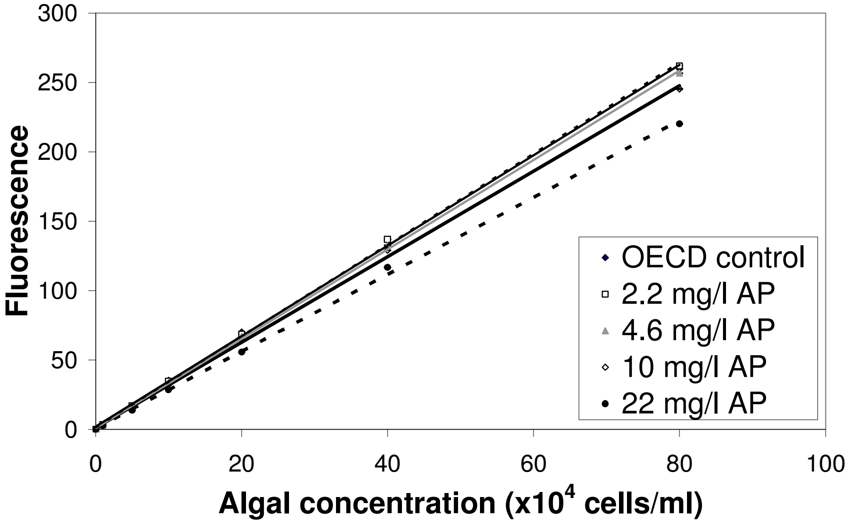
300
250
200
150
100
50
0
Fluorescence
0
20
40
60
80
100
Algal concentration (x10^4 cells/ml)
◆ OECD control
□ 2.2 mg/l AP
▲ 4.6 mg/l AP
◇ 10 mg/l AP
● 22 mg/l AP

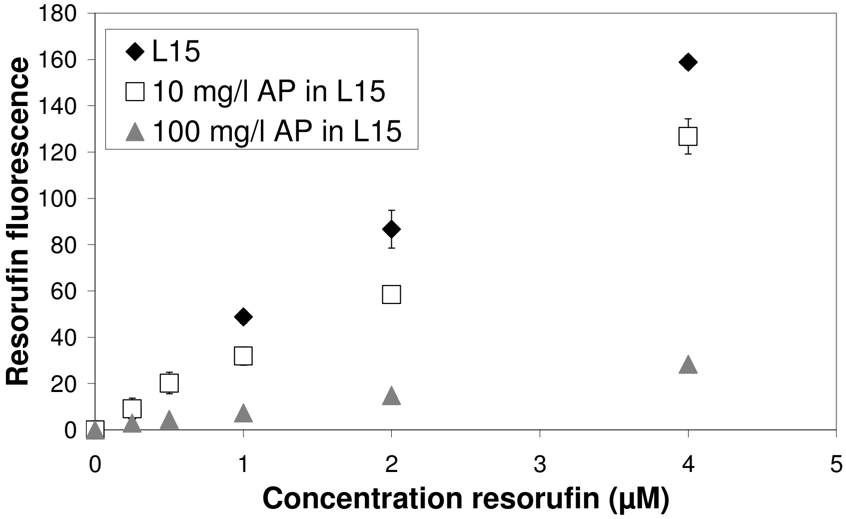
180
160
140
120
100
80
60
40
20
0
0
1
2
3
4
5
Resorufin fluorescence
Concentration resorufin (µM)
◆ L15
☐ 10 mg/l AP in L15
▲ 100 mg/l AP in L15

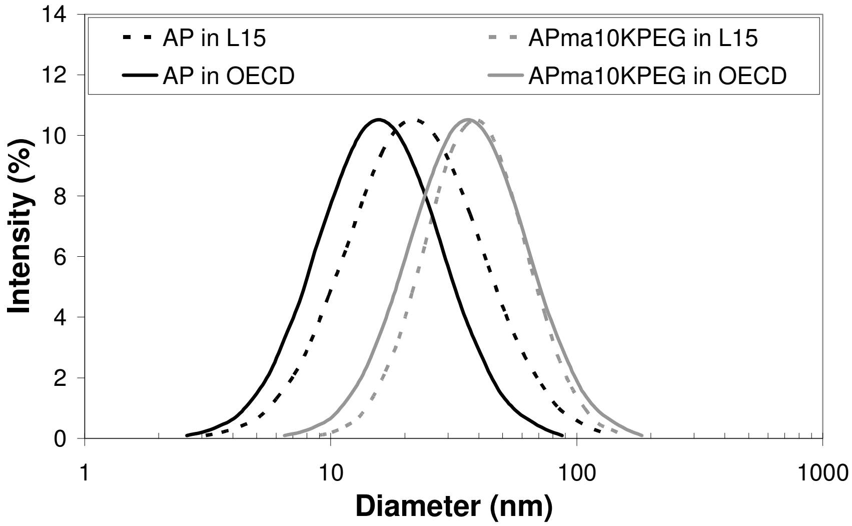
14
12
10
8
6
4
2
0
Intensity (%)
1
10
100
1000
Diameter (nm)
AP in L15
AP in OECD
APma10KPEG in L15
APma10KPEG in OECD

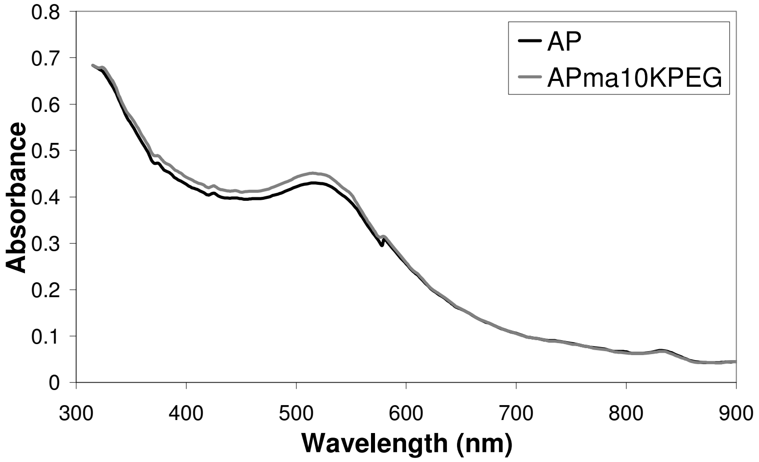
0.8
0.7
0.6
0.5
0.4
0.3
0.2
0.1
0
Absorbance
300
400
500
600
700
800
900
Wavelength (nm)
AP
APma10KPEG

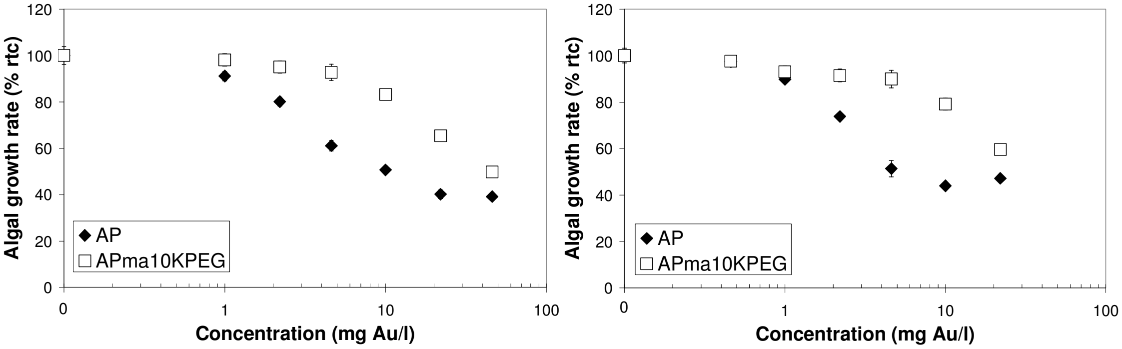
120
100
80
60
40
20
0
Algal growth rate (% rtc)
◆ AP
□ APma10KPEG
0
1
10
100
Concentration (mg Au/l)
120
100
80
60
40
20
0
Algal growth rate (% rtc)
◆ AP
□ APma10KPEG
0
1
10
100
Concentration (mg Au/l)

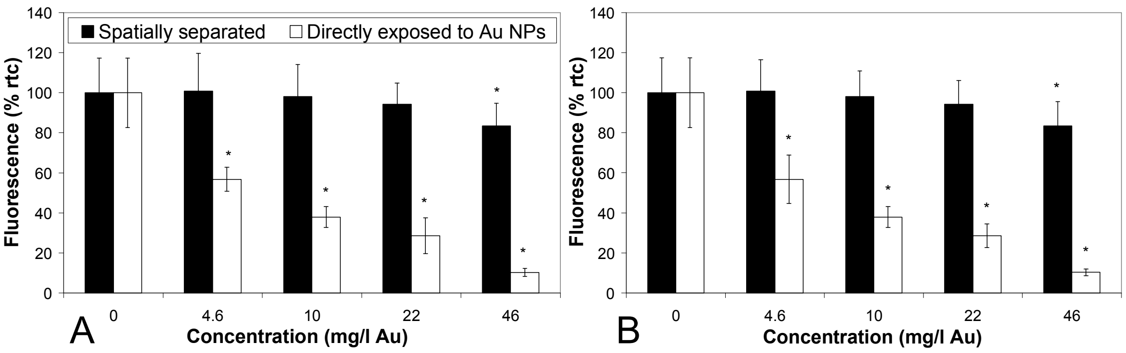
■ Spatially separated
□ Directly exposed to Au NPs
Fluorescence (% rtc)
140
120
100
80
60
40
20
0
0
4.6
10
22
46
Concentration (mg/l Au)
*
A
B

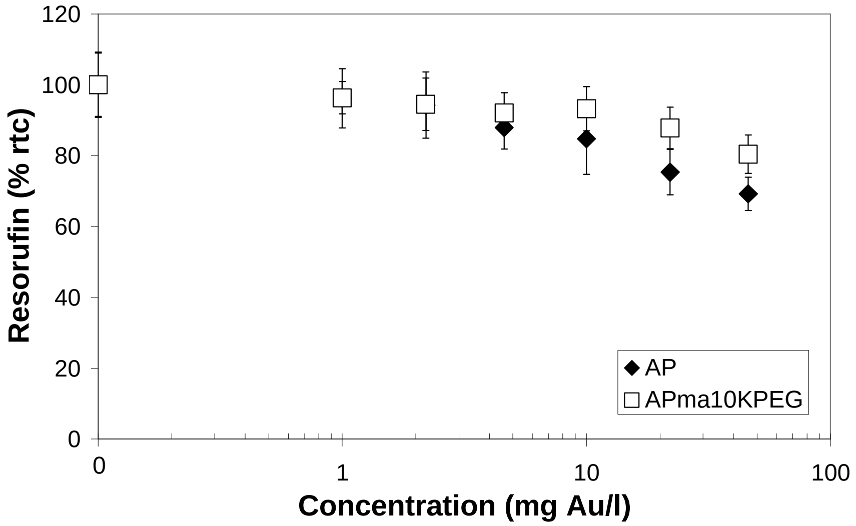
120
100
80
60
40
20
0
Resorufin (% rtc)
0
1
10
100
Concentration (mg Au/l)
◆ AP
□ APma10KPEG

G41

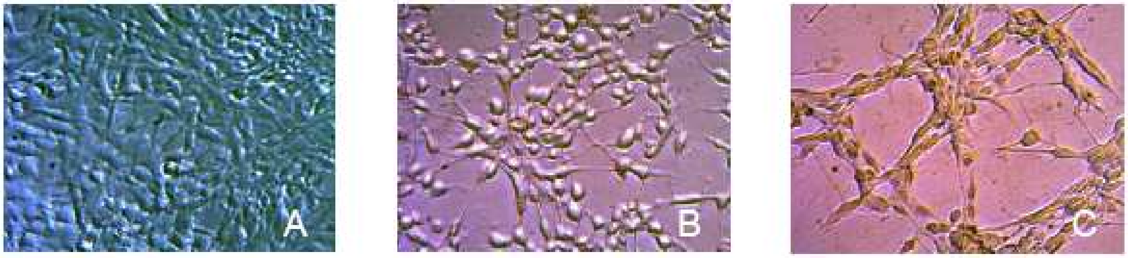
A
B
C

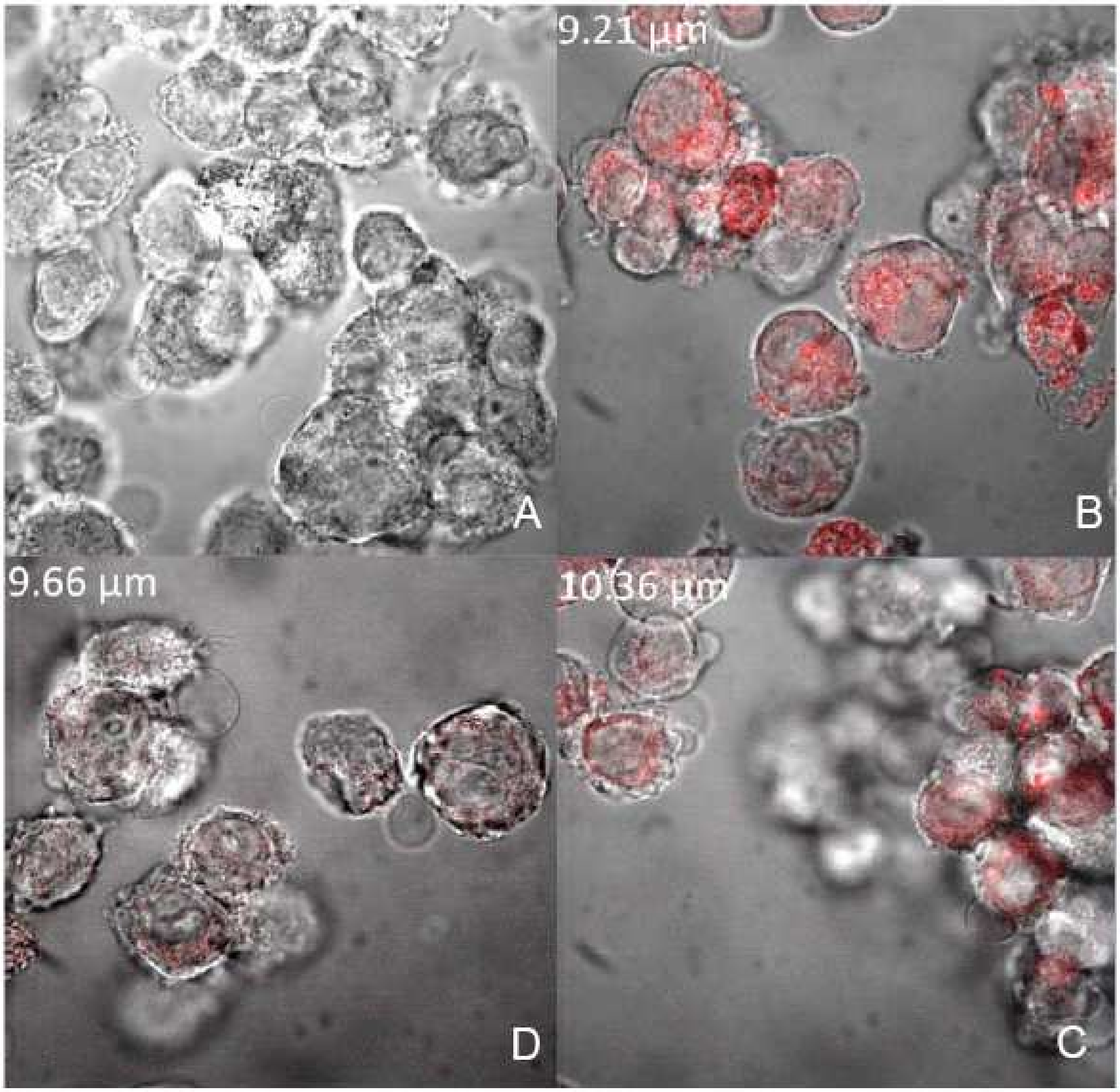
9.21 µm
A
B
9.66 µm
10.36 µm
D
C

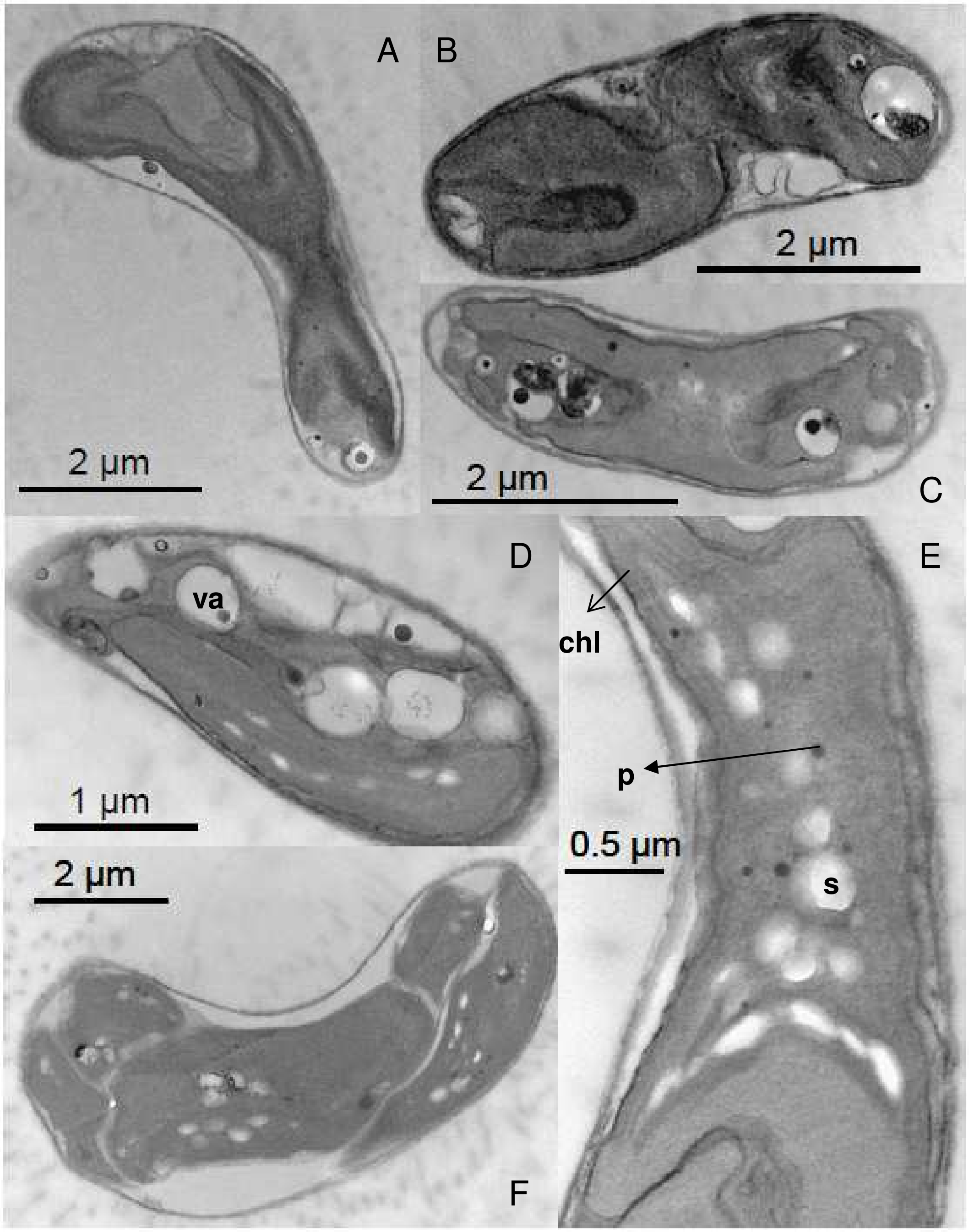
A
B
2 µm
2 µm
2 µm
C
D
va
1 µm
E
chl
p
0.5 µm
s
2 µm
F

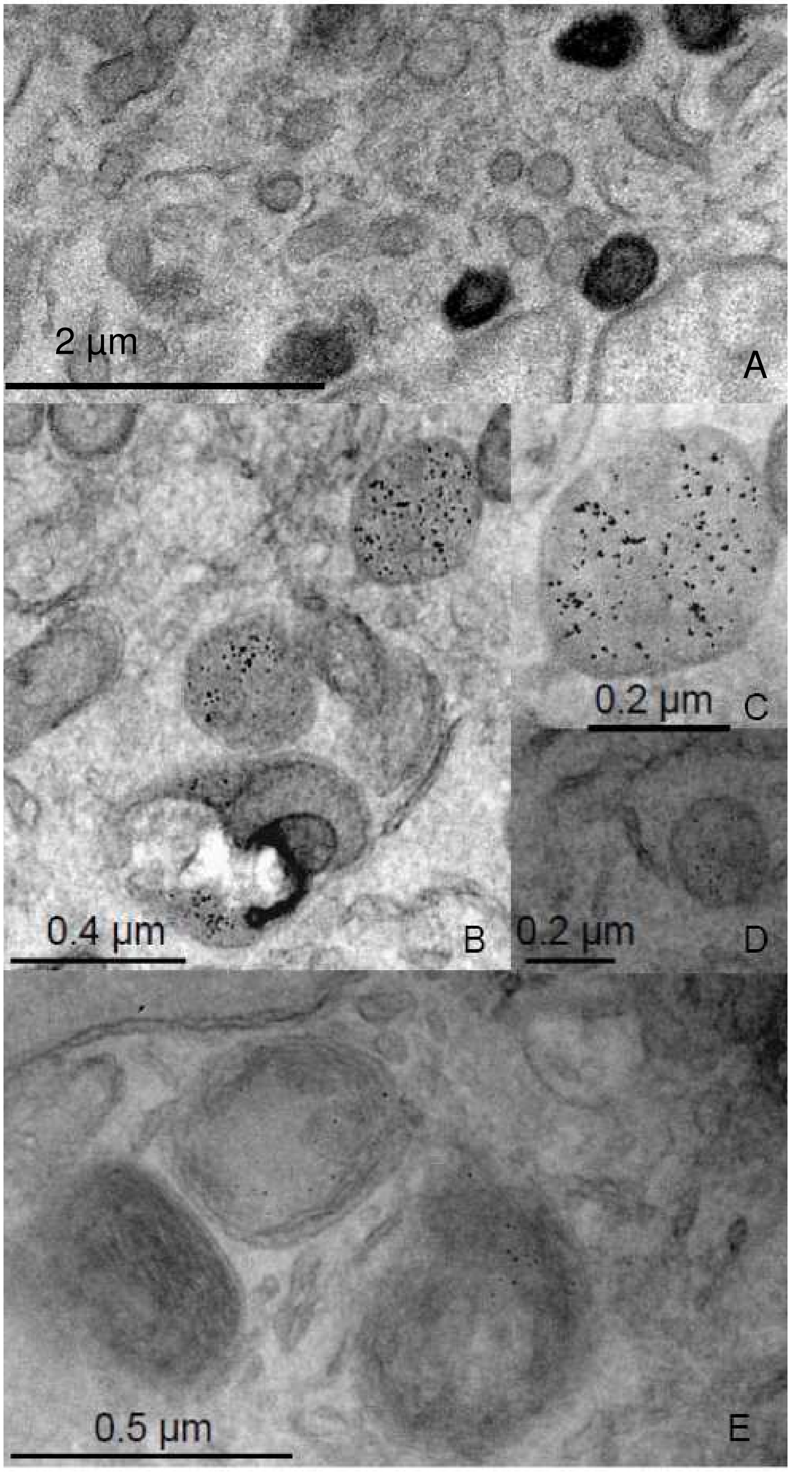

G45

Anal Bioanal Chem
DOI 10.1007/s00216-010-3609-8

TRENDS

In vitro and intracellular sensing by using the photoluminescence of quantum dots

Feng Zhang · Zulqurnain Ali · Faheem Amin · Andreas Riedinger · Wolfgang J. Parak

Received: 24 December 2009 / Revised: 18 February 2010 / Accepted: 21 February 2010

Abstract Quantum dots (QDs) have attracted increasing attention due to their unique physical and chemical properties. This article introduces recent advances in using QDs' photoluminescence (PL) for in vitro and intracellular sensing analytes, in particular ions, and biomolecules from the last 3 years. Different sensing strategies are demonstrated and compared for increasing the detecting/sensing selectivity. The perspectives for in vitro and intracellular sensing based on QDs' PL are also discussed.

Keywords Quantum dots · Ion sensing · Analyte detection · Fluorescence detection · FRET

Introduction

Quantum dots (QDs) are well-dispersed semiconductor nanocrystals, which have attracted increasing attention since their discovery in the early 1980s [1–3]. As a result of their small size of a few nanometers, QDs exhibit quantum confinement effects that are responsible for their intrinsic properties such as the size-dependent wavelength of their photoluminescence (PL) [4]. Compared with organic fluorophores, QDs posses advantageous characteristics such as narrow emission bands, high brightness, and increased photostability [5], which altogether makes them interesting for biological applications [6]. For applications in biomedical studies, QDs should be water soluble, which can be achieved in two ways: the first is to directly synthesize QDs in aqueous solution [7]; the other is to synthesize QDs in organic solvents [8] and then transfer the hydrophobic QDs into aqueous solution, for example, by ligand exchange [5, 9] or polymer coating [10, 11]. Although the second strategy is more time consuming, it offers some advantages such as the possibility of using higher synthesis temperatures, which is favorable for growing complex structures (e.g., core/shell) [12].

The early diagnosis of diseases can be envisaged at the cellular level because some chemical changes within cells are observable before tissue-level changes become evident [13]. Obtaining prognostic chemical changes at the molecular level is one significant aim of nanomedicine, which can be realized by using engineered devices and nanostructures, like nanoparticle sensors. Different kinds of nanoparticle sensors made for biomedical applications have already been reported since the pioneering work by Clark et al. [14]. QD-based fluorescence sensors have been an intensively studied field because of the unique features of QDs. Owning to their small size, QDs have a very high surface-to-volume ratio. The smaller the QD size is the more atoms are exposed on the surface. Subtle interactions between these surface atoms and surrounding molecules can significantly influence the QDs' PL characteristics, which is the main reason for them being one of the most potentially useful nanoparticles for biosensing. Although QDs are also used for electrochemically based sensing applications [15–18], in this article we will focus on QDs used in PL-based sensing applications.

PL-based sensing systems are generally designed such that interaction between the analytes and QDs leads to a distinguishable PL perturbation that can be displayed on a readout. To this end, the first strategy is to make use of direct PL changes upon analyte binding. Defects on the QD surface normally reduce their quantum yield, while such surface defects can be passivated via binding of analytes

---

F. Zhang (✉) · Z. Ali · F. Amin · A. Riedinger · W. J. Parak
Philipps Universität Marburg, Fachbereich Physik,
Renthof 7,
35037 Marburg, Germany
e-mail: feng.zhang@physik.uni-marburg.de

such as ions or molecules, which is called surface passivation (Fig. 1a). Conversely, some bound analytes can create more surface defects. This eventually will lead to a reduced PL readout, which is called depassivation (Fig. 1b). A good combination of specific depassivation and passivation effects can be cleverly harnessed in some sensing system designs. For example, reduced PL of QDs is obtained due to the binding of depassivation molecules, via a relatively weak affinity interaction, to the QDs' surface. This reduced PL can be restored upon binding of analytes which have higher binding affinities than the previously bound depassivation molecules. This in turn restores the PL in a concentration-dependent manner based on the competition between depassivation molecules and analytes for binding to the QD surface (Fig. 1c). Even more elegant QD-based sensing systems can be designed by two main methods. The first is also the most used and is based on fluorescence (Förster) resonance energy transfer (FRET, Fig. 2). In FRET sensing systems, QDs normally act as donor and transfer excitation energy to a vicinal fluorophore acceptor, leading to a reduced donor PL and a concomitant increased acceptor PL. The second method is photoinduced electron transfer (PET, Fig. 3). In PET sensing systems, the excited QDs act as the electron donor and transfer the excited electrons to acceptor molecules. This in turn results in a quenched QD PL and an increased acceptor PL (if possible). In both, FRET and PET sensing systems, the most significant advantage is that the transfer efficiencies can be used as a ratiometric readout without demanding an extra reference. The second advantage is that such sensing systems are more flexible and enable more complicated designs, resulting from the multiple components involved, e.g., donor, acceptor, and spacers. As QD-based sensing applications have been already reviewed [19–25], this article focuses on recent advances mainly from 2007 to 2009.

In vitro sensing

Ions

Since the first experiment in which changes in the PL of CdS-based QDs were reported upon the addition of Zn^{2+} and Cd^{2+} [26], QDs have provided the basis for PL-based sensing of many cations [27–29]. Selectivity in such devices was achieved by synthesizing the QDs out of different materials and by variation of the surface coating. In the last 2 years the scope of target cations has been extended to include bio-related heavy metal ions and transition metal ions. For example, Ag^+ was demonstrated to cause PL enhancement of CdS QDs modified with bismuthiol(II) potassium salt. This PL enhancement is due to a passivation effect via the formation of a CdS/Ag–bismuthiol(II) complex on the QD surface. This complex creates new radiative centers and blocks defect sites available for nonradiative electron/hole (e^-/h^+) recombination [30]. In contrast, CdTe QDs modified with denatured bovine serum albumin (BSA) were used for Ag^+ sensing, which shows a linear quenching behavior to increasing Ag^+

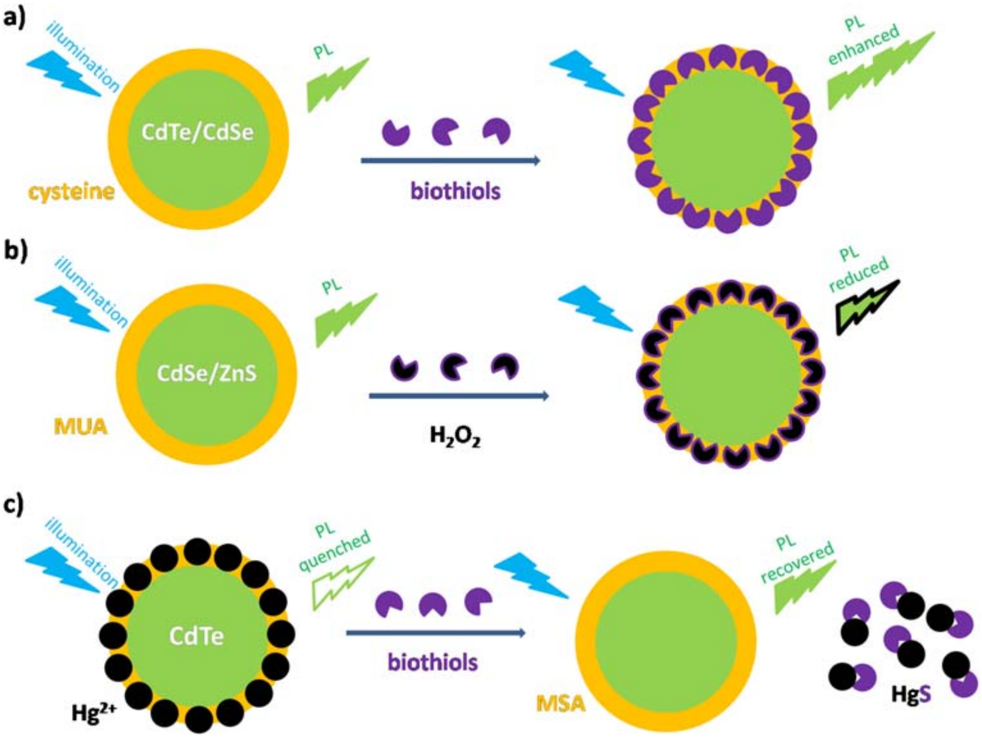

Fig. 1 Sensing mechanisms for QDs directly binding analytes. **a** Cysteine-capped CdTe/CdSe QD. Upon binding of biothiol molecules like cysteine, homocysteine, and GSH, the QD PL is enhanced due to passivation. **b** MUA-capped CdSe/ZnS QD. Upon binding of H_2O_2, the QD PL is reduced due to depassivation. **c** MSA-capped CdTe QDs are first quenched by Hg^{2+}. Upon binding to biothiols, due to the formation of stronger Hg–S bonds, the original QD PL is recovered

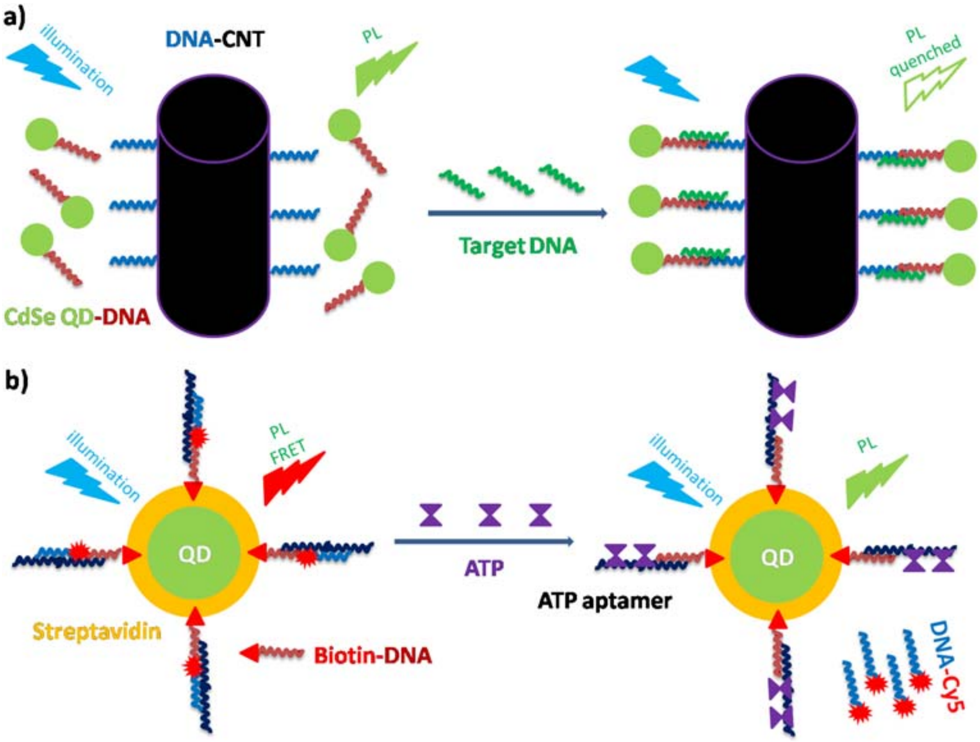

Fig. 2 FRET-based sensing. **a** CdSe QDs and CNTs are conjugated with two oligonucleotides. The two oligonucleotides can be hybridized upon binding a target DNA fragment. In the absence of target DNA, the QD has its original PL. In the presence of the target DNA fragment, hybridization brings QD and CNT close enough so that the QD PL is quenched by the CNT. **b** Streptavidin modified commercial QDs 'decorated' with biotinylated DNA fragments. An ATP aptamer binds with one side to the DNA attached to the QD and with one side to Cy5-labeled DNA. Upon excitation of the QD donor, FRET reduces the QD PL and increases the PL of the Cy5 acceptor. In the presence of ATP molecules, the aptamer dehybridizes and complexes the ATP. As soon as the Cy5-labeled DNA becomes detached from the ATP aptamer, the distance to the QD is increased and there is no longer FRET

concentration. This quenching is caused by a depassivation effect resulting from the formation of small Ag_2Te particles on the QD surface, which are believed to act as e^-/h^+ recombination centers and facilitate nonradiative e^-/h^+ annihilation [31]. Similar sensing has also been reported for other cations. Glutathione (GSH)-capped $Zn_{0.96}Hg_{0.04}Se$ QDs were used to sense Cu^{2+} ions by quenching their PL, which was explained by two possible mechanisms: one due to the depassivation effect in which Cu^{2+} replaces the Hg/Zn and forms insoluble CuS or CuSe on the QD surface; the

Fig. 3 PET-based sensing. **a** MTMA-capped CdSe/ZnS QD. Upon binding ATP/GTP molecules by electrostatic adsorption, the original QD PL is reduced as excited electrons are transferred to ATP/GTP molecules. **b** MPA-capped CdSe/ZnS QD. The PL is quenched by binding of the electron acceptor lucigenin to the QD surface. In the presence of Cl^-, due to the higher affinity between lucigenin and Cl^-, the bound lucigenin detaches from the QD surface resulting in a recovered PL

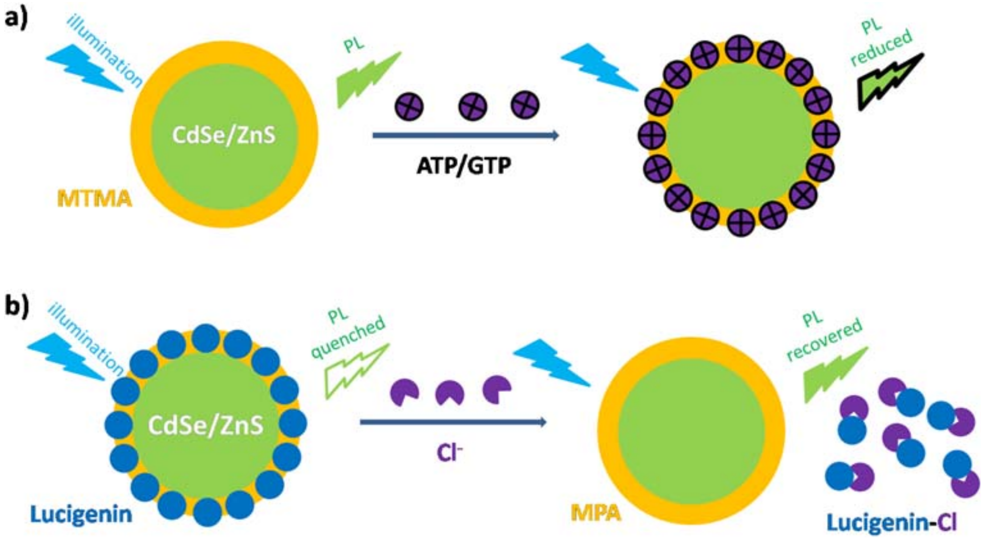

other electron transfer from GSH to Cu^{2+} [32]. The same sensing principle also works for core/shell CdTe/CdSe QDs capped with 3-mercaptopropionic acid (MPA) [33] and CdTe nanowires capped with cystein and thioglycolic acid (TGA) [34]. Pb^{2+} was found to reduce the PL of GSH-capped CdTe and CdZnSe-based QDs due to the detachment of GSH from the QD surface upon formation of a stronger Pb–S bond between Pb^{2+} and GSH [35]. The examples described so far rely on direct changes of the QD PL in the presence of ions on the QDs' surface. This principle is simple to realize, but arguably the selectivity to specific ions is limited. In general, moderate selectivity can be achieved as some cations stick better to the ligands protecting the QD surface than others [35]. Hence, the use of certain metal-specific ligands on the QD surface is an attractive approach to improve sensing selectivity. In fact, high selectivity for Cd^{2+} has been achieved with crown ether ligand-modified CdS:Mn/ZnS QDs. The crown ether ligands quenched the QD PL by a depassivation effect that formed an alternative annihilation pathway for e^-/h^+ pairs on the QD surface. In turn, binding Cd^{2+} to the ligands restored the PL due to the blocking of the depassivation effect via a ligand–Cd^{2+} complex in which the donor electrons from the ligands' amine groups stop transferring to the QDs [36].

Further improved systems can be made by involving additional compounds. For example, Wang et al. designed a FRET system between positively charged CdTe QDs capped with cysteamine and negatively charged gold nanoparticles capped with 11-mercaptoundecanoic acid (MUA). In this FRET system, the donor QDs' PL will be quenched by the close acceptor gold nanoparticle, which is due to the high extinction coefficient and broad absorption of gold nanoparticles. In the absence of Pb^{2+}, QDs and gold nanoparticles assemble into aggregates due to their mutual electrostatic attraction, leading to quenching of the QD PL. In the presence of Pb^{2+}, MUA-modified Au nanoparticles aggregate by means of ion template chelation, which in turn frees the QDs and thus results in a restored PL readout [37]. Using PL changes of the QDs instead of detecting changes in the surface plasmon resonance of the Au nanoparticles helps to improve the sensitivity. FRET can be also used in a fixed geometry, where the QDs act as donors (and carriers) for the excitation of an analyte-sensitive fluorophore as acceptor [38]. QD-based FRET sensors have been pioneered by the groups of Mattoussi [39] and Willner [40]. H^+-sensitive CdSe/ZnS QDs have been demonstrated based on this principle [41]. In addition, multi-analyte sensing with QDs was developed by Ruedas-Rama et al. who simultaneously detected two different types of ions, namely K^+ and Cl^-, by using polyacrylic particles containing QDs and two kinds of ion sensitive fluorophores, while the QDs were used to excite the organic fluorophores independently from each other and thus generating two different FRET pairs [42].

Anions have also been studied intensively. For example, based on PET, a sensor was designed to detect common anions [43]. In this paper, CdSe/ZnS QDs acted as the fluorophore (donor), 3-phenylthiourea as the acceptor, and $NH_2(CH_2)_2SH$ as spacer between the QD and the acceptor. In the presence of anions, such as F^-, Cl^-, or CH_3COO^-, the original PL of QDs was 90% quenched. This is attributed to an increase in the reduction potential of the receptor upon anion binding, which resulted in an increased efficiency of PET from the excited QD to the receptor. Other anions like Br^- or HSO_4^- did not show significant quenching effects [43]. In an alternative approach, Mulrooney et al. designed a sensor in which the PL of CdSe/ZnS QDs was first quenched by attached ferrocene ligands. Binding of anions modulates the rate of PET between ferrocene and QDs. For example, F^- can restore the PL of the QDs [44]. A similar strategy was applied to a Cl^- sensor based on MPA-capped CdSe/ZnS QDs [45] in which the Cl^--sensitive dye lucigenin (acridinium dication) self-assembled on the surface of negatively charged QDs driven by electrostatic adsorption and acted as electron acceptor. Within this QD–dye conjugate, the electron transfer from QD to lucigenin reduces the QD PL and also quenches the lucigenin. In the presence of Cl^- ions, PET is reduced and the QDs' PL is restored [45]. Another example exploiting this strategy is a CN^- sensor, in which CN^- was found to restore the Cu^{2+}-quenched PL of mercaptosuccinic acid (MSA)-capped CdTe QDs in aqueous media [46]. This effect is due to the higher binding affinity of Cu^{2+} to CN^- than to QDs, so that the presence of CN^- leads to Cu^{2+} desorption from the QDs and thus restores the QDs' PL. The same principle was also applied to sense CN^- by using hydrophobic tri-*n*-octylphosphine oxide (TOPO)-coated CdSe QDs which were previously quenched by 2,20-bipyridine-bound Cu^{2+} [47].

Small molecules

By making use of the specific properties of some molecules or integrating other well-established techniques, analytes like NO [48], urea [49], and the herbicide 2,4-dichlorophenoxyacetic acid (2,4-D) [50] were also sensed by QD-based systems. NO is, for example, easily oxidized by dissolved oxygen in water. This mechanism was applied to sense NO in aqueous solution. In one recent paper, triethanolamine (TEA)-capped CdSe QDs increased their PL by surface passivation due to the absorbed oxygen on their surface. In the presence of NO, the dissolved O_2 is consumed by the oxidation of NO, leading to the detachment of O_2 from the QDs' surface with a concomitant quenching of the original PL [48]. The abovementioned urea sensor is based on the previous finding that increasing pH enhances the PL of MSA-capped CdSe/ZnS QDs by a surface passivation effect [51]. It is well known that the degradation of urea by the enzyme urease produces HO^- ions, leading to increased solution pH. On the basis of these findings, a combination of both reactions was exploited for quantitatively analyzing urea. In practice, the mixture of urease and MSA-capped CdSe/ZnS QDs was added into the sensing solutions. Upon increasing urea concentration, the QD PL was demonstrated to increase linearly [49]. The abovementioned herbicide 2,4-D sensor is based on an integrated competitive fluoroimmunoassay technique [50] in which an immunoreactor column is first modified by using herbicide 2,4-D antibodies. The sensor was calibrated for zero 2,4-D by passing a defined amount of 2,4-D-modified CdTe QDs through the immunoreactor column. The PL of the eluted 2,4-D-modified CdTe QDs was then taken as the offset for zero concentration of free 2,4-D. Free 2,4-D competes with 2,4-D-modified CdTe QDs. Thus the PL of an eluted solution (containing free 2,4-D and a defined amount of 2,4-D-modified CdTe QDs) will be proportional to the concentration of free 2,4-D. The authors claimed that the detection limit in this way is higher compared with the indirect competitive ELISA method.

Biomolecules

The sensing of biological molecules is one of the most exciting and rapidly growing areas of analytical science. Small biomolecules can also directly passivate the QDs' surface to result in PL enhancement. For example, on the basis of the strong affinity binding of biothiol molecules to QDs, Zhang et al. used near-infrared CdTe/CdSe QDs to detect cysteine, homocysteine, and GSH in the presence of 20 other amino acids in biophysical fluids (Fig. 1a). The authors claimed that biothiol molecules enhance the PL of QDs by improving the surface passivation by decreasing the number of e^-/h^+ traps [52]. Here we want to point out again that surface passivation alone without specific binding typically does not afford high selectivity. On the other hand, biological science provides many strategies for highly selective recognition. Such interactions involve receptor–ligand, antigen–antibody, DNA–protein, sugar–lectin pairs, etc. FRET is often used to make use of these recognition pairs coupled to the QD sensor. Sensors for biomolecules such DNA [53–56], proteins [57], and enzymes in particular [58–60] have been demonstrated. A review of this topic was given by Medintz et al. [61]. As an example, we highlight the publication by Cui et al. [56] in which they employed multiwalled carbon nanotubes (CNTs) and QDs both capped with oligonucleotides as probe sequences. In the presence of target DNA complementary to both of the oligonucleotides attached to CNTs and QDs, the CNTs and the QDs assembled via DNA hybridization leading to a quenched PL due to FRET (Fig. 2a). To extend the hybridization principle to highly selectively sense other biomolecules, nucleic acid aptamers are a good example. They can specifically recognize various molecular targets such as small molecules, proteins, nucleic acids, and even cells, tissues, and organisms. Similar to the experiment described above, aptamers complementary to DNA sequences attached to a QD donor and fluorophore acceptor can bring QDs and fluorophores into close proximity. QD PL is thus quenched by FRET. In the presence of analytes which can capture the aptamer, the complementary DNA sequences will detach from the aptamer. In this way, QDs and fluorophores are no longer linked and QD PL is restored; this has been demonstrated by an ATP aptamer [62] (Fig. 2b). In comparison, Callan et al. found that ATP and GTP (guanosine triphosphate) can quench the PL of CdSe/ZnS QDs by PET if they are close enough. For designing a sensor, QDs were coated by (2-mercaptoethyl)trimethylammonium chloride (MTMA) to be positively charged. Negatively charged ATP and GTP molecules thus are strongly attracted by the electrostatic interaction (Fig. 3a) [63]. Comparing both strategies for ATP detection shows that higher selectivity was achieved by using aptamers as recognition site, compared with “recognition” based only on common electrostatic interaction. This emphasizes the point that sensors based on molecular recognition generally possess higher selectivity.

In a series of publications the Willner group demonstrated a variety of sophisticated QD-based sensing systems. In a first paper they designed a competitive FRET system for sensing vicinal saccharides and dopamine molecules [64] based on boronic acid's unique ability to form reversible covalent complexes with vicinal diols. Since the conjugation is reversible, it can be used for a competitive FRET design. In practice, fluorophore-modified monosaccharides or dopamines were linked to 3-aminophenylboronic acid-modified CdSe/ZnS QDs. In this configuration, FRET can be observed. On the other hand, in the presence of nonfluorescent analytes such as monosaccharides and dopamines, the FRET efficiency was reduced due to the competition between fluorescent and nonfluorescent analytes. In this way vicinal diols such as galactose, glucose, and dopamine could be sensed. However, this method is limited by the lack of selectivity of boronic acid toward different vicinal diols. An improved competitive FRET system was not only able to detect different small molecules, but also their chiralities. Thus, the above described boronic acid-conjugated CdSe/ZnS QDs were further functionalized with beta-cyclodextrin (beta-CD). The idea behind the sensor is that the hydrophobic cavity of beta-CD has different affinities toward different organic molecules. In the absence of analytes, Rhodamine B binds to the cavity, producing FRET. When analytes compete with Rhodamine B to occupy the cavity this leads to a reduced FRET readout.

In addition, because of the chiral nature of beta-CD, this sensor could also discriminate between D,L-phenylalanine and D,L-tyrosine [65].

Another concept for biomolecule sensing is the integration of signal cascades. The Willner group has already demonstrated several such FRET-based biomolecular sensors. In one recent case, glucose and acetylcholine esterase (AChE) were sensed by MUA-capped CdSe/ZnS QD-based sensors [66]. The main principle is the following: H_2O_2 can effectively quench the PL of QDs due to a surface depassivation effect, in which the oxidation of S^{2-} surface states yields Zn^{2+} surface traps for electrons (Fig. 1b). This can be used to sense reactions which produce H_2O_2. An example for sensing the direct production of H_2O_2 is the detection of glucose by glucose oxidase (GOD), which catalyzes conversion of glucose to gluconic acid and H_2O_2. Also H_2O_2 produced by a signal cascade can be detected. Acetylcholine esterase (AChE) is an enzyme able to cleave acetylcholine into choline. Choline can be further oxidized to betaine by a second enzyme, choline oxidase (ChOx). This second reaction leads to a concomitant formation of H_2O_2. Coming back to the glucose detection described above, the authors designed a FRET system in which fluorescein isothiocyanate (FITC) was conjugated to avidin-modified commercial CdSe/ZnS QDs. GOD was also immobilized to the QDs via biotin–avidin linkages. In the presence of glucose H_2O_2 was produced by the attached enzyme GOD, which in turn quenched the QDs' PL in a concentration-dependent manner. With the same FRET system inhibitors which can block the enzymatic production of H_2O_2 could be detected as well [66] (Fig. 4b). In another recent paper from the Willner group, the design of a new nicotinamide adenine dinucleotide (NADH) and glucose sensor was demonstrated. The basis was a specific dye (methylene blue, MB^+), which loses its color after being reduced by NADH to MBH [67]. To allow for a ratiometric design, the authors designed a FRET system in which MB^+ dye-modified avidin molecules were covalently conjugated to GSH-capped CdSe/ZnS QDs. In the presence of NADH, the FRET efficiency decreased since MB^+ is converted to MBH. Because NADH is concomitantly formed as glucose is oxidized by glucose dehydrogenase (GDH), this principle can be also applied to quantitatively sense glucose [67].

Intracellular sensing

For many applications, knowledge of intracellular concentrations of certain analytes would be desirable. Han et al. [68] recently reported the detection of biothiols such as GSH, homocysteine, and cysteine from the cytosolic fluid of Hela cells. However, this cannot be called a real intracellular sensing because they just delivered the QD sensor (Hg^{2+}-impregnated CdTe QDs) into lysed Hela cells. The idea is that Hg^{2+} can strongly quench the QDs' PL. In the presence of biothiols, the Hg^{2+} departs from the QD surface because of the formation of much stronger Hg–S bonds, and thus the PL readout is restored (Fig. 1c). The results showed that the restoration ability of these three biothiols followed the order GSH > homocysteine > cysteine, which was attributed to decreasing steric hindrance effects. Furthermore the authors found that cysteine

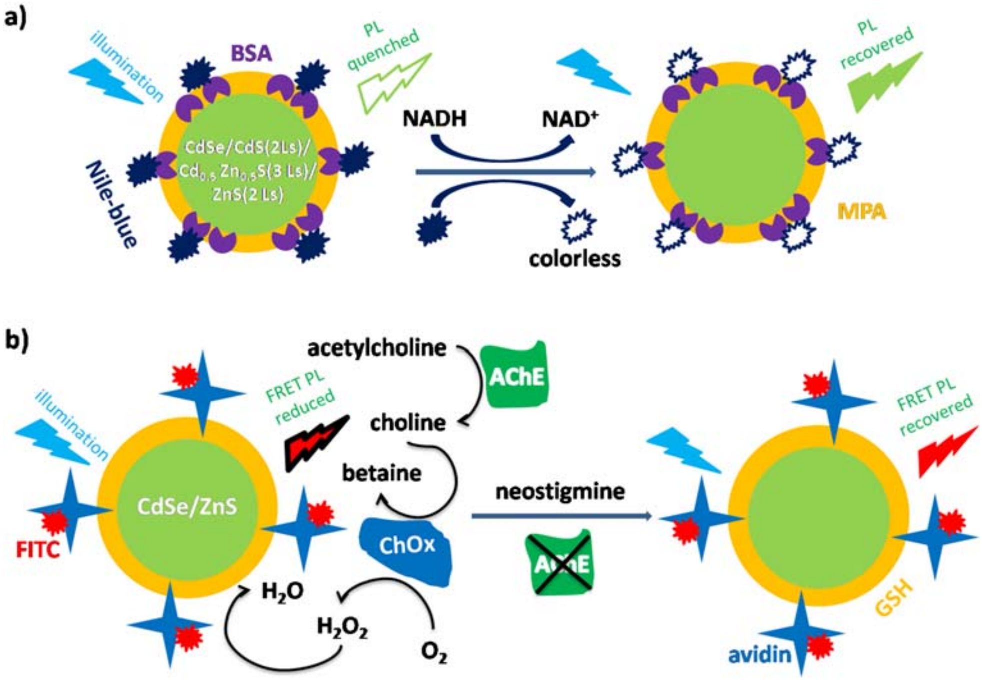

Fig. 4 Sensing involving bio-cascades. **a** MPA- and BSA-capped QDs are modified with Nile blue molecules. Due to strong quenching by FRET, the QD PL is quenched. In the presence of NADH, Nile blue is reduced to a colorless form, whose absorption does not overlap with the QD emission any more. This results in recovered QD PL. **b** GSH-capped CdSe/ZnS QDs are modified with FITC dye-labeled avidin molecules. In a signal cascade, acetylcholine is processed to choline by AChE. Choline is catalytically converted into betaine by the enzyme ChOx with a concomitant formation of H_2O_2. H_2O_2 quenches the QD PL. Quenching can be decreased by addition of neostigmine, which is an inhibitor the enzyme AChE

H 6

showed a high selectivity among other 19 natural amino acids [68]. Naturally, one would also like to perform sensing within living cells. To demonstrate real intracellular sensing, Freeman et al. conjugated Nile blue to BSA-modified MPA QDs, and delivered the complex into Hela cells by electroporation. The authors used this complex to sense the intracellular NAD^+-dependent metabolism. The principle is that oxidized Nile blue dye can strongly quench QDs by FRET. In the presence of NADH, Nile blue is reduced to a form in which it does not absorb in the visible region. In this configuration, the QD donor emission will not match the Nile blue acceptor absorption; thus no FRET occurs and the QDs' PL is restored (Fig. 4a). In this way the authors were able to sense NADH and its related cascades inside cells [69]. Another intracellular sensing was demonstrated by Orndorff et al. [70]. In this paper, QDs with different emission colors were protected by two types of peptide-based neurotoxins as ligands. These ligands can bind to corresponding protein targets which are endogenously expressed in cancer cells. By using fluorophore-labeled antibodies for colocalization experiments, the authors were able to prove that neurotoxin-protected QDs can specifically bind to endogenously expressed targets inside cancer cells. The authors claimed that QD–neurotoxin complexes could be used for the live assessment of the presence of markers inside cancer cells.

Outlook

QDs have been widely demonstrated for in vitro sensing of analytes ranging from ions to biomolecules with different strategies. The PL of QDs guarantees the high sensitivity of QD-based sensors. However, high sensing selectivity is still a big challenge, especially for sensing ions and small molecules. Sensing strategies based only on direct passivation/depassivation will not be able to achieve much higher sensitivity. Development of specific ligands/chelators which can bind to one analyte with a considerably higher affinity than to other analytes certainly will be one improvement. From this point of view, efforts should be put into synthesizing such ligands/chelators. An alternative approach is to learn from the natural selection mechanisms involved in living organisms, such as molecular recognitions in biocascades. Because of the explosive development of molecular biology, we envision a rapid improvement of high sensing selectivity by using molecular recognition. From a strategic point of view, a good strategy may be to use the combination of FRET/PET with molecular recognition. FRET/PET can provide a highly sensitive ratiometric readout, whereas molecular recognition can afford high selectivity. We think that this will be an important direction in QDs-based sensing in the future.

Compared with in vitro sensing, intracellular sensing is still in its infancy. There are only a few successful attempts published so far. Because the intracellular environment is much more complicated than in vitro conditions, QDs-based intracellular sensing still faces several challenges. First of all, there are still no reliable and general methods for delivering QDs into the cytosol without using physical force. Although QDs can be directly delivered into the cytosol by using "physical" methods such as microinjection or electroporation, obviously such methods are invasive and risk impairing cells. Naturally, QDs can be also incorporated into cells via uptake mechanisms such as endocytosis. However, in this case the QDs remain trapped in acidic intracellular vesicles instead of being suspended in the cytosol [71, 72]. In fact, delivery of QDs to the cytosol is already under discussion [73, 74], but is far from being completely understood. Second, the cellular environment is "hostile" to QDs. Though nowadays QDs with high colloidal stability exist [10], many QD-based sensors are not very stable in solutions with high ionic strength. In fact, any stabilizing coating shields the QD surface and thus might interfere with the detection mechanism. In addition, nonspecific binding of biomolecules to the QD surface will also interfere with intracellular sensing. Hence, we envision the increased use of QDs with biocompatible coating such as proteins, peptides, DNA, saccharides, and with chemical modifications such as polyethylene glycol. Quantitative studies of protein adsorption on nanoparticle surfaces [75] will help to optimize coatings. The vision of a "nanosubmarine" for intracellular detection [76] is still far from being ready in practice.

Acknowledgements This work was supported by the European Union (grant NANOGNOSTICS).

References

1. Ekimov AI, Onushchenko AA (1982) Sov Phys Semicond 16:775–778
2. Efros AL, Efros AL (1982) Sov Phys Semicond 16:772–775
3. Brus LE (1983) J Chem Phys 79:5566–5571
4. Parak WJ, Manna L, Simmel FC, Gerion D, Alivisatos P (2004) In: Schmid G (ed) Nanoparticles-from theory to application. Wiley-VCH, Weinheim, pp 4–49
5. Chan WC, Nie S (1998) Science 281:2016–2018
6. Wu MX, Liu H, Liu J, Haley KN, Treadway JA, Larson JP, Ge N, Peale F, Bruchez MP (2003) Nat Biotechnol 21:41–46
7. Rogach AL, Katsikas L, Kornowski A, Su D, Eychmüller A, Weller H (1997) Ber Bunsen Phys Chem 101:1668–1670
8. Murray CB, Norris DJ, Bawendi MG (1993) J Am Chem Soc 115:8706–8715
9. Pinaud F, King D, Moore H-P, Weiss S (2004) J Am Chem Soc 126:6115–6123
10. Pellegrino T, Manna L, Kudera S, Liedl T, Koktysh D, Rogach AL, Keller S, Rädler J, Natile G, Parak WJ (2004) Nano Lett 4:703–707

11. Lin C-AJ, Sperling RA, Li JK, Yang T-Y, Li P-Y, Zanella M, Chang WH, Parak WJ (2008) Small 4:334–341
12. Dabbousi BO, Rodriguez-Viejo J, Mikulec FV, Heine JR, Mattoussi H, Ober R, Jensen KF, Bawendi MG (1997) J Phys Chem B 101:9463–9475
13. Soper SA, Brown K, Ellington A, Frazier B, Garcia-Manero G, Gau V, Gutman SI, Hayes DF, Korte B, Landers JL et al (2006) Biosens Bioelectron 21:1932–1942
14. Clark HA, Barker SLR, Brasuel M, Miller MT, Monson E, Parus S, Shi ZY, Song A, Thorsrud B, Kopelman R et al (1998) Sens Actuators B Chem 51:12–16
15. Stoll C, Kudera S, Parak WJ, Lisdat F (2006) Small 2:741–743
16. Yildiz HB, Tel-Vered R, Willner I (2008) Angew Chem Int Ed 47:6629–6633
17. Stoll C, Gehring C, Schubert K, Zanella M, Parak WJ, Lisdata F (2008) Biosens Bioelectron 24:260–265
18. Privett BJ, Shin JH, Schoenfisch MH (2008) Anal Chem 80:4499–4517
19. Medintz IL, Uyeda HT, Goldman ER, Mattoussi H (2005) Nat Mater 4:435–446
20. Costa-Fernández JM, Pereiro R, Sanz-Medel A (2006) Trends Anal Chem 25:207–218
21. Sapsford KE, Pons T, Medintz IL, Mattoussi H (2006) Sensors 6:925–953
22. Lin C-AJ, Liedl T, Sperling RA, Fernández-Argüelles MT, Costa-Fernández JM, Pereiro R, Sanz-Medel A, Chang WH, Parak WJ (2007) J Mater Chem 17:1343–1346
23. Somers RC, Bawendi MG, Nocera DG (2007) Chem Soc Rev 36:579–591
24. Raymo FM, Yildiz I (2007) Phys Chem Chem Phys 9:2036–2043
25. Gill R, Zayats M, Willner I (2008) Angew Chem Int Ed 47:7602–7625
26. Moore DE, Patel K (2001) Langmuir 17:2541–2544
27. Chen YR, Rosenzweig Z (2002) Anal Chem 74:5132–5138
28. Fernandez-Argüelles MT, Jin WJ, Costa-Fernandez JM, Pereiro R, Sanz-Medel A (2005) Anal Chim Acta 549:20–25
29. Susha AS, Munoz_Javier A, Parak WJ, Rogach AL (2006) Colloids Surf A Physicochem Eng Asp 281:40–43
30. Lai S, Chang X, Mao J, Zhai Y, Lian N, Zheng H (2007) Ann Chim 97:109–121
31. Wang JH, Wang HQ, Zhang HL, Li XQ, Hua XF, Cao YC, Huang ZL, Zhao YD (2007) Anal Bioanal Chem 388:969–974
32. Liu FC, Chen YM, Lin JH, Tseng WL (2009) J Colloid Interface Sci 337:414–419
33. Xia Y, Zhu C (2008) Analyst 133:928–932
34. Tang B, Niu J, Yu C, Zhuo L, Ge J (2005) Chem Commun (Camb) 4184–4186
35. Ali EM, Zheng Y, Yu HH, Ying JY (2007) Anal Chem 79:9452–9458
36. Banerjee S, Kar S, Santra S (2008) Chem Commun (Camb) 3037–3039
37. Wang X, Guo X (2009) Analyst 134:1348–1354
38. Fernández-Argüelles MT, Yakovlev A, Sperling RA, Luccardini C, Gaillard S, Medel AS, Mallet J-M, Brochon J-C, Feltz A, Oheim M et al (2007) Nano Lett 7:2613–2617
39. Medintz IL, Clapp AR, Mattoussi H, Goldman ER, Fisher B, Mauro JM (2003) Nat Mater 2:630–638
40. Patolsky F, Gill R, Weizmann Y, Mokari T, Banin U, Willner I (2003) J Am Chem Soc 125:13918–13919
41. Snee PT, Somers RC, Nair G, Zimmer JP, Bawendi MG, Nocera DG (2006) J Am Chem Soc 128:13320–13321
42. Ruedas-Rama MJ, Wang X, Hall EA (2007) Chem Commun (Camb) 1544–1546
43. Callan JF, Mulrooney RC, Kamila S, McCaughan B (2008) J Fluoresc 18:527–532
44. Mulrooney RC, Singh N, Kaur N, Callan JF (2009) Chem Commun (Camb) 686–688
45. Ruedas-Rama MJ, Hall EA (2008) Analyst 133:1556–1566
46. Shang L, Zhang L, Dong S (2009) Analyst 134:107–113
47. Touceda-Varela A, Stevenson EI, Galve-Gasion JA, Dryden DT, Mareque-Rivas JC (2008) Chem Commun (Camb) 1998–2000
48. Yan XQ, Shang ZB, Zhang Z, Wang Y, Jin WJ (2009) Luminescence 24:255–259
49. Huang CP, Li YK, Chen TM (2007) Biosens Bioelectron 22:1835–1838
50. Vinayaka AC, Basheer S, Thakur MS (2009) Biosens Bioelectron 24:1615–1620
51. Wang Y, Tang ZY, Correa-Duarte MA, Pastoriza-Santos I, Giersig M, Kotov NA, Liz-Marzan LM (2004) J Phys Chem B 108:15461–15469
52. Zhang Y, Li Y, Yan XP (2009) Anal Chem 81:5001–5007
53. Wu CS, Cupps JM, Fan X (2009) Nanotechnology 20:305502
54. Lee J, Choi Y, Kim J, Park E, Song R (2009) Chemphyschem 10:806–811
55. Zhou D, Ying L, Hong X, Hall EA, Abell C, Klenerman D (2008) Langmuir 24:1659–1664
56. Cui D, Pan B, Zhang H, Gao F, Wu R, Wang J, He R, Asahi T (2008) Anal Chem 80:7996–8001
57. Kim GI, Kim KW, Oh MK, Sung YM (2009) Nanotechnology 20:175503
58. Boeneman K, Mei BC, Dennis AM, Bao G, Deschamps JR, Mattoussi H, Medintz IL (2009) J Am Chem Soc 131:3828–3829
59. Xia Z, Xing Y, So MK, Koh AL, Sinclair R, Rao J (2008) Anal Chem 80:8649–8655
60. Yao H, Zhang Y, Xiao F, Xia Z, Rao J (2007) Angew Chem Int Ed Engl 46:4346–4349
61. Medintz IL, Mattoussi H (2009) Phys Chem Chem Phys 11:17–45
62. Chen Z, Li G, Zhang L, Jiang J, Li Z, Peng Z, Deng L (2008) Anal Bioanal Chem 392:1185–1188
63. Callan JF, Mulrooney RC, Kamila S (2008) J Fluoresc 18:1157–1161
64. Freeman R, Bahshi L, Finder T, Gill R, Willner I (2009) Chem Commun 764–766
65. Freeman R, Finder T, Bahshi L, Willner I (2009) Nano Lett 9:2073–2076
66. Gill R, Bahshi L, Freeman R, Willner I (2008) Angew Chem Int Ed 47:1676–1679
67. Bahshi L, Freeman R, Gill R, Willner I (2009) Small 5:676–680
68. Han B, Yuan J, Wang E (2009) Anal Chem 81:5569–5573
69. Freeman R, Gill R, Shweky I, Kotler M, Banin U, Willner I (2009) Angew Chem Int Ed 48:309–313
70. Orndorff RL, Rosenthal SJ (2009) Nano Lett 9:2589–2599
71. Sun YH, Liu YS, Vernier PT, Liang CH, Chong SY, Marcu L, Gundersen MA (2006) Nanotechnology 4469
72. Parak WJ, Boudreau R, Gros ML, Gerion D, Zanchet D, Micheel CM, Williams SC, Alivisatos AP, Larabell CA (2002) Adv Mater 14:882–885
73. Delehanty JB, Mattoussi H, Medintz IL (2009) Anal Bioanal Chem 393:1091–1105
74. Luccardini C, Yakovlev A, Gaillard S, Hoff Mvt, Alberola AP, Mallet J-M, Parak WJ, Feltz A, Oheim M (2007) J Biomed Biotechnol 2007: Article ID 68963
75. Röcker C, Pötzl M, Zhang F, Parak WJ, Nienhaus GU (2009) Nat Nanotechnol 4:577–580
76. Peteiro-Cattelle J, Rodriguez-Pedreira M, Zhang F, Rivera Gil P, del Mercato LL, Parak WJ (2009) Nanomedicine 4:967–979

Academic Career

April 2007 - Current	**Promotion nach Abschluss (Doctorate)** from Philipps Universität Marburg, at Physics Department, Group of Biophotonics (Chair; Prof. Dr. Wolfgang J. Parak)
Sep. 2004 - 2006	**M.Phil in Physics** from Quaid-i-Azam University Islamabad, Pakistan
Sep.2002 – 2004	**Master of Physics** from Quaid-i-Azam University Islamabad, Pakistan.
Sep.2000 – 2002	**Bachelor of Science** from Punjab University Lahore, Pakistan.
Sep.1998 - 2000	**Higher secondary** from Government College Kahuta, Pakistan.